ABSTRACT

Title of dissertation: CIRCUMSTELLAR MATERIAL ON AND OFF THE MAIN SEQUENCE

Amy Samantha Steele
Doctor of Philosophy, 2020

Dissertation directed by: Dr. John Debes
Space Telescope Science Institute, Maryland

Circumstellar (C-S) dust is present around stars throughout their entire life cycles. About 20-50% of sun-like stars on the main sequence (MS) have belts of rocky material like the Solar System's asteroid and Kuiper Belts. Observations of white dwarfs (WDs), the endpoints of stellar evolution for stars 0.8 to 8 times the mass of our sun, reveal that 20-50% of them have accreted metals typically found in rocky bodies like the Earth. Between the MS and WD stages, stars expand, engulfing any nearby companions, and lose mass, destabilizing their planetary system. So, this "pollution" is unexpected because the inner regions of system near a WD should be barren.

The focus of this thesis is on the observation and characterization of C-S gas and dust around stars of increasing age, with the goal of studying the evolution of the material in planetary systems. Are we seeing unchanged Earth-like bodies survive long enough to pollute a WD? What are the stellar systems like along the way? To address these questions, we explore several case studies.

We present submillimeter observations with the Submillimeter Array (SMA), the Combined Array for Research in Millimeter-wave Astronomy (CARMA), and the Atacama Large Millimeter/submillimeter Array (ALMA) at ∼2" resolution that spatially resolve the C-S dust or debris disks around five nearby (d ∼50 pc) young solar analogues. We perform an MCMC analysis to fit for basic structural parameters, including the inner radius and width of the debris ring, the total mass of the disk, and the characteristic dust grain size. We find that the cold outer belts around the solar analogues in our sample generally exhibit properties consistent with scaled-up versions of the Solar System's Kuiper Belt. The composition of the dust is consistent with an astronomical silicate.

Dust around post-MS stars is expected as a result of stellar evolution, but if a star has not yet reached a stage of predicted mass loss, then the dust is unexpected. We analyze a set of post-MS stars with excess IR emission, using the most recent *Gaia* data release (DR2) to investigate the stellar age, and *Herschel* observations at far-IR and submillimeter wavelengths to constrain the thermally emitting dust. We find that all but one of the 20 stars are post-MS. For the stars detected at submillimeter wavelengths, we find that their spectral indices, α are more shallow than the α that would be expected of grains in the interstellar medium (ISM), pointing toward grain growth in these systems. A fraction of the sample presents characteristics (fast rotation, enhanced lithium abundance, and excess IR emission) that point toward an external source causing the dust excess. One explanation for this trifecta of properties is that these stars have recently engulfed a planet.

Due to the relatively fast gravitational settling times of heavy elements in a

WD atmosphere, the presence of those heavy elements is linked to the accretion of planetesimals perturbed by one or more outer planets to within the white dwarf's tidal disruption radius. We present an updated high signal-to-noise ratio spectrum, a new Keck HIRES spectrum, an updated white dwarf atmosphere analysis, and a self-consistent model of the C-S gas around white dwarf WD 1124-293. We constrain the abundances of Ca, Mg, Fe, and a number of other elements in both the photosphere of the white dwarf and the circumstellar disk. We find the location of the gas is approximately one hundred white dwarf radii, the C-S and photospheric compositions are consistent, the gas is not isothermal, and the amount of C-S Ca has not changed in two decades. We also demonstrate for the first time how the radiative transfer code Cloudy can be used to model C-S gas viewed in absorption around a polluted white dwarfs.

Modeling the abundances of C-S gas around polluted white dwarfs with Cloudy provides a new method to measure the instantaneous composition of the material sublimating from the polluting planetesimals. Expanding the work with WD 1124-293, we use Cloudy to predict the physical conditions of C-S gas around model WD photospheres with temperatures ranging from 9000 K to 24,000 K. The models can be used to determine the gas temperature with distance from the star, predict optical depths, constrain the hydrogen number density, and possibly constrain the location of the gas. We compare our models to a small sample of WDs with emission features, and show how the equivalent width can be useful as a diagnostic tool in these systems.

We find, unsurprisingly, that it is difficult to determine the composition of dust

around stars on and off the MS. However, the modeling of gas around WDs offers an opportunity to determine the composition of planetesimals in evolved stellar systems. We find that the compositions of C-S gas around polluted WDs are consistent with the bulk Earth, but recommend further modeling. The radiative transfer code, Cloudy can and should be used to search for trends among these planetary systems, to provide unprecedented insight to the composition of extrasolar planetesimals that have survived the evolution of their host stars.

CIRCUMSTELLAR MATERIAL ON AND OFF THE MAIN SEQUENCE:
Methods and tools for constraining the composition of gas and dust around stars

by

Amy Samantha Steele

Dissertation submitted to the Faculty of the Graduate School of the
University of Maryland, College Park in partial fulfillment
of the requirements for the degree of
Doctor of Philosophy
2020

Advisory Committee:
Dr. John Debes, Research Advisor
Professor Drake Deming
Professor Meredith Hughes
Dr. Marc Pound
Professor Rajarshi Roy, Dean's Representative
Professor Stuart Vogel, Chair

Preface

The work in this thesis has partially been published in peer-reviewed journals and presented at international conferences.

Chapter 2 was published in the Astrophysical Journal, Volume 816, Issue 1, as "Resolved Millimeter-wavelength Observations of Debris Disks around Solar-type Stars" (Steele et al. 2016). The work for this chapter was partially completed at Wesleyan University as part of my Masters thesis. The work was completed in my first year at the University of Maryland.

Chapter 4 is currently accepted for publication in the Astrophysical Journal.

Preliminary results in Chapters 3, 4, and 5 have been presented at meetings of the American Astronomical Society (#230, #231, #233, and #235) and at Extreme Solar Systems IV, in Reykjavik, Iceland (2019).

Foreword

Why is this thesis important? This is a great question. When I consider the suffering experienced and lived by millions of humans on this particular planet, devoting my modest mental efforts to the study of objects that might as well be imaginary seems a bit wasteful. That being said, things that exist and existed so long ago that it doesn't make sense for a human being to consider them given the time elapsed, are truly fascinating. Few sights give pause (in a good way) to all homo sapiens with that gift. The beauty of the night sky is one of them.

At a time of relative tumult (yet another wave of civil rights activism, a reckoning for the institutionalized racism rampant in the US at the time of writing, and a world-wide pandemic–predicted, but unprepared for), paying special attention to stars and their bits of dirt and gas seems small, and to be honest, it is (considering daily experiences).

However, given humanity's and my own love for the night sky and the weird objects that exist in this universe, a little "Black girl magic" (i.e. Black Excellence) in whatever form is needed in the world right now. I tackled so much astronomy in this thesis that I ended up surprising myself. I hope you will bear with me.

About the science: this work presents examples of how we attempt to and eventually figure out what the stuff around stars is made of—over astronomical time scales. The births and deaths of stars are violent events, yet the planets and asteroids orbiting these stars do their best to weather their situations. In the cases presented in this work, those celestial bodies succeed.

Dedication

To my parents,

Ruth Steele and Clyve Steele

Acknowledgments

This entire thesis is dedicated to and written for my parents, Ruth and Clyve Steele. They left their home country, Grenada, in search of greater opportunities and eventually settled in the United States. Everything that my parents did was to allow me and my sisters to have it better. They have never placed any limitations on what they believe I can do and they supported my interest in science when most others expected little to nothing from me. I would not have accomplished what I have thus far without their love and endless support. I like you and I love you. Thank you for everything from the bottom of my heart.

Dr. Katie Jameson, my stint at the University of Maryland is all thanks to you (good and bad, but mostly good). You have the high honor of being mentioned first after family due to the impact you've made on my life, and because you have become family. I truly doubt that I would have made it through the program without your constant and steady guidance and support.

Speaking of chosen family members and support, thank you Sara Frederick for being my person in Maryland. I don't believe I gave you a choice when I decided that we would be friends, but I'm eternally grateful that you acquiesced. UMD would've been an unflattering shade of gray without you. To anyone who reads any significant chunk of this work, know that it is readable thanks to Sara's and Katie's efforts (and the comments from my committee). Thank you, Sara. Sergio Mundo-Santiago, you are and will always be one of my favorite people. To Laura Lenkic, thank you for being such a good friend to me. I strive to reach your level of

kindness and talent.

I had a shift of research advisors in my second year. Two people who are responsible for helping me find ways to pay my rent and thereby supporting this PhD work, are Chrissy Richey and Meagan Thompson. Chrissy, you are an amazing person and I'm lucky to know you. Meagan, thank you for giving me a job at NASA Headquarters and for being patient with me as I attempted to juggle working for you, a new research project, and being a part-time teaching assistant. I will try my best to pay it forward.

Barbara, Dorinda, Susan, Mona, and the other front office staff: thank you for your kindness, support, and patience with me as I navigated the department and university policies. The department would crumble without you. Barbara, you are a Queen.

To the basement boys/men/PhDs, Marc Pound, Mark Wolfire, and Peter Teuben. You three were consistently the majority of the kindest and scientifically supportive members in the department during my time at the University of Maryland. Thank you for always answering my questions as if I were a scientist (I am), and for being infinitely supportive of me and my CASA/computer woes. Mark, you are a magical human. Peter, I wish you good health, and happiness with all coding languages. Marc, I started the program hanging out with you and it seems like things will end that way. I appreciate you.

Matthew Knight, thank you for always asking me how I was doing and for listening to the answer. UMD is a little less bright without you. Brad Cenko, you and your Asics are a delight. Thank you for the free, impromptu therapy sessions

at Trader Joe's.

Stuart Vogel, where to begin? I would have likely been forced to leave the program without your countless interventions on my behalf (including the ones of which I'm aware). I decided that we would be buddies when I learned of our shared alma mater and you seemed to be okay with that. Thank you for being the main full faculty member who consistently had my best intentions at heart throughout my time at UMD and beyond.

To my classmates, and especially to Dana Louie and Pradip Gatkine, thank you for being such fantastic examples of kindness and academic excellence. Dana and Jeff, you welcomed me into your home more times than I can count, and I'm lucky to be able to call you friends. Pradip, your kindness and spirit are like neutrinos—so much and so swift. I can't wait to watch your career unfold. To Blake Hartley, thank you for your friendship and (bad) jokes.

To my past (research) advisors: Aki Roberge, Andy Harris, and Drake Deming, thank you for the time you spent attempting to mold me. I'm aware that I can be like marble instead of clay.

To Meredith Hughes, you know more than anyone about my marble-like nature, but you are an artist with any medium. I have you to thank for seeding my current scientific prowess. Your patience with me when I was a master's student at Wesleyan was integral to me not feeling rejected by academia as I dove into astronomy research following a four-year hiatus. You taught me radio astronomy—which is still like magic to me, even though I know it's science—and showed me what it takes to do research properly. I have always been and will always be in awe of you.

Thank you for your continued support and encouragement.

To Shaye Storm and Diana Windemuth, thank you for your tutelage when I needed help, and for your lasting friendship. Shaye, I've never made a friend so fast. Thank you for collecting me. Diana, you taught me how to study, opened my eyes to the power of Python when everyone was still using IDL, and introduced me to your favorite things. Thank you! To Maggie and Mark McAdam, I appreciate you both. Thank you for lending an ear when I needed to talk, for teaching me to boulder (rock climbing), and for inviting me into your life with love and open arms. To Ben Kolesar, thank you for feeding me on your trips to the states and letting me vent about grad school.

To everyone who gave time and energy to GRAD-MAP (Graduate Resources Advancing Diversity with Maryland Astronomy and Physics), thank you for supporting a program that will hopefully contribute to future "baby" Amys having at least one Black astronomy professor. My work with this program saved me numerous times as I struggled with my place in this field.

Thank you W. M. Keck Observatory for being so welcoming and showing me that there's at least one place that could be comfortable for a black, female astronomer. To Sherry Yeh, thank you for choosing to invite me to work with you as a visiting scholar. I aspire to your level of knowledge and chill.

To Siyi Xu, thank you for financially supporting me and showing me (and the rest of the world) just how cool WD 1145+017 is. You are an incredible scientist and I am lucky to have gotten to work with you.

To my thesis committee members: thank you for agreeing to take this journey

with me, and for reading my work! Your feedback greatly improved this dissertation, and it will greatly improve my future publications and how I approach my research.

Finally, to Dr. John Debes, my main research advisor, thank you for saying "yes" to being my advisor when others said "no." This thesis exists with the grace of your decision. Thank you, thank you, thank you.

Table of Contents

List of Tables

List of Figures

Chapter 1: Introduction

Planetary system evolution is studied observationally by examining snapshots in time as the process unfolds over millions to billions of years. Circumstellar (C-S) disks are the flat reservoirs of material remaining after a star forms, containing the byproducts of stellar formation: planets, asteroids, comets, and smaller bits of debris or dust. We study our own Solar System 4.5 billion years after it formed through analysis of meteorites, multi-wavelength observations, and typically uncrewed missions to different bodies. However, the chemical make-up of the planets and dwarf planets (i.e., how much of the periodic table elements are present relative to hydrogen) is incomplete compared to what we know about Earth.

Comparisons among elemental abundances in the Solar System, elemental abundances of dying stars, and isotopic compositions of pre-solar grains give insight into galactic chemical evolution. As enough snapshots and data are collected, we begin to answer the following questions: Is Earth normal? How unique are the compositions of the Solar System's terrestrial planets and rocky bodies? For how long do planets and asteroid belts survive the evolution of their host stars off the main sequence?

From observations with *Kepler*, we now know that nearly every star has at least one planet (Swift et al., 2013). Observationally, it is easier to detect a Jupiter-sized planet around a sun-like star, yet many of those Jupiter analogues are closer to their host stars than Mercury is to our Sun. Additionally, observations of young circumstellar disks show planet embryos currently forming, and analyses of C-S gas

Figure 1.1: The Evolutionary path of a sun-like star

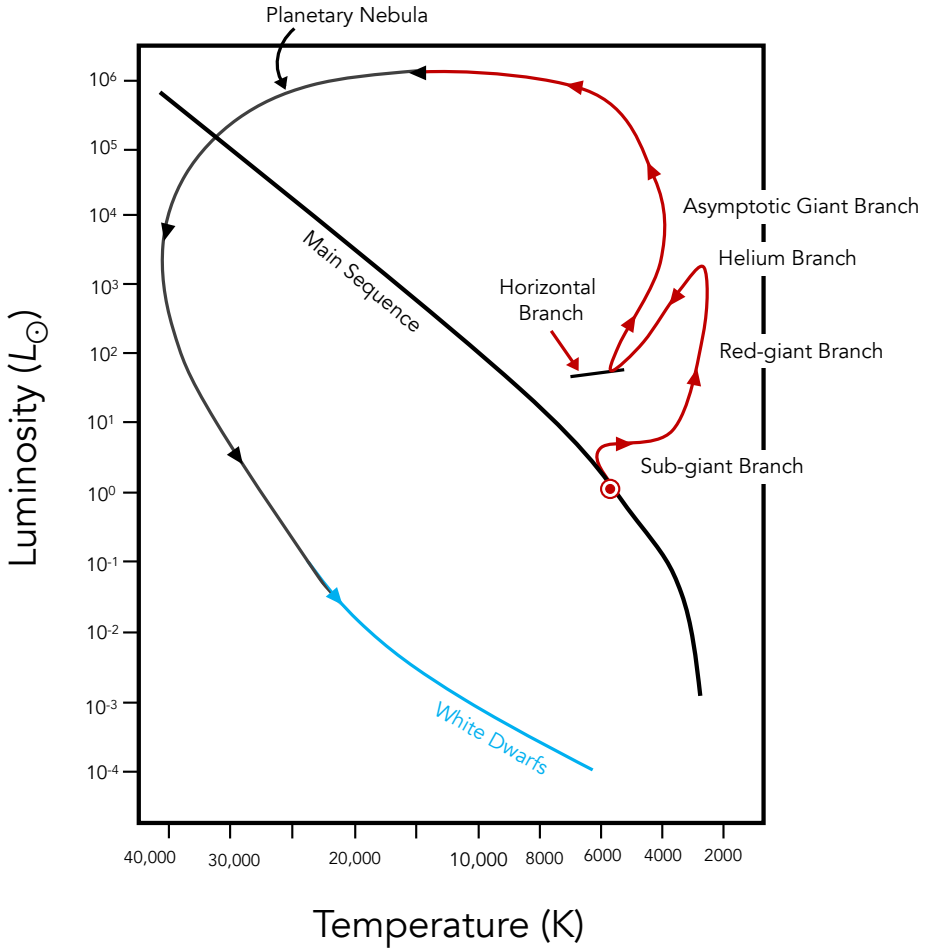

NOTE – The evolutionary path of a sun-like star.

around dead stars show evidence that giant planets have survived.

1.1 The Evolution of a Sun-like Star

Stars form from large clouds of gas and dust. The initial mass of a star determines its fate and is the most important characteristic.[1] The most massive stars have the shortest lifetimes and the least massive stars have ages that rival

[1]The metallicity of the star is also important.

the age of the universe.[2] The Sun is approximately 4.5 billion years old and is currently radiating energy due to the fusion of hydrogen into helium, the hallmark of stars in the primes of their lives. The inner workings of a star, i.e., which light elements are fusing into heavier ones, and the method by which the resulting energy is transported (i.e., conduction, radiation, convection), characterize each stage of its life. If planets form and settle into stable orbits, then there is likely at least one reservoir of leftover material, akin to the asteroid and Kuiper Belts in the Solar System.

If one observes the luminosity and temperature of enough stars, the life cycle of stars en masse can be discerned. One such cycle for a sun-like star is shown in Figure 1.1. The cycle begins on the main sequence (MS) where stars fuse hydrogen into helium. Once the hydrogen is depleted, the star undergoes internal physical changes and leaves the MS. As the star moves through the sub-giant and red-giant branches, it contracts and cools. When the conditions in the core are such that helium begins to fuse into heavier elements, this marks the "helium flash." The ensuing path on the horizontal branch (HB) is analogous to the main sequence, except on the HB, the fusing element is helium. When the helium is depleted, the star moves up the asymptotic giant branch (AGB). The relationship between luminosity and temperature is $L = 4\pi\sigma R^2 T^4$, where R is the radius of the star and T is the temperature of the star. The increase in luminosity and decrease in temperature observed post-main sequence means the radius of the star increases. This increase in stellar radius leads to planets within a few astronomical units (au)[3] being consumed by the star by tidal evolution and subsequent engulfment.

During the AGB, the star begins shedding mass in the form of ash, or complex

[2] In this way, stellar lives mirrors human lives in the sense that the Janis Joplins and Jimi Hendrixes of us live fast and die young, while those who go about their business quietly can live beyond 100 years.

[3] The astronomical unit (au) is the distance from the Earth to Sun, 1 au $= 1.496 \times 10^{13}$ cm $= 9.296 \times 10^7$ miles.

molecules containing carbon. During this stage, the star is surrounded by large amounts of dust and molecular gas. The core of this dying star is now fusing carbon into oxygen. Following this stage, the outer layers of the star are expelled, producing a planetary nebula (many images of these have been captured by the Hubble Space Telescope (HST)). The mass loss in the system means the orbits of leftover bodies move outward, possibly leading to a destabilization of remnant reservoirs of material. Following the planetary nebula stage, the leftover carbon/oxygen core of the star is now visible as a white dwarf (WD). Though this evolutionary process describes the life cycle of a sun-like star, WDs are the remnants of evolution for stars with initial masses $0.5 - 8\,M_{\odot}$.

If a star shining due to nuclear fusion is like a flame, then a white dwarf is like an ember. With no internal source of heat, WDs cool predictably over time until they are no longer visible. The spectra of WDs are very sparse of absorption features as compared to the solar spectrum, and typically only show hydrogen or helium absorption lines. The WD spectral type, DA for hydrogen and DB for helium, depends on which gas remains in the outermost layer of the WD photosphere. If the photosphere of a WD is polluted by some metal heavier than He[4], then the metal is easily detectable as an absorption feature in the spectrum.

1.2 Observing Circumstellar Gas and Dust

Circumstellar material persists around stars from the main sequence to the white dwarf stage, changing as the host star evolves.

[4]Metals in this work constitute any element heavier than helium; oxygen is lumped in with the metals in this work.

1.2.1 Debris Disks on the MS

Debris disks are found around main sequence stars and were discovered in 1984 by the Infrared Astronomical Satellite (IRAS) from excess emission around the star Vega (Aumann et al., 1984). The C-S disks of planetary systems change over time from being gas-rich protoplanetary disks in a dynamic, feedback-driven relationship with the host star, to the skeletal reservoirs of the dusty remnants of planet formation. Debris disks are optically thin and their gas masses are extremely low. Submillimeter CO emission is not detected for most debris disks, which suggests that most of the primordial gas has been removed or captured by planets.

C-S dust absorbs light from its host star and reradiates it at longer, infrared (IR) wavelengths. Debris disks (and dust) are detectable in the spectral energy distribution (SED) of a stellar system as excess infrared flux detected above the level of the stellar photosphere. The thermal emission from the dust around a sun-like star peaks at wavelengths of $\sim$100 μm and dominates the SED of the star-disk system in this wavelength regime. Debris disks tend to show two distinct humps in an SED spanning 1 μm to 1000 μm, with the dip between them revealing that the inner region of the disk has been cleared. For several disks (β Pic, HR 8799, etc.), this inner clearing can be related to the presence of a planet. We show a cartoon stellar system and representative SED in Figure 1.2 to further clarify these points. It should be noted that the dust emission can overpower the stellar spectrum in systems where the dust is optically thick and around stars losing mass.

Millimeter-wavelength interferometry provides sufficient angular resolution to reveal the spatial distribution of dust grains large enough to resist radiation pressure. Millimeter-wavelength observations are highly complementary to observations at optical and infrared wavelengths which probe the spatial distribution of smaller dust grains that are subject to different physical processes. Many disks have been

Figure 1.2: Observing Debris Disks

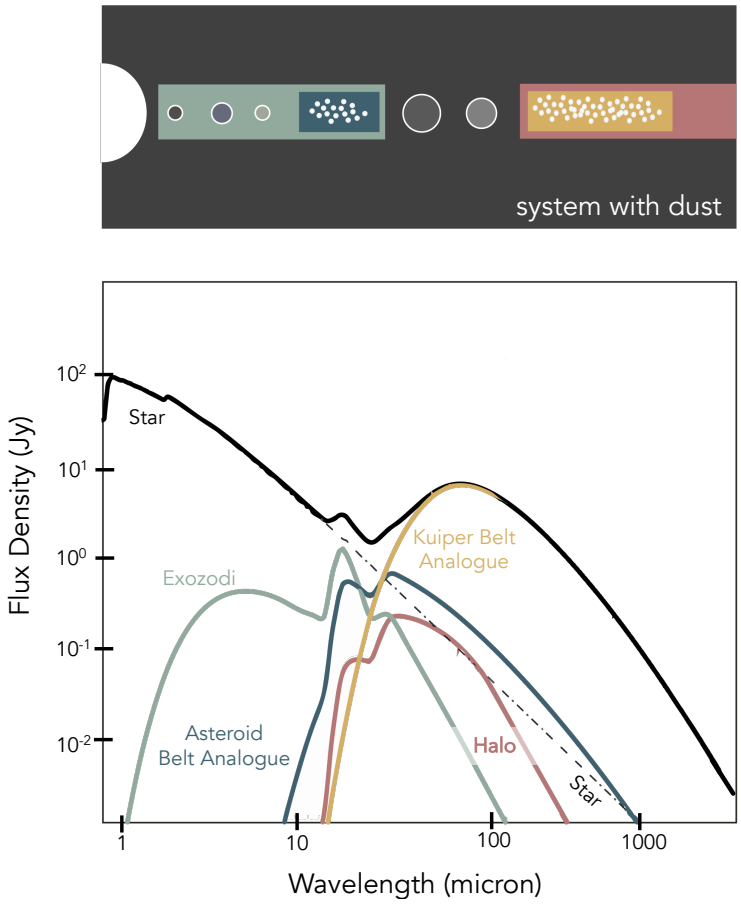

NOTE — Figure adapted from Hughes et al. (2018). The top panel shows a stellar system with planets and dust viewed edge-on. The contributions to the SED are color-coded to match where they arise in the disk. The exozodi is the swath of small grains that might fill the inner stellar system where there is a reservoir of material in an asteroid belt analogue. We view this exozodi contribution as the zodiacal light. Small grains can be forced out to large distances by stellar radiation pressure, forming a halo. The Kuiper Belt analogue also contributes to the production of grains in the halo, and at its cooler temperature, peaks at IR wavelengths.

spatially resolved using (sub)millimeter interferometry: Fomalhaut (Boley et al., 2012), HR 8799 (Hughes et al., 2011), AU Mic (MacGregor et al. 2013; Wilner et al. 2012), β Pictoris (Dent et al. 2014; Wilner et al. 2011), HD 107146 (Corder et al. 2009; Hughes et al. 2011; Ricci et al. 2015), HD 61005 (Ricarte et al., 2013), HD 32297 (Maness et al., 2008), and HD 21997 (Kóspál et al. 2013; Moór et al. 2013). These observations have revealed a striking diversity of debris disk properties: narrow millimeter rings with or without scattered light haloes, broad rings with or without haloes, unusually large quantities of molecular gas, and evidence for interactions with the interstellar medium (ISM).

1.2.2 RGB disks and AGB debris

Debris disks and the planets that sculpt them are a common occurrence around main sequence stars, yet little is known regarding their fate as their host star evolves off the main sequence. Stars with initial masses $0.5 - 8 M_{\odot}$ will eventually evolve along the red giant branch (RGB) and the asymptotic giant branch (AGB). While on the RGB, the number of stars with detectable debris disks decreases (Bonsor & Wyatt, 2010).

Material within a few au of their host stars is engulfed by the growing red giant, producing observable gas and dust. De la Reza et al. (2015) suggest that the interaction of the strong winds from the K giants with their persisting asteroidal/cometary disks leads to the liberation of carbon from the debris, and the formation of polycyclic aromatic hydrocarbons (PAHs) in a circumstellar shell. For giants that have begun mass loss, Dong et al. (2010) describe a mechanism through which wind drag of planetesimals could boost collisional cascades, creating a debris disk out to $\sim$50 au persisting to the white dwarf stage.

While on the AGB, stars produce C, N, O, and s-process elements through the triple alpha process in a helium shell surrounding an inert C/O core. Molecules

(e.g. CO, H_2, CN, and TiO), and dust grains form in the cooler, outer layers of the stellar atmosphere that are levitated by pulsation. The star loses mass due to radiation pressure expelling the newly formed grains and gas. This mass loss leads to the formation of expanding circumstellar envelopes (CSEs), whose constituents help replenish the ISM. CSEs can be observed via the detection of infrared excesses (IR) (e.g. R Sculptoris), which can often be confused with debris disks (e.g. κ CrBor) and binary/planetary interactions. However, the chemical compositions of the gas and dust in a CSE reflect the composition of the stellar atmosphere at the time when the material was ejected (Höfner & Olofsson, 2018).

These different pathways for producing C-S dust can inform how the remnants of planetary systems evolve off the main sequence. By studying material around these "retired" stars we can begin to separate these effects and understand their evolutionary state and the nature of their IR-excesses.

1.2.3 White Dwarfs with Circumstellar Gas

Observations of polluted WDs provide a singular opportunity to discover the composition of the planetesimals that survive beyond the giant phase. About 25-50% of WD atmospheres contain elements heavier than helium (Koester et al. 2014; Zuckerman et al. 2003). These elements should sink rapidly into the stellar interior, so their presence on the surface of a WD hints at current replenishment. While the evolution of the progenitor star obliterates material inward of ∼a few au, planets and minor bodies beyond ∼a few au survive post-main-sequence (post-MS) evolution. Recent work suggests that many WDs are in the process of accreting material from tidally disrupted planetesimals from the progenitor stars's planetary disk (e.g. Mustill et al. 2014; Veras et al. 2014, 2015). The existence of white dwarf stars with terrestrial elements heavier than C and O in their atmospheres, and transiting, disintegrating planetesimals requires that rocky bodies survive stellar evolution. After

Figure 1.3: Transits of WD 1145+017

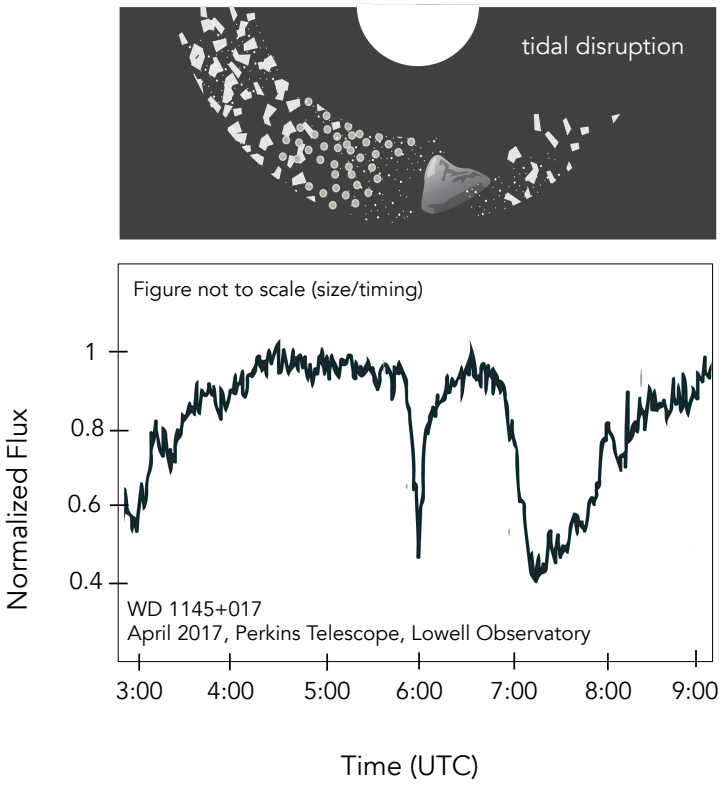

NOTE — In the top panel is my artistic rendition of the transiting, disintegrating planetesimal around WD 1145+017. The WD is shown with the half circle. The relative distances are not to scale. In the lower panel I show a light curve of WD 1145+017 from April 22, 2017 taken with the Perkins 72" telescope at Lowell Observatory (now owned by Boston University). The period of the transit is ~ 4.5 hours and the transit depth reached 60%. Noteworthy here is the asymmetric shape of all features (ingress and egress).

the white dwarf progenitor leaves the main sequence and undergoes mass loss, the progenitor's planetary system destabilizes, perturbing planetary orbits to the white dwarf's Roche limit (Debes & Sigurdsson 2002; Debes et al. 2012).

This phenomenon was first reported by Vanderburg et al. (2015) with WD 1145+017 (WD 1145). WD 1145 has a transiting, disintegrating planetesimal. Similar to observations of exoplanetary transits, the disintegrating planetsimal of WD 1145 is observed to transit the star, yet with transit shapes indicative of a non-solid body that vary on a weekly timescale. The transit period is about 4.5 hours and the transit depths reached about 60% during periods of high activity.[5] In Figure 1.3, I show a light curve of WD 1145 collected with the Perkins Telescope at Lowell Observatory (instrument: PRISM, date: 04/22/2017, filter: V, calibration with averaged sky/chromey spot flat and bias frames, exposure time: 45 seconds).

High-resolution spectroscopy is extremely useful in analyzing WDs with C-S gas. The composition of the accreted material and the total deposited mass can be determined via metal absorption or emission lines in the white dwarf spectra, as well as fits to an infrared excess, if present. The elemental abundances of metals in the photospheres have been shown to match the abundances of the C-S gas in at least one case (Fortin-Archambault et al., 2020). These abundances are consistent with the accretion of large asteroids like Ceres or Vesta in our own solar system.

The shapes of the spectral lines are used to place constraints on the location of the gas responsible for the feature. Emission lines of WDs with C-S gas display a double-peaked shape, indicating the gas is orbiting the WD on an inclined orbit. Absorption features of WDs with polluted photospheres and C-S gas show the following features: (1) C-S lines that are broadened due to the Doppler effect; (2) spectra containing two sets of features for species visible in the photosphere and the C-S gas; and (3) photospheric absorption features that are gravitationally redshifted

[5]The 60% transit depth occurs thanks to the small size of a WD, typically $\sim$ 1.6 times the radius of the Earth.

by ~ 30 km s^{-1}.[6] The properties of the metals in the photosphere do not necessarily match those in the C-S gas due to different diffusion (sinking) timescales, which depend on the WD properties and element. Observations of the spectrum of WD 1145 with a baseline of 3+ years show evidence that the gas is in an eccentric, precessing orbit. In Figure 1.4, I show how these features manifest in WD 1145.

1.3 Characterizing Circumstellar Dust

1.3.1 Absorption and Emission Efficiency

Circumstellar dust grains absorb light from their host star and re-radiate it at longer wavelengths. The efficiency with which a grain can absorb and emit radiation depends on the size of the grain and the wavelength of observation. The thermal emission from small grains is inefficient when the wavelength of observation, λ, is much larger than the size of the grain. This inefficiency leads to small grains being hotter than expected if they were to emit like a black body. The wavelength and grain size a dependent efficiency parameter, $Q(a, \lambda)$, for absorption and/or emission is

$$Q(a, \lambda) = \frac{4}{3}\kappa_{\rm tot}\rho_{\rm gr}a(1 - \omega(\lambda)) \tag{1.1}$$

where the opacity, $\kappa_{\rm tot}$, and albedo, $\omega(\lambda)$, are calculated using Mie theory as implemented in the radiative transfer code MCFOST (Pinte et al., 2006, 2009)[7], and $\rho_{\rm gr}$ is the grain density. Grains with $a \sim 1$ cm behave like blackbodies (see Figure 1.5).

[6] WDs are compact objects—the electron-degenerate second cousin of the stellar mass black hole.

[7] Mie theory is the solution to Maxwell's equations when light encounters a sphere. See Bohren & Huffman 1983

Figure 1.4: Transits of WD 1145+017

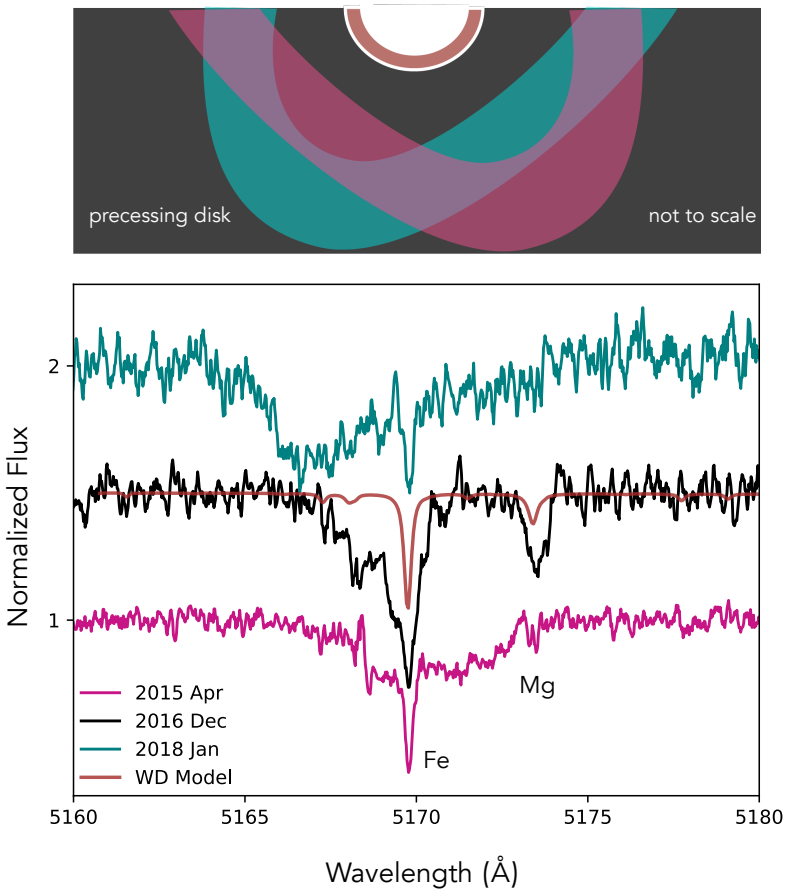

NOTE — In the top panel is my artistic rendition of the precessing, C-S gas disk around WD 1145+017. The WD is shown with the half circle. The brown region represents a metal-polluted photosphere that would produce absorption lines. Connecting to the lower panel by matching color, metals in the photosphere produce the narrow absorption line, while the C-S gas produces a broad feature superimposed on the photospheric line. The colors are also consistent with the dates of observations. Precession of the gas disk results in the overall red- and blue-shift observed with the broad C-S absorption feature, which is centered on the Fe II 5170 line. The variable feature to the right is due to Mg. The bottom panel is recreated from Siyi Xu, (*private communication*). The data is from HIRES on Keck and is available on the archive Keck Observatory Archive. The data are single observations that were calibrated with the default pipeline using MAKEE. Similar work is presented in Fortin-Archambault et al. (2020).

Figure 1.5: Efficiency of Absorprtion

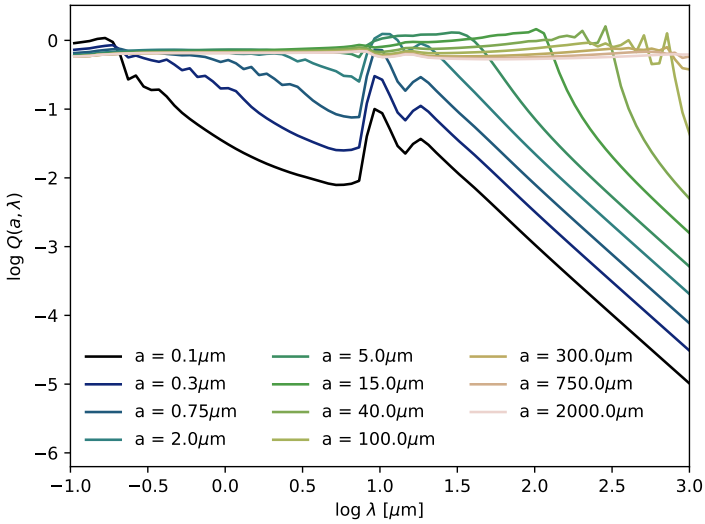

NOTE — The efficiency of absorption $Q(a, \lambda)$ for grain sizes a ranging from 0.1μm to 2000μm . The feature at $\sim$ 10μm is due to the presumed presence of silicates. The steep decline at longer wavelengths leads to a deviation from a blackbody Rayleigh-Jeans slope. Deviations here point toward the presence of small grains in a dust population. The efficiency of emission is assumed to be equal to the absorption efficiency. These data are based on Draine's "smoothed UV astronomical silicate" and were calculated by Gaspard Duchêne in 2013 using the MCFOST code.

1.3.2 Grain size distribution and the Rayleigh-Jeans tail

A major consequence of a grain size distribution is the inefficiency of emission of the small grain population at far-IR and submillimeter wavelengths. This inefficiency leads to the Rayleigh-Jeans slope of the SED being suppressed, i.e., having a power law index more steep than that of a black body. To model a grain size distribution for each system would require knowledge of the dust mass per grain size bin and an equilibrium temperature calculation for each grain size present.

We simulate the behavior of a distribution of grain sizes with their different efficiencies by parameterizing the efficiency $Q(a, \lambda)$ as a function of only wavelength,

$$Q(\lambda) = 1 - \exp\left[-\left(\frac{\lambda_0}{\lambda}\right)^{\beta}\right], \tag{1.2}$$

where $\lambda_0 = 2\pi a$ is the critical wavelength (with values $\lambda_0 \sim 100\mu$m), and β is the opacity spectral index (Williams et al., 2004). Circumstellar dust can therefore be characterized by two parameters: a characteristic grain size a of the dust distribution and the power law index of grain emission efficiency β. When $\lambda \gg \lambda_0$, it should be the case that $Q(\lambda) \equiv (\lambda/\lambda_0)^{-\beta}$. When $\lambda \ll \lambda_0$, $Q(\lambda) \equiv 1$. I use this parameterization of Q to efficiently simulate the asymptotic properties of a grain size distribution.

1.3.3 Dust Mass and Blowout Size

For optically thin dust, the mass is directly proportional to the observed flux, F_ν,

$$M = \frac{F_\nu d^2}{\kappa_\nu B_\nu(T)} \tag{1.3}$$

where κ_ν is the dust opacity, d is the distance to the source, and B_ν is the Planck function (Williams & Cieza, 2011).

For a spherical grain with radius a in orbit around a star with luminosity $L_\star$ and mass $M_\star$, the inward force due to gravity on the grain must exceed the outward force of radiation pressure from the star. This balance leads to a minimum sized grain with radius $a_{\rm min}$ that will survive around the star where

$$a_{\rm min} > \frac{3L_\star}{16\pi GM_\star c\rho_{\rm gr}}, \tag{1.4}$$

where $\rho_{\rm gr}$ is the the density of the grains (Jura 1999; also see, Backman & Paresce 1993, pp. 1253–1304).

1.3.4 Flux from the dust

For a known inner radius, $R_{\rm in}$ and outer radius, $R_{\rm out}$ for the dust belt, the flux density at each wavelength, F_λ is

$$F_\lambda = \frac{\pi a^2 Q(\lambda)}{d^2} \int_{R_{\rm in}}^{R_{\rm out}+\Delta R} 2\pi r\, B_\lambda(T_r)\, N(r)\, dr \tag{1.5}$$

where a is the characteristic grain size, d is the distance to the star, r is the distance of the grain from the star, and $N(r)$ is the surface number density of the grains. If a disk is optically thin, the observed flux, F_ν is proportional to the mass of the emitting particles

$$F_\nu \equiv \frac{2k\nu^2}{c^2}\frac{\kappa(\nu)M_{\rm d}T_{\rm d}}{d^2}, \tag{1.6}$$

with $B_\nu \sim 2kT_{\rm d}\nu^2/c^2$.[8]

1.3.5 Forces affecting dust

Destructive processes act to create gas and dust within a disk. The gas can dissipate or accrete, while the dust can vaporize, or move radially within the disk–

[8]Flux density can be relative to wavelength or frequency, and it seems like the choice is personal preference. To convert from one to the other, $B_\nu d\nu = B_\lambda d\lambda$, with $c = \nu\lambda$.

being destroyed by the host star or blown out of the system. The presence of planets can affect grains large enough to "feel" gravitational forces. Interactions with the ISM can lead to features resembling bow shocks that are seen around some systems. For dust disks around MS stars, the dust is created through collisions of larger bodies, resulting in smaller grains, which collide with each other, and so on. This "collisional cascade" produces grains whose size distribution can be described by a power law (Dohnanyi, 1969).

Once dust is created, a minimum grain size is set by the smallest grain that can resist radiation pressure, stellar winds, gas drag, and Poynting-Robertson (PR) drag. If the force of radiation pressure from the host star on a grain exceeds gravity, then the grain will become unbound from the system. PR drag leads to orbital decay and causes small grains to spiral inward toward the star. Stellar winds can be decomposed into stellar wind pressure and stellar wind drag forces. In the solar system, the stellar wind pressure is minimal, while the stellar wind drag is up to $\sim$30% PR drag forces (Krivov, 2007).

In a debris disk, the timescale of survival for an average grain against stellar radiation forces is about 10^4 years (Su et al., 2013), much shorter than the age of the star ($\gg$ 10 Myr). The grains are thus not primordial and instead are a second-generation result of on-going dust production replenished through grinding collisions of asteroids and Kuiper belt-like planetesimals. The grinding can occur due to the gravitational perturbations or stirring of a large Pluto-like object (Wyatt, 2008b) and so the presence of grains hints at the existence of large planetesimals in the disk.

1.4 Composition

In most cases, the C-S gas of a white dwarf has a composition pointing toward pollution of a rocky body. Given the clearing of the inner stellar system by the

increasing radius of an evolving progenitor star, some reservoir of rocky bodies must survive the evolution of the star to the white dwarf stage. In the Solar System, the most likely candidates would come from the Kuiper Belt or the Oort cloud[9].

The compositions of the Sun, Earth, rocky planets, gas giants, ice giants, and remnants (asteroid, Kuiper Belts, and Oort Cloud contents) are known to varying degrees.[10] A target-specific mission to study a planetary body is usually required to determine its composition. Without a spacecraft fly-by, lander sent to the surface, and/or finding a meteorite, observations of sunlight reflecting off the surfaces of planets or moons and passing through tenuous atmospheres are the only way to determine the composition of their outer layers. Scientific inferences are made about the internal structure and core composition.

The composition of comets and asteroids are slightly easier to study than the giant planets.[11] There have been (to date) five missions to comets, and missions to asteroids, where *in situ* measurements of the body were taken. Samples of asteroids are also studied on Earth. Meteorites are pieces of other rocky bodies (asteroids, the Moon, Mars), that enter the Earth's atmosphere and land on the surface. Meteorites that are pieces of asteroids and have not been altered by heat or other processes are useful as diagnostic tools to understand the Solar System as it was forming. Slicing a meteorite in half reveals that most ($\sim 86\%$) contain millimeter-sized droplets of quenched silicate melt, called chondrules (McSween Jr. & Huss, 2011). The meteorites that contain these rounded chondrules were dubbed chondrites. Chondrites formed within the solar nebula through accretion of solid particles onto the surfaces

[9]The Oort cloud is a reservoir of icy bodies at a few 10,000 au from the Sun, and where long-period comets are thought to originate.

[10]I have mentioned "Sun" and "composition" in the same sentence, therefore Dr. Celia Payne deserves to be mentioned. She explained the dependence of the appearance stellar spectra on temperature, and determined that the Sun is mostly made of hydrogen and helium, four years before Henry Russell (the "R" in HR diagram).

[11]Determining the general makeup of a thing is not always a straightforward process. Without ingredient labels, most people would have no idea what is in their food. If only planets came with nutritional labels.

of growing planetesimals. Some of the grains found in chondrites are older than the Solar System and originated in the cores of dying stars. There are 15 compositional groups of chondrites that are known. The chondrites that are most representative of the Solar System (i.e., the solar photosphere) are the calcium inclusion (CI) chondrites.

Observations of dust in the ISM reveal that silicates produce broad features at 9.7μm and 18μm. The features are produced through stretching of the Si-O bond and bending of the O-Si-O structure (respectively), and can be seen in emission or absorption. The 9.7μm feature is sometimes referred to as the silicon-bump. The structure of the material producing these features can be amorphous or crystalline. Some AGB stars, comets, and T Tauri star disks have crystalline features.

Polycyclic aromatic hydrocarbons (PAHs) are structures of carbon atoms arranged in hexagonal rings with hydrogen attached on the periphery. PAHs produce spectral features at 3.3, 6.2, 7.7, 8.6, 11.3, and 12.7μm through vibrational transitions. The resulting appearance of the feature depends on whether the material is crystalline or amorphous, and also on the charge of the PAH structure (e.g. it can have a net positive charge from losing an electron).

The broad observational features of grains are modeled by considering their composition, shape, size, and size distribution. Mathis et al. (1977) modeled silicate and graphite spheres with a power-law size distribution, finding that they were able to reproduce the extinction due to dust reprocessing radiation from the near-IR to the UV. Building upon this work, Draine & Lee (1984) synthesized a dielectric function for graphite and silicates using all available data that was consistent with laboratory measurements and astronomical observations, deriving the optical properties that describe an "astronomical silicate," or *astrosilicate*.

In Figure 1.6, I show the relative abundances by number of the solar photosphere, the bulk Earth, CI chondrites, and the ISM. I also show the known abun-

Figure 1.6: Elemental Abundances of Different Bodies

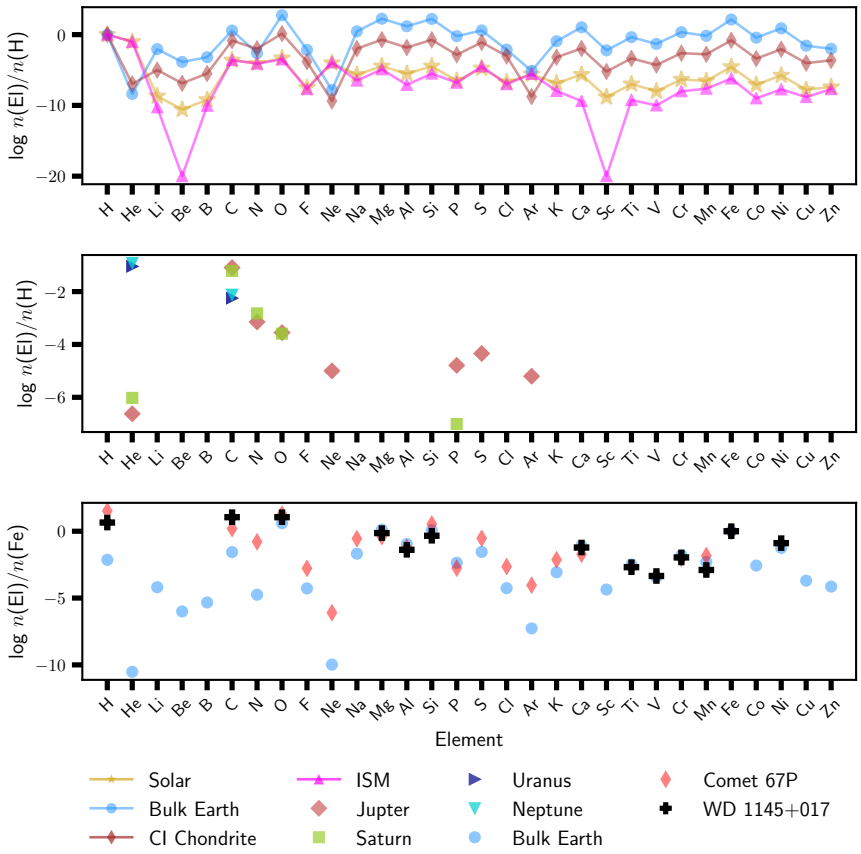

NOTE — Top panel: the abundances by number relative to the hydrogen of the solar photosphere, the bulk Earth, CI chondrites, and the ISM. See Appendix A for the references of these abundances. Middle panel: the known abundances of Jupiter, Saturn, Uranus, and Neptune. Bottom panel: the abundances of different metals relative to iron for comet 67P, the bulk Earth, and the C-S gas around WD 1145+017. Notice how much we can glean about the WD C-S gas composition.

dances of Jupiter, Saturn, Uranus, and Neptune to highlight the difficulty in determining these values for the Solar System's giant planets. The composition of comet 67P determined from the Rosetta mission is compared to the bulk Earth and to the composition of the C-S gas of a white dwarf. If exo-asteroids (asteroids around another star) are polluting WDs, then we are potentially seeing the building blocks of that stellar system billions of years after it formed.

1.5 Outline of Thesis

Collisions within the Solar System's asteroid belt produce small grains that flood the inner solar system. From Earth, we can see light reflecting off of these grains with the naked eye. What would we see of systems of various ages with dust of different compositions if we were 30 parsecs (pc) away? What would we be able to determine about their grains and (remnant) planetary systems, and how?

In Chapter 2, I explore a selection of debris disks around main sequence stars observed at submillimeter wavelengths. Steele et al. (2016) modeled the debris disks around five solar-type stars, resolving two of the disks at millimeter wavelengths for the first time. The model relies on an MCMC algorithm with an affine-invariant sampler (Goodman & Weare, 2010), to explore the space of physical disk parameters, including the radius of the inner disk edge, disk width, disk mass, typical grain size, and the parameterized ratio of large to small grains.

In Chapter 3, I characterize a set of evolved stars with excess infrared emission that were observed by the ESA *Herschel* Space Observatory. These post-MS stars have dust and other unexpected properties that can be used to investigate processes within the star and interaction in the circumstellar environment. By studying material around these "retired" stars we access snapshots of post-MS system evolution that might result in a remnant WD with pollution. We perform SED fitting for each

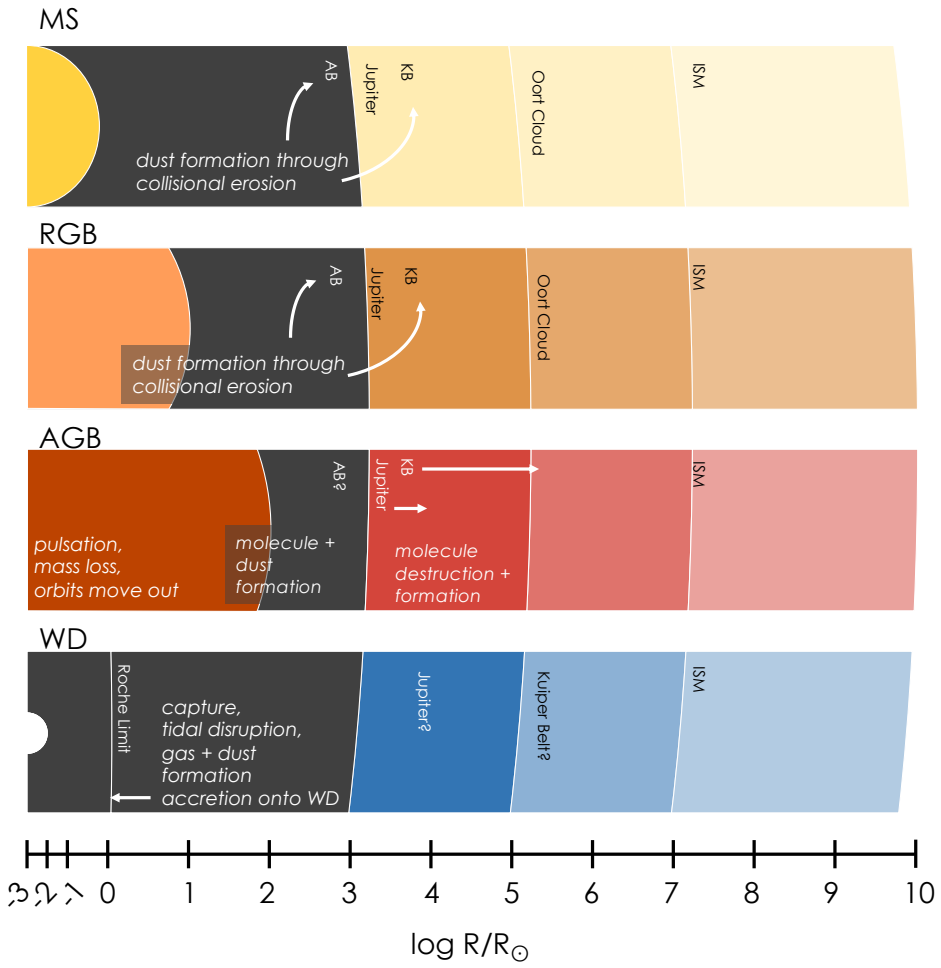

Figure 1.7: Objects Explored in this Thesis

NOTE – Chapter 2 describes a characterization of debris disks around sun-like stars on the MS. Chapter 3 explores a set of post-MS and pre-WD stars that are either on the RGB or AGB, placing constraints on the dust population. Chapter 4 revisits a previously studied white dwarf with evidence of CS metallic calcium gas and present a characterization of the gas using the radiative transfer code, Cloudy. Chapter 5 builds upon the previous chapters, and presents applications of Cloudy to different types of white dwarfs and lays the foundation for applications to MS stars with a gas rich disks and AGB stars surrounded by large amounts of dust.

of the stars, determine the evolutionary status of each star using isochrones, and calculate spectral indices for the RJ tail of the thermal emission. We also report the existence of a thermally pulsing early AGB star surrounded by an extensive dust shell.

In Chapters 4 and 5, I show how observations of polluted WDs provide a singular opportunity to discover the composition of the planetesimals that survive beyond the giant phase. In Chapter 4, I present a case study on WD 1124-293, where I use the radiative transfer code Cloudy to model the C-S gas producing a single Ca II K absorption feature. In Chapter 5, I present a grid of Cloudy models describing gas of different compositions around DA WDs of different temperatures. This work should lead to a better understanding of the physical conditions of the gas orbiting WDs.

In Chapter 6, I summarize my findings and discuss next steps for this work.

Chapter 2: Resolved Millimeter-Wavelength Observations of Debris Disks around Solar-Type Stars

Observations of circumstellar disks provide a method of studying planet composition, formation, and evolution. The observable dust in the optically thin, low gas mass remnant of a protoplanetary disk, or *debris disk*, is the product of grinding of larger planetesimals. The size and chemical composition of the dust can be probed by the presence of emission features and multi-wavelength imaging (e.g. Beichman et al. 2011; Dutrey et al. 2014; Lebreton et al. 2016). The dust composition should trace the parent planetesimals, giving cosmochemical and mineralogical clues to the processes and conditions during planet formation (Matthews et al., 2014).

2.1 Introduction

Planets form in circumstellar disks as a natural by-product of star formation. From observations with the *Kepler* telescope, we now know that planetary systems are a common outcome of the planet formation process with an average frequency of at least one planet per star (Swift et al., 2013). At the relatively small semimajor axis range probed by Kepler ($\lesssim 1$ au) the properties of these systems differ dramatically from those of our solar system, but far less is known about the properties of planetary systems at large semimajor axis, particularly Uranus and Neptune analogs.

Optically thin, second-generation[1] debris disks are similarly a very common phenomenon, occurring around $\sim$17% of FGK stars (DEBRIS survey, Matthews et al. 2014). The existence of debris disks around a large fraction of solar-type stars suggests that leftover planetesimal belts analogous to the asteroid and comet reservoirs of the solar system are common (Moro-Martin, 2013). Observations that spatially resolve the radial distribution of dust around these stars provide insight into the semimajor axis distribution of Kuiper Belt analogs, and can hint at the properties of wide-separation planets that may be sculpting the belts.

Millimeter-wavelength interferometry provides sufficient angular resolution to reveal the spatial distribution of large dust grains that are not significantly affected by radiation pressure. Millimeter-wavelength observations are highly complementary to observations at shorter wavelengths that probe the spatial distribution of smaller dust grains that are subject to different physical processes. At the time of writing, eight debris disks have been spatially resolved using (sub)millimeter interferometry: Fomalhaut (Boley et al., 2012), HR 8799 (Hughes et al., 2011), au Mic (MacGregor et al. 2013; Wilner et al. 2012), β Pictoris (Dent et al. 2014; Wilner et al. 2011), HD 107146 (Corder et al. 2009; Hughes et al. 2011; Ricci et al. 2015), HD 61005 (Ricarte et al., 2013), HD 32297 (Maness et al., 2008), and HD 21997 (Kóspál et al. 2013; Moór et al. 2013). These observations have revealed a striking diversity of debris disk properties: narrow millimeter rings with or without scattered light haloes, broad rings with or without haloes, unusually large quantities of molecular gas, and evidence for interactions with the interstellar medium. Each uses a different analysis technique, and the wide range of stellar masses, distances, and angular resolutions represented by these observations makes it difficult to draw general conclusions about the spatial distributions of large grains around nearby stars.

[1] A second-generation disk is not primordial and is instead the result of on-going dust production replenished through grinding collisions of planetesimals.

In this paper, we assemble a uniform sample of debris disks around solar-type stars observed using millimeter interferometry and analyzed in a consistent manner to allow for robust comparisons of debris disk properties. The five disks in this sample (HD 377, HD 8907, HD 61005, HD 104860, and HD 107146) were drawn from the Formation and Evolution of Planetary Systems (FEPS) Spitzer Legacy Science Program. The survey made extensive and uniform IR observations of 328 nearby stars with ages ranging from 3 Myr to 3 Gyr and masses within $0.8-1.5\,M_{\odot}$, (95% of the sample), with the goal of detecting disks at varying stages of evolution. The program utilized all three Spitzer science instruments, IRAC (Infrared Array Camera), IRS (Infrared Spectrograph), and MIPS (Multiband Imaging Photometer), for all stars in the sample to collect photometry and spectroscopy at 24, 70, and 160 μm to infer the approximate radial distribution of dust in these systems. They detected continuum excess around 54 sources at either 24 or 33 μm, which Carpenter et al. (2008) characterized with blackbody fitting. In addition to providing a uniform sample of stars, photometry provided by the FEPS survey is well-sampled. The five sources in this work are the only debris disk sources that were detected in long-wavelength follow-up observations by Roccatagliata et al. (2009) at wavelengths of both 350 μm and 1.2 mm. Roccatagliata et al. (2009) present a summary of previous studies of the disks in this sample, with Ertel et al. (2011) expanding upon the studies of HD 107146. The basic properties of the sample are given in Table 2.1.

Here we present a set of submillimeter-wavelength observations of the five disks in our sample (Section 2). HD 377 and HD 8907 are resolved for the first time and HD 104860 is resolved at millimeter wavelengths for the first time. We simultaneously model the excess flux from the spectral energy distribution (SED) and spatially resolved visibilities, and fit for basic physical characteristics of the disks (mass, characteristic grain size, inner radius, belt width, and long-wavelength slope of the dust opacity, β), with a uniform analysis. We describe the modeling process

in Section 2.3.1, and present the results of the analysis in Section 2.3.3. We focus on the following major topics: (1) By spatially resolving the disks, we unambiguously determine the radius of the debris belts. We can use this spatial information to derive basic properties of the dust size distribution. (2) The spatially resolved data allows us to place constraints on the radial width of the debris belts, which can be compared with observations at other wavelengths to provide insight into the physics of collisional particle grinding and radiation pressure effects. (3) Finally, we search for deviations from axisymmetry, which may be caused by the dynamical influence of unseen Uranus and Neptune analogs in the disk. We discuss the implications of our results and place our observations in context with multiwavelength debris disk studies in Section 2.4.

2.2 Observations

We selected targets for observation in order to complete the sample of five debris disk-hosting stars detected by the FEPS survey at both 350 μm and 1.2 mm wavelengths (HD 191089 was excluded from the sample due to a non-detection at 1.2 mm). The resulting sample of five systems spans stellar ages from $\sim$30$-$300 Myr, spectral types from F8 to G3/5V, and luminosities from $0.6 - 2\,L_{\odot}$. Properties of the host stars for each of the observed disks are listed in Table 2.1. Each of the disks in this sample was observed with the Submillimeter Array (SMA). Additional observations were made with the Combined Array for Millimeter-wave Astronomy (CARMA) and the Atacama Large Millimeter/sub-millimeter Array (ALMA) for a subset of the sample. The disks were observed at 230 GHz (1.3 mm), and/or 345 GHz (0.87 mm). The frequency and antenna configurations for each disk was chosen to best match the predicted disk size based on SED modeling.

The Submillimeter Array (SMA) is an 8-element radio interferometer located

Table 2.1: Stellar Properties

Source	d (pc)	Age (Myr)	R.A. (J2000)	Decl. (J2000)	Spectral Type	$T_{\rm eff}$ (K)	$\log(L/L_{\odot})$
HD 377	40	32	00:08:26	+06:37:01	G2 V	5852	0.09
HD 8907	34	320	01:28:34	+42:16:04	F8	6250	0.32
HD 61005	35	100	07:35:47	−32:12:14	G3/5 V	5456	−0.25
HD 104860	48	32	12:04:34	+66:20:12	F8	5950	0.12
HD 107146	29	100	12:19:06	+16:32:54	G2 V	5859	0.04

Reference—Hillenbrand et al. (2008)

on the summit of Mauna Kea at an altitude of nearly 13,800 ft.[2] Each antenna is 6m in diameter. Our observations utilized the Subcompact, Compact, and Extended configurations of the SMA to sample baselines between 9 and 226 m, and to achieve an angular resolution as fine as 2.2" at 230 GHz and 0.6" at 345 GHz. The sources were observed for two to four nights between 2008 and 2012. The SMA observations of HD 107146 have been previously published by Hughes et al. (2011), and observations of HD 61005 have been previously published by Ricarte et al. (2013); more detail about those data are available in their respective publications.

Solar system bodies with well-determined flux models were used to calibrate the absolute flux scale of the observations. Quasars close to the target region were selected as gain calibrators, so that frequent reference could be made to them throughout each track to monitor changes in the instrumental and atmospheric gains. For source HD 104860, recalibration was necessary halfway through one track, so the additional gain calibrator and derived flux are provided. Table 2.2 presents basic parameters of the SMA observations for each night of observation, including the

[2]The SMA is a collaborative project of the Smithsonian Astrophysical Observatory (SAO) and the Academia Sinica Institute of Astronomy and Astrophysics (ASIAA).

Table 2.2: SMA Observations

Source	Date(s)	Ant.	Baselines (m)	$\tau_{225\,\mathrm{GHz}}$	LO Freq (GHz)	RMS Noise (mJy/beam)	Synth. Beam (")	Flux Cal	Gain Cal	Derived Flux (Jy)
HD 377[a]	2012 Jun 25	7	16 – 77	0.03 – 0.06	340.794	0.64	2.16 × 1.98	Uranus	J0006-063	0.66
	2012 Sep 04	7	44 – 226	0.03 – 0.07	340.773	0.64	0.76 × 0.55	Neptune/Uranus	J0010+109	1.1
HD 8907[a]	2012 Jun 29	7	16 – 77	0.04 – 0.05	225.477	0.30	3.61 × 3.18	Neptune	J0113+498	0.43
	2012 Jul 24	···	···	···	···	···	8.19 × 7.60	···	···	···
	2012 Jul 25	···	···	···	···	···	8.17 × 7.52	···	···	···
	2012 Aug 14	···	···	···	···	···	7.92 × 7.68	···	···	···
	2012 Aug 16	···	···	···	···	···	8.76 × 7.22	···	···	···
HD 61005[b]	2008 Dec 16	7	16 – 68	0.10 – 0.15	225.499	0.69	2.74 × 2.17	Uranus/Titan	J0747-331	0.90
	2009 Dec 29	8	16 – 77	0.06	225.169	0.6	5.7 × 2.9	Uranus/Titan	J0747-331	0.80
	2010 Apr 13	8	16 – 69	0.04	225.169	0.8	6.2 × 3.0	Titan	J0747-331	1.02
	2012 Jan 29	7	50 – 226	0.03 – 0.1	225.482	0.69	2.74 × 2.17	Uranus/Callisto	J0747-331	0.95
HD 104860[a]	2012 Jan 12	7	9 – 45	0.05 – 0.1	225.472	0.12	3.19 × 2.83	Titan	J1153+495; J1048+717	0.994,0.70
HD 107146[c]	2009 Jan 06	8	16 – 69	0.07	340.783	0.97	···	Titan	3C274	1.3
	2009 Jan 21	8	9.5 – 69	0.03 – 0.06	340.783	0.97	···	Titan	3C274	1.2
	2009 Feb 01	8	9.5 – 69	0.06	340.783	0.97	···	Ceres	3C274	1.1
	2009 May 02	7	25 – 139	0.05	340.737	0.97	3.12 × 2.52	Titan	3C274	1.1

NOTE — [a]This work; [b]Ricarte et al. (2013); [c]Hughes et al. (2011)

number of antennas, baseline lengths, 225 GHz opacity (a measure of the transparency of the atmosphere), the RMS noise in the naturally weighted map, the synthesized beam size, the solar system object used as the flux calibrator for each track, the quasar used as the gain calibrator, and the flux derived for the gain calibrator. For all observations, the correlator was configured to provide maximum sensitivity across the full 8 GHz available bandwidth.

The dust continuum emission toward HD 104860 was observed at a wavelength of 1.3 mm by the 15−antenna CARMA array over the course of three nights. Mars and MWC349 were used to calibrate the flux, while the time-variable atmospheric and instrumental gains were calibrated with the quasar J0958+655. The weather was very good for the first two nights of observation with sky RMS (a measure of phase stability) values close to 80 μm and $\tau_{225\,\mathrm{GHz}} \sim 0.2$. The third night suffered from lower quality weather with $\tau_{225\,\mathrm{GHz}}$ steadily increasing from 0.1 to 0.3 and sky RMS $\sim 200\,\mu$m, although the early parts of the night were usable. The observation utilized the full 8 GHz bandwidth of the CARMA correlator to maximize continuum

Table 2.3: CARMA Observations

Source	Date(s)	Antennas	$\tau_{230\,\mathrm{GHz}}$	LO Freq (GHz)	RMS Noise μm	Synth. Beam (")	Flux Cal	Gain Cal	Derived Flux (Jy)
HD 104860	2012 Apr 10	15	0.183	227.5343	78.9 (0.24 mJy/beam)	2.83×2.51	Mars	0958+655	0.53
	2012 May 8	15	0.159	227.5329	86.95	···	Mars	0958+655	0.80
	2012 Jun 5	15	0.185	227.5343	164.7	···	MWC349[1]	0958+655	0.88

NOTE– [1]A flux of 1.72 Jy was assumed.

Table 2.4: ALMA Observations[a]

Source	UT Date	Antennas	Baselines (m)	pwv (mm)	LO Freq (GHz)	Flux Cal	Bandpass Cal	Gain Cal
HD 107146	2012 Jan 11	17	19 – 269	2.29	239.53	Mars	3C273	J1224+213
	2012 Jan 27	16	19 – 269	3.02	239.55	Mars	3C273	J1224+213
	2012 Jan 27	16	19 – 269	2.86	239.55	Mars	3C273	J1224+213
	2012 Dec 16	23	15 – 382	1.13	239.53	Titan	3C273	J1224+213
	2013 Jan 01	24	15 – 402	2.82	239.53	Titan	3C273	J1224+213

NOTE–[a]Ricci et al. (2015)

sensitivity.

The 1.3 mm wavelength ALMA continuum data on HD 107146 originate from Cycle 0 observations by Ricci et al. (2015). The data collection and reduction processes are fully described in their paper. The main observational parameters for these observations are listed in Table 2.4. For this work, visibility weights were estimated by calculating the variance of the real and imaginary parts of the visibilities across all channels in the data set, separately for each polarization and spectral window.

2.3 Analysis and Results

Spatially resolved observations of debris disks reveal the radial and azimuthal distribution of large dust grains. The SED allows us to constrain the temperature

of the dust grains. The combination of the two observables (SED + visibilities) is powerful because the spatial and thermal information, in conjunction with an assumption of standard astrosilicate opacities, allows us to infer basic properties of the size distribution of dust grains in the disk.

In this section, we describe the theoretical framework we use to create a simple, but computationally efficient method of modeling the SED and visibilities (Section 2.3.1). The general modeling approach closely follows that described in Ricarte et al. (2013). The SED modeling utilizes a modified blackbody approach that will be described in detail below; similar approaches have been adopted by other authors to fit millimeter data and broad-band SEDs, including Williams et al. (2004), Hughes et al. (2011), and Booth et al. (2013). While we do not implement a true grain size distribution, we approximate the effects of a grain size distribution through a combination of two parameters: the characteristic grain size a, analogous to the minimum grain size, and the long-wavelength slope of the grain absorption/emission efficiency β, which can be related to the power-law slope of the grain size distribution. This approximation, which reduces the computational complexity of the code, decreases the run time per model by more than an order of magnitude, thereby allowing us to perform a robust statistical analysis of the data using an affine-invariant MCMC sampler (described in Section 2.3.2).

2.3.1 SED and Visibility Modeling

The SEDs are modeled with three components: 1) a Kurucz-Lejeune model photosphere (Lejeune et al., 1997), 2) a cold, spatially resolved outer debris disk, and when necessary, 3) a warm, compact dust belt. The Kurucz-Lejeune photosphere is not a free parameter in our model. Including the warm inner asteroid belt is necessary to reproduce the mid-IR fluxes in the SEDs for all the disks except HD 8907, since the contribution from the combination of the disk and star is insufficient to reproduce the overall flux in the mid-infrared. We used the Akaike information criterion (AIC) to place a 3σ upper limit on the warm belt mass of HD 8907 (see Table 2.7). The relative likelihood of a model with a second component is given by $\exp[(\mathrm{AIC}_{\mathrm{1belt}} - \mathrm{AIC}_{\mathrm{2belts}})/2]$, where $\mathrm{AIC} = \chi^2 + 2k$, and k is the number of parameters. The interpretation of two-temperature SEDs is discussed elsewhere in the literature in great detail (see, e.g., Kennedy & Wyatt, 2014), and in some cases the presence of an inner asteroid belt may be degenerate with an additional population of small (and therefore hot) grains significantly smaller than the blowout size located in the outer belt, but for simplicity we assume that excess short-wavelength flux, when required, arises from spatially disparate populations of grains.

We calculated the centroid of the disk using an elliptical Gaussian (or, for HD 107146, an elliptical ring) fit to the continuum visibilities with the MIRIAD[3] task `uvfit`. All of the offset positions were consistent with the expected position of the star to within the uncertainties, taking into account the measured proper

[3]See `http://www.cfa.harvard.edu/sma/miriad/`

Table 2.5: Disk Properties

Star	Flux (mJy)	Frequency (GHz)	Position Angle (°)	Inclination (°)
HD 377	3.5 ± 1	345	30^a	50^a
HD 8907	1.3 ± 0.4	230	55^a	65^a
HD 61005	8.0 ± 0.8	230	70.3 ± 1^b	84.3 ± 1^b
HD 104860	5.5 ± 2	230	1 ± 7^c	52 ± 6^c
HD 107146	70 ± 20	345	58 ± 5^d	25 ± 5^d

NOTE– [a]These values were determined with a grid search. [b]The position angle and inclination of HD 61005 (Buenzli et al., 2010). [c]The position angle and inclination of HD 104860 at 100 μm (Morales et al., 2013). [d]The position angle and inclination of HD 107146 (Ardila et al., 2004). For the last column, we report $R_{\rm in}/R_{\rm BB}$, where $R_{\rm in}$ is determined through our modeling and fitting analysis, and $R_{\rm BB}$ is determined by assuming the disk is radiating like blackbody and in equilibrium with its host star (see Section 2.3.1 for details).

motion. We obtained initial flux estimates from these `uvfit` results as well, listed in Table 2.5. The position angle (PA) and inclination (i) used in the modeling process of HD 61005 and HD 107146 were adopted from scattered light observations of the disks (see Buenzli et al. 2010 and Ardila et al. 2004), which are more precise than we were able to derive from the millimeter data alone. For HD 104860, the PA and i were taken from Morales et al. 2013; these values are consistent with (but slightly more precise than) the geometry derived from the major and minor axis lengths and position angle value calculated with `uvfit`. For HD 377 and HD 8907, the PA and i were not well constrained by the `uvfit` results, so a grid search fit of PA and i was used to maximize the visibility amplitudes; the results were consistent with the `uvfit` results. These geometric parameters are highly uncertain; it is clear from the images and visibilities that these disks are marginally resolved by the interferometric data. Table 2.5 summarizes the measured fluxes and geometries for the five disks in the sample.

We calculate the temperature of the grains by assuming that they are in radia-

tive equilibrium with the central star and that the disk is optically thin. The grains absorb and emit like graybodies with an absorption/emission efficiency $Q(a, \lambda)$ that is composition- and wavelength- dependent.

The efficiency is a function of λ and the grain size a:

$$Q_{a,\lambda} = \frac{4}{3} \cdot \kappa_{tot} \cdot \rho \cdot a(1 - \omega(\lambda)) \tag{2.1}$$

where $\kappa_{\rm tot}(a, \lambda)$ is the grain opacity in $\rm cm^2\,g^{-1}$, $\omega(a, \lambda)$ is the albedo or reflection coefficient, and ρ is the grain density in $\rm g\ cm^{-3}$.

The grain opacity, $\kappa_{\rm tot}(a, \lambda)$ can be calculated for spherical grains using predictions from Mie theory and geometric optics (Draine, 2006a). We assume that the grains are astronomical silicates (astrosilicates) with a bulk density of $2.7\,\rm g\ cm^{-3}$ (Draine & Lee, 1984). The energy per unit time absorbed by the grains, $\Gamma_{\rm in}$ is

$$\Gamma_{\rm in} = \pi a^2 \int_0^\infty Q(a, \lambda)\, F_\lambda(r, \lambda)\, d\lambda. \tag{2.2}$$

where F_λ is the flux density from a tabulated Kurucz model photosphere (Lejeune et al., 1997) drawn from the FEPS Legacy Survey archive[4]. The power emitted by the grains is the product of the Planck function, $B_\lambda(\lambda, T)$, and the emission efficiency, which equals the absorption efficiency:

$$\Gamma_{\rm out} = \pi a^2 \cdot 4\pi \int_0^\infty Q(a, \lambda)\, B_\lambda(T, \lambda)\, d\lambda. \tag{2.3}$$

[4] `http://irsa.ipac.caltech.edu/data/SPITZER/FEPS/links.html`

By setting $\Gamma_{\rm in} = \Gamma_{\rm out}$, we solve for the equilibrium temperature of the grains as a function of their size and distance from the central star.

We model each disk with a set of six parameters: an inner disk radius ($R_{\rm in}$), a characteristic grain size (a), a disk mass ($M_{\rm D}$), a warm inner belt mass ($M_{\rm B}$), a grain emissivity parameter (β), and a disk width (ΔR). $R_{\rm in}$ affects the equilibrium temperature of the dust grains and is constrained by the disk visibilities. The characteristic grain size, a, determines the temperature of the grains. A smaller a will shift the peak of the SED to shorter wavelengths as grains get hotter. $M_{\rm D}$ is essentially a vertical scaling factor for the flux of the cold outer disk, which typically peaks at wavelengths of tens to hundreds of microns, while M_B serves as a vertical scaling factor for the flux of the warm inner belt, which contributes most of its flux at shorter wavelengths. Given the limited information in the mid-infrared regime—primarily the fact that the inner belt has not been spatially resolved—the temperature and mass of the warm belt are highly degenerate, so we fix the temperature at 100 K and vary only the mass. As discussed in Section 4.2.1 in Ricarte et al. (2013), varying the temperature of the warm inner belt produces a noticeable change only in $M_{\rm B}$. Ricarte et al. (2013) demonstrate that the analysis of the cold belt is independent of the assumed belt temperature. The emissivity parameter β determines the slope of the long-wavelength tail and can be related to the slope of the grain size distribution. ΔR describes the width of the outer belt and is also constrained primarily by the visibilities.

We parameterize the surface mass density as $\Sigma(r) = \Sigma_{100} \cdot (r/100\,{\rm au})^{-p}$, where Σ_{100} is the surface density in g cm^{-2} at a distance of 100 au from the central star

and p is the power law index that describes the radial dependence of surface density. There is a well-known degeneracy between p and the outer radius (see section 4.2.2 of Ricarte et al. 2013), but its effects are not significant in the case of a disk with spatially unresolved width. Since the radial width of disks in our sample is typically not spatially resolved, and therefore p is not constrained, we fix p at a value of 0 for all disks except HD 107146. Ricci et al. (2015) show that the structure of HD 107146 warrants using p as a free parameter. The surface number density of the grains, $N(r)$, is related to the surface mass density as $\Sigma(r) = N(r)m_g$, with $m_g = 2.7\,\mathrm{g\ cm^{-3}} \cdot 4\pi a^3/3$.

When calculating the output SED, we approximate the grain emission efficiency following Williams et al. (2004): $Q(\lambda) = 1 - \exp(-(\lambda_0/\lambda)^\beta)$, where $\lambda_0 = 2\pi a$ is the critical wavelength and β is the opacity spectral index, instead of using the aforementioned tabulated astrosilicate opacities (which are used for the equilibrium temperature calculation only). This analytical parameterization is extremely computationally efficient and has the desired asymptotic properties for a grain size distribution with characteristic radius a, namely that $Q(\lambda) \approx (\lambda/\lambda_0)^{-\beta}$ for $\lambda \gg \lambda_0$ and $Q(\lambda) \approx 1$ for $\lambda \ll \lambda_0$. While this parameterization of Q preserves the asymptotic behavior, it smooths over features in the grain opacities used in the initial temperature calculations, so the code is not entirely internally self-consistent. The tradeoff is that the hybrid approximation to the grain size distribution allows our code to be efficient enough to run a thorough MCMC uncertainty analysis with a week of computing time on our local machines. The flux density at each wavelength

is then,

$$F_\lambda = \frac{\pi a^2 Q(\lambda)}{d^2} \int_{R_{\rm in}}^{R_{\rm in}+\Delta R} 2\pi r\, B_\lambda(T_r)\, N(r)\, dr \tag{2.4}$$

where a is the characteristic grain size, d is the distance to the star, r is the distance of the grain from the star, and $N(r)$ is the surface number density of the grains.

To analyze the visibilities, we generate a high-resolution model image for comparison and calculate flux as a function of position, as described by equation 2.4. The pixel size is set to be 1% of the spatial scale sampled by the longest baseline. We then sample the model image at the same spatial frequencies as the data, using the MIRIAD command `uvmodel`. These model visibilities are compared with the observed visibilities in the visibility domain, using the appropriate statistical weights.

2.3.2 Error Analysis

We perform two separate chi-squared calculations, one comparing the model disk SED to photometric data from the literature (see table) and a second comparing the disk visibilities to the model image of the disk. We add the chi-squared values for the SED and visibilities and use the total χ^2 as the statistic for goodness-of-fit: $\chi^2 = \chi^2_{\rm SED} + \chi^2_{\rm VIS}$. As discussed in Andrews et al. (2009), the high quality of the low number of SED points balances the large numbers of visibilities, so that neither the SED nor the visibilities dominate the final fit. The uncertainties in the parameters of the fit can be determined through the use of a probabilistic sampling algorithm.

The MCMC technique is a random sampling algorithm (Press et al., 2002)

Table 2.6: Broad-band photometry for all sources (flux densities in units of mJy)

λ (μm)	HD 377			HD 8907			HD 61005			HD 104860			HD 107146			References
1.24	4260	±	80.0	8380	±	180	2730	±	70	2940	±	50	7100	±	150	a
1.65	3640	±	70.	6720	±	110	2450	±	100	2450	±	40	5980	±	110	a
2.16	2380	±	50.0	4510	±	70	1740	±	40	1670	±	30	4040	±	60	a
3.35	1160	±	50.0	2100	±	120	819.0	±	32.0	806	±	32	1870	±	110	b
3.6[a]	1029.1	±	22.1	1918.2	±	41.2	753.5	±	16.2	724.8	±	15.6	1711.3	±	36.7	c
4.5[a]	648.6	±	14.9	1223.7	±	28.1	472.3	±	10.8	455.3	±	10.5	1074.8	±	24.7	c
4.60	651.0	±	13.0	1380	±	30	453.0	±	9.0	442	±	9	1230	±	30	b
8.0[a]	234.7	±	5.0	427.3	±	9.1	169.2	±	3.6	162.5	±	3.5	384.4	±	8.2	c
11.6	105.0	±	1.0	193	±	2.0	78.3	±	1.1	74.3	±	1.0	176	±	2	b
13[a]	81.6	±	5.0	154.1	±	9.4	62.3	±	3.8	57.3	±	3.5	138.9	±	8.5	c
22.1	41.7	±	1.7	61.5	±	1.6	44.4	±	1.6	23.1	±	1.1	69.6	±	1.9	b
24[a]	36.6	±	1.5	51.3	±	2.1	41.5	±	1.7	19.9	±	0.8	59.8	±	2.5	c
33[a]	37.8	±	2.7	41.8	±	3.5	110.0	±	6.7	17.8	±	1.8	86.7	±	5.7	c
70[a]	162.0	±	16.9	247.4	±	19.7	628.7	±	45.4	183.1	±	14.8	669.1	±	47.8	c
100[b]		···			···			···		277.0	±	3.5		···		d
160[a]	187.5	±	50.4	243.8	±	42.3	502.6	±	160.1	202.7	±	27.0		···		c
160[b]		···			···			···		243.4	±	5.2		···		d
350		···			···		95	±	23	50.1	±	14	319	±	64	e
450		···		22	±	13		···		47	±	18	130	±	40	f
850		···		4.8	±	1.3		···		6.8	±	1.4	20	±	4	f
880[c]	3.5	±	1.4		···			···			···		36	±	1	g
1200	4.0	±	1.2	3.2	±	1.0		···		4.4	±	1.3		···		e
1300[c]		···		1.3	±	0.4	7.98	±	0.8	5.5	±	1.8		···		g
1300[c]		···			···			···			···		12.5	±	1.3	h

NOTE–[a] 2MASS (Kharchenko & Roeser, 2009); [b]WISE (Cutri & et al., 2012); [c]FEPS (Hillenbrand et al., 2008): the uncertainties include both internal and calibration terms. [d]Herschel photometry (Morales et al., 2013). [e]CSO and IRAM (Roccatagliata et al., 2009): the uncertainties include additional 20% calibration uncertainties on the 350 μm fluxes and 16% calibration errors on the 1200 μm fluxes. [f]JCMT/SCUBA (Najita & Williams, 2005): the uncertainties include additional 30% calibration uncertainties on the 450 μm fluxes and 10% calibration errors on the 850 μm fluxes. [g]From this work. [h]ALMA (Ricci et al., 2015): the uncertainty reflects a 10% systematic flux uncertainty.

that provides a powerful method of determining the uncertainties on the model parameters, taking into account both the uncertainties on individual data points and degeneracies between parameters in the model. We utilize the affine-invariant MCMC fitting technique described in Goodman & Weare (2010).

Affine invariant sampling efficiently explores degenerate parameter spaces due to its lack of bias in treating distributions that are highly anisotropic. Assigning a dimension to each model parameter, the resulting N-dimensional space is initialized with a uniformly distributed set of walkers, or vectors in the space that contain parameter values. In the Goodman & Weare (2010) *stretch move*, the walkers (sets of model parameters) explore the space by moving along lines containing other walkers. The decision for a walker to explore the space depends on whether the likelihood function will be maximized by this move. We implement a sampler that utilizes only stretch moves, similar to the affine-invariant MCMC sampler, `emcee`, written in Python (Foreman-Mackey et al., 2013). Online documentation and a full description of the `emcee` likelihood function are available at `http://dan.iel.fm/emcee/current/`. We assume uniform priors for all variables.

In the initialization of the walkers, trial states for a, $M_{\rm D}$, and $M_{\rm B}$ are generated in logarithmic space, while states for $R_{\rm in}$ and β (and p for HD 107146) are generated in linear space. Please see Section 4.2 of Ricarte et al. (2013) for a discussion of the parameter degeneracies. We run 50 walkers through 5000 trials and discard trials for which the χ^2 values have not yet converged (the "burn-in" phase, typically a few hundred trials). The posterior probability density functions for each parameter, marginalized over all other parameters, are calculated from the ensemble of walkers

Table 2.7: The Best-fit Parameters for All Disks

Source	$a(\mu\mathrm{m})$	$M_D(10^{-3}M_\oplus)$	$M_B(10^{-5}M_\oplus)$	β	$R_{\rm in}$(au)	$R_{\rm in,avg}$	ΔR (au)	p	Total χ^2	$\chi^2_{\rm Red}$
HD 377	19.8	5.57	3.26	0.76	31	47	32	···	269023.48	1.40
	33.5^{+39}_{-16}	$8.38^{+4.64}_{-2.99}$	$3.13^{0.33}_{-0.36}$	$0.96^{+0.51}_{-0.21}$	$30.1^{+8.4}_{-6.3}$		32.9^{+16}_{-18}	···		
HD 8907	24.9	4.93	2.68×10^{-5}[a]	1.13	28	54	52	···	357244.56	1.89
	$15.4^{+13}_{-7.6}$	$4.49^{+2.05}_{-1.57}$	···	$1.05^{+0.16}_{-0.15}$	36.4^{+19}_{-10}		53.2^{+31}_{-32}	···		
HD 61005	1.17	0.854	2.99	0.46	69.4	71	...[b]	···	456165.08	1.85
	$1.03^{0.46}_{0.54}$	$0.71^{+0.54}_{-0.43}$	$4.26^{+0.17}_{1.3}$	0.43 ± 0.08	$70.9^{+3.0}_{-4.7}$		...[b]	···		
HD 104860	4.27	7.20	1.68	0.75	57	110	108	···	377760.86	2.38
	$4.00^{1.63}_{-1.12}$	$6.87^{+2.42}_{-2.17}$	$0.193^{+2.3}_{-0.019}$	0.74 ± 0.08	63.3^{+24}_{-11}		87.9^{+24}_{-43}	···		
HD 107146	4.71	8.85	0.197	0.74	29.4	94	129	-0.57	490862.26	1.18
	$5.05^{+0.81}_{0.78}$	$9.51^{+1.27}_{-1.95}$	$0.241^{+0.069}_{-0.049}$	$0.75^{+0.02}_{-0.05}$	$30.8^{+2.0}_{-1.7}$		$129^{+2.1}_{-1.9}$	$-0.50^{+0.08}_{-0.07}$		

NOTE—[a]This belt mass is an upper limit based on a 3σ significance to the best fit with one (cold) belt. [b]To maintain consistency with Ricarte et al. (2013), the width of the belt was fixed at 5% of the inner radius. The top row for each source gives the global χ^2 minimum and the second row gives the median $\pm$ 1σ uncertainty. $R_{\rm in,avg}$ is defined as $R_{\rm in}+\Delta R/2$. We include it in the table for easier comparison with other models that report the midpoint as the radius of the ring.

across all trials excluding burn-in.

2.3.3 Results

By simultaneously modeling the SED and the visibilities, we constrain basic properties for each disk in our sample. Figures 2.1-2.5 show the posterior probability density functions and the best-fit SED and images for each source. The global best fit model is chosen from the MCMC walker position with the lowest χ^2 value across the entire set of walkers and trials. To generate residual images, we subtract the model from the data in the visibility domain, and then image the residual visibilities using the same imaging parameters as for the data and model images. The most probable value in the posterior PDF typically corresponds well with the best-fit value. The uncertainties on the best-fit parameters reported in Table 2.7 represent the range of values in the PDF which encloses 1σ (68%) of the models. The errors are not consistently symmetric about the best fit.

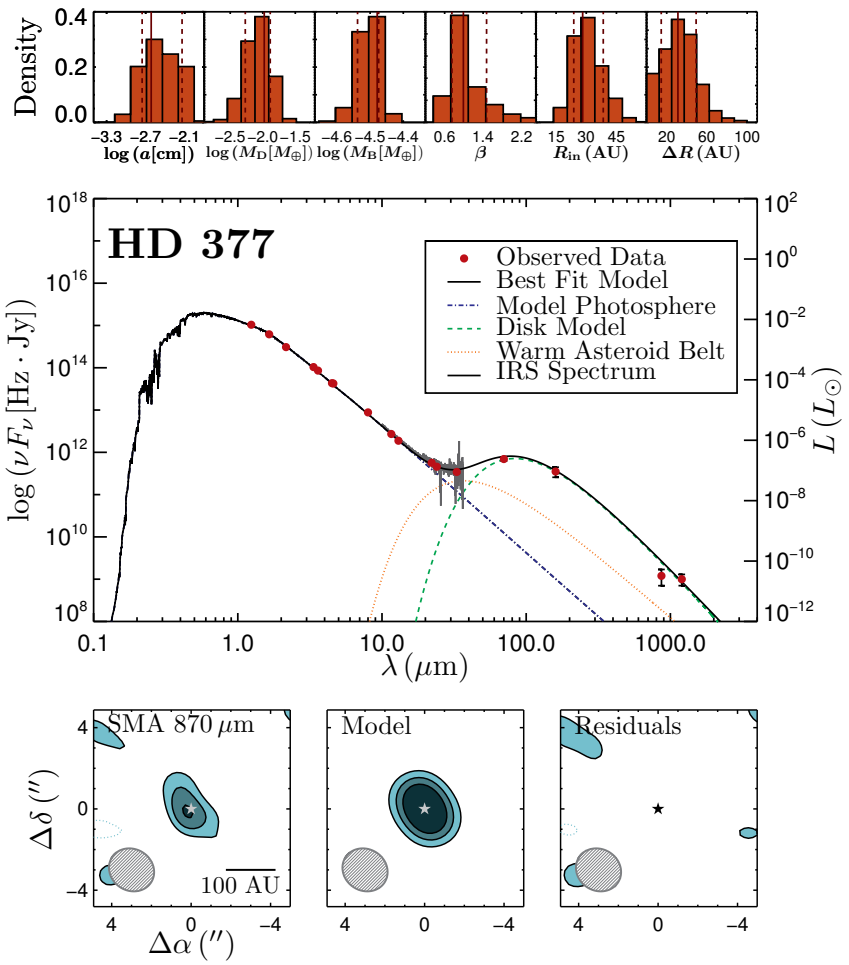

Figure 2.1: Modeling results for HD 377

Top: marginalized posterior probability density functions (PDFs) for the model parameters as derived from the MCMC analysis. The dashed gray vertical lines mark the $\pm 1\,\sigma$ range that encloses models within one standard deviation of the most probable value. The solid line marks the most probable value determined from the analysis. Middle: SED of the system. The total model SED is the sum of three components: a Kurucz-Lejeune model photosphere, a modified blackbody modeled to the debris belt, and a warm asteroid belt. The IRS spectra are not included in the modeling process, yet they provide visual check of the total model at mid-infrared wavelengths. Bottom: the interferometric image of the emission from the disk around each star. The image has been constructed using data with all-array configurations. Contours are drawn at $[2, 3, 4] \times 0.7$ mJy beam^{-1} (the rms noise). The axes have been set such that the (0,0) position corresponds to the expected position (corrected for proper motion), of the star, which is marked with a $\star$ symbol. A gray ellipse indicating the size of the synthesized beam is drawn in the lower left corner. The black bar in the lower right corner illustrates the linear scale.

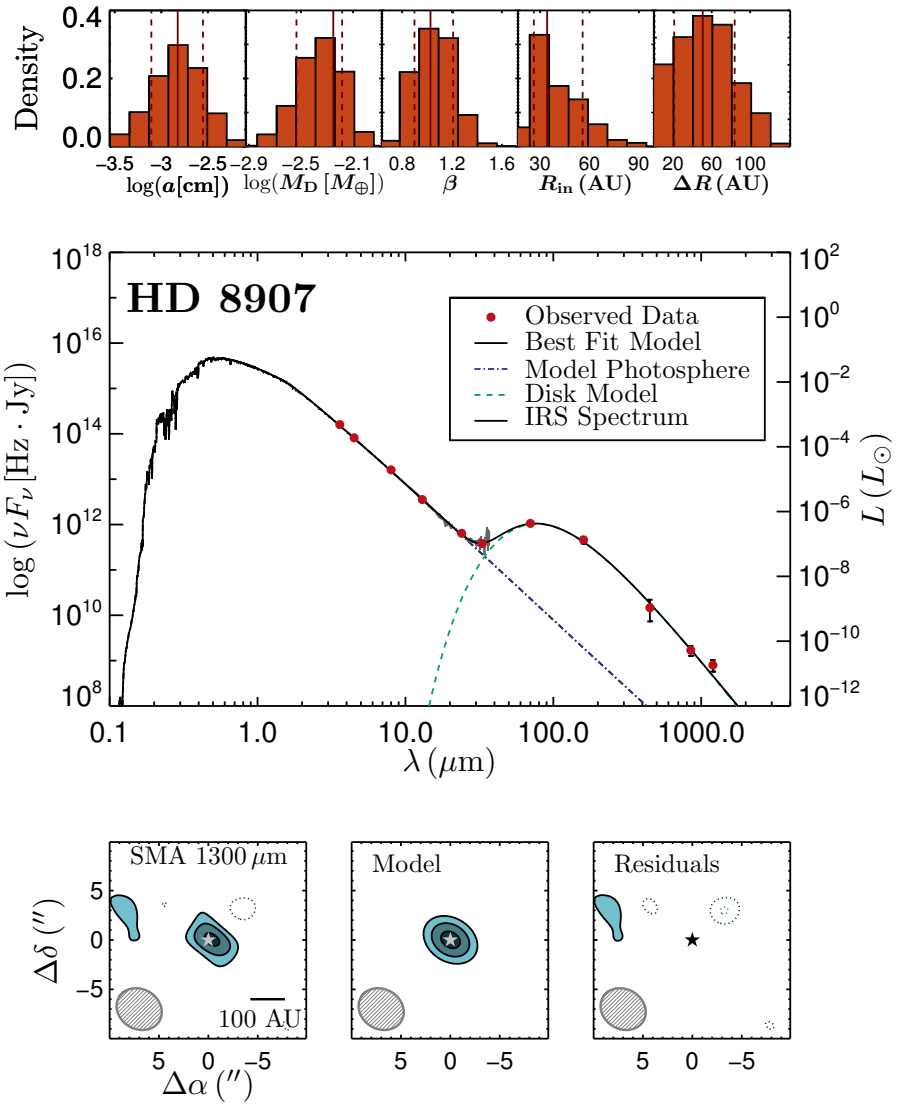

Figure 2.2: Modeling results for HD 8907
Same caption as Figure 2.1, but for HD 8907.

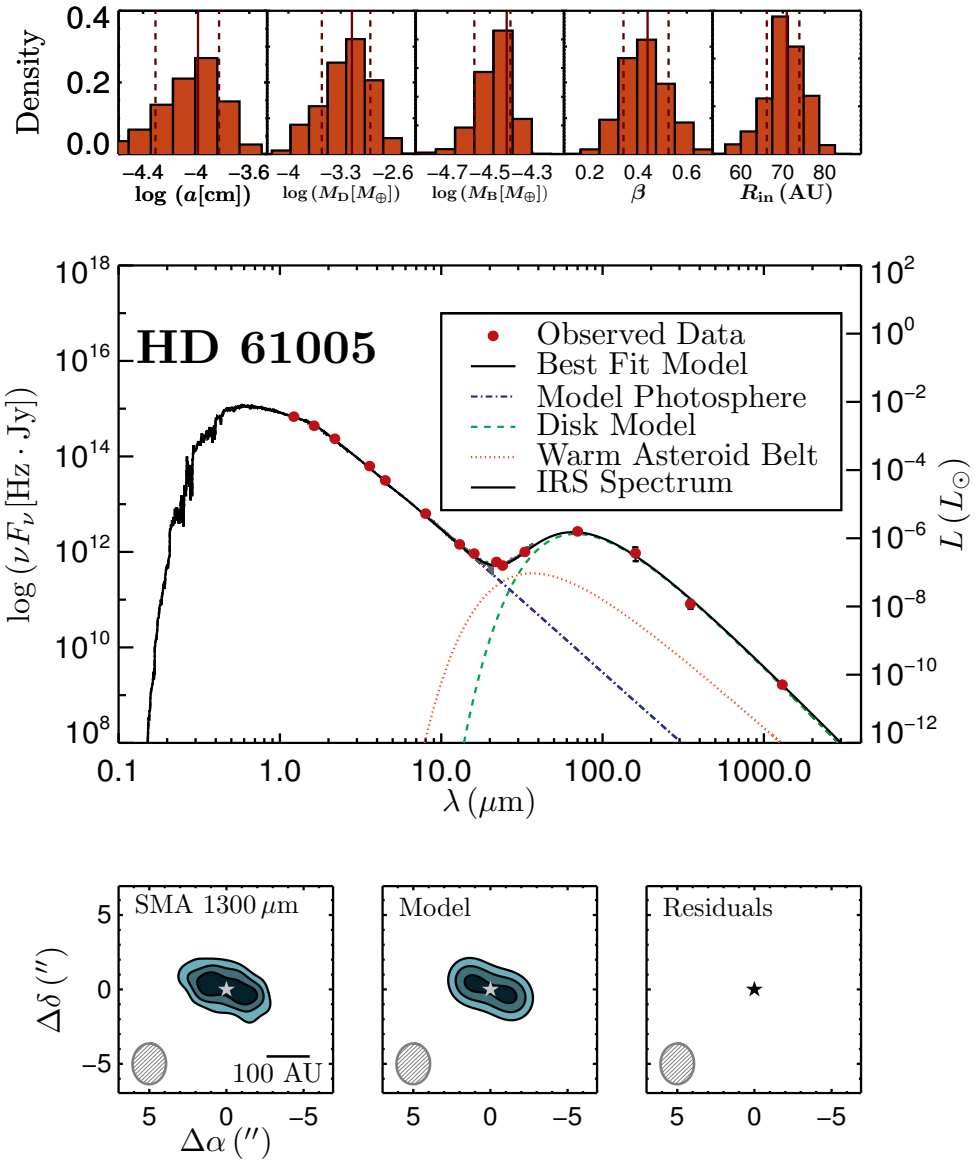

Figure 2.3: Modeling results for HD 61005
Same caption as Figure 2.1, but for HD 61005.

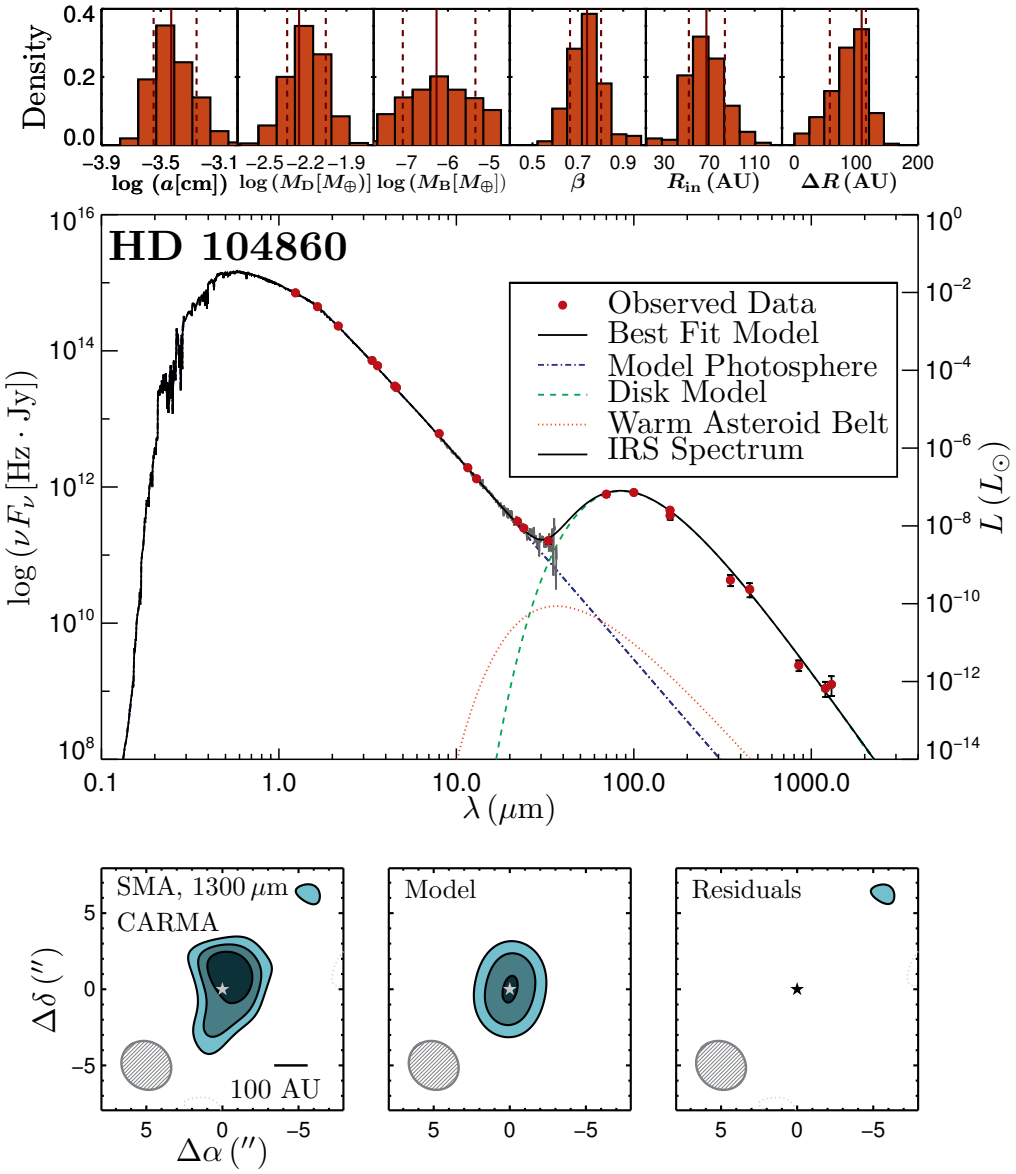

Figure 2.4: Modeling results for HD 104860
Same caption as Figure 2.1, but for HD 104860.

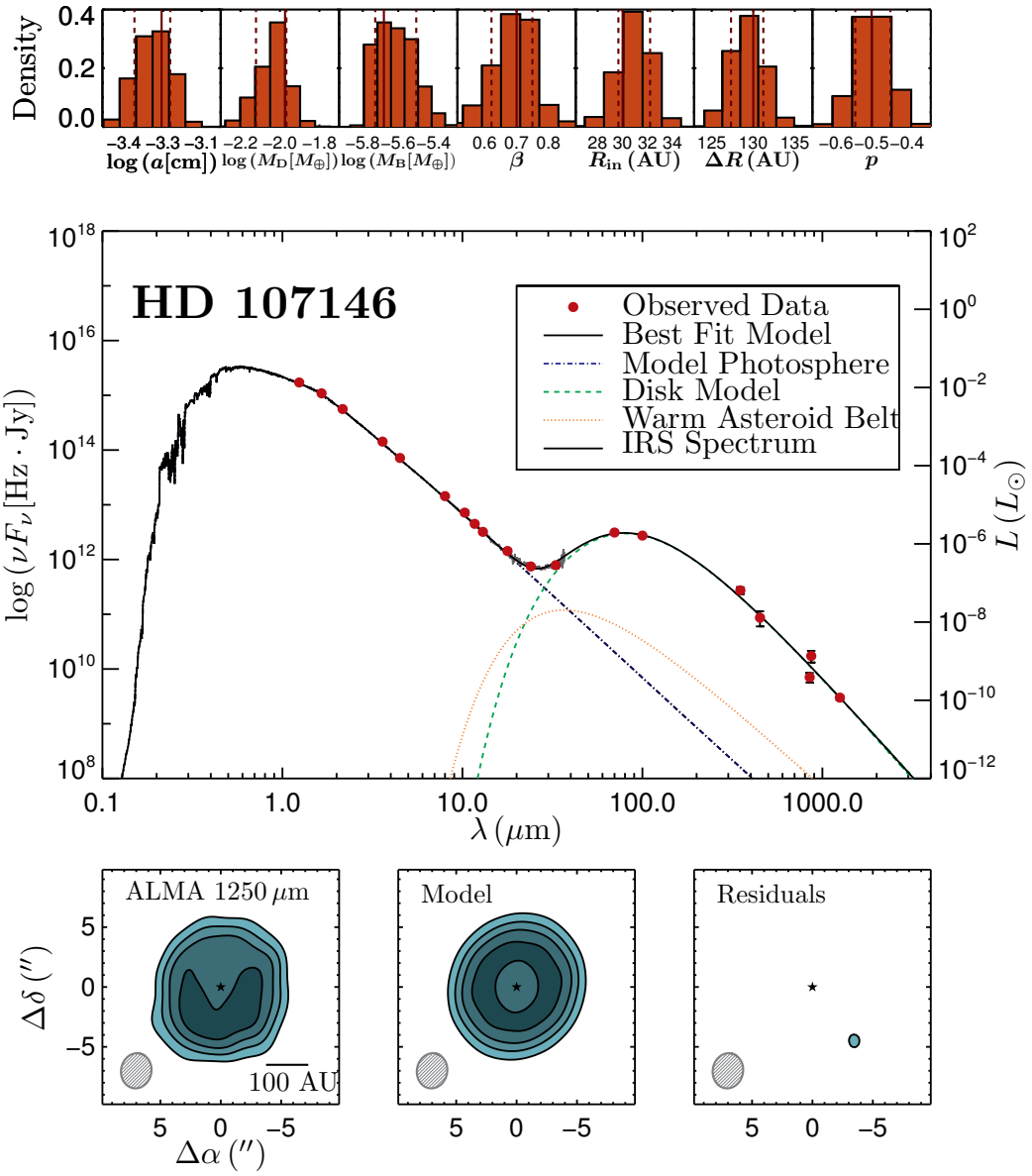

Figure 2.5: Modeling results for HD 107146

Same caption as Figure 2.1, but for HD 107146. Due to the greater dynamic range, the contours are drawn at $[3, 8, 13, 18] \times 0.08$ mJy beam^{-1}. The additional parameter p is the slope of the radial power law of the parameterized surface mass density (see Section 2.3.1). We discuss the implications of this parameter in Section 2.3.1.

2.4 Discussion

2.4.1 Grain Sizes

The disks have characteristic grain sizes ranging from $\sim 1\,\mu$m to $\sim 30\,\mu$m. We can estimate a minimum grain size that should be observable in a debris disk by calculating the grain size for which radiation pressure balances the gravitational force exerted on the orbiting dust grain:

$$a_{\rm blow} = \frac{3\,L_\star}{16\pi G M_\star c \rho} \tag{2.5}$$

where $L_\star$ is the stellar luminosity, $M_\star$ is the mass of the star, c is the speed of light, and ρ is the grain density (e.g., Backman & Paresce 1993). Grains smaller than this blowout size are efficiently removed from the disk on timescales much shorter than the age of the star. The average blowout sizes here are $\sim 0.3\,\mu$m, roughly an order of magnitude smaller than the average characteristic grain size. All of the SEDs are therefore reproduced well with distributions that only include grains larger than the blowout grain size. HD 377 and HD 8907 have slightly larger characteristic grain sizes of $\sim 10\,\mu$m, which may point toward grain growth, although these are the most poorly spatially resolved disks in the sample and the grain sizes in these systems are therefore particularly uncertain.

β controls the long-wavelength slope of the SED and reflects the slope of the grain size distribution, or the number of small grains compared to large grains in the

disk (Wyatt, 2008b). Typical β values observed in protoplanetary disks are $\beta = 2$ for interstellar medium grains, $0 < \beta < 1$ for pebbles of the order of 1 mm, and $\beta = 0$ for large grains (Beckwith & Sargent, 1991). The values of $0 < \beta < 1$ for most debris disks point toward grain growth. To connect the measured values of β to the slope of the grain size distribution, we use the relationship derived by Draine (2006b): $\beta \approx (q - 3)\beta_s$, where β_s is the dust opacity spectral index in the small particle limit, which Draine (2006b) find to be $\approx 1.8 \pm 0.2$), and q is the slope of the grain size distribution $dn(a) \propto a^{-q}da$. Solving for q, we find that $q \approx (\beta/\beta_s) + 3$. The median value of beta in our sample was ~ 0.9, with typical uncertainties of $\pm \sim 0.1$ depending on the sampling of the long-wavelength portion of the SED. We therefore derive a typical q value of 3.5 ± 0.5. This result is consistent with the q values anticipated for most theoretical models of collisional cascades, including $q = 3.51$ (Dohnanyi, 1969), $q = 3.65$ (for the fiducial model presented in Gáspár et al., 2012), as well as the range of values derived by Pan & Schlichting (2012). The β values in our sample are therefore typical of what we expect of the grain size distribution in a disk undergoing a collisional cascade.

2.4.2 Inner Radii and Disk Widths

The inner radii of the disks in our sample range from 28 au to 69 au with typical uncertainties of ± 10 au. The median value was 42 au, and all but one of the disks (HD 61005) was consistent with that median value to within the uncertainties.

Looking at a sample of 34 debris disks around stars of spectral types A through

M resolved in various *Herschel* programs (including HD 104860, Vega, au Mic, and Fomalhaut), Pawellek et al. (2014) modeled the SEDS and *Herschel*-resolved images of debris disks, focusing on the cold, outer component. They report radii ranging from 40 au to 290 au, with only weak correlation to luminosity of the host stars. Of the 21% of disks with radii <100 au, the median radius is 60 au, while for the 79% with radii >100 au the median radius is 154 au. Large inner radii can hint at the presence of fully formed planets and would reflect the semi-major axis distributions of those planets. However, these disks were resolved at much shorter wavelengths and may not trace the parent planetesimal belts as reliably as millimeter wavelengths. In addition, the authors compare a modified blackbody fitting method to a full grain size distribution method and find that while there are some quantitative differences between the results, the trends in grain temperatures and disk radii are consistent across the two methods. They suggest that a modified blackbody approach like the one used here is simple, transparent, and may be appropriate for stars with relatively sparse SEDs.

The radius of the disk is commonly estimated using two distinct methods. $R_{\rm BB}$ represents the radius estimated from the SED, assuming that grains are in blackbody equilibrium with the central star, while $R_{\rm in}$ represents the inner radius determined by a simultaneous fit to the SED and visibilities, assuming modified blackbody grains. The ratio of $R_{\rm in}$ to $R_{\rm BB}$ is typically greater than one since the small grains are hotter than the blackbody equilibrium temperature. Morales et al. (2013) compare the disk sizes resolved by *Herschel* relative to the expectation from blackbody emission and find that the ratio of resolved radii to blackbody equilibrium radii depends on the

luminosity of the star. We find that the radii resolved in this work are consistent with typical values observed for solar-type stars. Radiation pressure will clear a disk of its smallest grains, so the greater the host star's luminosity, the closer the ratio $R_{\rm in}/R_{\rm BB}$ is to unity. We find that a solar analogue disk tends to have a ratio $R_{\rm in}/R_{\rm BB} \sim 2$ (see Table 2.5), consistent with the values determined for Solar-type stars by Morales et al. (2013). Pawellek et al. (2014) also find that the ratio is slightly greater than one using a modified blackbody approach and $\sim$2 using a size distribution at infrared wavelengths.

From the mid-IR portions of the SEDs, we find that at least three disks in this sample require two-temperature belts, which we interpret as two radially distinct debris belts, similar to Chen et al. (2006), Chen et al. (2009), Su et al. (2009), and Morales et al. (2011). Chen et al. (2014) find that the majority of sources with 13, 31, and 70 μm excesses require multiple components to simultaneously fit the observed range of excesses. The debris disk around HD 104860 has been fit with one component (Pawellek et al., 2014) and two components (Morales et al., 2013). We analyzed the SED and visibilities with one component as well as two, and find that a two-component disk best reproduces the thermal SED with at least a 3σ significance using the Bayesian Information Criterion (BIC). HD 8907 is the only disk in the sample that clearly requires only one component, yet we also place an upper limit on the warm belt mass (see Table 2.7). The lack of excess warm dust implies that this disk has an inner radius of at least tens of au.

HD 107146 is the only disk in this sample with an unambiguously resolved disk width. Recent ALMA results of HD 107146 demonstrate that in fact its disk

surface density is likely quite complicated with a deficit of flux between the inner and outer radii (Ricci et al., 2015). The other disks around solar-type (F and G types) have widths that are smaller than their inner radii (< 100 au) and are not spatially resolved by the observations. For comparison, the Solar System's Kuiper belt begins at a radial distance of 40 au from the Sun. The "classical" Kuiper belt truncates at a distance of 50 au and its "scattered" component extends for hundreds of au (see review articles in Barucci et al. 2008, pp. $3-10$).

Significant differences in radial width at different wavelengths have now been observed for several different debris disk systems. Two particularly striking examples are the edge-on disks around au Mic and β Pic, which exhibit narrow millimeter-wavelength rings embedded in significantly broader scattered light distributions (Apai et al., 2015; Kalas et al., 2013, 2004; Krist et al., 2005; Schneider et al., 2014; Smith & Terrile, 1984; Wilner et al., 2011, 2012). The location of the narrow millimeter ring corresponds with the radius of a break in the surface brightness power law observed in scattered light, which dovetails with theoretical predictions by Strubbe & Chiang (2006). Their analysis of the brightness distribution of au Mic predicts the presence of a "birth ring" of large planetesimals at the radius of the break in the scattered light power law. Because small grains are influenced by the effects of radiation pressure, they are blown to much larger radii, creating a "halo" around the birth ring. The millimeter grains, by contrast, are far less affected by stellar radiation pressure, and more faithfully trace the location of the parent planetesimal belt.

At the time of writing, only two of the disks in our sample have been resolved in

scattered light, namely HD 61005 and HD 107146 (Schneider et al., 2014; Soummer et al., 2014). The disk around HD 107146 exhibits only a slight extension of scattered light beyond the extent of the millimeter grains (Ertel et al., 2011; Ricci et al., 2015). The ratio of the width of the disk observed in scattered light, $\Delta R_{\rm sl}$, to the width of the disk observed at millimeter wavelengths, $\Delta R_{\rm mm}$, is approximately 1.2 (given the approximate inner radius of 60 au and outer radius of 220 au quoted for the scattered light extent of HD 107146; see Table 5 in Schneider et al. 2014). By contrast, both the au Mic and β Pic debris disks exhibit scattered light haloes that extend to several times the radius of their millimeter counterparts (Wilner et al., 2011, 2012), although au Mic's millimeter disk exhibits a low surface brightness component that extends in toward the central star with no detectable inner radius (MacGregor et al., 2013). From analyses of the HD 61005 disk (Buenzli et al. 2010; Hines et al. 2007; Ricarte et al. 2013), the scattered light images can reveal external physical processes that shape the disk. For example, Ricarte et al. (2013) show that the millimeter grains are more strongly confined to the parent planetesimal belt than the more spatially extended scattered light morphology, providing support for an ISM-related origin to the dramatic swept-back morphology of the disk. Conversely, ALMA observations of the same disk reveal millimeter-wavelength emission from an extended halo component (MacGregor et al., 2018).

2.4.3 Deviations from an Axisymmetric Model

Non-axisymmetric features such as eccentric rings, warps, and spiral arms, have been observed in several debris disks, primarily at optical and near-IR wavelengths. These features are generally thought to be caused by dynamical interactions between the disk and its (usually unseen) planets. In at least two cases (β Pic: Currie et al. 2011; Lagrange et al. 2010, 2012; Mouillet et al. 1997; Smith & Terrile 1984; and Fomalhaut: Chiang et al. 2009; Holland et al. 2003; Janson et al. 2012; Quillen 2006; Wyatt & Dent 2002), such features have pointed the way to the discovery of directly imaged planetary-mass companions orbiting the central star. While other mechanisms have been proposed to explain some of these non-axisymmetric features (for example, gas pressure gradients may cause eccentric rings (Lyra & Kuchner, 2013); stellar flybys may cause warping (Malmberg & Davies 2009; Malmberg et al. 2011, 2007; Marzari & Picogna 2013; Zakamska & Tremaine 2004); and interactions with the ISM may cause large-scale asymmetries including swept-back structure (Debes et al. 2009; Maness et al. 2010), the success of direct imaging studies demonstrates that at least in some cases structure in debris disks does reveal the presence of planets far from their host star.

A long-standing theoretical prediction holds that millimeter wavelengths, with their sensitivity to macroscopic particles that are insensitive to the effects of stellar radiation pressure, should be ideal for observing resonant clumpy structure generated by resonant interactions between a planet and nearby dusty debris (Wyatt 2003, 2006, 2008a). This prediction is consistent with the observation that Kuiper

belt objects have been trapped in Neptune's major resonances, likely as a result of its past migration through the early solar system's planetesimal disk (Chiang et al. 2003; Hahn & Malhotra 2005). However, attempts to detect clumpy structure in debris disks using millimeter wavelength interferometry have a somewhat checkered history: early observations of clumps consistent with resonances in Vega's debris disk (Koerner et al. 2001; Wilner et al. 2002) were not confirmed using more sensitive observations (Hughes et al. 2012; Piétu et al. 2011), and apparent clumpy structure in the HD 107146 debris disk (Corder et al., 2009) was later demonstrated to be consistent with random noise in low-signal-to-noise ratio (S/N) images (Hughes et al., 2011). To date, the only dust continuum asymmetry observed in a debris disk observed using millimeter-wavelength interferometry is a relatively subtle brightness asymmetry between the two ansae of the edge-on β Pictoris debris disk (Dent et al., 2014). All other interferometric observations of debris disks, including several sensitive studies with the ALMA observatory (Boley et al. 2012; MacGregor et al. 2013, Ricci et al. 2015), have been well reproduced by a smooth, axisymmetric density distribution. It is also worth noting that there is no evidence for clumpy structure in the HR 8799 debris disk (Booth et al. 2016; Hughes et al. 2011; Patience et al. 2011), despite the known presence of at least four giant planets orbiting just interior to the outer dust disk (Marois et al. 2010, 2008).

Our results, which demonstrate that all five disks in our sample are similarly well reproduced by axisymmetric density distributions, are in line with these previous results. There is a localized 3-sigma peak in the ALMA HD 107146 residual map, although a single 3σ peak is consistent with chance noise properties and re-

quires confirmation through future observations of this system. The sensitivity and spatial resolution are limited, and sufficient only to detect a very strong degree of non-axisymmetry. We can make a simple estimate of our ability to detect non-axisymmetry using the peak S/N per beam in the images: assuming that we want to detect non-axisymmetry at the 3σ level, we would require beam-to-beam surface brightness changes of 100% for disks with a peak S/N of 3-4, perhaps 50% for disks with peak SNR of 5-8, or as little as 15-20% for the S/N/beam of 20 reached by the ALMA observation of HD 107146. It is certainly possible that more sensitive future observations could detect a more subtle density contrast around the disk, especially for the lower-S/N detections in our sample. The lack of clumpy structure, even in systems with known giant planets, is consistent with theoretical work by Kuchner & Stark (2010), demonstrating that collisions can smooth out structure even for millimeter grain sizes in disks with embedded planets.

2.5 Summary and Conclusions

We have analyzed millimeter-wavelength interferometric observations from the SMA, CARMA, and ALMA of a sample of debris disks around Solar-type stars. Two of the disks are spatially resolved for the first time by our observations. We simultaneously model both the resolved millimeter-wavelength visibilities and the broadband SED of each system, which yields information about the geometry and basic dust grain properties in each disk. The inner radii of the debris belts tend to be a factor of a few larger than predicted from blackbody equilibrium calculations

alone, implying that the disks contain small grains produced in a collisional cascade. The characteristic grain sizes derived from our modified blackbody approach are typically several times larger than the blowout size predicted for stars with Solar luminosities, consistent with results from previous studies. Only one of the five disks, HD 107146, has a spatially resolved radial width ($\Delta R/R_{\rm in} \gtrsim 1$). We detect no asymmetries in the disks, to within the limits of our relatively low S/N ratio. Overall, the five debris disks in our sample are consistent with scaled-up versions of the Solar system's Kuiper belt.

Chapter 3: A Sample of Post-Main-Sequence Stars Observed with *Herschel*

3.1 Introduction

The evolution of stars with initial masses $\sim 1 - 8\,M_{\odot}$ involves ∼Myr to Gyr spent as a red giant and an asymptotic giant, with their internal structures and chemistry changing over time and affecting material and planets within their spheres of influence. While 20-50% of MS stars have debris disks and IR excesses (see Review by Hughes et al. (2018) and references therein), only about 7% of K giants show IR excess from circumstellar material (Rebull et al., 2015).[1] Circumstellar dust should be present around evolved stars due to mass loss, planet system evolution, and common envelope/binary interactions. All of these processes can have similar observational signatures, i.e., excess IR emission due to thermal reprocessing of star light by grains. Understanding the dust around these evolved stars can help improve our understanding of grain growth and evolution.

Draine (2006) showed that a warm dust population with grain sizes characterized by a power law distribution with index q emits a spectrum whose behavior at

[1]The large spread for the MS debris disks is due to a dependence on stellar spectral type (with A stars displaying the highest detection rates).

Rayleigh-Jeans wavelengths follows the power law $\beta = (p-3)\beta_s$ (Hughes et al., 2018). The parameter p is related to the observed spectral index, $\alpha_{\rm obs}$ at (sub)millimeter wavelengths. Values of $\beta \approx 1$ point toward the growth of grains up to sizes $\geq$ 3mm (Draine, 2006). Since the lifetimes of post-MS evolutionary stages grow increasingly shorter with time, if large grains are found, this could potentially place strong constraints on the time-scale of grain growth (Scicluna et al., 2020)$\cdots$-if the grains are being created rather than eroded. While observations of C-S dust are useful in placing constraints on processes within a planetary system, knowledge of the chemical composition of the stellar photosphere might also provide some clues.

As stars evolve on the main sequence, they deplete a large fraction of their lithium through the proton-proton (pp) chain. This pp chain fusion in the core leads to a decrease in the surface lithium abundances as convection extends deeper into the star (see seminal work by Icko Iben in the late 1960s). By the time a star with an initial mass $\sim 1\,M_{\odot}$ is a red giant, the lithium abundance is depleted by a factor of 30 to 50 (Iben, 1967), and has $\log \epsilon(^7\mathrm{Li}) \sim -1$ to 1 (Brown et al., 1989; Sackmann & Boothroyd, 1992).[2] However, there are a number of giant stars with enhanced lithium abundances. The lithium in these systems could be produced by some internal process, or it could be deposited by some external object, e.g., collisions with metal-rich small bodies or star-planet interactions.

Cameron & Fowler (1971) propose a mechanism of internal ^{7}Li production (during helium shell flashes) from ^{7}Be at the base of a convective zone. As the

[2]For the reporting of lithium abundances as $\log \epsilon(^7Li)$, this is actually $\log \epsilon(^7Li) = \log[n(Li)/n(H)] + 12$, where n is the number density.

^{7}Be convects outward, it captures electrons, appearing on the stellar surface as ^{7}Li. While this mechanism provides a method of Li production for post-MS stars, it requires convective envelope temperatures that are much hotter than those seen in Li-rich giants (Carlberg et al., 2012).

Alternatively, Alexander (1967) first suggested that the accretion of Earth-like planets could result in Li-enriched giant stars. In two-body models of a star and smaller body, Nordhaus & Spiegel (2013) showed that the orbit of the smaller body changes due to mass loss and radial expansion of the star, and dissipation of orbital energy through tidal interactions. Jupiter analogues with initial orbital semi-major axes $\gtrsim 3$ au avoid engulfment, and instead their orbits expand farther from the star (Villaver & Livio, 2007). Planets of differing masses that are within $\lesssim 3$ au of the star, will likely spiral in and evaporate completely during the AGB phase (Livio & Soker, 1984; Villaver & Livio, 2007). Siess & Livio (1999) modeled the accretion event of a giant planet or brown dwarf being engulfed by a red giant star. They identify six different observational signatures of accretion, some of which include: a potential increase in ^{7}Li by 2 orders of magnitude, an increase in rotation rates for the star, X-ray emission through a magnetic dynamo, and the ejection of shells, as mass is lost during the accretion event. Taking a minimum mass of an object like Neptune (0.05 $M_{\rm Jupiter}$), and the minimum and maximum radii from their models (10.72 and 137.10 $R_\odot$), 6.7% to 14.8% (respectively) of known exoplanets could potentially interact with their hosts on the RGB. These estimates are larger than those from Siess & Livio 1999 (4% - 8%) due to the increase in the number of planets detected on close orbits.

The typical rotation rate of a giant star is $\sim$1 km s^{-1}, yet a select few exhibit uncharacteristically rapid rotation rates in excess of 10 km s^{-1}. A star's rotational velocity can increase through tidal interactions within a planetary system. Those tides can cause torques that act on both the star and planets in that system (e.g., Brown et al. 2011). Alternatively, as described above, planets eventually engulfed by their host stars can cause the rotation rate of the star to increase, through conservation of angular momentum. This transfer would produce a spin-up of the star and suggests that the accretion of planets could be the source of enhanced rotation and Li-enrichment seen in some evolved stars (Carlberg et al., 2013; Da Silva et al., 2015). A number of giants with enhanced rotation also have strong IR excesses.

Post-MS evolution can naturally explain an IR excess. While on the AGB, stars produce C, N, O, s-process elements, molecules, while dust grains form in the cooler, outer layers of the stellar atmosphere. The star loses mass due to radiation pressure expelling the newly formed, and loosely bound, grains and gas. This mass loss leads to the formation of expanding circumstellar envelopes (CSEs), whose constituents help replenish the ISM. CSEs can be observed via the detection of infrared excesses (IR) (e.g., R Sculptoris), which can often be confused with debris disks (e.g., κ CrBor). If a star is obviously no longer on the MS and not yet a white dwarf, then knowledge of its distance (to accurately determine the absolute magnitude, inferring the luminosity and temperature) is required. Without an accurate distance, a giant star experiencing an accretion event can look like a pre-MS star.

Knowledge of the exact evolutionary stage of post-MS stars for which we have

photometric observations and infrared maps, can help in the characterization of an infrared excess. If the IR excess is around a star prior to mass loss and the rotation rate is higher than expected, it is likely that the IR excess is due to planet engulfment. If the IR excess is around a star experiencing mass loss, then the IR excess is likely a side effect of the stellar evolution, and the emitting material should contain molecules, stellar ash (PAHs), and dust grains. Improving the timeline for post-MS planetary engulfment might improve understanding of how material ends up polluting white dwarfs that have unexpected metals in their photospheres and circumstellar gas disks (see Chapter 4).

In this chapter, we present archival infrared *Herschel* data on a sample of post-MS stars. We revisit known stars that now have accurate distances and focus on a broad characterization of the coldest thermally emitting dust for the detected stars in the sample. We present new photometric flux densities for these post-MS stars at IR and submillimeter wavelengths, and provide recommendations for future follow-up with submillimeter interferometric observations. In Section 3.2, we describe the observations and archival data retrieval. In Section 3.3, we introduce the targets, summarizing knowledge to-date of each star. In Section 3.4, we describe our modeling process, or how we investigate the evolutionary status and dust population. In Section 3.5, we present overall characteristics of the sample determined from a systematic analysis, highlighting particular targets of special interest. We present our conclusions in Section 3.6, and discuss future work in Section 6.

3.2 Observations

Table 3.1: Basic properties of the sample

Target	RA (h m s)	Dec (d m s)	Distance (pc)	$T_{\rm eff}$ (K)	Rad ($R_\odot$)	Lum $L_\odot$	log g (g cm^{-2})	Evol Stage
BD+47 3700	22 08 05.72	+48 02 09.65	566.57	5102.90^{203}_{46}	7.26	32.16	2.96	RGB
BP PSC	23 22 24.70	-02 13 41.38	358.76	4498.00^{399}_{124}	3.20	3.78	3.51	RGB
CD-30 11814	14 55 28.63	-30 41 55.49	514.22	4869.41^{179}_{95}	5.80	17.03	2.82	RGB
CPD-53 295	01 17 43.49	-52 33 30.79	414.68	7142.00^{159}_{174}	1.62	6.15	4.02	PrMS
HD 100764	11 35 42.75	-14 35 36.66	301.22	4921.29^{75}_{75}	7.55	30.16	2.74	RGB
HD 219025	23 13 52.78	-68 17 28.82	312.05	4604.30^{119}_{164}	16.04	104.18	1.81	RGB
HD 233517	08 22 46.71	+53 04 49.23	878.89	4372.12^{139}_{122}	21.58	153.37	1.64	RGB
IRAS 12327-6523	12 35 40.32	-65 39 41.38	2783.9	3539.00^{136}_{130}	144.09	2934.09	-0.52	EAGB
IRAS 17596-3952	18 03 06.77	-39 51 54.00	1709.9	4034.25^{124}_{98}	16.84	67.65	2.26	RGB
PDS 100	19 31 01.23	+05 23 53.49	732.71	4138.39^{147}_{93}	16.86	75.08	2.15	RGB
PDS 365	13 34 37.42	-58 53 32.35	1340.7	4017.00^{398}_{93}	10.44	25.56	2.78	RGB
TYC 3151 931 1	20 11 16.81	+37 30 52.09	1958.9	3991.30^{178}_{174}	34.23	267.84	1.38	RGB
TYC 3983 224 1	22 27 05.11	+54 21 29.03	1391.0	4320.00^{138}_{61}	24	180.69	1.53	RGB
TYC 4004 1409 1	23 44 34.43	+55 44 00.25	4081.6	4124.09^{118}_{109}	47.42	586.12	0.84	RGB
TYC 4144 329 2	10 23 09.87	+61 36 43.43	393.65	5143.45^{1880}_{852}	...	...	...	...
TYC 4167 629 1	13 22 17.75	+62 33 38.11	1309.2	4935.33^{72}_{88}	11.06	65.35	2.16	CHEB
TYC 596 145 1	00 29 18.59	+09 52 30.82	505.36	4631.02^{125}_{92}	10.24	43.44	2.37	RGB
TYC 6312 824 1	19 46 31.99	-15 43 48.25	782.35	4614.71^{593}_{192}	5.16	10.88	3.07	RGB
TYC 6687 100 1	12 33 42.07	-24 34 27.75	...	...	...	...	...	...
TYC 7246 979 1	12 29 55.01	-35 49 28.59	1943.26	4489.97^{173}_{133}	30.26	335.39	1.64	RGB

NOTE — The distance, effective temperature, star radius, star luminosity (Lum) and log g are from Gaia Collaboration et al. (2018). The evolutionary (Evol) status is confirmed in this work. The stages are: pre-main sequence (PrMS), main sequence (MS), sub giant branch (SGB), red giant branch (RGB), core helium burning (CHEB), and early asymptotic giant branch (EAGB).

The sample of PMS stars were observed by the Photodetector Array Camera and Spectrometer (PACS; Poglitsch et al. 2010) on the *Herschel Space Observatory*. The basic properties of the sample are given in Table 3.1. The stars presented in this work are from Cycle 1 opentime program (OT1_cmelis_1, PI: C. Melis) with a total of 20 sources. For the sources obtained through this OT1 program, the PACS imaging for the blue 70μm ($60-85\mu$m), green ($85-125\mu$m), and red 160μm ($130-210\mu$m) bands was obtained simultaneously in scan mode along a scan map position angle of 70°. Each field was scanned with a medium scan speed of 20 arcsec s^{-1}, 10 scan legs of length 3.0 arcmin, a 4.0 arcsec scan leg separation, and a repetition factor of one. The total time per observation is 276 seconds.

Each star in the sample was also observed by the Spectral and Photometric Imaging Receiver (SPIRE) (Griffin et al., 2010) onboard *Herschel* as part of a Cycle 1 program (OT1_cmelis_1, PI: C. Melis) with a total of 20 sources. Within each observation from the program, two scans were performed at nearly orthogonal angles with the nominal $30''$ s^{-1} scan speed that resulted in a $\sim 5'$ diameter area of homogeneous coverage in all three SPIRE wavebands centered at 250, 350, and 500μm.

All of the archival OT1_cmelis_1 observations with PACS are available reduced to "Level 2.5", a science-ready product. The archival SPIRE data from the same program are available reduced to "Level 2.0", also a science-ready product. We use the Herschel Interactive Processing Environment (HIPE) version 15.0 (Ott, 2010) to perform aperture photometry on the Scanamorphos-produced maps[3] to extract flux densities of the sources.

To perform the aperture photometry, we first convert the map units from Jy beam^{-1} to Jy pixel^{-1}. We next visually inspect each image to see if the source is visible above the background. We place circular apertures manually over sources that are visually detected. To estimate the local background, we include a concentric annulus around the source aperture. Four regions within this annulus are sampled by an additional set of apertures to calculate the background root-mean-square (RMS). There are a small number of sources in fields with other emitting sources. We avoid these regions when placing the apertures to estimate the background. We

[3]Scanamorphos is an IDL map-making software for Herschel and other similar bolometers (Roussel, 2013).

use the `annularSkyAperturePhotometry` routine on SPIRE quality 2 maps and the `pacsAnnularSkyAperturePhotometry` routine on PACS quality 2.5 maps. The maps are not PSF-subtracted leading to a tri-lobe shape for systems that have emission to overfill the beam.[4] The beam sizes for PACS are $5.4'' \times 5.7''$ (70μm), $6.7'' \times 5.9''$ (100μm), and $10.5'' \times 12.1''$ (160μm) with a scan speed of $20''$/s. The beam sizes for SPIRES are $18.4'' \times 17.4''$ (250μm), $24.9'' \times 23.6''$ (350μm), and $37.0'' \times 33.8''$ (500μm) with a scan speed of $30''$/s. The flux densities for targets that were detected are given in Table 3.2.

3.3 The Sample

The sample of stars was found serendipitously in the *Herschel* archive while searching for an IR excess around HD 233517. Expanding the search revealed that a principal investigator (PI, Carl Melis) had a similar interest in investigating thermal emission around post-MS stars and was successful in obtaining time (OT1_cmelis_1, PI: C. Melis), yet data are unpublished at the time of writing. Before presenting our findings on this sample considering the "new" *Herschel* data, we summarize published findings for each star below.

3.3.1 BD+47 3700

BD+47 3700 was observed at millimeter wavelengths to search for SiO maser emission (Jiang et al. 1999) and ^{12}CO emission (Kerton & Brunt 2003), but none

[4]The PSF or point spread function characterizes a telescope's response to a point source. The tri-lobe structure results from the secondary mirror supports of the telescope.

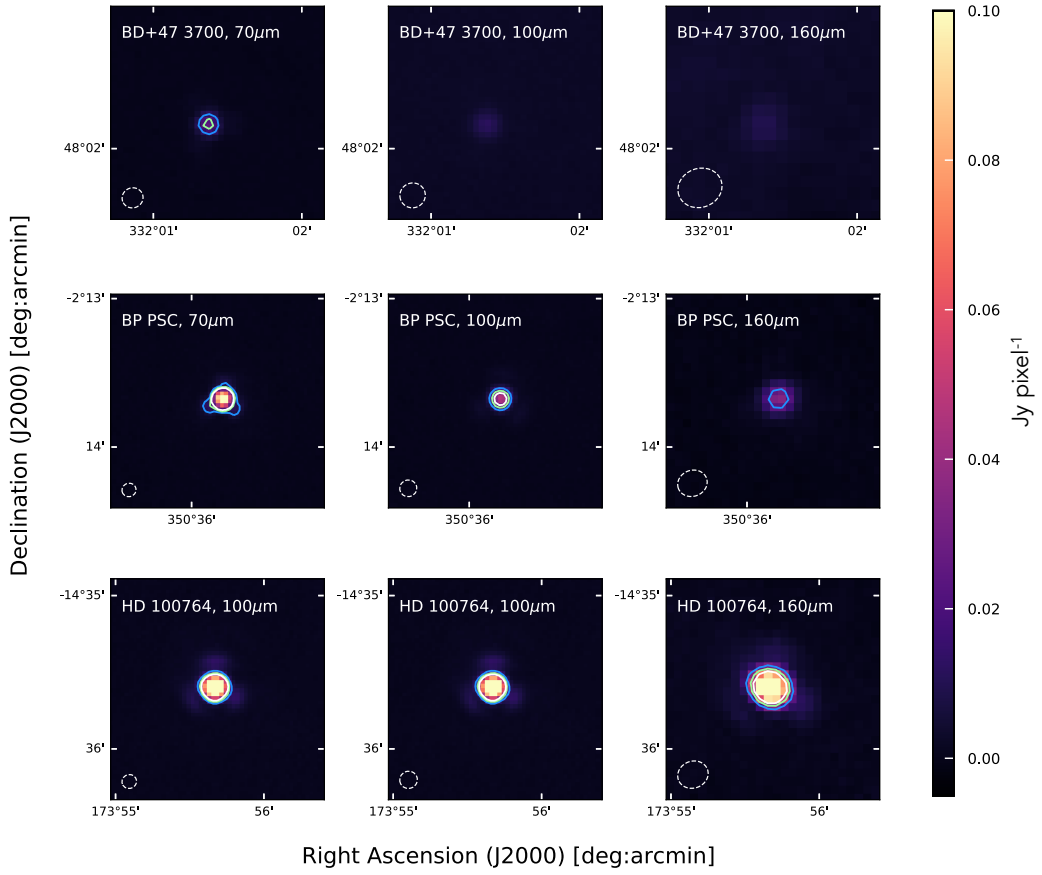

Figure 3.1: PACS images of the sources with a detection at 70μm

The target name and reference wavelength are noted in the top left corner. There is one target per row. The white circle with a dashed "- - " line style shows the beam size and orientation. Contours are drawn at $3, 5, 7 \times$ RMS in each frame, in blue, green, and white (respectively). The color scale is linear and the map units are Jy pixel^{-1}. The beam sizes for PACS are $5.4'' \times 5.7''$ (70μm), $6.7'' \times 5.9''$ (100μm), and $10.5'' \times 12.1''$ (160μm) with a scan speed of $20''$ s^{-1}.

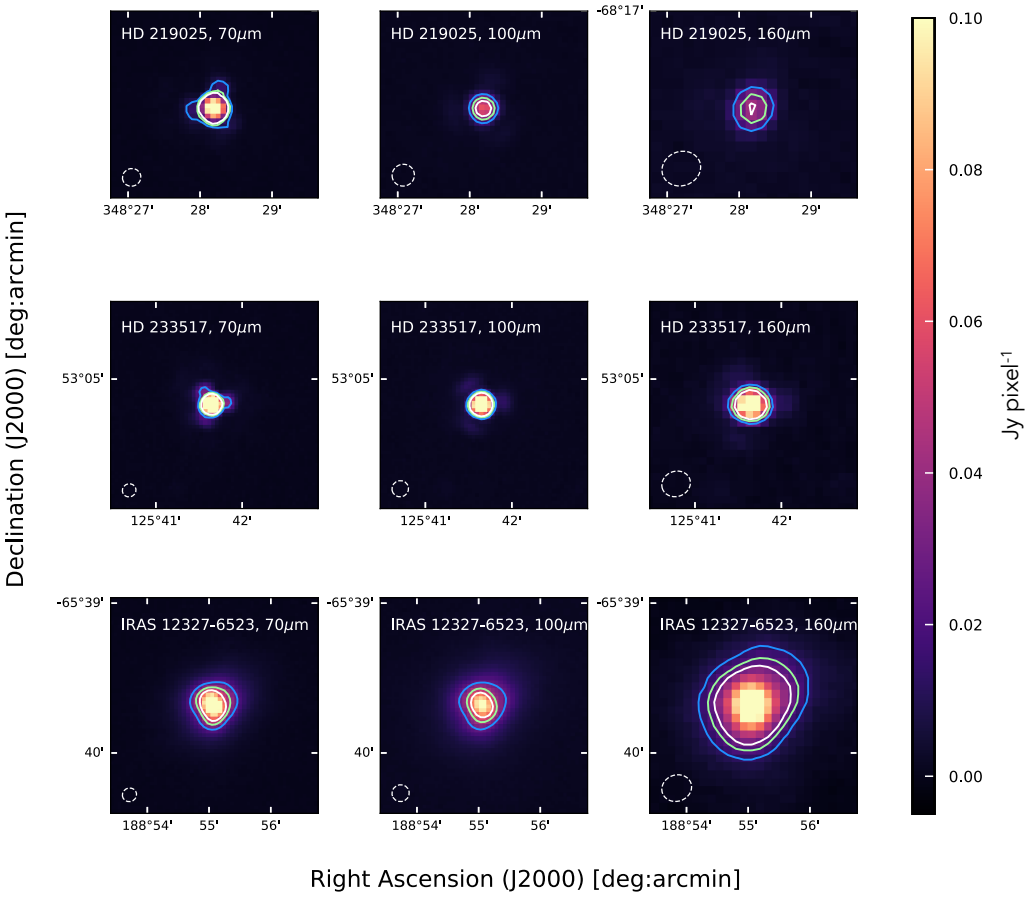

Figure 3.2: Caption same as Figure 3.1.

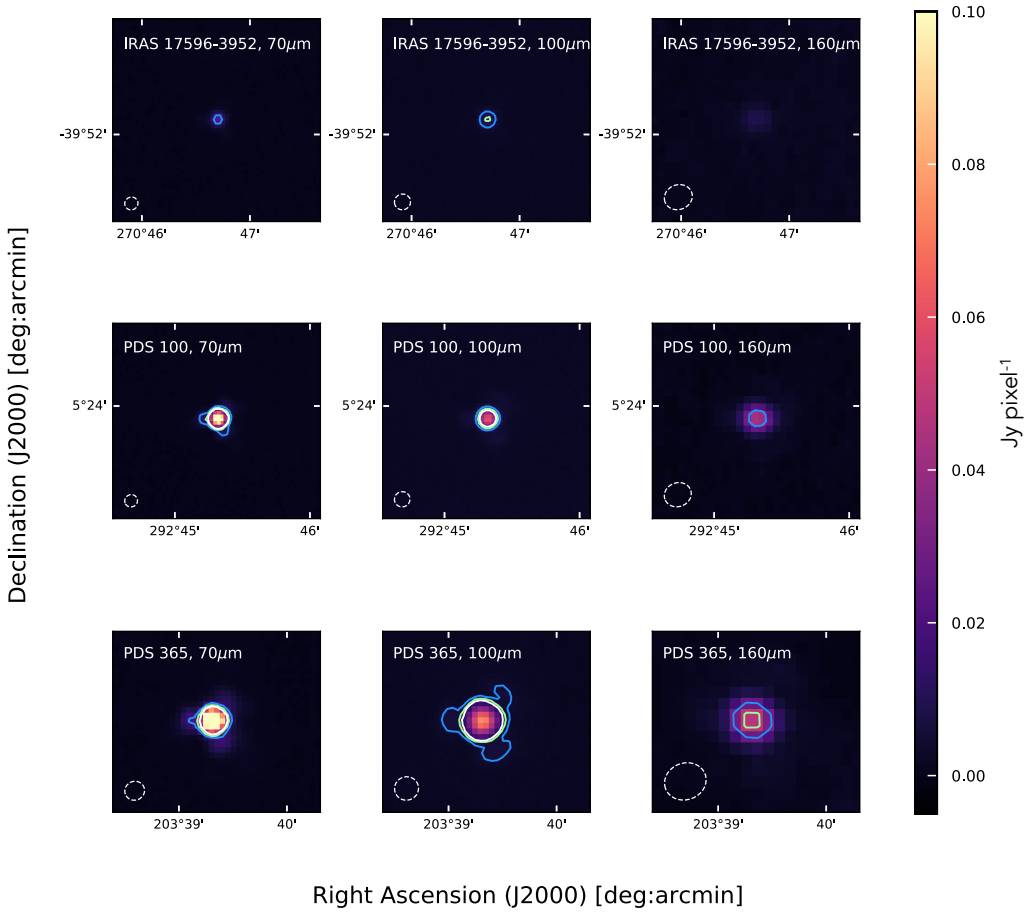

Figure 3.3: Caption same as Figure 3.1.

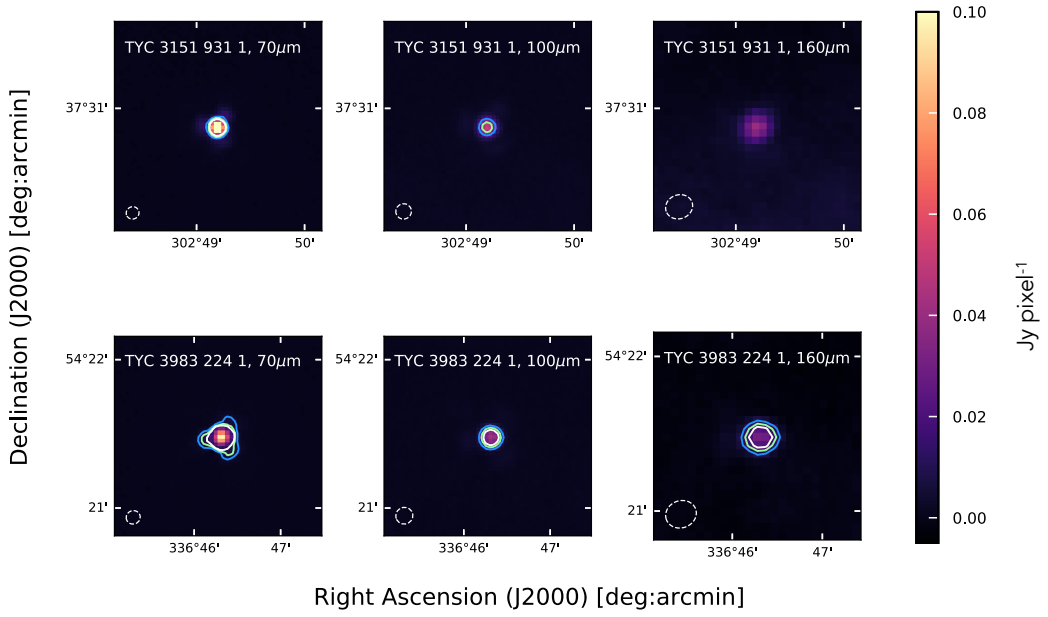

Figure 3.4: Caption same as Figure 3.1.

was detected. It was also observed by IRAS as part of a survey of B type stars with infrared excess (Miroshnichenko et al., 2007). Their results show that the central star is an A3-type dwarf with no line emission and a slight asymmetry of the H line profile. They also suggest that BD+47 3700 is a member of a recently discovered, but not yet studied type of evolved early-type star with C-S dust.

3.3.2 BP Piscium

Previous observations of BP Piscium (BP Psc) revealed strong Hα and forbidden line emission (Stephenson, 1986); an orbiting, dusty circumstellar disk, and a parsec-scale system of highly collimated outflows (Zuckerman et al., 2008); a weak lithium 6708 Å line, gravity-sensitive photospheric absorption, highly crystalline sub-micron-sized dust grains detected with the Spitzer Infrared Spectrograph (Melis

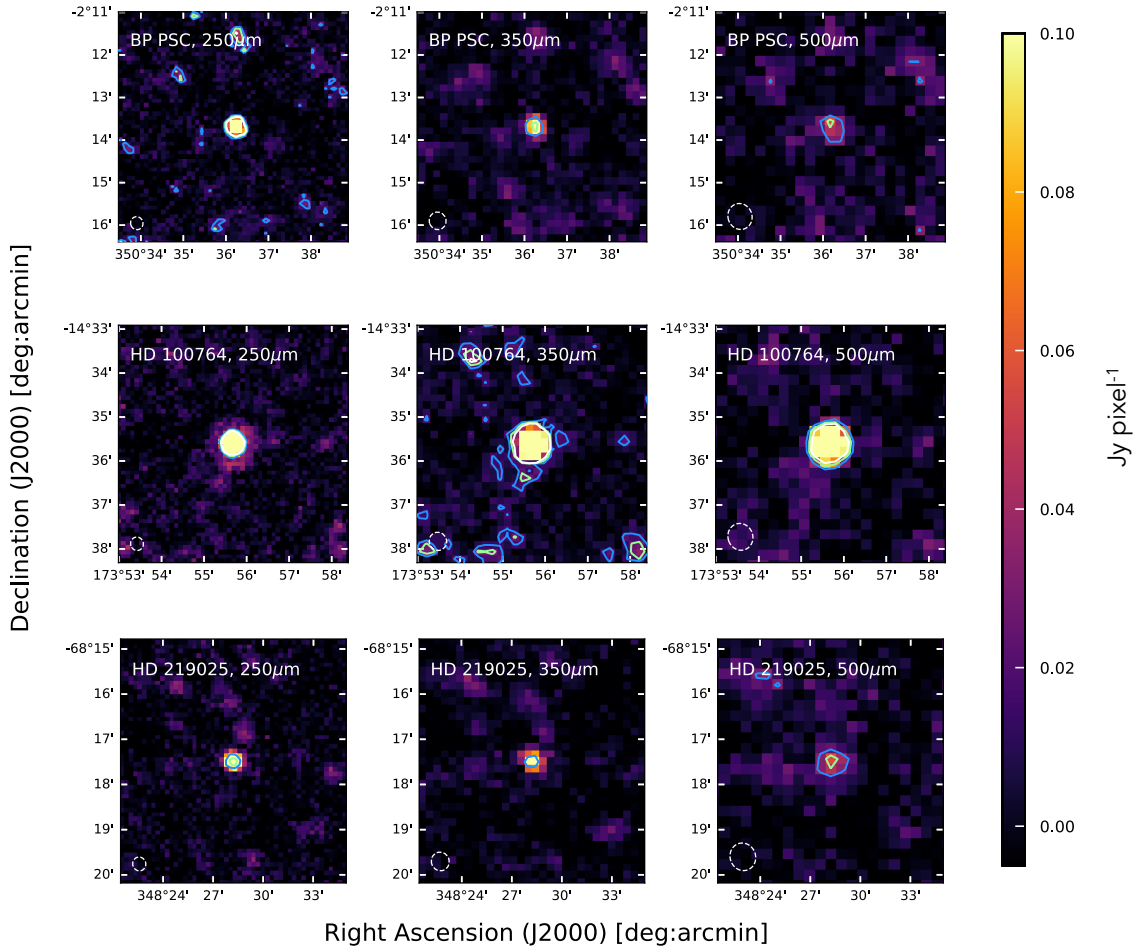

Figure 3.5: SPIRE images of the sources with a detection at 250μm

The target name and reference wavelength are noted in the top left corner. There is one target per row. The white circle with a dashed "- - " line style shows the beam size and orientation. Contours are drawn at $3, 5, 7 \times$ RMS in each frame, in blue, green, and white (respectively). The color scale is linear and the map units are Jy/pixel. The beam sizes for SPIRES are $18.4'' \times 17.4''$ (250μm), $24.9'' \times 23.6''$ (350μm), and $37.0'' \times 33.8''$ (500μm) with a scan speed of $30''$/s.

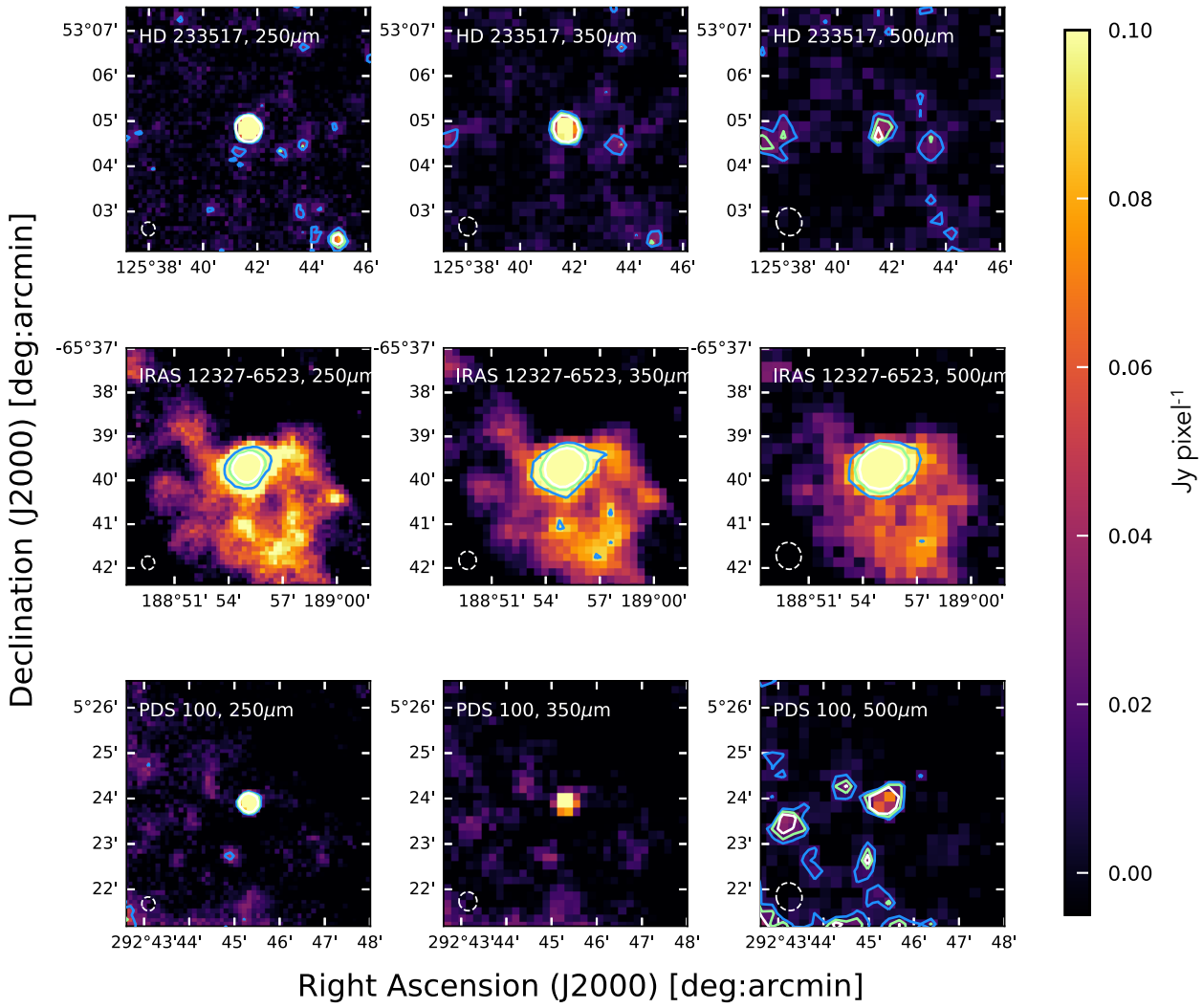

Figure 3.6: Caption same as Figure 3.5.

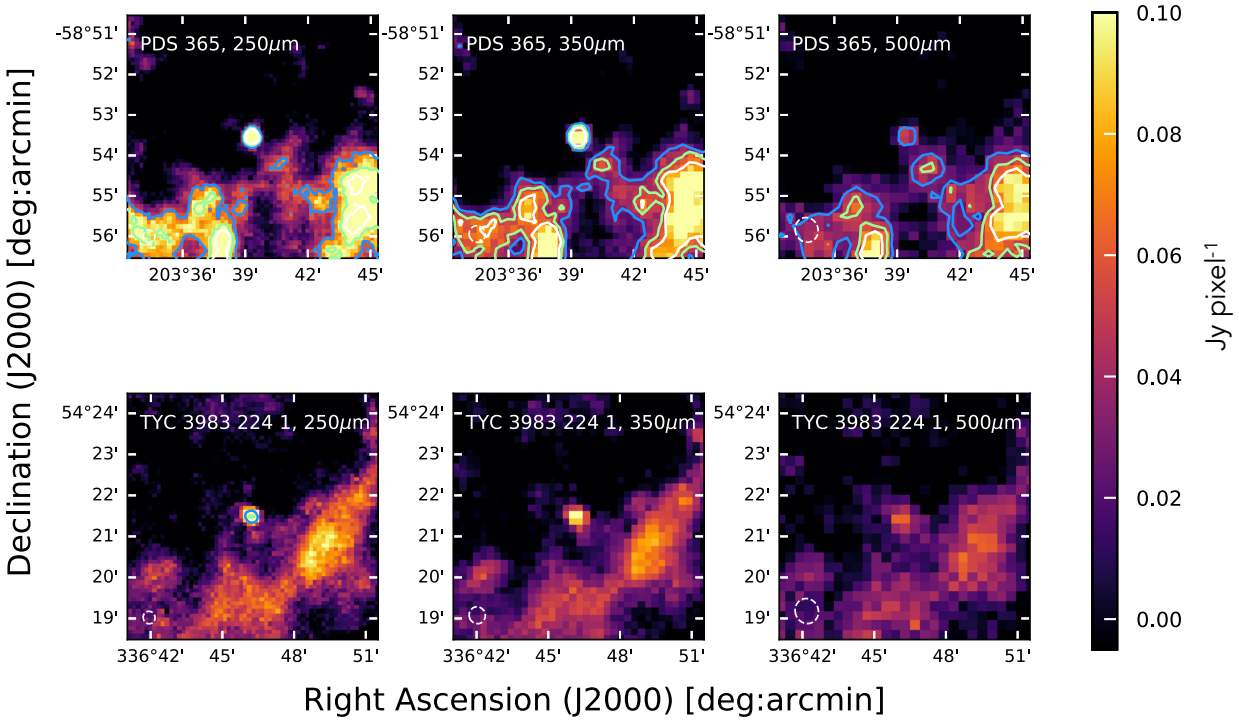

Figure 3.7: Caption same as Figure 3.5.

et al., 2010); and a central star that is a weak X-ray point source (Kastner et al., 2010). These characteristics can belong to a young star with a protoplanetary disk, or to an evolved star with a disk derived from the engulfment of a companion or planet.

3.3.3 HD 100764

HD 100764 is a warm carbon star with an IR excess. Warm carbon stars (class R) are expected to show an overabundance of *s*-processes elements, but HD 100764 does not. Skinner (1994) obtained an IR spectrum of HD 100764 to investigate the composition of the dust producing the IR excess and found that there are no strong features present in the IR, concluding that the dust composition is amorphous carbon. Sloan et al. (2007) obtained a high-resolution IRS spectrum of HD 100764 and found that there are "class C" polycyclic aromatic hydrocarbon (PAH) features present.[5]

There has been some contention about the evolutionary status of HD 100764. A carbon star is the natural result of ascending the AGB, but the luminosity of HD 100764 is too low for the star to be on the AGB (Parthasarathy, 1991). If HD 100764 is on the RGB, then it should be oxygen-rich like other stars at this evolutionary stage (e.g., HD 233517) (Sloan et al., 2007). HD 100764 also appears to have a warm ($\sim$1500 K) dust component (Melis et al., 2009) and a detached, colder dust shell, which is an expected result of the AGB. So, HD 100764 could possibly be beyond the

[5]A source with "class C" PAH emission does not display the pair of features centered on 7.7μm (Peeters et al., 2002), see Section 1.4.

AGB. Lastly, it is listed in Cox et al. (2012) as an AGB star that shows no obvious bow shocks. Alternatively, HD 100764 could be an *extrinsic* carbon star (McDonald et al., 2017) that is still on the RGB, and the carbon polluting the atmosphere could have originated from a more evolved binary companion.

3.3.4 HD 233517 and HD 219025

HD 233517 has been identified as a first ascent K giant[6] with a large infrared excess caused by a flared disk with a radius > 50 au. The spectrum of HD 233517 shows features from class C PAHs and signs of the engulfment of a companion (Jura, 2003; Jura et al., 2006). The possible engulfment theory comes from observations (Jura et al., 2006) of photospheric lithium ([Li]/[H]$= 1.7 \times 10^{-8}$), rapid rotation ($v \sin i = 17.6$ km s^{-1}), and a marginal CO(3-2) line detection (Dent et al., 2005) at 345 GHz (see Table 1). Its spectral type and luminosity class were determined through high resolution spectroscopy, but its distance was unknown before *Gaia* DR2 (Fekel et al., 1996).

The star with optical properties most similar to HD 233517 is HD 219025. HD 219025 has a well-documented IR excess (Bharat Kumar et al. 2015; Jasniewicz et al. 1999; Whitelock et al. 1991) and lithium excess (e.g., Kumar et al. (2011)). It is also a fast rotator, with $v \sin i = 23$ km s^{-1} (Holanda et al., 2020; Jasniewicz et al., 1999). The Hα profile is very different from that of the other stars mentioned in this section in terms of the variability of the profile. It resembles the changes seen in the

[6] On the first ascent of the red giant branch of the H-R stellar evolutionary diagram, with a temperature placing it in the K spectral class.

absorption features of WD 1145+017. However, the Hα line of HD 233517 is broad with a blue-shifted asymmetric core and a blue-shifted emission peak, implying that the star is undergoing significant mass loss (Fekel et al. 1996).

3.3.5 IRAS 12327-6523/PDS 355

IRAS 12327-6523 (IRAS 12327) or PDS 355, is an evolved star with excess IR emission. The system has previously been classified as an early AGB star (Charbonnel & Balachandran 2000; De la Reza et al. 2015) and it could be an analogue to R Sculptoris—an AGB star with IR excess due to a natural by-product of evolution (Maercker et al., 2012). Prior to the first Gaia data release, the distance to this star was unknown, casting doubt on the exact age of the star. IRAS 12327 was studied in detail as possibly being a lithium-enriched star with log ϵ(Li) $\sim$ 1.4, but standard dilution by the first dredge-up *could* have resulted in this lithium abundance (Reddy & Lambert, 2005). Additionally, the carbon isotope ratio, $^{13}C/^{12}C$ (=6) is much lower than the predicted ratio of 20-30 (Reddy & Lambert, 2005). Lower than predicted C isotope ratios have been observed for tip and clump giants (Gilroy & Brown, 1991), and mixing in excess of that predicted by standard theories is needed to account for the depletion. Excess mixing can be induced post-first-dredge-up by meridional circulation currents due to stellar rotation (Charbonnel & Balachandran, 2000; Fekel & Balachandran, 1993).

3.3.6 IRAS 17596-3952

IRAS 17596-3952 (IRAS 17596) or PDS 485, is part of the sample from De la Reza et al. (1997), was identified in Bharat Kumar et al. (2015) as having an IR excess, and is a confirmed Li-rich, first dredge-up K giant (e.g., Kumar et al. 2011; Reddy & Lambert 2005). IRAS 17596 has unusually broad lines due to rapid rotation. The Hα line has an asymmetric profile with a blue-shifted core. This star is part of the RGB "bump clan" (Reddy & Lambert, 2005). IRAS 17596 provides further support to the idea that all Li-rich rapid rotators have a far-IR excess.

3.3.7 PDS 100

PDS 100 is a Li-rich K giant according to the literature (Reddy et al. 2002, among others), and a long-period variable star in SIMBAD. It was first identified as having an IR excess by Bharat Kumar et al. (2015) and also appears in De la Reza et al. (1997). PDS 100 is a rapid rotator and also has asymmetric absorption lines (notably Hα and Na D 5889.9 Å and 5895.9 Å). The Na D line profile is complex with strong absorption at -16 km s^{-1} (relative to the systemic velocity), and shallow, broad blue-shifted absorption. The blue-shifted component is described as having a circumstellar origin (Reddy et al., 2002).

We note that PDS 100 appears close to a molecular cloud in the PACS and SPIRE images.

3.3.8 PDS 365

PDS 365 has similar properties to HD 233517 and HD 219025· · ·-it is confirmed as both a Li-rich K giant and a rapid rotator (e.g., Drake et al. 2002; Kumar et al. 2011). PDS 365 was first identified as having an IR excess by Kumar et al. (2015). Due to the Li-enrichment, IR excess, and rapid rotation, Drake et al. (2002) strongly support the idea of PDS 365 having recently engulfed a planet (a view not necessarily adopted by other authors). However, Simbad categorizes PDS 365 as a post-AGB star.

Like several of the other targets, PDS 365 has asymmetric absorption line profiles with a blue-shifted core and slightly blue-shifted emission. These features (blue-shifted core and blue-shifted emission) resemble those of late-type supergiants with chromospheric winds.[7]

3.3.9 TYC 3983 224 1 and TYC 3151 931 1

TYC 3983 224 1 or IRAS 22251+5406 appears in a survey of AGB stars and based on its SED, is listed as a possible post-AGB star (Blommaert et al., 1993). The 12 μm flux did not vary over a 6 year period suggesting that the star is not losing mass. If the mass loss phase were over, then IRAS 22251+5406 would be associated with a planetary nebula, but it is not. TYC 3151 931 1 or IRAS 20094+3721 is

[7]These profiles are P Cygni profiles, containing both absorption and emission for a single spectral line. These features are indicative of a dense stellar wind near the star (emission) and radiation passing through circumstellar material expanding in the direction of the observer (blueshifted absorption).

Table 3.2: Flux densities for a subset of stars from OT1_cmelis_1

Target	F_{70} (Jy)	F_{100} (Jy)	F_{160} (Jy)	F_{250} (Jy)	F_{350} (Jy)	F_{500} (Jy)
BD+47 3700	0.332 ± 0.006	0.189 ± 0.006	0.09 ± 0.02	...	...	...
BP PSC	2.034 ± 0.003	1.139 ± 0.005	0.471 ± 0.006	0.206 ± 0.02	0.092 ± 0.01	0.046 ± 0.01
CPD-53 295	0.570 ± 0.004	0.323 ± 0.003	...	...	...	...
HD 100764	6.005 ± 0.005	4.460 ± 0.005	2.289 ± 0.009	1.150 ± 0.007	0.666 ± 0.019	0.277 ± 0.01
HD 219025	2.572 ± 0.003	1.511 ± 0.006	0.911 ± 0.007	0.227 ± 0.025	0.122 ± 0.005	0.056 ± 0.01
HD 233517	5.994 ± 0.009	4.346 ± 0.006	2.219 ± 0.008	0.562 ± 0.043	0.192 ± 0.027	0.028 ± 0.009
IRAS 12327-6523	10.15 ± 0.008	10.56 ± 0.009	7.301 ± 0.031	2.773 ± 0.044	1.629 ± 0.068	0.638 ± 0.05
IRAS 17596-3952	0.390 ± 0.006	0.263 ± 0.002	0.209 ± 0.016	...	...	...
PDS 100	2.266 ± 0.003	1.428 ± 0.004	0.676 ± 0.011	0.270 ± 0.008	0.137 ± 0.008	0.055 ± 0.005
PDS 365	3.220 ± 0.006	1.847 ± 0.002	0.964 ± 0.027	0.375 ± 0.056	0.212 ± 0.030	0.057 ± 0.028
TYC 3151 931 1	2.300 ± 0.011	1.321 ± 0.023	0.675 ± 0.088	...	...	...
TYC 3983 224 1	1.683 ± 0.001	0.954 ± 0.003	0.623 ± 0.003	0.217 ± 0.012	0.145 ± 0.055	0.089 ± 0.004

Flux densities for a subset of the sample. Flux and uncertainty estimations were calculated using HIPE (see the Observations section for details) for stars that were detected visually at each particular wavelength. The uncertainties do not include systemic uncertainties.

listed as a post-AGB Star (proto-PN) in Simbad[8].

3.3.10 The Other Targets

CPD-53 295/PDS 2 is a possible Herbig Ae/Be star with a C-S excess. The rest of the targets that appear in OT1_cmelis_1 are relatively uncharacterized and have a publication record of 0 to 1 papers. For TYC 4004-1409-1, TYC 4167-629-1, TYC 6312-824-1, and TYC 6687-100-1, this work presents their characteristics for the first time.[9]

3.4 Modeling and Analysis

The primary goals of our efforts to analyze each system are to (1) compare the evolutionary states of the stars to prior determinations in the literature by using

[8] `http://simbad.u-strasbg.fr/simbad/`

[9] TYC 596-145-1 appeared in a survey searching for planets, but has an unknown status there (International Deep Planet Survey results, Galicher et al. 2016).

improved measurements of the stellar distances and assumed temperatures, and (2) determine if there are signs of grain growth for the stars with PACS and SPIRE detections by fitting the SEDs and determining the spectral index of the RJ tail.

3.4.1 Evolutionary status determination

Using the *Gaia* DR2 values of luminosity and $BP - RP$ color (BP: 516.47nm and RP: 783.05nm, Weiler 2018), we place the stars for which we have flux densities on a color-luminosity diagram. For isolated stars, isochrones can be used to estimate their evolutionary state given a luminosity and temperature. A set of isochrones are, like the name suggests, a snapshot of stellar population with some initial distribution of masses after some specified amount of time. A single track in a set of isochrones would provide basic parameters for an individual star in the HR or color-luminosity diagram.[10]

The isochrones are based on PARSEC release v1.2S + COLIBRI S_35[11] Bressan et al. (2012); Chen et al. (2014, 2015); Marigo et al. (2017); Pastorelli et al. (2019); Tang et al. (2014). The PARSEC tracks are computed for a solar composition scaled in mass. The tracks follow the $Y = 0.2485 + 1.78Z$ relation, with $Z_\odot = 0.01524$, where X, Y, and Z are the mass fractions of hydrogen, helium, and metals in the solar photosphere (Bressan et al., 2013; Caffau et al., 2011). The COLIBRI tracks extend the PARSEC tracks to the end of the thermal pulse asymptotic giant branch phase (TP-AGB), taking into account mass loss and dredge-up

[10] Figure 1.1 is an example of what a "track" for a sun-like star would look like in an HR diagram plotting stellar temperature vs luminosity.

[11] `https://github.com/timothydmorton/isochrones`

parameters. Modeling thermal pulses is complex and so the code uses a simplified AGB track, allowing the user to essentially pick the number of thermal pulse cycles by setting the number of points $n_{\rm inTPC}$ between the start and end of the thermally pulsing stage. When generating the isochrones, we set the resolution of the thermal pulse cycles (TPCs) during the TP-AGB phases to $n_{\rm inTPC} = 10$. Mass-loss on the RGB is not well-determined (Miglio et al., 2012), but can be described empirically as a function of stellar luminosity, radius, and surface gravity using the Reimers relation

$$\frac{{\rm d}M}{{\rm d}t} = 1.27 \times 10^{-5}\, \eta\, M^{-1}\, L^{1.5}\, T_{\rm eff}^{-2}, \tag{3.1}$$

where M is the star mass in solar units, L is the star luminosity in solar units, t is time in years, η describes the efficiency of the RGB mass-loss rate, and $T_{\rm eff}$ is the effective stellar temperature in K (Miglio et al., 2012; Reimers, 1975). No mass loss corresponds to $\eta = 0$. We generate the models with the default $\eta_{\rm Reimers} = 0.2$.[12]

We output Gaia DR2, Tycho2, and 2MASS model photometry using VEGAMAG and Gaia passbands described in Evans et al. (2018). For bolometric corrections, we chose the YBC package (Chen et al., 2019). We set the total interstellar extinction to $A_V = 0.0$ and to $A_V = 0.75$ for comparison.[13] We choose $A_V = 0.75$ because this is approximately the median value for the rest of the sample ($A_V = 0.758$). The models include the effects of light reprocessing by circumstellar dust produced in the circumstellar environments (CSE) of AGB stars (Marigo et

[12]Mass loss for this code converges under the condition $\eta_{\rm Reimers} < 0.5$.

[13]From Draine (2006b): The extinction, A_V (measured in magnitudes), characterizes the amount of radiation scattered due to interactions with dust. A_V is related to the "reddening" $E(B-V)$ by the dimensional ratio $A_V/E(B-V) = R_V$ for the B and V filters or passbands. R_V has a typical value of 3.1 in the Milky Way Galaxy.

al., 2017). As the composition of an AGB is primarily carbon, the dust produced in the CSE is composed of primarily amorphous carbon (AMC) and partially silicon carbide (SiC) (Marigo et al., 2017). To account for mass loss and dust production on the AGB branch, we include an 85% AMC + 15% SiC mix around C stars. We choose a Kroupa two-part power law initial mass function for the population that is corrected for binaries. We generate the population for 5 dex to 10.13 dex years after the Big Bang in steps of 0.1 dex to sample the PMS, RGB, and AGB, among which there was historic confusion for at least one star in the sample.[14]

In Figure 3.8, we use the two sets of isochrones (with $A_V = 0.0$ and $A_V = 0.75$) to investigate the sample. The tracks for initial stellar masses are binned to account for a changing population at different ages, leading to a spread in values for some binned masses and stages. Stars for which we have no estimates of reddening are plotted against the isochrones with $A_V = 0.75$ with open/empty markers.

The temperatures, radii, and luminosities reported by Gaia DR 2 come with some uncertainties (Andrae et al., 2018). The effective stellar temperatures are estimated from the colors assuming that the star has zero extinction. The interstellar extinction is estimated independently from the temperature using the three bands G, $G_{\rm BP}$, and $G_{\rm RP}$. A third model is used to estimate the reddening $E(BP - RP)$, where BP and RP are the observed magnitudes in bands $G_{\rm BP}$, and $G_{\rm RP}$. The luminosity is calculated using a bolometric correction that depends solely on the effective temperature, and becomes highly uncertain for $T_{\rm eff} < 4000$ K, which affects

[14]The term "dex" is shorthand to refer to powers of 10. So 5 dex is 10^5 and 10.13 dex is $10^{10.13} \approx 13.5$ billion.

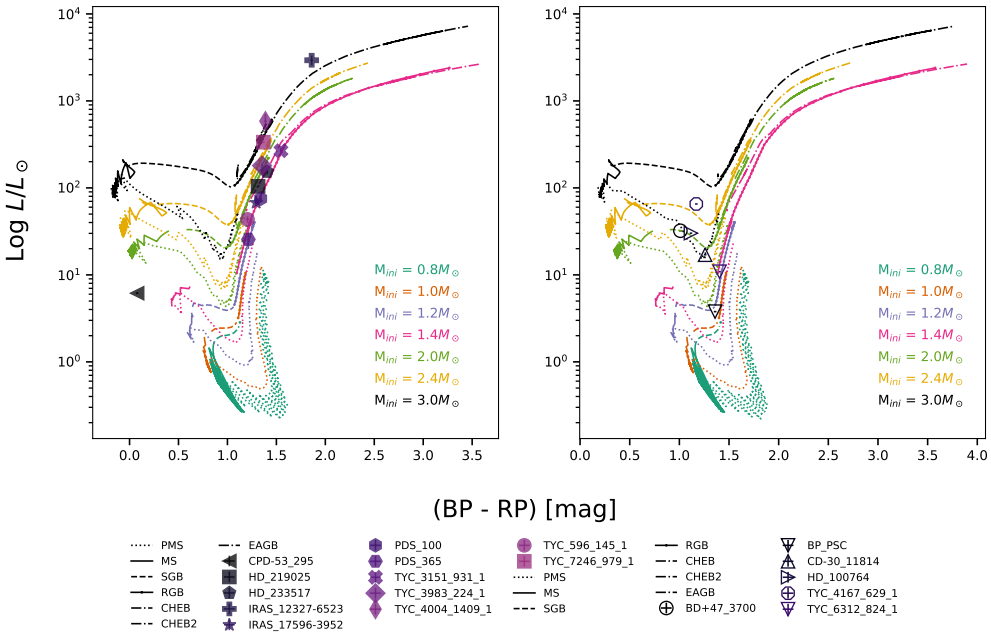

Figure 3.8: Evolutionary tracks for the sample.

$\cdots$ NOTE — The sample on a $\log(L/L_\odot)$ vs. $T_{\rm eff}$ diagram. Both Panels: the theoretical solar-metallicity evolutionary tracks (PARSEC tracks; Bressan et al. (2012); Marigo et al. (2017)) for M =0.8,1,1.2,1.4,2.0,2.4, and 3 $M_\odot$ are depicted by dotted (pre-main sequence, PrMS), solid (main sequence, MS), dashed (- -) lines (sub giant branch, SGB), solid (red giant branch, RGB), and dashed-dot lines: core helium burning (CHEB) and early asymptotic giant branch (EAGB) stages. Left: PARSEC tracks with $A_V = 0.0$ and stars from the sample with de-reddened colors using $E(BP-RP)$ from *Gaia* DR2. Right: PARSEC tracks with $A_V = 0.75$ and stars from the sample with no reported $E(BP-RP)$ from *Gaia* DR2.

at least one star in our sample. that there could be self-absorption from circumstellar material that could add some uncertainty to the SED fitting of the source.

3.4.2 Properties of the dust

We fit the spectral energy distribution (SED) of each system to probe the dust temperature and investigate the degree to which the thermal emission of the coldest detectable dust deviates from a blackbody (if at all). We model each star using a

Castelli and Kurucz model photosphere from the grid of ATLAS9 fluxes . We choose grids with metallicity, $[M/\mathrm{H} = +0.5]$ and microturbulent velocity $v_{\mathrm{turb}} = 2.0$ km s^{-1} Reddy & Lambert (2005). We scale the flux by a factor of $(R_\star/D)^2$, where $R_\star$ is the stellar radius and D is the distance to the star from Earth.

If there are micron-sized grains present in the dust population, then the emission from the dust will deviate from a black body due to the inefficiency of emission of the small grain population at far-IR and sub-millimeter wavelengths. Assuming micron-sized grains are present and the grain size distribution follows a power law, we model the thermal dust emission (present in the SED as excess emission at infrared wavelengths) as a set of modified blackbodies where the total flux density equals their sum.

This inefficiency of small grains to re-radiate emission from the host star leads to the Rayleigh-Jeans slope of the SED being suppressed, i.e., having a power law index more steep than that of a black body. To model a grain size distribution for each system would require knowledge of the dust mass per grain size bin and an equilibrium temperature calculation for each grain size present. We simulate the behavior of a distribution of grain sizes with their different efficiencies by parameterizing the efficiency $Q(a, \lambda)$ as a function of only wavelength,

$$Q(\lambda) = 1 - \exp\left[-\left(\frac{\lambda_0}{\lambda}\right)^{\beta}\right], \tag{3.2}$$

where $\lambda_0 = 2\pi a$ is the critical wavelength and β is the opacity spectral index

(Williams et al., 2004). The total flux F_ν from the system is then

$$F_\nu = B_{\nu,\star} + \sum_n m_n \cdot B_{\nu,n} \cdot Q(\lambda)_n, \tag{3.3}$$

where m is a vertical scaling factor that encapsulates the mass present and requires knowledge or an assumption of geometry and a minimum grain size, B_ν is the Planck function in frequency space, and n is the dust belt/shell number. We attribute the different temperature components to belts or shells of different temperature at different distances from the star. The SEDs of the stars in this sample mostly require more than 2 dust components to fit the existing photometric data. We choose the number of components after a visual inspection. We fit the available photometry using a non-linear least squares Python SciPy routine (curvefit). This routine provides an estimate of the covariance of the computed parameters. The grain size and β-parameter are not well-estimated, but we provide the one standard deviation errors (1σ) for the temperatures of the outermost belts when the temperature is constrained. The error is estimated by taking the square root of the diagonals of the covariance matrix.

These fits are not unique, highly degenerate, and require the location of the dust to be known in order to break the degeneracy. We fit all available photometry longward of $\sim 1\mu$m, given our focus on determining the spectral indices. The SEDs are shown in Figures 3.9, 3.10, 3.11 and 3.12. The flux contributions from the thermally emitting dust are shown with dashed gray lines and the black line shows the best fit to the photometric data combining the stellar and dust components.

Though we fit the entire SED, we report only the dust properties of the outermost belt in Table 3.4, given the new sub-millimeter fluxes. The relatively cold dust that peaks at $\sim 100\mu$m and is probed by the PACS and SPIRE observations typically has a RJ slope, or spectral index, steeper than that of a blackbody.

We determine the spectral index of the thermal emission from the dust by fitting the logarithm of the fluxes F_ν to a line such that

$$\log F_\nu = \alpha \log \lambda + b \tag{3.4}$$

where λ is the wavelength, α is the spectral index, and b is the y-intercept, following Scicluna et al. (2020). The spectral index at mm-wavelengths α is related to the β parameter as $\beta = \alpha - \alpha_{\rm Pl}$, where $\alpha_{\rm Pl}$ is the spectral index of the Planck function and depends on the dust temperature, with $\alpha_{\rm Pl} = 2$ in the RJ limit (Draine, 2006; Hughes et al., 2018; MacGregor et al., 2016).

We use the SciPy routine `curvefit` to determine α for stars detected with both PACS and SPIRE, and report those values in Table 3.4.[15] Only fluxes $\geq 160\mu$m are used to determine α. Deviations from a blackbody spectral index ($\alpha = 2$) hint at grain growth (see Discussion). We also estimate the expected fluxes at 0.87 mm and 1.3 mm, relying heavily on the SPIRE fluxes presented in this work. These expected fluxes are also reported in Table 3.4.

We measured upper limits for the spatial extents for 12 out of the 20 stars

[15]While this work is similar to that in Chapter 2, the big difference is that the location of the dust is not constrained here, leading to uncertainty in β. Therefore, we focus on α.

(without a PSF deconvolution).[16] One star has an IR excess resolved by PACS (IRAS12327-239) in all bands, and one star is marginally resolved by PACS at 70μm (HD 100764). SED modeling with knowledge of spatial extent from the Herschel PACS and SPIRE maps helps to break the degeneracy between grain size and grain location, but only an upper limit is available for most systems.

3.5 Results

The results of this work are summarized in Tables 3.1 - 3.4.

3.5.1 Isochrones

We find good agreement with the isochrone tracks after de-reddening the stars with known $E(BP-RP)$ values. For those stars with no reddening estimates, we find good agreement when we assume $A_V = 0.75$. The majority of the stars are on the RGB for initial stellar masses $\sim 0.9 - 3 M_{\odot}$ (see Figure 3.8). We find that IRAS 12327 is on the early AGB, though the extent of the dust suggests that it should be at the thermally pulsing stage. Another outlier, CPD-53 295 is much bluer than any of the provided tracks with $A_V = 0.0$. If $A_V = 0.75$ along the line of sight to BP Psc, then it is on the RGB. While HD 100764 appears to be on the RGB, it is a carbon star$\cdots$-a typical product of ascending the AGB. Depending on the initial mass of HD 233517, the star could be on the RGB or AGB.

[16]The spatial extents were determined by a friendly post doc, Dr. Jonty P. Marshall, but the effects of the PSF have not been removed.

3.5.2 Spatial Extents

The spatial extents of the targets shown in Figures 3.1 - 3.7, are given in Table 3.3. Without deconvolving the thermal emission from the PACS and SPIRE beams, we are limited in what we can determine about the spatial extent of the dust. We provide upper limit estimates of the emission from IRAS 12327-293 and HD 100764. At a distance of 2784 pc with angular size of $\sim$ 11", the dust toward IRAS 12327-293 has a spatial extent of $\sim 31,000$ au. For comparison, the dust around thermally pulsing AGB star R Sculptoris has an extent of $\sim 15,000$ au (Hankins et al., 2018). For HD 100764, with an angular size of $\sim$ 6.7" and at a distance of $\sim$ 300 pc, the dust has a spatial extent of $\sim$ 2000 au.

3.5.3 Dust Characteristics

Modeling the SEDs without knowledge of the grain location leads to degenerate fits when also fitting the characteristic grain size. We chose to limit the grains to be micron-sized and use a minimization routine to find best fits given our assumptions. From the fitting, we find that a typical grain size is 0.1 μm and the β-parameter ranges from 0.2 to $\sim$1.5. Typical values of β are $\beta = 2$ for interstellar medium grains, $0 < \beta < 1$ for pebbles of the order of 1 mm, and $\beta = 0$ for large grains. The values of $0 < \beta < 1$ for most debris disks point toward grain growth and further support of coagulation processes of planetesimal formation.

Interstellar dust is expected to have $\alpha \sim 3.6$, with typical opacity spectral index values of $\beta \sim 1.6$ (Planck Collaboration et al., 2014; Scicluna et al., 2020).

Grain growth is inferred by $\alpha > 3.6$, suggesting that grains are larger and thus approaching the behavior of a blackbody, which has $\alpha = 2$. We find that the spectral index α at submillimeter wavelengths ranges from about 2 to 3 for the stars in our sample. Stellar mass loss is a source of the dust in the ISM (Draine, 2011), but the spectral indices of the stars departs from what would be expected in the ISM. These IR excesses could either point toward grain growth Scicluna et al. (2020), or the recent disruption of a body. The temperatures of the outermost grains that are constrained by the *Herschel* PACS and SPIRE fluxes and fit with a modified blackbody range from $\sim$ 30 K to $\sim$several 100 K.

Next, we highlight a number of popular systems, and discuss planetary engulfment and the Li-enrichment, fast rotation, IR excess connection in the context of this sample.

3.5.4 HD 233517

HD 233517 has flux density of $\sim$ 2.6 mJy at 1.35 mm, detected by SCUBA (Sylvester & Mannings, 2000). From our SED fitting, we predict a flux of $\sim$ 7 mJy. The dust producing the IR and submillimeter emission has been modeled as an opaque flared disk (Jura, 2003), with parameters representative of circumstellar silicates with a size $\sim$100 μm (Jura, 2003). We find similar temperatures for the grains, but very different spatial extents for the grains, which is a perfect example of the grain size-distance degeneracy inherent in this type of modeling. Jura (2003) find that the dust has a temperature of 70 K and has an outer radial extent of 45

Table 3.3: Angular extents of *Herschel* maps

	Distance	FWHM$_x$	FWHM$_y$	PA
Star	(pc)	arcsec	arcsec	(°)
BD+47 3700	566.6	5.39	5.35	160
BP PSC	358.8	···	···	···
CD-30 11814	514.2	···	···	···
CPD-53 295	414.7	···	···	···
HD 100764	301.2	6.71	6.59	-80
HD 219025	312.1	···		···
HD 233517	878.9	5.39	5.31	49
IRAS 12327-6523	2784.0	11.57	10.51	-10
IRAS 17596-3952	1710.0	···	···	···
PDS 100	732.7	5.39	5.31	51
PDS 365	1340.7	···	···	···
TYC 3151 931 1	1958.9	5.39	5.31	-0.1
TYC 3983 224 1	1391.0	5.42	5.28	53
TYC 4004 1409 1	4081.6	5.28	4.67	41
TYC 4144 329 2	393.7	5.58	5.35	74
TYC 4167 629 1	1309.2	5.65	5.31	38
TYC 596 145 1	505.4	5.43	5.05	53
TYC 6312 824 1	782.4	5.50	5.24	51
TYC 6687 100 1	···	···	···	···
TYC 7246 979 1	1943.3	···	···	···

NOTE — The spatial extents of the sample assuming a 2-D Gaussian fit resulting in a full-width at half max in the x (FWHM$_x$) and y (FWHM$_y$) directions. None of the maps have been PSF-subtracted and all sources are unresolved, except IRAS 12327-6523. The position angle (PA) is also provided. As a reminder, the beam sizes for PACS are $5.4'' \times 5.7''$ and $6.7'' \times 5.9''$ for 70μm , 100μm , respectively. The 70μm maps were used for all of the 2-D Gaussian fits, except for HD 100764, where the 100μm map was used.

	star			outermost belt				RJ tail		
Star	Distance	$T_{\rm eff,\star}$	$R_\star$	a	β	$T_{\rm gr}$	$R_{\rm gr,BB}$	Spectral Index	$F_{0.87\rm mm}$	$F_{1.3\rm mm}$
	(pc)	(K)	($R_\odot$)	(μm)		(K)	(au)		(mJy)	(mJy)
BD+47 3700	566.6	5103	7.3	0.4	0.7	149 (430)	19.72	-2.1	0.8	0.3
BP PSC	358.8	4498	4.3	0.1	0.3	45:	99.94	-1.97 (0.07)	16.6	6.9
CD-30 11814	514.2	4869	5.8	2.8	2.0	142:	15.94	···	···	···
CPD-53 295	414.7	7142	1.6	2.4	0.5	133:	10.87	···	2.9	1.1
HD 100764	301.2	4921	7.6	1.5	0.2	87:	55.92	-2.6 (0.7)	92.7	40
HD 219025	312.1	4604	16.0	20.3	2.0	27 (2)	1081.42	-2.9 (0.2)	6.5	1.5
HD 233517	878.9	4372	21.6	35.5	2.0	110 (10)	79.74	-3.12 (0.09)	6.9	1.5
IRAS 12327-6523	2784.0	3539	144.1	1.4	0.7	47 (60)	1900.41	-2.2 (0.1)	170	63
IRAS 17596-3952	1710.0	4034	16.8	0.1	0.1	159 (13)	25.26	-2.7 (0.1)	4.5	1.9
PDS 100	732.7	4138	16.9	3.2	0.1	168 (25)	23.71	-2.08 (0.04)	21.7	9.5
PDS 365	1340.7	4017	10.4	100.0	0.1	213 (15)	8.60	-2.1 (0.1)	22.4	9.9
TYC 3151 931 1	1958.9	3991	34.2	92.7	0.1	230:	24.02	-1.6 (0.3)	17.1	7.6
TYC 3983 224 1	1391.0	4320	24.0	4.8	0.1	181:	31.98	-2.0 (0.2)	18.0	8.0
TYC 4004 1409 1	4081.6	4124	47.4	4.9	0.3	92:	222.31	···	6.2	2.6
TYC 4144 329 2	393.7	5143	···	0.4	1.6	150:		···	···	···
TYC 4167 629 1	1309.2	4935	11.1	2.3	0.7	97:	66.21	···	0.4	0.1
TYC 596 145 1	505.4	4631	10.2	0.6	1.1	131:	29.66	···	0.1	···
TYC 6312 824 1	782.4	4615	8.8	2.8	2.0	118:	31.55	···	···	···
TYC 6687 100 1	···	5500	0.9	11.8	0.1	177 (300)	1.92	···	1.6	0.7
TYC 7246 979 1	1943.3	4490	50.0	70.5	0.1	137 (230)	124.48	···	6.0	2.7

Table 3.4: Properties of the C-S material for the sample.

NOTE··· The results of the SED fitting. Columns are: star name, the effective temperature of the star, the radius of the star in solar radii, the characteristic grain size used for the outermost belt, the β-parameter used for the outermost belt, the resulting temperature $T_{\rm gr}$ of the dust from the SED fit, the radius $R_{\rm gr,BB}$ at which that temperature would be reaching assuming blackbody absorption and emission, the spectral index of the Rayleigh-Jean (RJ) tail (calculated for system with SPIRE detections), the predicted flux at 0.87mm, and the predicted flux at 1.3mm. For the grain temperatures, 1σ error estimates are provided in parentheses. Especially uncertain values have a ":".

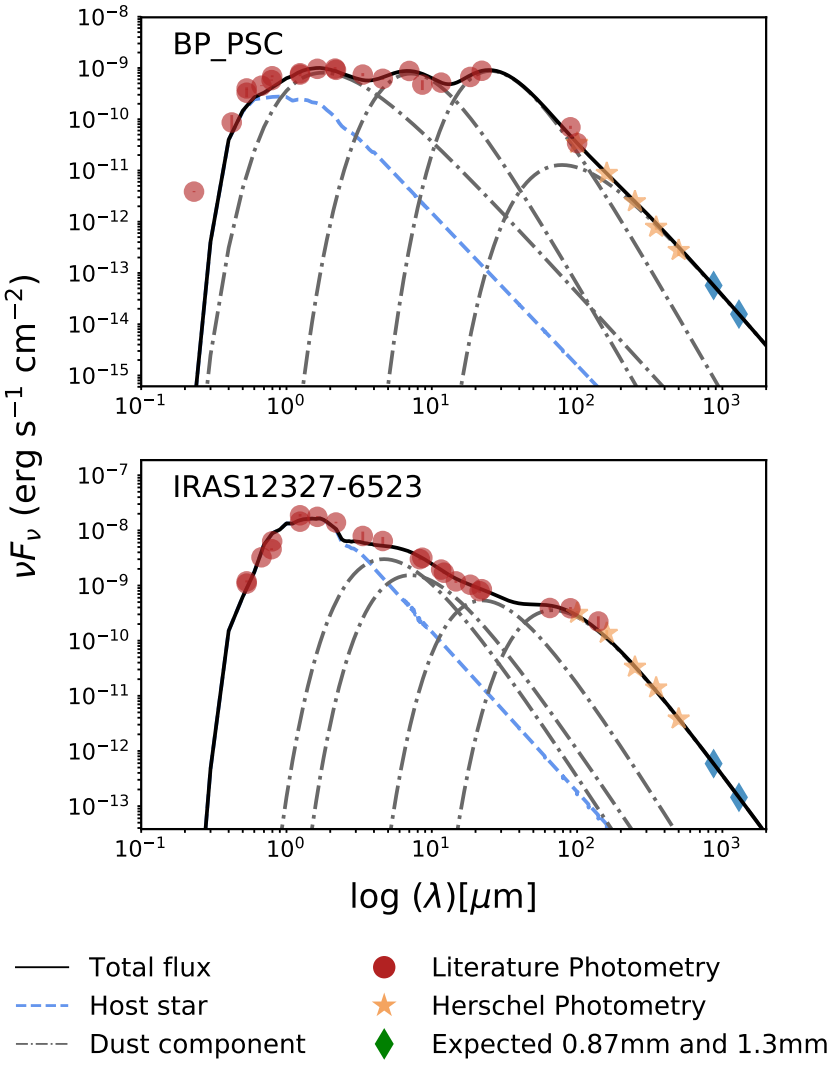

Figure 3.9: *Herschel* Post-MS Star SEDs, 1 of 5

NOTE — Fits to the SEDs. Contributions are as follows: the host star is shown with a blue dashed line, contributions from the dust fitting are shown with a dot-dash gray line, the photometry is shown with red circles, the new *Herschel* flux densities are shown with gold stars, and the black line is the best fit to the summed components. The star symbols highlight the *Herschel* photometry and green diamonds show the estimated fluxes for the SMA at 0.87 mm and 1.3 mm (in all panels).

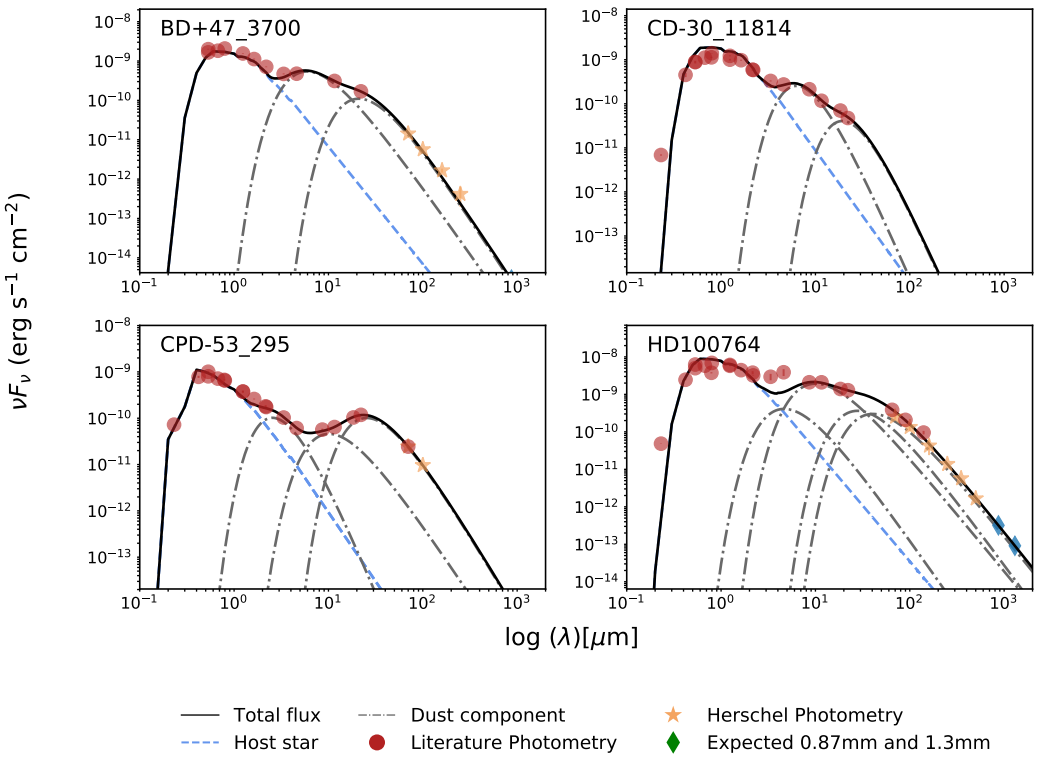

Figure 3.10: *Herschel* Post-MS Star SEDs, 2 of 5.
Caption same as Figure 3.9.

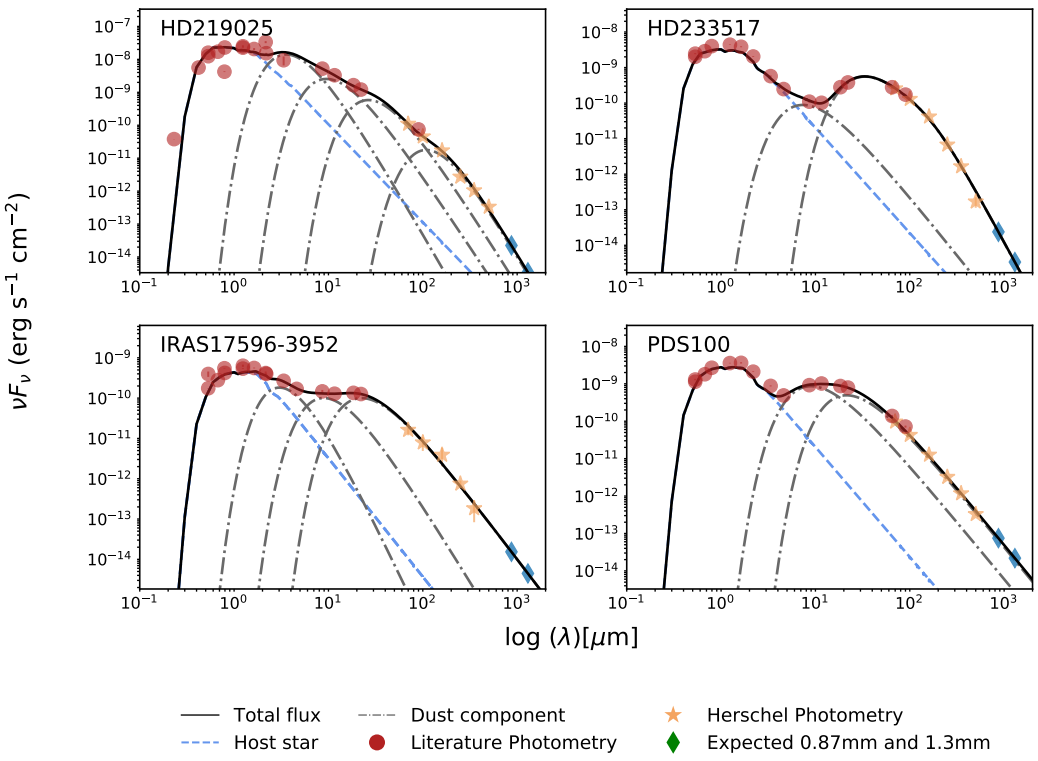

Figure 3.11: *Herschel* Post-MS Star SEDs, 3 of 5.
Caption same as Figure 3.9.

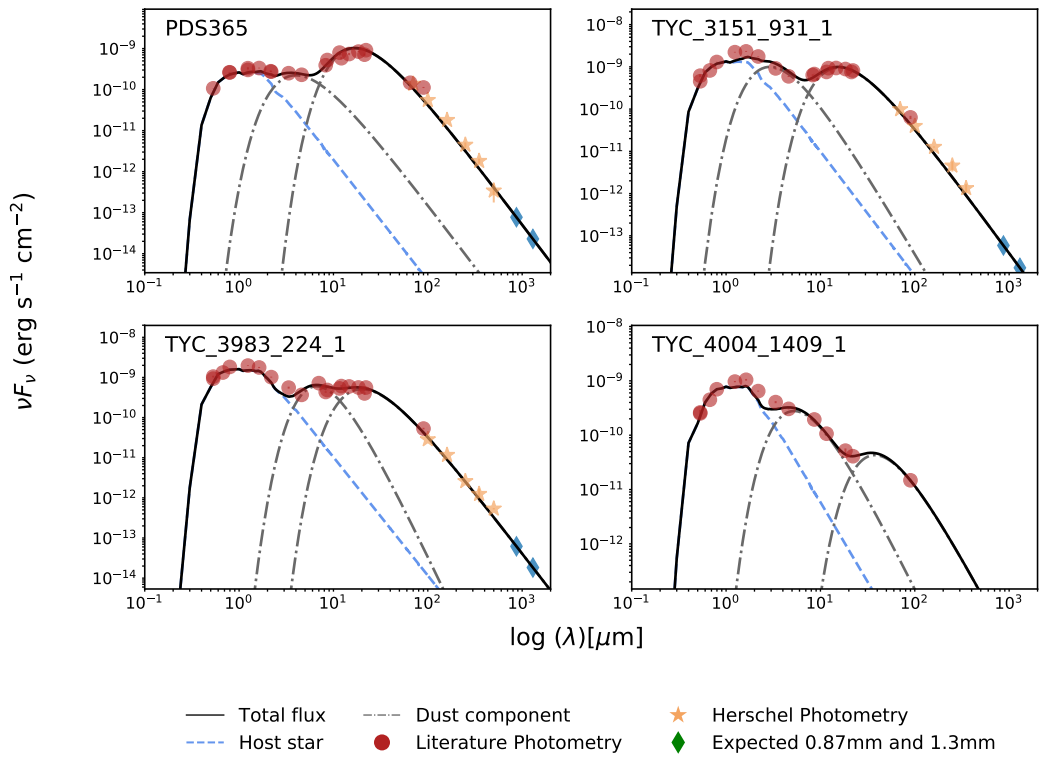

Figure 3.12: *Herschel* Post-MS Star SEDs, 4 of 5.
Caption same as Figure 3.9.

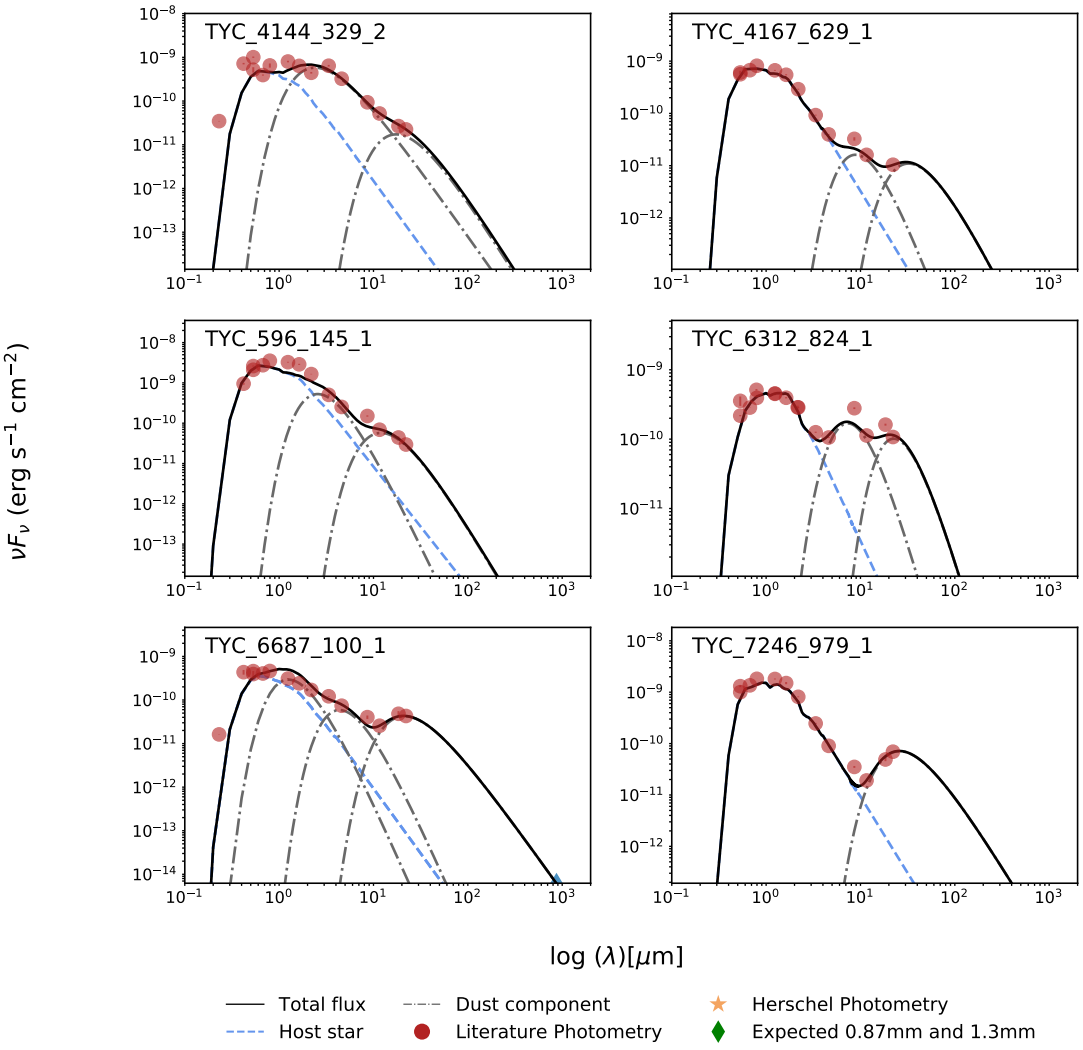

Figure 3.13: *Herschel* Post-MS Star SEDs, 5 of 5.
Caption same as Figure 3.9.

au. We find an outer disk temperature of 110 K, and characteristic grain size of 36μm , with a distribution characterized by $\beta = 2.0$. HD 233517 is unresolved in the PACS 70μm images, so we can only place an upper limit on the radial extent. At 878.9 pc (Gaia Collaboration et al., 2018), the 5.3" beam size implies an upper limit to the radius of 2300 au.

Jura et al. (2006) suggest that if HD 233517 engulfed a companion then the formation of a disk would be a natural result. The IR spectrum of HD 233517 reveals that it is surrounded by PAHs. Jura et al. (2006) also suggest that the PAH emission could be synthesized in situ or be incorporated from the ISM; it is likely not the result of mass loss from HD 233517. As an oxygen-rich star, mass loss from HD 233517 would be composed of silicates (Sylvester et al. 1994, 1998; Speck et al. 2000).

From our isochrone fitting, we determine that depending on the initial mass, HD 233517 could be on the RGB or AGB.

3.5.5 HD 100764

While we find that HD 100764 appears to be on the RGB, it is a carbon star$\cdots$a typical product of ascending the AGB. There are PAHs present in the dust, which was previously modeled to have a warm (800-1000K) component, mean temperature of $\sim$ 140 K, and a radial extent of $\sim$ 80 au (Parthasarathy, 1991). We find that the outer belt has a temperature of 120 K, is at 30 au, and has a character grain size of 10 μm. Skinner (1994) modeled the circumstellar dust and find that

there are no silicate features and that there are a range of grain sizes, r_g in the disk, with a best fit having sizes $0.5 < r_g < 500\mu$m. Given the stellar type and composition of the dust, they propose that the dust origin is from a companion that already evolved through the AGB and planetary nebula phases.

HD 100764 is not technically resolved in the *Herschel* images[17], but has an extent that is slightly larger than a single beam. At a distance of ~ 300 pc, interferometric observations would be useful to resolve the dust distribution to search for structure and signs of accretion from a companion.

3.5.6 BP Psc

There was uncertainty over the age or evolutionary stage of BP Psc for over a decade given the lack of a parallax measurement. Zuckerman et al. (2008) explored possibilities for the evolutionary stage of BP Psc. They found that if the star is at a distance of around 80 pc then it would be considered pre-main-sequence, and if the distance were ~ 300 pc, then it would be post-main-sequence. BP Psc has a parallax of 2.8 milli-arcseconds and is at a distance of 358.8 pc (Gaia Collaboration et al., 2018). It is worth noting that the evolutionary status of this star was uncertain until the Gaia mission, but both Zuckerman et al. (2008) and De Boer et al. (2017) favored the post-main-sequence scenario.

BP Psc is one of two stars in this sample that has been observed at sub-millimeter wavelengths. Zuckerman et al. (2008) observed BP Psc with the Submillimeter Array (SMA) and detected CO emission. The gaseous disk was detected out

[17]Resolve would mean having a spatial extent $3\times$ the size of the beam.

to ~ 200 au, but the dust could only be constrained to a distance of a few au due to a chosen fit to the SED. De Boer et al. (2017) observed BP Psc with SPHERE[18] at wavelengths $\lambda = 626.3$ nm and $\lambda = 789.7nm$, resolving the disk. They fit the SED using a radiative transfer code with grain sizes from 0.05μm to 3 mm, decreasing with a power law. We estimate that the radial extent of the dust in their model is ~ 20 au based on their Figure 4.

From the modified blackbody modeling of BP Psc and fits to the SPIRE data, we find that the expected flux density at 0.87 mm is 1.66×10^{-2} Jy and at 1.3 mm, 7.33×10^{-3} Jy. From the SMA data, Zuckerman et al. (2008) found that the BP Psc has a flux density of $1.8 \pm 0.2 \times 10^{-2}$ Jy at 0.88mm (880μm). Our fit is in good agreement with this observed value. The spatial extent of the (unresolved) dust at 0.88 mm is 0.81 ± 0.2 arcsec or 291 au, which serves as an upper limit for the spatial extent of the dust.

We fit the IR excess of BP Psc with four components. The most constrained component has a temperature of 38 K, a characteristic grain size $a = 0.1$, and $\beta = 0.2$. If dust in the outermost belt were emitting as a black body (which it is not), then it would be located ~ 140 au from the star. Zuckerman et al. (2008) suggest that there is a reservoir of cool dust at a temperature of 36 K.

If we assume that BP Psc is reddened by $A_V = 0.75$, then it falls on the RGB based on the isochrones. While this value is just an estimate, we justify applying some sort of reddening because BP Psc is enshrouded in gas and dust.

[18]The Very Large Telescope/Spectro-Polarimetric High-contrast Exoplanet REsearch (SPHERE)/Zurich IMaging Polarimeter (ZIMPOL).

3.5.7 IRAS 12327-293/PDS 355

IRAS 12327-293 (IRAS 12327) has very strong IR emission above the photosphere and is the only star resolved in the *Herschel* images (70μm, 100μm, and 160μm). We present images of the system in Figure 1. From the 70μm PACS map, we see that a fit to the emission is likely an elliptical gaussian, which would hint at an inclined emitting region. If the dust emission were from a spherical shell, we would expect this gaussian to be circular. The material could also be moving away from the star in a triaxial shell, or nested shells. A spectrum of IRAS 12327 near the Hα line shows that the absorption due to hydrogen is asymmetrical. As described in Section 3.5.2, the diameter of the dust is roughly 30,000 au in extent based on the size determined from the fit from the 70μm PACS map.

One previous study of this system found that the star has $T_{\rm eff} = 4200 \pm 100$ K and a luminosity of $L = 2.9 L_{\odot}$ (Reddy & Lambert, 2005), values that differ from those derived from the Gaia DR2 dataset. It is unclear if the reported L is the logarithm of the true value from their study. Reddy & Lambert (2005) determined the luminosity (and mass) using evolutionary track fitting, i.e., by matching a spectroscopically derived log g and effective temperature to a particular track in a set of isochrones. We find that IRAS 12327 is on the early AGB, consistent with previous descriptions of this star's evolutionary status. Though we did not use a fitting process with the set of isochrones, we can nonetheless compare the properties of the group to which IRAS 12327 appears to belong$\cdots$-stars with initial masses around $3 M_{\odot}$. For this group, the early AGB stage to which IRAS 12327 appears to belong,

the average stellar luminosity is $\sim 2500 L_{\odot}$ (compared to $2934 L_{\odot}$ reported by Gaia DR2).

Observing IRAS 12327 at (sub)millimeter wavelengths would allow for a more complete multi-wavelength analysis of this interesting and understudied star. High-angular resolution interferometric observations of IRAS 12327 are necessary to spatially resolve the dust around this star, which is likely an R Sculptoris analogue. A single dish measurement of CO would also be helpful to further solidify the evolutionary state of IRAS 12327, trace kinematics if gas is present, and provide a detailed map of the extended emission. It would also present an interesting target for other space- and southern-based observatories.

3.5.8 Planetary Engulfment Candidates

While we can not say definitively that any of the evolved stars in this sample are actively destroying other bodies in their systems, three stars present striking evidence. BP Psc has a parsec-scale system of highly collimated outflows (Zuckerman et al., 2008) and a central star that is a weak X-ray point source (Kastner et al., 2010). These features would be expected for a proto-stellar system, but observing them around a post-MS star has been explained by suggesting that BP Psc recently engulfed a companion. HD 233517 has also been described as a potential planetary engulfment candidate (Jura, 2003).

We propose that HD 219025 also engulfed a companion, possibly a planet. We base this hypothesis on the Hα absorption of the system viewed over several years.

An asymmetrical Hα absorption feature is seen in other systems (IRAS 12327, HD 233517, etc.), and is indicative of mass loss (Drake et al., 2002). The absorption feature for these three systems is broad and asymmetrical. However, for HD 219025, there are observations of the Hα absorption feature over a multi-year baseline. The feature appears to shift from being blueshifted to redshifted.

This type of absorption line behavior is observed with WD 1145+017, a white dwarf with a disintegrating planetesimal and a precessing gas disk. If HD 219025 did indeed engulf a companion, then one consequence would be the formation of a circumstellar gas disk. This hypothesis could be tested by obtaining several high resolution spectra of this system over several years to investigate whether there might be a precessing disk of gas around HD 219025 and to compare the abundances of other metals to other post-MS stars. The alternative hypothesis is that the absorbing material transitioned from inflowing to outflowing, which requires an abrupt shift in geometry, and is therefore unlikely (Cauley et al., 2018).

Cloudy/dynamical modeling+futher spectroscopic monitoring could produce a self-consistent CS gas model that could firm up the engulfment scenario.

3.5.9 On the Li-enrichment, IR excess, rotational velocity issue

Dust surrounding stars that have evolved off the main sequence could be in a remnant, long-lived debris disk (sub-giants), the product of stellar evolution (AGB), or the product of engulfing a companion (RGB). Li-enrichment is common among rapidly rotation K giants, but is rare among slowly rotating giants (Drake

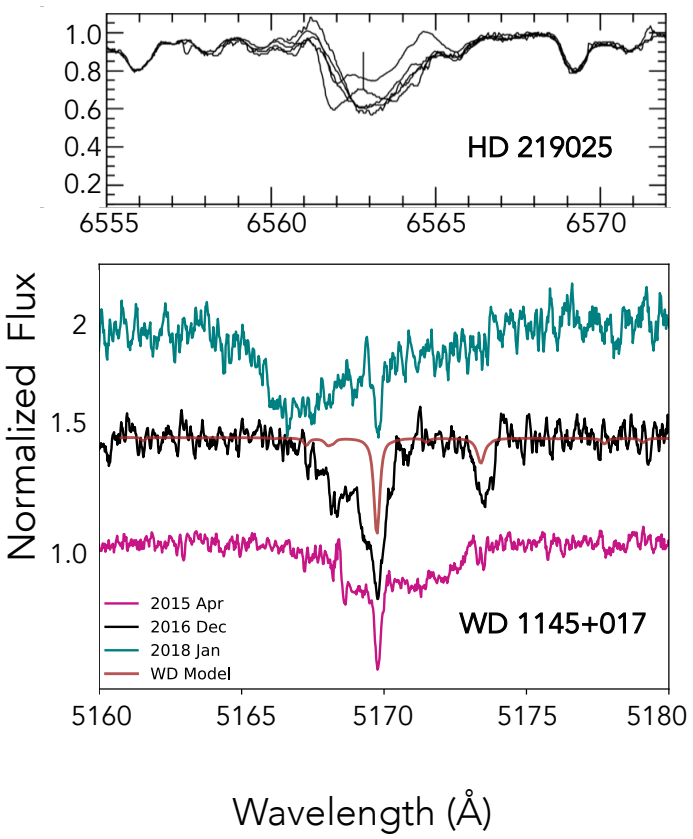

Figure 3.14: A Planetary Engulfment Candidate: HD 219025

NOTE — Evidence of orbiting gaseous disk in two very different systems. Top Panel: the Hα line for the candidate, HD 219025, a star on the RGB (figure borrowed from Drake et al. 2002). Bottom panel: Evidence of a precessing, metallic, gaseous disk around white dwarf WD 1145+017 (See description in caption of Figure 1.4). Similar work presented in Fortin-Archambault et al. (2020).

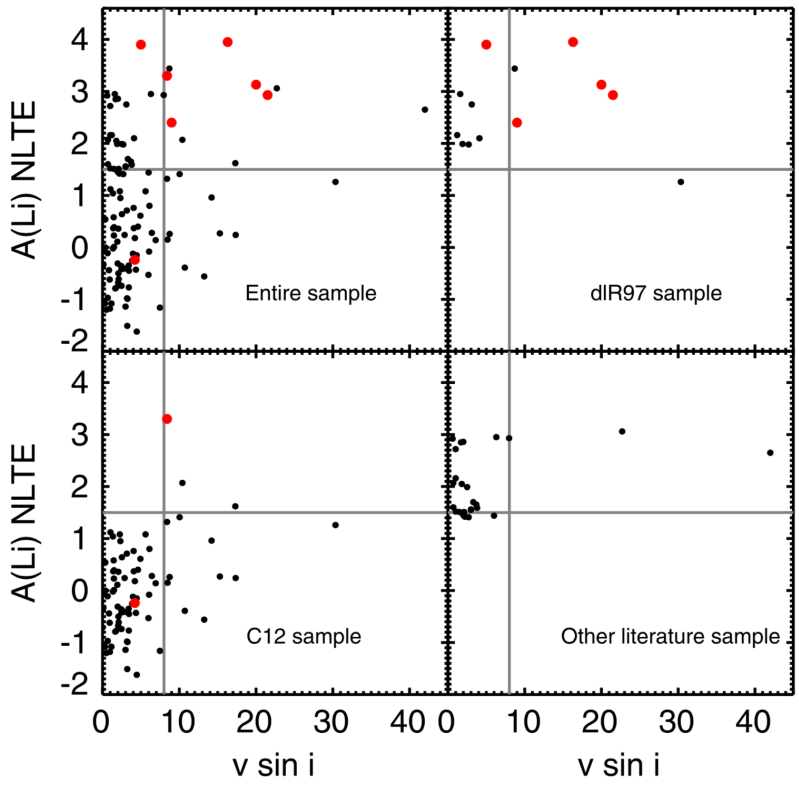

Figure 3.15: Li, v sin i, and IR excess

NOTE — Figure from Rebull et al. (2015). Stars with IR excesses are in red. Black data points denote those from the Rebull et al. 2015 sample. The vertical line denotes the threshold for a rapid rotator, and the horizontal line denotes the threshold for Li-rich stars.

et al., 2002). Jasniewicz et al. (1999) find that there is no correlation between Li-enrichment and rotation for Li-rich giants, citing the absence of IR emission for stars with enriched Li as a "puzzle". Rebull et al. (2015) find that the largest IR excesses, while rare, are all in Li-rich K giants. These dusty disks also tend to be found around the fastest rotators.

A subset of the stars present in this work also appear in Rebull et al. (2015). Rebull et al. (2015) explore this correlation among their sample of $\sim$ 300 stars.

We reproduce their image displaying this mild correlation in Figure 3.15. It is an intriguing idea to consider that the systems presenting this "trifecta" of characteristics have absorbed a companion (star or planet). If the engulfment occurred and the composition of the circumstellar material could be constrained, those abundances would provide constraints on the mechanics of stellar evolution (timescales for dredge-up(s) and chemistry), and possible reveal the accretion histories of dying stars.[19] A number of authors have recommended that C, N, and O abundances be determined for these systems to begin to address this mystery of the origin of "the trifecta." We further stress the utility of attaining these abundances. It would also be useful to attain Li abundances and high-resolution spectra for the remaining stars in this sample. A number of them have an IR excess, but no measurements of Li abundance or $v \sin i$.

It might be expected that we find more debris disks around post-main-sequence stars due to the observation of organic compounds in first ascent giant branch K stars. These K giants were main sequence A stars, which have a debris disk incidence of $\sim 30\%$. De la Reza et al. (2015) suggest that the interaction of the strong winds from the K giants with their persisting asteroidal/cometary disks leads to the liberation of carbon from the debris, and the formation of polycyclic aromatic hydrocarbons (PAHs) in a circumstellar shell. For giants that have begun mass loss, Dong et al. (2010) describe a mechanism through which wind drag of planetesimals could boost collisional cascades, creating a debris disk out to ~ 50 au persisting to the white dwarf stage. Paired with expected planetary engulfment, interpreting

[19] Like a blood panel completed during a health exam for a human.

the origin of dust around post-MS stars is a non-trivial process. This can obfuscate the understanding of how the remnants of planetary systems evolve off the main sequence.

The existence of white dwarf stars with: terrestrial elements heavier than C and in O in their atmospheres (see Manser et al. 2016 and references therein); transiting, disintegrating planetesimals (e.g., WD1145+017, Vanderburg et al. 2015; Xu et al. 2016, etc.); circumstellar gas; and planets in $\sim$ 1 day orbits (Vanderburg et al., 2020), requires that some version of stellar systems survive the evolution of their host stars. There might be observable signatures prior to the planetary nebula stage that lead to these features in the WD stage. By studying material around these evolved stars we can begin to separate these effects, and understand their evolutionary state and the nature of their IR-excesses.

3.6 Conclusion

We analyzed a sample of post-MS stars with infrared excesses, using the most recent *Gaia* data release (DR2) to investigate the stellar age, and *Herschel* observations at far-IR and submillimeter wavelengths to constrain the thermally emitting dust. We characterize the dust by measuring the flux densities at far IR wavelengths and fitting the SEDs using a set of modified blackbodies. We determine the basic properties of the dust, finding that most systems have micron-sized grains at temperatures around 100K.

We also lend support to theories in the literature about evolutionary statuses of

some of the stars. We report a significant, resolved IR excess around the AGB star IRAS 12327-693 (PDS 355) and recommend multi-wavelength observations (HST STIS, ALMA, and JWST) to better characterize the dust around this star. As an AGB star, it is likely surrounded by a shell of material rather than a disk.

Analogous to WD 1145+017 and its precessing disk, we note that HD 219025 presents similar features and suggest that this system could also have a precessing disk. The existence of white dwarf stars with terrestrial elements heavier than C and in O in their atmospheres, and transiting, disintegrating planetesimals (e.g., WD1145+017, Vanderburg et al. 2015) requires that rocky bodies survive stellar evolution. There is evidence of current planetary engulfment and mass loss for a number of the targets in our sample. We report the spectral indices of the long wavelength emission and find evidence of grain growth. The systems that show evidence of planetary engulfment and spectral indices approaching the black body value can potentially be used to constrain the timescale for grain growth in the environment of a post-MS star.

Chapter 4: Polluted White Dwarfs

Between one third and one fourth of WDs cooler than 20,000 K are "polluted," or display the presence of atoms heavier than helium in their atmospheres (Jura & Young, 2014). Due to the relatively fast gravitational settling times of heavy elements in a WD atmosphere, the presence of those heavy elements is linked to the accretion of dust from planetesimals perturbed by unseen planetary systems. Most importantly, spectroscopic determination of the abundances of these heavy elements in the atmospheres of WDs provides an indirect, but uniquely powerful tool to determine the detailed elemental compositions of accreted extrasolar planetesimals (Jura & Young, 2014).

4.1 Polluted Whites Dwarfs as the Best Probes of the Composition of Extra-solar Material, Case Study: WD 1124-293

The spectra of white dwarfs (WDs) should show only pressure-broadened hydrogen and/or helium absorption lines, yet at least 27% of young WDs with temperatures less than ∼27,000 K have photospheres polluted by elements heavier than helium (Koester et al., 2014). These metals should settle out of the atmospheres of WDs on timescales of days to Myr depending on the WD temperature, surface

gravity, and main atmospheric composition (H vs. He) (Koester, 2009).[1] For isolated WDs, the pollution could arise from grains in the interstellar medium (ISM) (Dupuis et al. 1993a; 1993b), or more likely, from the accretion of solids that have been liberated from a captured planetesimal (e.g., WD 1145+017l Vanderburg et al. 2015). The gas phase of the latter accretion process can exist as a circumstellar disk observable as a double peaked line in emission (e.g., Manser et al. 2016) or a Doppler broadened profile in absorption (e.g., Xu et al. 2016). WD 1124-293 is one of a few WDs that shows both metal photospheric absorption and circumstellar absorption features.

We investigate the gas toward WD 1124-293 to explore the conditions necessary to produce the observed absorption. WD 1124-293 is of spectral type DAZ (a hydroden dominated atmosphere with metal lines), has an effective temperature $T_{\rm eff} \sim 9367$K, and surface gravity $\log g = 7.99$ (see Table 4.1). The one observed C-S Ca K absorption feature detected at 8σ (Debes et al., 2012) provides an opportunity to explore the physical conditions that result in this type of spectrum. We use the microphysics code, Cloudy, to model the metal-rich gas polluting WD 1124-293 by creating a grid of models of C-S gas to explore the abundances of elements from He to Zn relative to hydrogen. Due to the lack of an infrared excess (Barber et al., 2016), we exclude grains from our models. From the code, we obtain line optical depths, species column densities, and the temperature profile through the gas cloud. With these models, we place constraints on the potential masses and abundances of

[1]For examples, a diffusion timescale of days is seen for most metals in DA WD $T_{\rm eff} \sim 25,000$ K and $\log g = 8$, while a timescale of Myr is seen for most metals in a DB WD with $T_{\rm eff} \sim 13,000$ K and $\log g = 8$.

Table 4.1: Properties of WD 1124-293

Parameter	Value	Reference
RA, Dec (J2000)	11:27:09.25, −29:40:11.20	[a]
Spectral Type	DAZ	[b]
G (mag)	15.0139	[a]
$T_{\rm wd}$ (K)	9367	[c]
$\log g$ (cm s^{-2})	7.99	[c]
$R_{\rm wd}$ ($R_\odot$)	0.0129	[c]
$M_{\rm wd}$ ($M_\odot$)	0.593	[c]
Luminosity ($L_\odot$)	0.00115	[c]
Distance (pc)	33.691	[a]

NOTE — [a]Gaia Collaboration et al. (2018), [b]Subasavage et al. (2017), [c]see footnote.[2]

the C-S gas.

In Section 2, we present new observations of WD 1124-293 with Keck *HIRES* and an improved co-added MIKE spectrum. In Section 3, we describe how we know the pollution of WD 1124-293 visible in the new, higher resolution Keck spectrum is not due to the ISM. In section 4, we describe how we model a polluted white dwarf with Cloudy and apply this method to WD 1124-293, showing how we can determine the characteristics of its C-S gas using Cloudy. In short, we build a grid of models and place constraints on the column densities needed for detecting features. In section 5, we present our results and conclude in section 6.

4.2 Observations

WD 1124-293 was observed 16 times between 1998 and 2011 (Debes et al., 2012) with the MIKE echelle spectrograph (Bernstein et al., 2003). We observed WD 1124-293 using the HIRES echelle spectrograph (Vogt et al., 1994) on the

Table 4.2: Keck/*HIRES* Observations of WD 1124-293 and Standards

Target	Dist (pc)	Sep (")	Exp (s)
WD 1124-293	33.7	–	1200s
HIP56280A	26.3	79	30s
HIP56280B	26.3	79	30s
HIP55864	117	16	100s
HIP55901	401	24.6	100s

NOTE — The distance, separation from WD 1124-293, and exposure time for the target and standards. The observation date was 2018 April 24, at a resolution $\sim 40,000$ with a wavelength range of 3100 - 5950 Å.

Keck I telescope for 1200s on April 24, 2018. For the HIRES observations, the blue collimator and C5 decker were used with a slit width of 1.148 arcsec, typically giving a spectral resolution of $\sim 40,000$. However, the seeing during the observation was ~ 0.5 arcsec, and the effective resolution is $\sim 80,000$. The data were reduced with the MAKEE package.[3] The Ca K line was extracted over two orders and averaged, while the H line was extracted over one order. We continuum-normalized 10 Å regions of the spectrum by fitting a polynomial to the continuum to remove effects due to the instrument response function. The signal-to-noise (S/N) ratio is ~ 38 in a 10 Å region (3935 Å to 3945 Å), which corresponds to ~ 75 per resolution element. We detect C-S and photospheric absorption at the Ca K line and only photospheric absorption at the Ca H line. We report that no new absorption or emission features have been detected.

Additionally, we reanalyzed the many epochs of spectra presented in Debes et

[3]MAKEE (MAuna Kea Echelle Extraction): `https://www2.keck.hawaii.edu/inst/common/makeewww/`

Table 4.3: Ca absorption line properties for WD 1124-293

Ca K : $\lambda_0 = 3933.6614$ Å, Ca H : $\lambda_0 = 3968.4673$ Å										
	Circumstellar				Photospheric					
Dataset	λ_c (Å)	v_c (km/s)	Eq Width (mÅ)	FWHM (km/s)	λ_c (Å)	v_c (km/s)	Eq Width (mÅ)	λ_c (Å)	v_c (km/s)	Eq Width (mÅ)
MIKE	3933.623	−2.9	7.1	9.91	3934.020	27.3	113 ± 2	3968.841	28.25	52 ± 1
HIRES	3933.637	−1.9	7.8	5.97	3934.053	29.8	105 ± 1.5	3968.879	31.1	65 ± 3

NOTE — The Ca H and K line wavelengths are given in air. We only detect a C-S feature at the Ca K line. For the C-S line, the central wavelength of the line is λ_c, the Doppler shift velocity is v_c, the equivalent width of the line assuming a Gaussian profile is "Eq Width," and the full width at half max is FWHM.

al. (2012). The multiple MIKE epoch spectroscopy was extracted over two orders that contained the Ca H and K lines. For this work, we took the reduced spectra of WD 1124-293 from both the red and blue CCDs at each epoch and flux calibrated the orders against a model DA atmosphere (Koester, 2010)[4] with the appropriate $T_{\rm eff}$ and $\log g$ (see Table 4.1) based on WD 1124-293's parallax and spectro-photometry from APASS, 2MASS, and ALLWISE catalogs. Once all epochs were flux calibrated, we median combined the spectra to a common wavelength grid with a sampling of 0.05 Å between 3350 Å and 5030 Å and 0.08 Å between 5030 Å and 9400 Å. The typical resolution for the MIKE spectra is $\sim 34,000$. Near the Ca K line, the final S/N ratio of the data as measured in the continuum corresponds to ∼194 per resolution element.

We present the Ca absorption line properties for WD 1124-293 in Table 4.3 for the co-added MIKE spectrum and Keck HIRES spectrum presented in this work. We fit the circumstellar and photospheric absorption features with Gaussians to calculate the equivalent widths of the lines, as well as the FWHMs. The photospheric lines are gravitationally red-shifted. All line center velocities for the Ca K and H

[4] http://svo2.cab.inta-csic.es/theory/newov2/index.php

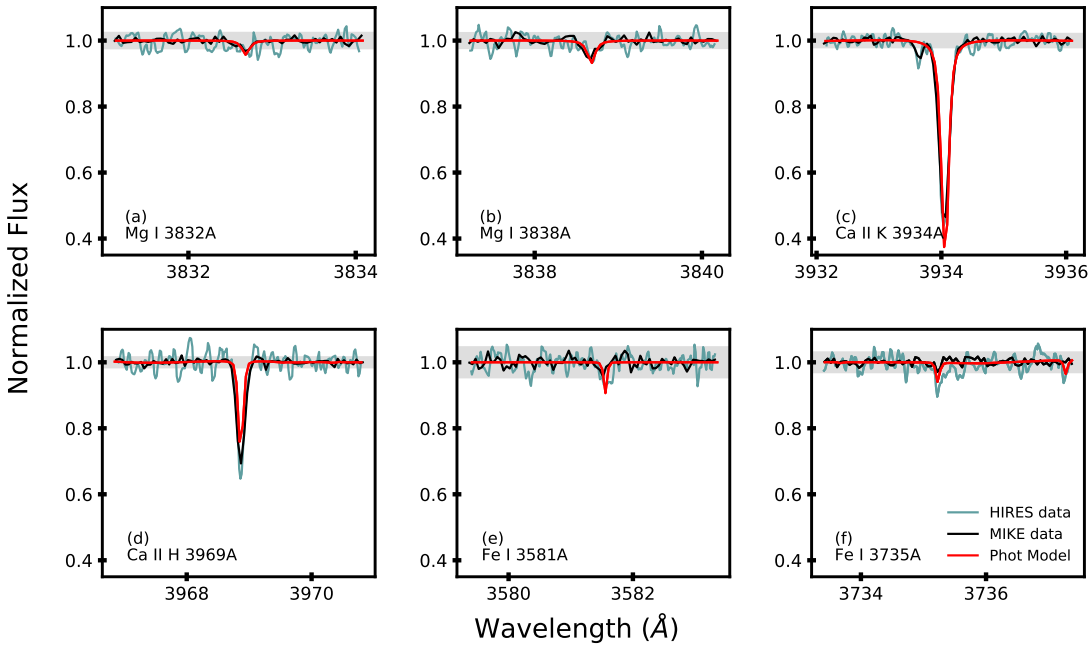

Figure 4.1: Detection of metal photospheric absorption lines for WD 1124-293

NOTE – We detect metal photospheric absorption lines for WD1124-293 using a co-added MIKE spectrum. For each square panel, the MIKE data are shown in black, new Keck HIRES data are shown in teal, and a model of the photosphere is shown in red. The model is convolved with a Gaussian kernel with a width determined by a resolution, $R = 60,000$. The gray region highlights a $\pm 3\sigma$ region for the MIKE spectra.

lines are also presented in Table 4.3. The HIRES dataset has the highest resolution of the three sets, and so we use it to constrain the location of the gas. The co-added MIKE spectrum has the highest S/N, so we use it to constrain the abundances of different species. In Figure 4.1, we show selected photospheric absorption features due to Mg, Ca, and Fe that appear in both the co-added MIKE spectrum and new HIRES spectrum.

4.3 Pollution and the ISM

Debes et al. (2012) first investigated the possibility that the weak Ca absorption detected towards WD 1124-293 could be explained by coincident local ISM absorption by comparing against high SNR spectra of stars located closely in the sky. For that study, Debes et al. (2012) looked at HIP 56280A, HIP 55864, HIP 55731, HIP 55901, and HIP 55968, but did not have sufficient parallax information on all of the stars to correctly sort them in terms of increasing distance from the Earth. With the advent of the Gaia mission, secure parallaxes now exist for that sample of stars. We re-observed HIP 56280A, HIP 55901, and HIP 55864 and in addition observed HIP 56280B, the physically bound companion to HIP 56280A. HIRES has higher spectral resolution compared to MIKE, and thus higher sensitivity to weak spectral features. The addition of HIP 56280B also ensures tighter constraints on the amount of Ca present in the ISM interior to $\sim$30 pc with two independent measurements of that part of the sky.

In order to search for weak lines from the ISM we first had to fit and remove the continuum near the expected rest frame velocity of the Ca K line in question

Figure 4.2: The normalized flux for the (a) target and nearby sources (b) - (d) HIP 56280A, HIP 56280B, and HIP 55864

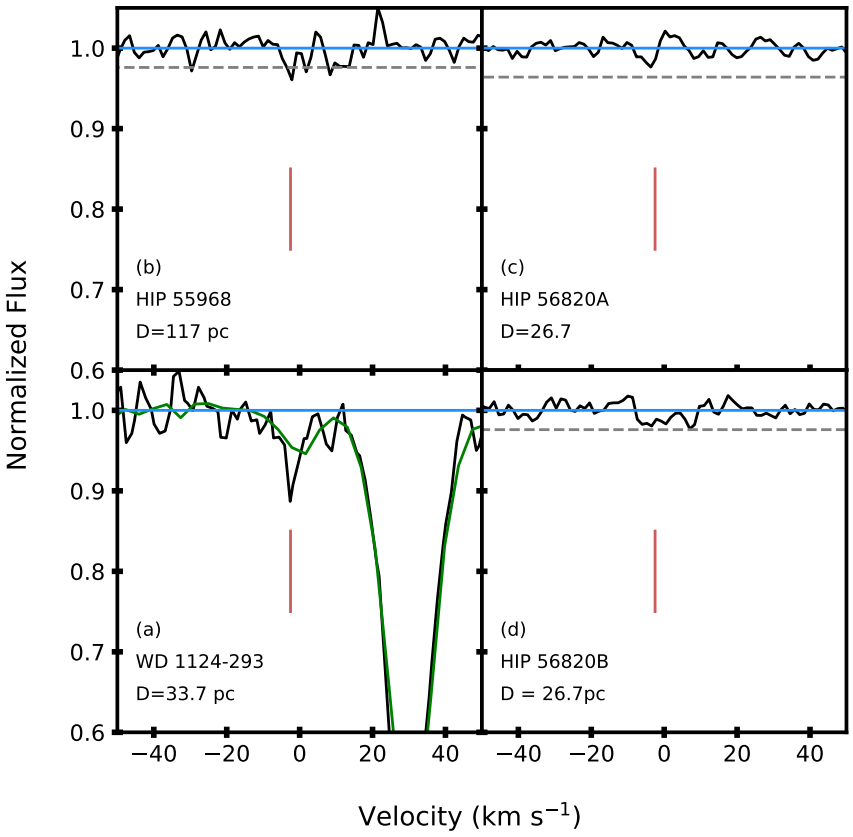

For all panels, the blue line is drawn at a value of 1.0 to guide the eye, the 2019 HIRES data are shown in black, and the red vertical line gives the approximate velocity of the C-S line for WD 1124-293, -2.5 km s^{-1}. In panels (b) - (d), the dashed gray is drawn at 3σ below the continuum. In panel (a), the green curve is the normalized flux from the Magellan MIKE observations described in Debes et al. (2012).

for each standard star. This was relatively straightforward for HIP 55901 and HIP 55864, which show broad Ca absorption due to the rapid rotation of the host stars– the continuum can be fit with a high order polynomial Debes et al. (2012).

Our approach for HIP 56820A and HIP56820B was slightly different, due to the later spectral type of these two stars. Both objects are roughly consistent with F stars and are likely nearly the same effective temperature and gravity. Both stars show Ca emission in the line core due to stellar activity, though HIP56820A shows stronger emission. For both stars we fit the broad Ca component with a spline fit and then fit the Ca line core with a two component Gaussian curve. We verified that our fits did not unintentionally fit any absorption lines coincident with the rest velocity of the C-S line seen in WD 1124-293. Our resulting continuum fit lines are shown in Figure 4.2, along with the expected 3σ upper limit to detectable absorption for each star. We estimated this upper limit by taking the standard deviation of flux in the normalized spectra, assuming that we would detect anything 3σ below the continuum level. We note that we do not show the spectrum of HIP 55901, which shows strong absorption consistent with that observed previously in Debes et al. (2012). None of these comparison stars near WD 1124-193 show Ca absorption at the velocity of the observed Ca line, so we confidently rule out an ISM contribution to the WD spectrum.

4.4 Modeling WD Circumstellar Gas with Cloudy

In Cloudy, the gas temperature is solved by balancing heating and cooling self-consistently, per zone. Zones are determined by Cloudy and demarcate regions

of where gas conditions are relatively constant. A new zone is created when there is a change in physical conditions (e.g., a change in H ionization or a change in the electron density). Though Cloudy is typically used to model high energy regions (H II bubbles, active galactic nuclei, etc.), the code will accept temperatures from 2.8 K to 1.001×10^{10} K.

4.4.1 Cloudy Model Inputs

We aim to constrain the abundances of metals in the circumstellar gas of WD 1124-293. A Cloudy input file requires an ionizing source, the geometry of the gas, the density of hydrogen in the gas, and the abundances of He to Zn, relative to H. In this section, we describe how we determine these inputs for WD 1124-293 and how we use the Cloudy output, thereby describing our method for using Cloudy to model the C-S environment of a polluted white dwarf. Calculations were performed with version 17.01 of Cloudy, last described by Ferland et al. (2017).

4.4.1.1 The ionizing source

For the Cloudy model, we use an interpolated Koester DA photosphere (Koester, 2010; Tremblay, & Bergeron, 2009)[5] with a temperature of 9420 K and luminosity of $0.00111 L_{\odot}$ as the input, or ionizing continuum. The continuum is mapped to an energy mesh with a resolution of 0.05, (20x the native course grid of $R \sim 300$).

4.4.1.2 Geometry

The geometry of the C-S gas around WD 1124-293 is unknown. We choose to set the geometry in a disk, rather than a sphere because we have shown that it is

[5]Models were downloaded from the Spanish Virtual Observatory database.

highly unlikely that the ISM is the source of the pollution. Debes et al. (2012) place constraints on the location of the C-S gas, with a minimum distance of $7^{+11}_{-3}\,R_{\rm wd}$, maximum distance of 32000 au, and dynamical estimate of $\sim$54 $R_{\rm wd}$, where $R_{\rm wd}$ is the radius of WD 1124-293. The dynamical estimate of the location of the gas is determined assuming the gas is in a circular Keplerian orbit and using the FWHM of the gas absorption feature to determine the upper limit to the disk's orbital velocity. The distance of the gas from the WD, $R_{\rm Kep}$, is

$$R_{\rm Kep} \approx (GM_{\rm wd})^{1/3} \left[\frac{2R_{\rm wd}}{\rm FWHM\ (cm\ s^{-1})}\right]^{2/3}, \tag{4.1}$$

where G is the gravitational constant. From the new HIRES dataset, we measure the FWHM of the C-S absorption feature assuming the line profile is Gaussian. With the resulting FWHM $\sim$ 6 km/s, and the radius listed in Table 4.1, $R_{\rm Kep} \sim 106\,R_{\rm wd}$ for WD 1124-293, a value almost double that in Debes et al. (2012) due to the high spectral resolution of the *HIRES* data. $R_{\rm Kep}$ is the best estimate of the minimum distance of the gas to the star and it depends on the width of the absorption feature. If the C-S absorption feature were more narrow, then $R_{\rm Kep}$ would be larger.

The outer edge of the gas is unknown, but we can consider a sublimation radius and a tidal disruption radius. The sublimation radius, $R_{\rm sub}$ is the distance at which the equilibrium temperature of particles equals their sublimation temperature, $T_{\rm sub}$, and is defined by Metzger et al. (2012) as,

$$R_{\rm sub} = \frac{R_{\rm wd}}{2}\left(\frac{T_{\rm wd}}{T_{\rm sub}}\right)^2. \tag{4.2}$$

This equation represents the smallest possible sublimation radius for optically thin

distributions of dust and it assumes the particles absorb and emit radiation perfectly. $R_{\rm sub}$ depends on the shape, size, and composition of the particle. Graphite grains (0.01μm) and astronomical silicate grains (0.1 μm) would sublimate at 54 $R_{\rm wd}$ and 93 $R_{\rm wd}$, respectively (see Figure 4.3). In Section 4.5, we discuss why the detectable gas at $R_{\rm Kep}$ is farther than $R_{\rm sub}$.

The tidal disruption radius, $R_{\rm tide}$ (Davidsson, 1999; Jura, 2003; Veras et al., 2014), also depends on the composition of the material with

$$\frac{R_{\rm tide}}{R_\odot} = C_{\rm tide}\left(\frac{M_{\rm wd}}{0.6M_\odot}\right)^{1/3}\left(\frac{\rho_b}{3\ {\rm g\ cm^{-3}}}\right)^{-1/3} \tag{4.3}$$

where $C_{\rm tide}$ has typical values of 0.85 to 1.89 (Bear & Soker, 2013), and ρ_b, the density of the disrupting body, satisfies $\rho_b \geq 1\,{\rm g\ cm^{-3}}$ (Carry, 2012; Veras et al., 2014). For WD 1124-293, the maximum tidal disruption radius is $R_{\rm tide} \sim 200\,R_{\rm wd}$. We show typical ranges of tidal disruption radii for comets and asteroids ($R_{\rm tide,comet}$ and $R_{\rm tide,asteroid}$) in Figure 4.3.[6]

We take $R_{\rm Kep}$ as our minimum radius of the gas and assume that these radii follow the relation $R_{\rm tide} > R_{\rm Kep} > R_{\rm sub}$ (see Figure 4.3). We set the gas to extend from $100\,R_{\rm wd}$ to $200\,R_{\rm wd}$ (approximately $R_{\rm Kep}$ to $R_{\rm tide}$). The aspect ratio of the gas disk is shown to be $h/r \sim 10^{-3}$ by Metzger et al. (2012), so we truncate the gas to a cylinder with a height of 10% $R_{\rm wd}$. We discuss the implications of this relation among radii in Section 4.5.

[6]For comparison, for comet Shoemaker Levy 9 had $C_{\rm tide} \sim 1.31$ and $\rho_b \lesssim 0.702$ (Boss, 1994), and would have a disruption radius of $\sim 110\,R_{\rm wd}$ near WD 1124-293.

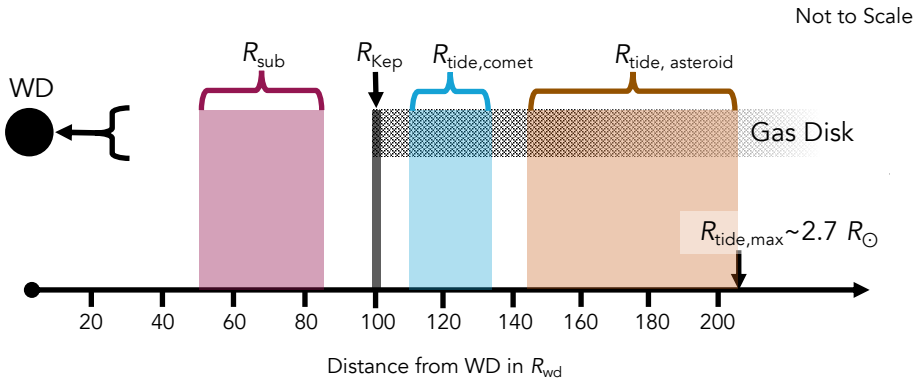

Figure 4.3: Cartoon model of WD 1124-293

A not-to-scale cartoon of the model for WD gas and debris disks inspired by Metzger et al. (2012), where a solid debris disc typically forms near the tidal disruption radius which happens to be $\sim R_\odot \sim 120 R_{\rm wd}$. There is no evidence that WD 1124-293 has a dusty debris disk, so we exclude it. The gas is shown with the speckled black and white region. We show 4 different radii $R_{\rm sub}$, $R_{\rm Kep}$, $R_{\rm tide,comet}$, $R_{\rm tide,asteroid}$ and a range of their possible values, with the shaded regions brought down to the axis for ease of reading, where applicable. The outer extent of the gas is unknown, as is the exact accretion mechanism. The maximum tidal radius for WD 1124-293 is $\sim 211 R_{\rm wd} \sim 2.7 R_\odot$.

4.4.1.3 Hydrogen density

Most planetesimals accreted onto WDs are water poor, so there should be very little hydrogen gas present around WD 1124-293, assuming a planetesimal origin (see section 5.3 of Jura & Young 2014, and references therein). However, Cloudy uses the number density of hydrogen, $n_{\rm H}$, to set the conditions of a cloud. If a C-S gas spectrum has features due to hydrogen, one could probe the maximum amount of hydrogen present in the system by calculating the column density due to H, $N_{\rm H}$, assuming every H atom participates in the line transition. With no such features and a gas temperature too low for the Balmer Hα line to form, we turn to a geometrical argument.

The area of the column along the line of sight which subtends the white dwarf is $\sim 2 \times H \times R_{\rm wd}$ and the volume is $2 \times H \times \Delta R \times R_{\rm wd}^2$, where H is the gas height and $\Delta R = R_{\rm out} - R_{\rm in}$ is the gas extent in units of $R_{\rm wd}$, with an outer radius, $R_{\rm out}$, and an inner radius, $R_{\rm in}$. The column density is equal to the number density times the volume of the gas column, divided by the area of the column along the line of sight which subtends the white dwarf. Solving for $n_{\rm H}$,

$$n_{\rm H} \lesssim \frac{N_{\rm H}}{\Delta R \cdot R_{\rm wd}}. \tag{4.4}$$

The minimum value is typical of the diffuse H II ($n_{\rm H} \sim 0.3 - 10^4$ cm^{-3}) and warm neutral medium ($n_{\rm H} \sim 0.6$ cm^{-3}) phases of the ISM (Draine, 2011). For a maximum plausible value, we rely on observations of specific circumstellar disks

around protoplanetary and transition disks.[7] For gas with a height of 10% $R_{\rm wd}$, extending from 100 $R_{\rm wd}$ to 200 $R_{\rm wd}$, with $\log N_{\rm H} \sim 19$, $n_{\rm H} \lesssim 10^9$ cm^{-3}. We therefore explore the dependence of our models on the hydrogen density with a grid of models that have $-1 \leq \log(n_{\rm H}/{\rm cm}^{-3}) \leq 10$. For each model, the hydrogen density is constant with distance from the star. The most likely model is the one that minimizes the amount of H while allowing for metal lines to form.

4.4.1.4 C-S Gas Abundances

Calcium is the only C-S gas with a positive detection in WD 1124-293. Therefore, we consider the abundances of elements relative to Ca. Table 4.4 lists the elements that are typical polluters of WDs for which we have photospheric abundance limits, and are thus explored with our modeling. We focus on the strongest optical transitions for these species that have photospheric detection (Mg I 3838 and Fe II 3228), and detection upper limits (K I 4043, Ni I 3480, Mn I 4032, Al I 3961, Si I 3905, Na I 5890). All other elements from He to Zn are left at the default solar composition values, relative to Ca. We approach the abundances in this way for two reasons. First, the ratios of potential metals of interest are very similar for a solar and chondritic composition (see Figure 4.6). Second, there is thus far only one detected C-S feature in the optical part of the spectrum for WD 1124-293. A UV spectrum would likely show more absorption features that could be used to better constrain the C-S metal abundances (see Figure 4.9).

[7]The maxmimum possible value of $N_{\rm H}$ for TW Hydrae is $\log(N_{\rm H\ I}/1\ {\rm cm}^2) \sim 19.75$ (Herczeg et al., 2004), and the H column density for β Pictoris is $\log(N_{\rm H}/1\ {\rm cm}^2) \sim 18.6 \pm 0.1$, (Wilson et al., 2017).

We use the C-S column density of Ca II 3934 to constrain the modeling by varying the abundance ratios of metals relative to calcium. Beginning with a hydrogen number density $n_{\rm H} = 0.1$ cm^{-3} (a lower limit inspired by low density ISM regions), we first find abundance ratios that, when paired with the overall hydrogen density, result in optical depths that lead to a calculated absorption line with a depth at the 3σ limit to the observed continuum. For the rest of the metals considered, we ensured that their abundances were such that no lines were formed (see Figure 4.5). We then fix those abundance ratios and vary the hydrogen density over 10 orders of magnitude, while increasing the abundance of Ca relative to H to explore the model dependence on the amount of hydrogen present. The resulting grid of models is presented in Figure 4.4.

4.4.2 Cloudy Model Output

We choose to save the general overview, line optical depths, and line population for each Cloudy run. The general overview contains an output transmitted spectrum, but it does not include line broadening mechanisms, such as micro thermal motion, macro circular motion, or instrument effects, for an unresolved line. The net transmitted spectrum from Cloudy can however be used to check the validity of a set of input parameters (by investigating whether other absorption or emission features are produced), and to predict a spectrum ranging from the far UV to near IR (see Discussion).

We use the optical depth and column density to compare Cloudy models to

MIKE spectrum. We save the optical depths, τ, for all species with $\tau > 0.001$ to calculate an absorption line profile, and the populations of upper and lower levels for all lines to calculate the column densities of different species. The column densities are calculated for each line by multiplying the lower level population per zone by the length of the zone. Zones are automatically calculated by Cloudy. We only consider the lower level populations in the column density calculation because we are not in a regime where stimulated emission is important.

4.5 Results and Discussion

We investigate the gas toward WD 1124-293 to explore the conditions necessary to produce the observed absorption. We further constrain the location and amount of Ca present in the C-S gas, reproduce the observed C-S Ca K absorption line profile, and place upper limits on the amounts of H, Mg, Ca, Fe, and other metals present around WD 1124-293 by using Cloudy to determine their optical depths and expected line column densities. We place limits on the total amount of gas and show the temperature profile through the model disk. We then connect these results to other similar studies and argue for future UV observations.

4.5.1 Location of the gas

From the new HIRES observations, we show that the previously detected C-S and photospheric Ca gas is still present. Calcium in the atmosphere of WD 1124-293 has a settling time of $\sim$1000 years (Dufour et al., 2017), so it is expected for the

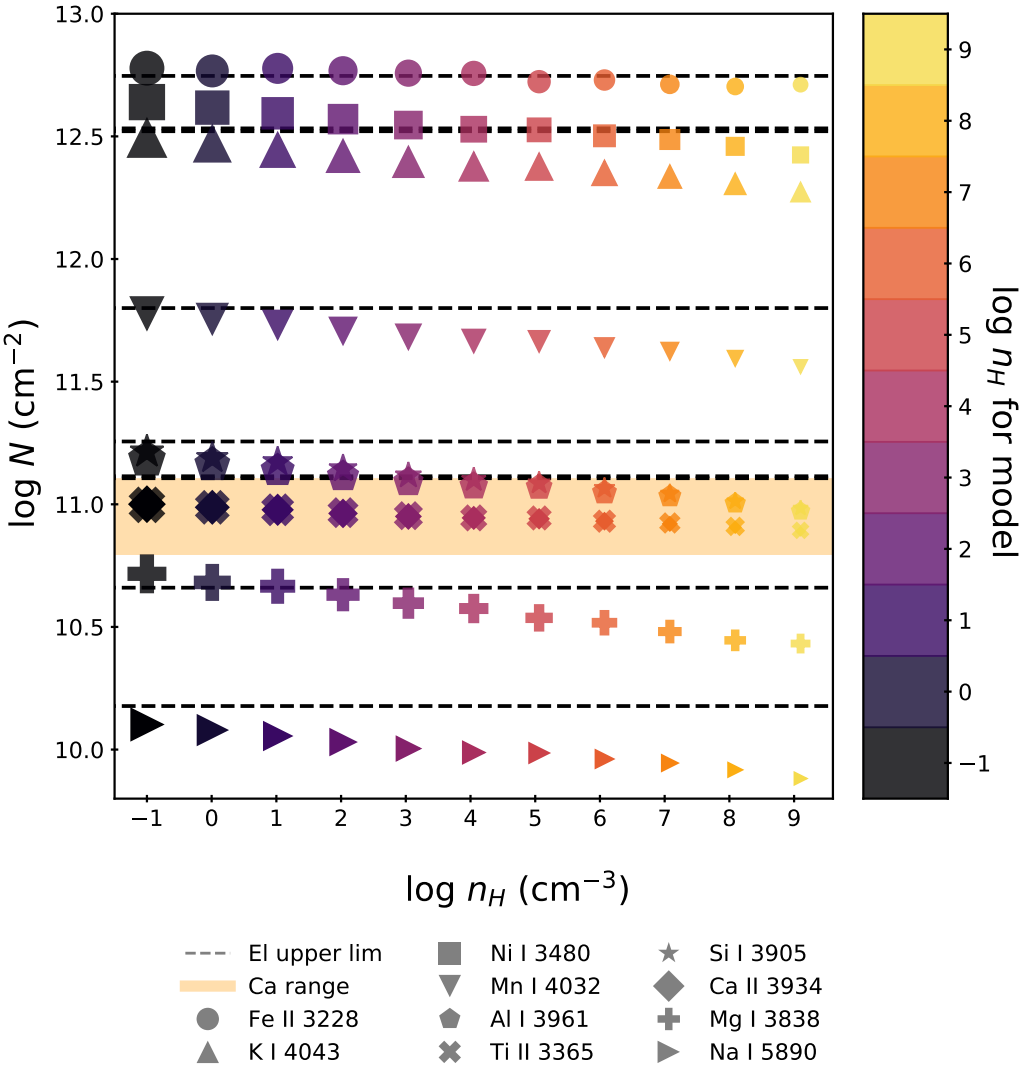

Figure 4.4: Column Densities for metals toward WD 1124-293

The column densities for a number of metal species in Cloudy models over hydrogen number densities from $\log n_H$: -1 to 9 [cm^{-3}]. The orange horizontal bar highlights the range of expected Ca II column densities (Debes et al., 2012, and this work) and this work), and the dashed lines highlight the maximum column densities for other species. The size of each marker is related to the absolute value of the element abundance. The metal abundances are not sensitive to the number density hydrogen.

photospheric line to persist.

With the new observations we also find that the gas is farther away from WD 1124-293 than previously detected (Debes et al., 2012). Gaseous disks can accrete inward and spread outward due to angular momentum transport by turbulent viscosity (Metzger et al., 2012). However, why do we not observe gas at radii less than 100 $R_{\rm wd}$ if the gas is created through sublimation at smaller radii? Even with no IR excess due to dust grains, if the particle density is low enough, it is possible that destructive grain-grain collisions near the tidal disruption radius could be creating gas (Jura et al., 2007) at $R_{\rm Kep} \sim 100 R_{\rm wd}$. Alternatively, there could be a collection of sub-micron grains, which are inefficient emitters, and would thus sublimate at much larger distances than what would be assumed in a blackbody approximation.

4.5.2 Column Densities

We determine the column density of the C-S Ca gas by finding the range of optical depths that lead to an absorption feature at a depth of $\pm 3\sigma$ relative to the depth of the Ca C-S line in the MIKE dataset, resulting in $\log N({\rm Ca}) = 11.01^{+0.09}_{-0.26}$ (Debes et al. 2012 find $\log N({\rm Ca}) = 11^{+0.1}_{-0.2}$). The downward trend in column density with increasing hydrogen number density seen in Figure 4.4 is due to a decrease in the calculated electron density. To investigate the dependence of our modeling on hydrogen, we explored 10 orders of magnitude in hydrogen number density, fixing the relative abundance ratios for all elements. The hydrogen number density is degenerate with the hydrogen abundance, so we are only able to constrain

the amount of hydrogen with a geometrical argument described in Section 4.2.2. The upper limits to the abundances of these different species are presented in Table 4.4.

4.5.3 Line Profiles

The Ca C-S absorption line is only marginally resolved, so we construct the absorption line profile by taking the convolution of (1) a Voigt line profile broadened due to Maxwellian distributed velocities and a gas temperature determined by Cloudy and (2) a Gaussian kernel with a width determined by the resolution of the Keck spectrum.[8] The Voigt line profile is approximated using a series expansion as $\phi(x) \propto \exp(-x^2) + a/(\pi^{1/2}x^2) + 2a/(\pi^{3/4}x^4)$, where a is the dampening constant for the transition in question, $x = (\nu - \nu_0)/\Delta\nu_{\rm Dopp}$, ν_0 is the center frequency for line, and $\Delta\nu_{\rm Dopp}$ is the FWHM of the line. The output intensity is $I = I_{\rm in} \exp[-\tau\phi(x)]$, where τ is the optical depth at line center. The output intensity considering the velocity profile is $\propto \exp(-\tau[\phi(x) * \phi(v)])$.

We show the calculated line profiles for the strongest optical transitions of these metals in Figure 4.5.

4.5.4 Metals in the gas around WD 1124-293

The calculated calcium K line column density corresponds to an abundance of 1.85 relative to hydrogen when $n_{\rm H} = 0.1$ cm^{-3}. As we increased the hydrogen

[8] If the absorption line were resolved, we would also convolve the Voigt line profile with a velocity profile, $\phi(v)$ describing the bulk motion of the gas disk.

Table 4.4: Photospheric and Circumstellar Metal Abundances and Masses

El	Phot	$\log \dot{M}(El)$ (g yr^{-1})	C-S	$\log M_{\text{C-S}}$ (g)
H	1	–	1	< 5.95
Na	< -8.30	< 13.62	< 3.35	< 10.67
Mg	-7.689 ± 0.024	14.30	< 7.85	< 15.19
Al	< -8.80	< 13.24	< 7.05	< 14.44
Si	< -7.50	< 14.54	< 6.65	< 14.06
K	< -8.00	< 14.20	< 7.05	< 14.61
Ca	-8.872 ± 0.188	13.33	$1.357^{+0.086}_{-0.257}$	$8.92^{+0.1}_{-0.3}$
Ti	< -8.50	< 13.86	< 1.2	< 8.84
Mn	< -8.50	< 14.01	< 4.65	< 12.34
Fe	-7.814 ± 0.130	14.69	< 5.7	< 13.40
Ni	-8.40	< 14.10	< 5.35	< 13.08
Total				< 15.38

NOTE — Photospheric and circumstellar (C-S) abundances by number relative to hydrogen, $\log n(\text{El})/n(\text{H})$, for our model. We show the C-S abundances that corresponding to a model with $n_{\text{H}} = 0.1$ cm^{-3}. $\dot{M}(El)$ is the mass accretion rate in the photosphere of WD 1124-293 for each element.

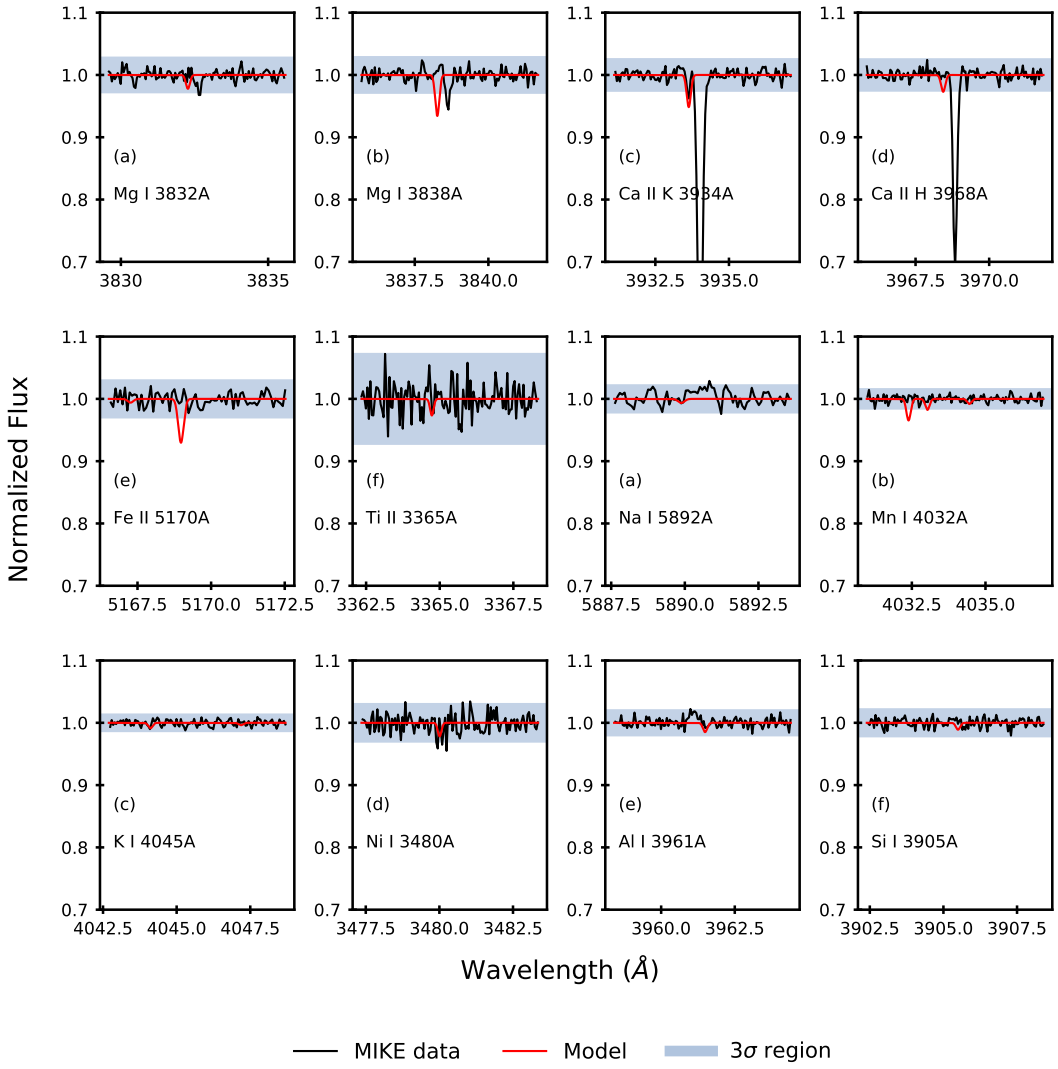

Figure 4.5: Calculated line profiles for species of interest for WD1124

NOTE – The calculated or model line profiles are shown in red. The black curves show the co-added MIKE spectra. The blue region highlights a $\pm 3\sigma$ region for the MIKE spectra. The strengths of the model absorption lines are limited by column density upper limits estimated from the MIKE spectrum. For the Ca features, the deeper photospheric component is gravitationally red-shifted.

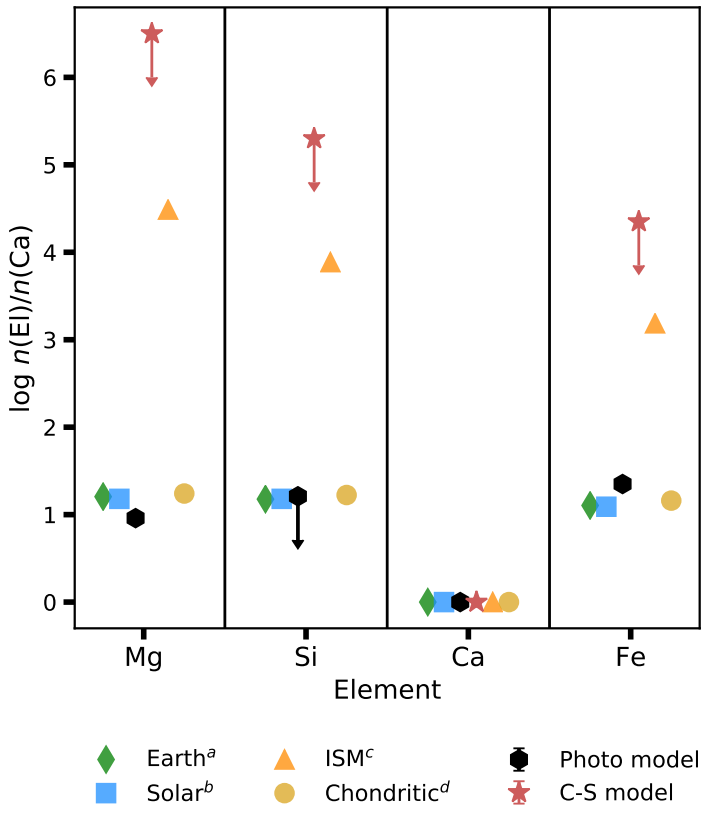

Figure 4.6: Abundances of metals relative to calcium

NOTE – Abundances relative to calcium for metals typically present in photospheric pollution of WDs. We show the upper limits for our Cloudy model with $n_{\rm H} = 0.1$ cm^{-3} with the star markers and the abundances derived from the photospheric model considering diffusion with the black hexagons. We only had a marginal detection of silicon in the photosphere and provide an upper limit there. [a]Allègre et al. (2001), [b]Grevesse & Sauval (1998); Holweger (2001), [c]Cowie & Songaila (1986), and [d]Lodders (2003).

number density, we let the calcium and hydrogen abundances vary from $-8.4 < \log n(\mathrm{Ca})/n(\mathrm{H}) < 1.85$ and $-1 < \log n(\mathrm{H}) < 11$. For the lowest H number density, the abundances of Mg and Fe that produce an absorption feature at a depth of 3σ are $\log n(\mathrm{Mg})/n(\mathrm{H}) = 8.1$ and $\log n(\mathrm{Fe})/n(\mathrm{H}) = 5.7$. We then fix the ratios of Mg and Fe relative to Ca with increasing density, such that $\log n(\mathrm{Mg})/n(\mathrm{Ca}) = 6.3$ and $\log n(\mathrm{Fe})/n(\mathrm{Ca}) = 3.9$ for all models shown in Figure 4.4. All other element abundances, El, are set such that $\log n(El)/n(\mathrm{Ca})$ is constant for models with increasing n_{H}. Figure 4.4 shows how the column density for the strongest observable optical transition in a species varies with increasing H number density and fixed element abundance ratios.

4.5.5 The mass of the gas around WD1124-293

Given our geometrical constraints (inner radius, R_{in}, and outer radius, R_{out}) and assumed disk height, H, the volume of the gas disk is $V = \pi H(R_{\mathrm{out}}^2 - R_{\mathrm{in}}^2)$, and the total gas mass M_{tot} is given by

$$M_{\mathrm{tot}} = V \cdot \left[\sum \left(10^{n_{\mathrm{H}}} \cdot 10^{\mathrm{abn}} \cdot m_{\mathrm{El}}\right) + 10^{n_{\mathrm{H}}}\right] \cdot m_{\mathrm{H}}, \tag{4.5}$$

where n_{H} is the hydrogen number density, abn is the abundance relative to hydrogen, m_{El} is the mass of an element in atomic mass units, and m_{H} is the mass of the hydrogen atom in g. Using the abundances and hydrogen density from our model with a maximum amount of hydrogen ($n_{\mathrm{H}} = 10^9$ cm^{-3}), we place an upper limit on the total gas mass, $\log M_{\mathrm{tot}} \approx 16.12$ g or $\sim$30 times the mass of C-type asteroid

162173 Ryugu (4.50×10^{14} g, Watanabe et al. 2019). Using our model with a minimum amount of hydrogen ($n_{\rm H} = 10^{-1}$ cm^{-3}), the upper limit on the total gas mass is $\log M_{\rm tot} = 15.38$ g or $\sim$5 times the mass of Ryugu. The lower limit is set by the total amount of mass required to produce the Ca feature, so the C-S gas mass, $\log M_{\rm C\text{-}S}$ is constrained to $8.92 < \log M_{\rm C\text{-}S} < 16.12$. Figure 4.6 shows the relative abundances of Mg, Si, Ca, and Fe for our best fit and the relative abundances of those same metals in the photosphere.

4.5.6 Gas Temperature

Cloudy also provides the temperature throughout the gas. For this model, the gas temperature ranges from $\sim$4994 K to $\sim$3965 K. We show the temperature profile for the best fit model in Figure 4.7, also including the optical depths of the two strongest lines at the same depths in the disk.

In our Cloudy models, the heating is dominated by Fe II and the cooling is dominated by Mg II (see bottom panel of Figure 4.7). The temperature of the gas is determined by Cloudy self-consistently and depends on heating and cooling mechanisms. Other efforts to model C-S around WDs tend to assume the temperature is isothermal, though at least one group calculates the temperature at different locations in the disk assuming a Shakura and Sunyaev viscous α-disk using the accretion-disk code AcDc (Hartmann et al., 2016; Nagel et al., 2004). For a WD with $T_{\rm eff} = 20\,900$ K, Hartmann et al. (2016) find the gas temperature decreases to a minimum value $\sim$ 6000 K a third of the way through the disk before rising

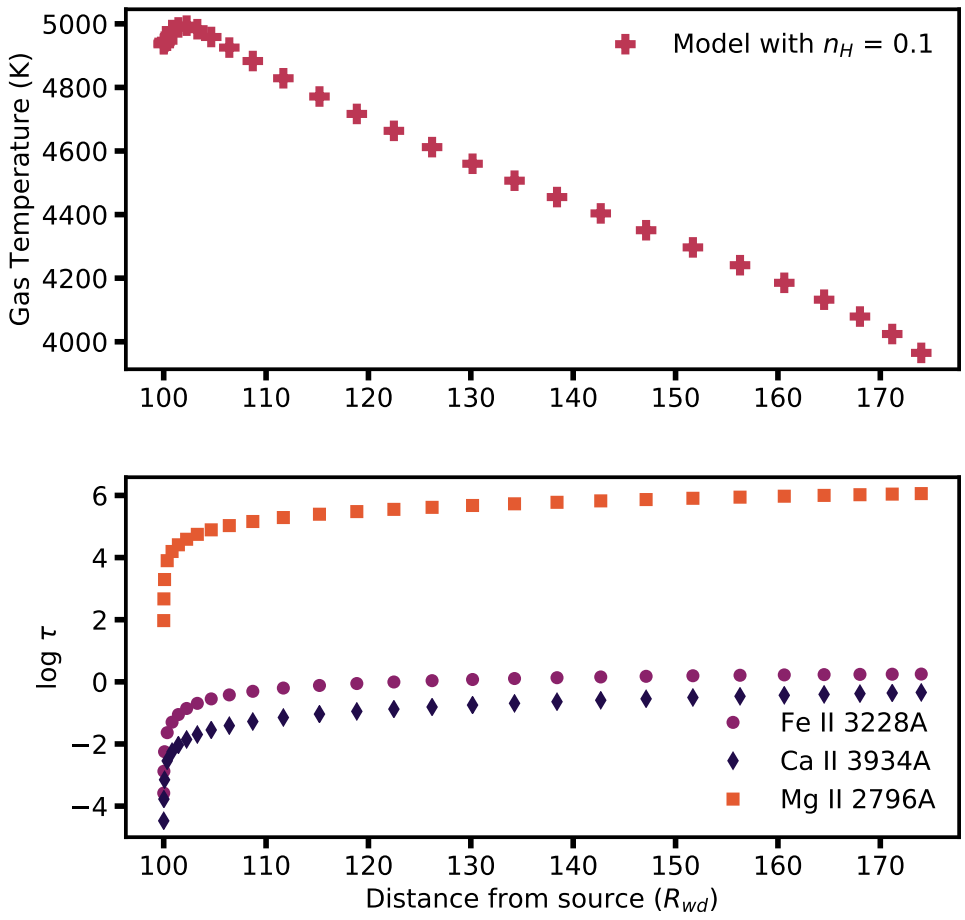

Figure 4.7: Radially variation of temperature and optical depth

NOTE – Top panel: The temperature profile through the disk. Some useful output from Cloudy is the ability to know the temperature profile within the cloud. Modeling of regions usually assume an isothermal environment which is not the case for many of the models. Lower panel: Optical depth with distance for the Ca K line, as well as the Fe and Mg lines responsible for heating and cooling, respectively.

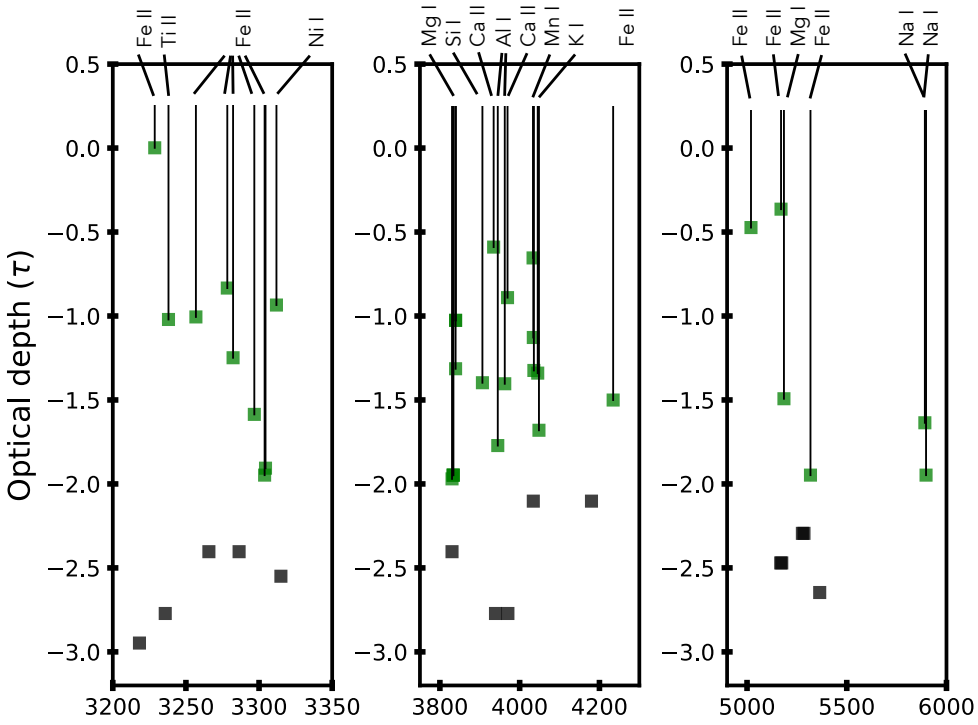

Figure 4.8: Optical depths versus wavelengths

NOTE – The optical depths versus wavelengths of the the strongest species for our model with the maximum amount of hydrogen. The green squares highlight lines with optical depths > -2.0 and the black squares arise from different Mg, Ca, and Fe species. There are many Mg I lines at $\sim$3800Å, though we only show one label for reading legibility.

to a maximum of $\sim$ 6600 K at the outer edge. The temperature profile of this gas disk is very different from that of WD 1124-293, as shown in the top panel of Figure 4.7. For WD 1124-293, the gas temperature profile declines roughly as the $T \propto r^{-0.35}$, with a mild inversion at the inner edge of the disk. Further investigation is needed to understand this discrepancy. Additionally, for hotter WDs, the temperature range probed by Cloudy could be much larger than the 20% changes seen for WD 1124-293.

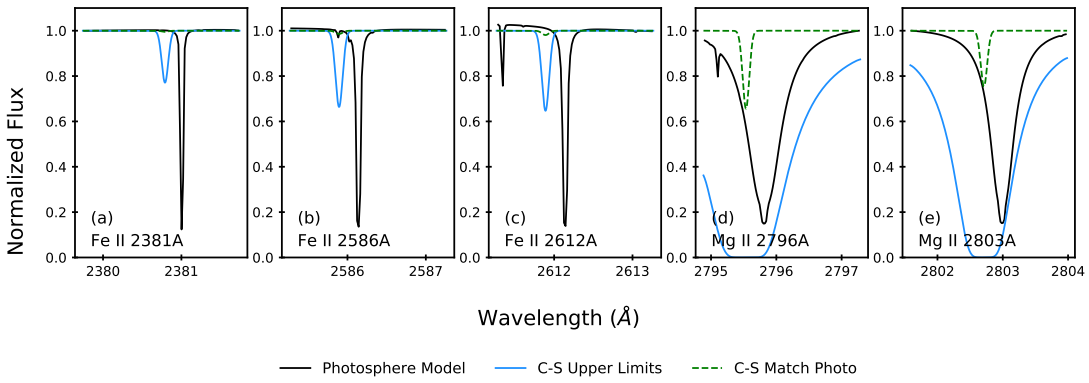

Figure 4.9: Predicted UV line profiles for Mg and Fef

NOTE – The models presented in our results section extend into the UV, so we explore two cases. In the first case, we set the abundance ratios of Mg/Ca and Fe/Ca to match the photospheric values. The solid black line is the best fit polluted photospheric model for WD 1124-293. In the second case, we set the abundance ratios at the modeled upper limits. The expected profiles for Fe/Ca and Mg/Ca equal to the photospheric abundance ratios are shown with the dashed green line. The expected profiles for the C-S abundance upper limits are shown with a solid blue line.

4.5.7 Strongest transitions and a need for UV observations

The strongest expected lines in the optical come from the enhanced Mg, Ca, and Fe in our solar-like composition around WD1123-293 (see Figure 4.8). To obtain the abundances of heavy elements for the photosphere, we proceed in a similar way as described in Xu et al. (2019), by computing grids of synthetic spectra for each element of interest using a pure DA atmospheric structure assuming the stellar parameters previously determined by fitting the photometric data and parallax measurement. The abundances are then obtained by minimizing χ^2 between the normalized spectroscopic data and the grid spectrum. Trace amounts of metals have a negligible effect on the thermodynamic structure for the grid spectrum.

The strongest transitions for most of these species that would help constrain the gas composition and therefore, the sublimation temperature (O, Fe, Si, and Mg), are in the UV. Our polluted photospheric model for WD 1124-293 predicts very strong Mg and Fe absorption lines at UV wavelengths, and as such, our upper limits are likely too large (see Figure 4.9).

FUV observations of other dusty WDs with $T_{\rm eff} \geq 12000$ K have shown absorption lines from as many as 19 unique elements (GD 362, Xu et al. 2013), providing detailed information about planetary material that orbits another star. For example, we can look for correlations between progenitor mass and elemental abundance, or seek to find correlations with specific elemental enhancements, such as Ca. With UV observations, better constraints would be placed on Mg and Fe, helping to further constrain the relative abundances of these metals.

4.5.8 Other work modeling WDs with Cloudy

Gänsicke et al. (2019) use Cloudy to model the C-S gas of WDJ0914+1914 viewed in emission, which contains signatures of the disruption and subsequent accretion of a giant planet. WDJ0914+1914 has $T_{\rm eff} = 27743 \pm 310$K and its photosphere shows evidence of ongoing accretion of oxygen and sulfur. At this temperature, the C-S gas is photoionized, and contains enough hydrogen for oxygen, sulfur, and Hα emission lines to form. The emission features are doubly peaked, indicating the gas is in disk undergoing Keplerian rotation. In their work, the C-S abundances for O and S are consistently determined by two independent methods for the first

time.

With this work, we follow up with the second instance to date of determining gas composition with two independent measurements, and show for the first time how to place constraints on abundances when only absorption features are present. This proof of concept for modeling absorption with Cloudy will be useful when applied to more complicated systems, such as WD 1145+017.

4.5.9 Our proof of concept in the context of WD 1145+017

WD 1145+017 was first shown to have a transiting, disintegrating planetesimal by Vanderburg et al. (2015) and has been since been the subject of much observation (e.g., Cauley et al. 2018; Croll et al. 2017; Fortin-Archambault et al. 2020; Xu et al. 2016, 2019) due to days to week transit and spectroscopic variability. Fortin-Archambault et al. (2020) present a new characterization of WD 1145+017's absorption features, showing how a simple model of nested concentric rings with high eccentricity can help account for the majority of the observed features, which include asymmetrical line profiles and Doppler shifting of the absorption features. These features are also seen in a number of other polluted WDs showing emission lines (e.g., Gänsicke et al. 2019; Manser et al. 2019; Wilson et al. 2014).

The addition of high-resolution spectra to the analysis in Fortin-Archambault et al. (2020) helped disentangle closely spaced features that led to an overestimated prior abundance calculation in Xu et al. (2016). A code like Cloudy could be useful in identifying components of such blends to obtain accurate abundances. They also

observe Si IV features in the UV at 1393.76Å and 1402.77Å and invoke an additional low eccentricity component to explain the presence of such highly ionized species. Cloudy would naturally be able to probe the conditions needed to produce Si IV features with its self-consistent microphysics.

4.6 Conclusion

With this work, we outline how to use the Cloudy radiative transfer code to model C-S gas viewed in absorption around WD 1124-293. We create a Cloudy grid of models for C-S gas around WD 1124-293 to explore the abundances of elements from He to Zn relative to hydrogen, and obtain line optical depths, species column densities, and the temperature profile through the gas disk. Our best fit model minimizes the total amount of hydrogen, while still producing the observed Ca K C-S absorption feature.

We detect photospheric absorption features due to Mg and Fe for the first time, determine a new location for the C-S gas, and place upper limits on abundances of other metals in the photosphere. The upper limit C-S abundance ratios of Mg, Si, and Fe to Ca are also consistent with the photospheric abundance ratios, and with a chondritic/bulk Earth composition.

With these models, we place constraints on the potential masses and abundances that could result in a spectrum dominated by calcium species for WD 1124-293, find that the C-S is likely not isothermal, and show that the Cloudy microphysics code, which is typically used to model active galactic nuclei and HII regions,

can also be used to model C-S gas absorption features of polluted white dwarfs. UV spectroscopic observations of WD 1124-293 are needed to further constrain the composition of its C-S gas.

Looking forward, we intend to explore the properties of C-S gas around DA WDs with temperatures 6000 K to 27,000 K using Cloudy, and will the make the grid of gas properties publicly available (Steele et al. *in prep*).

Chapter 5: A grid of models of C-S gas around WDs

5.1 Introduction

As discussed in previous chapters, up to 50% of white dwarf (WD) atmospheres contain elements heavier than helium (Koester et al. 2014; Zuckerman et al. 2003). These elements should sink rapidly into the stellar interior, so their presence on the surface hints at current replenishment. Recent work suggests that many WDs are in the process of accreting material from tidally disrupted planetesimals from the progenitor star's planetary disk (e.g., Mustill et al. 2014; Veras et al. 2014, 2015) and there is even evidence for the tidal disruption and accretion of a Jupiter-like planet by a hot WD (Gänsicke et al., 2019). After the WD progenitor leaves the main sequence and undergoes mass loss, the progenitor's planetary system destabilizes, perturbing planetary orbits to the white dwarf's Roche limit (Debes & Sigurdsson 2002; Debes et al. 2012). While the evolution of the progenitor star obliterates material inward of ∼a few au, planets and minor bodies beyond a few au can survive post-main-sequence evolution (Nordhaus & Spiegel, 2013; Villaver & Livio, 2007).

Photospheric WD pollution is not uncommon, but the presence of detectable circumstellar (C-S) dust and gas is relatively rare. The number of WDs with detected spectroscopic features due to orbiting circumstellar gas is of the order of ∼10,

with the majority of systems showing emission features (Manser et al., 2016). In Table 5.1, I present a complete (at the time of writing) set of characteristics of the most studied WDs with C-S gas pollution.

The elemental abundances of metals in the *photospheres* of these WDs are described as being consistent with the accretion of large bodies such as those in our own solar system: asteroids like Ceres or Vesta, comets, and gas giants (e.g., Farihi et al. 2013; Gänsicke et al. 2010, 2012; Zuckerman et al. 2007). In systems with calculated photospheric and circumstellar abundances, both sets match (Fortin-Archambault et al., 2020), indicating that the composition of the polluting body remained consistent throughout the accretion process and was not differentiated into layers with significantly different compositions. From this observation, it should follow that the WDs with polluted atmospheres and no C-S gas were likely polluted by a body with abundances matching those observed in the photosphere. However, this logical next step does not take into account that the diffusion of metals in a WD photosphere depends on the effective temperature of the star, the cooling age of the star, and the element in question (Koester, 2009).

Characterizing the photospheric and C-S abundances for polluted WDs with disks allows for the stages of accretion to be observed and tested. Optical and IR high-resolution spectra of a number of systems over many years reveal that the bulk of gas can be in a highly eccentric, precessing disk (e.g., Cauley et al. 2018; Manser et al. 2016), with one system requiring an additional stable component in a circular orbit (Fortin-Archambault et al., 2020). Doppler broadening due to relative speeds of gas along the line of sight constrains the location of the gas, assuming

Keplerian rotation (Horne & Marsh, 1986). Additionally, observations of polluted WDs provide a singular opportunity to discover and measure the composition of the rocky (and in at least one case, gaseous) bodies that survive beyond the giant phase. The composition of the accreted material and the total deposited mass is determined via metal absorption or emission lines in the WD spectra (e.g., Xu et al. 2016, Steele et al. *in prep*).

Though these objects are powerful probes of the composition of the remnants of stellar formation and evolution, there are some caveats. First, for a system like WD 1145+017 that has many metal absorption features, line blending and identification is often an issue (see discussion in Fortin-Archambault et al. 2020).[1] Second, Fortin-Archambault et al. (2020) and Gänsicke et al. (2012) report the detection of features due to triply ionized silicon, Si IV, which is unexpected and requires the gas be close to the WD surface. Third, while the width of a spectral feature places limits on the radial location of the gas, the existence and location of dust/the progenitor to the gas are unknown in systems with no infrared excess (or transiting planetesimal). Additionally, C-S gas is observed from $\sim$ 10s of WD radii ($R_{\rm wd}$) to $\sim 100 R_{\rm wd}$ (Melis et al., 2010), yet I show in Chapter 4 that for at least one system, the gas producing the Ca II K absorption feature has an inner edge at $\sim 100\,R_{\rm wd}$.

With these observed characteristics, I pose additional questions: is it possible that there is gas farther than the sublimation radius in other systems? Also, what is the mass of the C-S gas? To address at least some of these observed characteristics and questions, I use the photoionization code Cloudy to create a grid of models of

[1] Is the line due to some interesting metal, or is it just from Fe II?

C-S gas around white dwarfs with a DA spectral type. These models will provide a key to understanding the instantaneous composition and physical conditions of the material flowing from the planetesimals, could guide modeling of the transits and of the dust in these polluted systems, and will help constrain the radial locations of different gas components. In this work, I focus on the results of the DA, hydrogen-line-dominated WDs, leaving an analysis of the DB, helium-line-dominated, spectral types to a future paper.

In section 5.2, I introduce the Cloudy models and describe the input parameters to create each model. In section 5.3, I explain the gas characteristics (optical depth, line emissivity, temperature, etc.) predicted by the Cloudy Models. In section 5.4, I compare the outputs of the models to the set of WDs with known C-S features. In section 5.5, I discuss the success of the grid in explaining the characteristics of the C-S gas environment (e.g., gas temperature, number density, composition, etc.). In section 5.6, I conclude my findings and highlight next steps for future directions.

5.2 Methods for C-S Gas Modeling

I use the photoionization and radiative transfer code, Cloudy, to create sets of C-S gas models with hydrogen number density constant with radial distance, and fixed chemical composition around DA white dwarf photospheres. Calculations were performed with version 17.01 of Cloudy, described by Ferland et al. (2017). Given the shape and intensity of the ionizing source, the geometry of the gas, the number density of hydrogen, and the gas composition, Cloudy solves the equations

Name	Spectral Type	$\log g$ cm s^{-2}	Star Temp (K)	$M_{\rm wd}$ ($M_\odot$)	$\tau_{\rm cool}$ (Myr)	$\dot{M}$ ($\times 10^8$ g s^{-1})	CS Emission Lines seen	CS Absoprtion Lines seen	Excess IR Emission?	Ref
SDSS J0738+1835	DB	8.4 ± 0.2	14000 ± 100	0.841 ± 0.131	477 ± 160	1300	Ca II triplet	–	–	1
SDSS J0845+2257	DB	8.2 ± 0.2	19800 ± 250	0.73 ± 0.11	122 ± 44	160	Ca II triplet, Fe II	–	–	2
SDSS J0959-0200	DA	8.06 ± 0.03	13280 ± 20	0.64 ± 0.02	324 ± 17	0.32	Ca II triplet	–	–	3, 4
SDSS J1043+0855	DA	8.12 ± 0.033	17900 ± 195	0.693 ± 0.02	153 ± 10	(2.5 - 12)	Ca II triplet	–	–	5, 6, 7
WD 1144+0529	DA	7.74 ± 0.03	23000 ± 219	0.49 ± 0.03	21.2 ± 1.9	–	Ca II triplet	–	–	8
SDSS J1228+1040	DA	8.15 ± 0.09	20700 ± 281	0.705 ± 0.051	100 ± 5	5.6	Ca II triplet, O I, Mg I, Mg II, Fe II	Ca II K	Yes	6, 9, 10, 11, 12
HE 1349-2305	DA	8.133	18173	0.673	149.4	1.3	Ca II triplet	–	–	13, 14, 15
SDSS J1617+1620	DA	8.11 ± 0.08	13500 ± 200	0.68 ± 0.05	350 ± 50	(6.4 - 7.8)	Ca II triplet	–	–	16
WD J0914+1914	DA	7.85 ± 0.06	27700 ± 310	0.56 ± 0.03	13.3 ± 0.5	33	Hα, O I, S II	–	–	22
PG 0843+516	DA	7.902 ± 0.089	22400 ± 304	0.577 ± 0.047	42 ± 4	10.2	–	Si IV	Yes	11
WD 1054-226	DA	8.04 ± 0.03	7900 ± 16	$--$	1255 ± 92	–	–	Ca II K	–	17
WD 1124-293	DA	7.99 ± 0.07	9370 ± 240	0.593 ± 0.042	740 ± 20	1.3	–	Ca II K	–	18, 19, 23
WD1145+017	DB	$--$	15900 ± 500	$--$	180 ± 75	430	–	Mg I, Ca II, Ti II, Cr II, Mn II, Fe I, Fe II, Ni II	Yes	20, 21

NOTE— This table is reproduced from Manser et al. (2016). The full name of WD J0914+1914 is WD J091405.30+191412.25. [1]Dufour et al. (2012), [2]Wilson et al. (2015), [3]Farihi et al. (2012), [4]Xu & Jura (2014), [5]Gänsicke et al. (2007), [6]Melis et al. (2010), [7]Manser et al. (2016), [8]Guo et al. (2015), [9]Gänsicke et al. (2006), [10]Gänsicke et al. (2012), [11]Koester et al. (2014), [12]Manser et al. (2016), [13]Koester et al. (2005), [14]Voss et al. (2007), [15]Melis et al. (2012), [16]Wilson et al. (2014), [17]Vennes & Kawka (2013), [18]Koester & Wilken (2006), [19]Debes et al. (2012), [20]Vanderburg et al. (2015), [21]Xu et al. (2016), [22]Gänsicke et al. (2019), and [23]`http://www.montrealwhitedwarfdatabase.org/evolution.html`.

of statistical equilibrium, charge conservation, and conservation of energy. The code determines the ionization, temperature, and chemical state of a cloud and predicts its spectrum, self-consistently.

5.2.1 Ionizing Source

For the DA white dwarfs, I use photospheric models (Koester et al., 2005) from the Spanish Virtual Observatory (SVO) database. The effective stellar temperatures range from 9000 K to 24000 K, and I use models with a standard surface gravity $\log g = 8$ cm s^{-2}. The luminosity and radius for each model is determined using the Montreal White Dwarf Database (Dufour et al., 2017).[2]

5.2.2 Geometry of Gas

Metzger et al. (2012) model the creation of a gaseous C-S disk around a WD finding that the gas is created at the sublimation radius ($\sim 100\,R_{\rm wd}$, see Chapter 4), spreads inwards and outwards due to angular momentum transport by turbulent viscosity, and has a scale height $h_g \sim 10^{-3} R_{\rm wd}$. I therefore set the geometry of the gas to be in a cylinder of height 10% $R_{\rm wd}$, with the WD at the center. The inner radius of the gas is set to be the surface of the white dwarf and the outer radius of the gas is $10^2 R_{\rm wd}$.

[2]The Montreal White Dwarf Database: `http://www.montrealwhitedwarfdatabase.org/`

5.2.3 Hydrogen

The number density of hydrogen, $n_{\rm H}$, is a required input for a Cloudy model. In my first set of models (this current work), I set $\log(n_{\rm H}/\ {\rm cm}^{-3}) = 5$, which is within the upper limit for $n_{\rm H}$ for the C-S gas around a polluted WD (see Chapter 4). With these parameters, the models predict equivalents widths of the Ca II triplet (8498 Å, 8542 Å, and 8662 Å), that are within an order of magnitude of observed equivalent widths in WDs with C-S gas, allowing for a comparison with observed WDs.

5.2.4 Gas Composition

Following observations of WDs that are polluted by objects with relative metal abundance ratios matching comets and the (bulk) Earth, I choose two gas compositions for the DA grids: a mean CI chondrite and the bulk Earth (see Appendix A). I show these abundances relative to hydrogen for these two compositions in Figure 5.1. For each composition, I use the "metals deplete" command in Cloudy to deplete the abundances of elements by factors ranging from 1 to 1×10^{-4}. Elements with atomic numbers 20 through 28 are depleted more than the lightest elements, with Ca being depleted the most by a factor of 4 dex. These factors are given in Table A.2 in Appendix A. I include this command to simulate a portion of the gas being locked in grains as is observed in the ISM. So I run two sets of grids (4 total), with bulk Earth metallic gas and mean CI chondrite metallic gas.

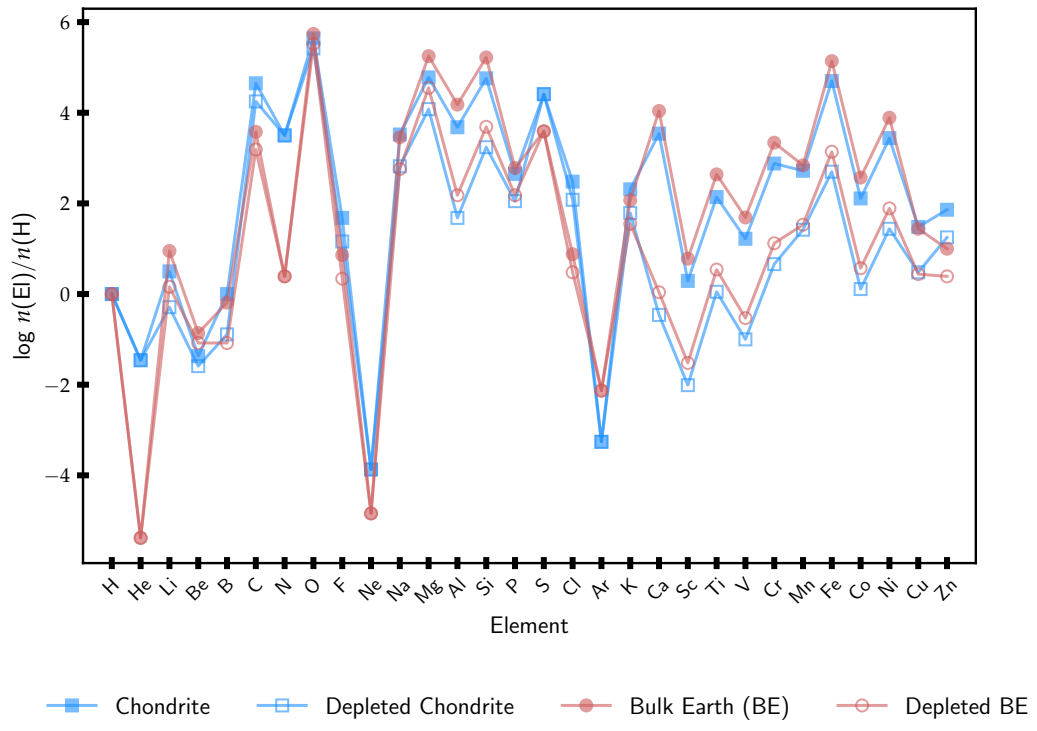

Figure 5.1: Relative Abundances for the Bulk Earth and Mean CI Chondrite

5.3 Gas Characteristics Explored in the Cloudy Models

I next present a subset of gas characteristics calculated in each Cloudy model. I choose to investigate the optical depths (which control the strength of absorption lines), specific line emissivities, the electron density profile, and the gas temperature profiles, including heating and cooling mechanisms. The equations in this section can be found in any text discussing radiative transfer, but I adhere to the notation presented the Cloudy manuals.[3,4] To date, no published work presenting observations of a polluted WD with C-S gas includes optical depths, line emissivities, and temperature profiles for the gas.

[3]Hazy 1: `http://web.physics.ucsb.edu/~phys233/w2014/hazy1_c13.pdf`
[4]Hazy 2: `http://web.physics.ucsb.edu/~phys233/w2014/hazy2_c13.pdf`

To help visualize Cloudy's capabilities, I created a sample grid of 16 models of C-S gas around black bodies with temperatures ranging from 9000 K to 24,000 K and luminosities comparable to the expected luminosity of a white dwarf at that temperature (Dufour et al., 2017). The gas extends from $10R_{\rm wd}$ to $\sim 330R_{\rm wd}$ with a hydrogen number density $\log[(n_{\rm H}/({\rm cm}^{-3})] = 5.0$, and abundances (He through Zn) that match a solar composition that has been increased by a factor of 6 dex.[5]

5.3.1 Optical Depths

The optical depth for a transition from an upper level, u to a lower level l is given by

$$d\tau_{l,u} = \alpha_\nu (n_l - n_u g_l/g_u)\, f(r) dr \tag{5.1}$$

where n_l and n_u are the populations for the lower and upper levels [cm^{-3}], $f(r)$ is the filling factor ($f(r) = 1$), α_ν is the line center atomic absorption cross section [cm^2], and the term in parenthesis is the population of the lower level n_l, with a correction for stimulated emission. In Cloudy, the term $n_u g_l/g_u$ is the only place where stimulated emission enters in the radiative balance.

Cloudy works with the line center optical depth, τ_0 during its calculations, but it reports the mean optical depth in the final output, τ_m, where $\tau_0 = \tau_m/\pi^{1/2}$. The line optical depths are calculated self-consistently.

In Figure 5.2, I show a selection of optical depths for Fe, Ca, H, Mg and Si,

[5] A set of abundances can be multipled by some factor by changing the hydrogen abundance. Cloudy requires the abundance of hydrogen to be 1, so a user-defined hydrogen abundance of -6 (log space) has the effect of Cloudy increasing all other abundances by 6 dex to make the logarithm of the hydrogen abundance 0.

with distance for the individual models. I include a Si IV line to probe when this feature might be observed, and see that it should be observed in C-S gas around a star with $T \gtrsim 14000$ K. The other features are extremely strong and would likely produce saturated absorption features.

5.3.2 Equivalent Width and Line Emissivity for Emission Lines

The strength of an absorption or emission line is described by the equivalent width, W

$$W_\lambda = \lambda W = \int \frac{F_\nu(0) - F_\nu}{F_\nu(0)} \frac{d\nu}{\nu_0} \approx -\lambda \frac{F_{\rm line}}{\nu F_\nu}, \tag{5.2}$$

where W_λ is negative for an emission line and positive for an absorption line, $F_\nu(0)$ is the flux of the incident continuum, F_ν is the flux at a particular frequency, and $F_{\rm line}$ is the flux at the line wavelength (erg $\rm s^{-1}$ $\rm cm^{-2}$). It is straightforward to save $F_\nu(0)$ and F_ν for specific lines within a Cloudy model. Given the reported measurements of equivalent widths (e.g., Gänsicke et al. 2012; Manser et al. 2016; Xu et al. 2016, etc.), I record line and continuum fluxes for specific species and use the equivalent width to test my models against the data.

I also investigate the line emissivity. The emissivity is the net emission $4\pi\bar{J} = n_u A_{ul} P_{ul} h\nu$ [erg $\rm cm^{-3}$ $\rm s^{-1}$] produced at a point and escaping the cloud, where n_u [$\rm cm^{-3}$] is the population or number density of the upper level, A_{ul} [$\rm s^{-1}$] is the Einstein coefficient describing the transition probability, and P_{ul} is the escape probability. The line intensity, $4\pi J$ is calculated by integrating the emissivity over radius, and the luminosity is calculated by integrating over volume.

Figure 5.2: Optical Depths of Gas around Black Body Photospheres

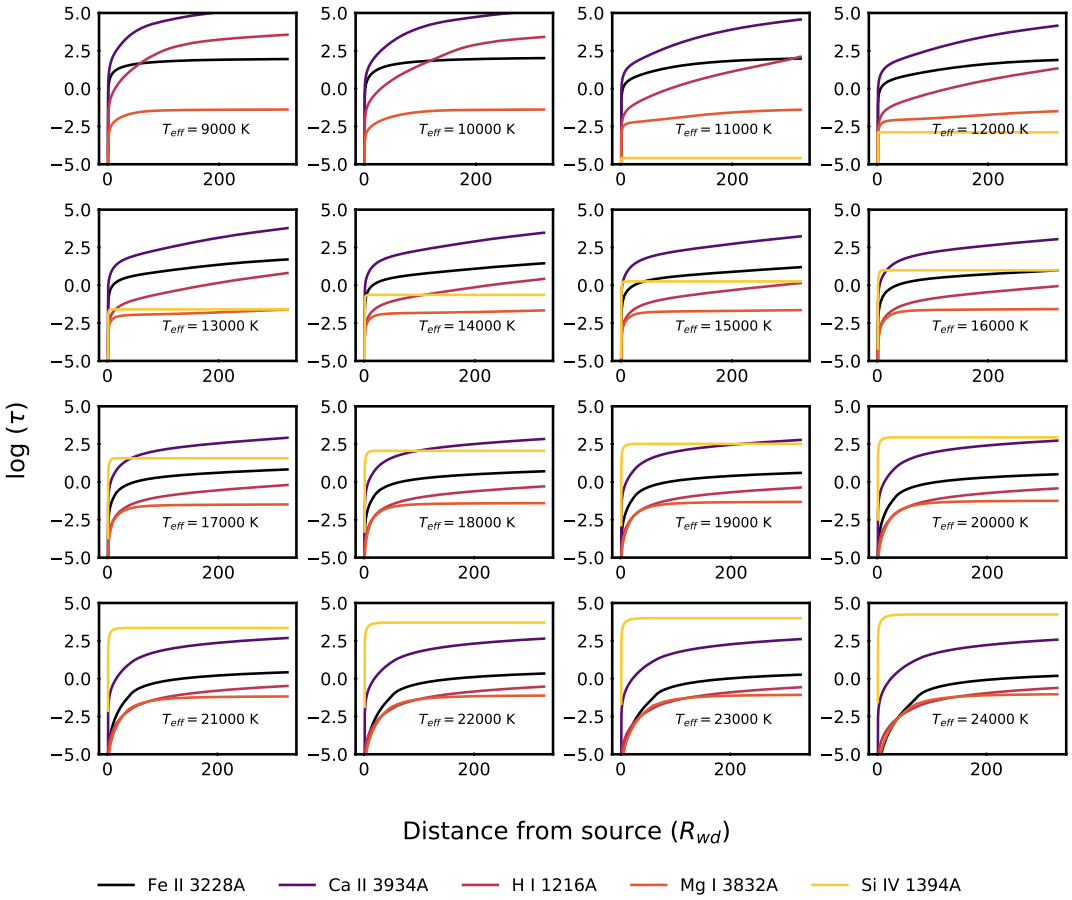

NOTE – Optical depths with distance for a number of species: Fe II, Ca II, H I, Mg I, and Si IV. The optical depths are not constant with distance for most species. Si IV absorption would be detected around black body photospheres with $T_{\rm eff} \gtrsim 14,000$K.

Many of the WDs described in the introduction show the presence of double-peaked emission lines. Those observed line profiles can be predicted with Cloudy by integrating the emissivity of the line over the computed structure. The line profile depends on the velocity field at each point in the integration. The line emissivities shown in Figure 5.3, show that this parameter varies with depth through the cloud, possibly affecting the resulting modeling of such features. I describe these profiles in greater detail in Section 5.5.4.

5.3.3 Gas Temperature

As discussed in Draine (2011), the dominant heating mechanism of gas is photoionization: a photon with an energy greater than the ionization threshold of some atom interacts with the atom, liberating a photoelectron with nonzero kinetic energy, which is added to the thermal energy of the gas. Other sources of heating are photoelectric emission from dust and cosmic rays. The dominant cooling mechanism is radiative recombination: kinetic energy is lost when electrons recombine with ions (producing recombination radiation), and thermal energy is lost when electron collisions excite ions from lower to higher energy levels, followed by the emission of photons (producing free-free emission). Another source of cooling is collisionally excited line radiation, producing emission lines (from N II, O II, O III, Ne II, S II, and S III). The gas stabilizes at a temperature where all heating processes balance all cooling processes.

The temperature profiles for the models are shown in Figure 5.4. For a constant

Figure 5.3: Select Line Emissivities of Gas around Black Body Photospheres

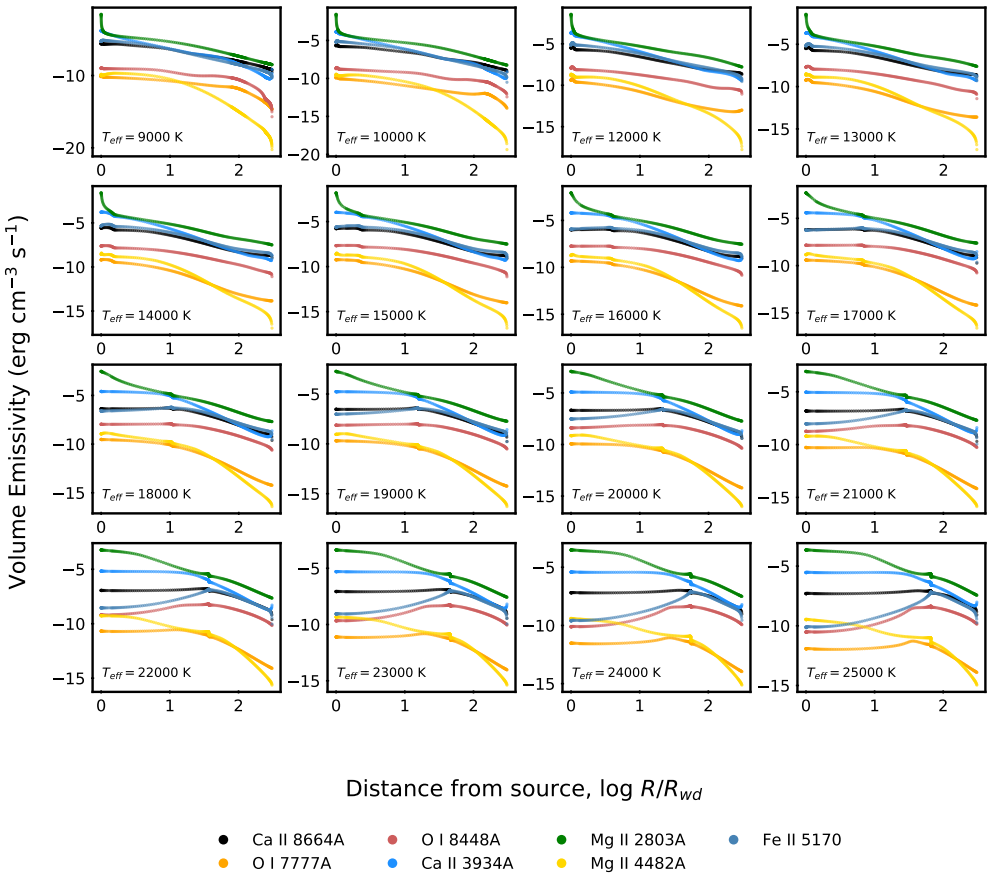

NOTE – Line volume emissivities vary with depth (or distance). Emission features, such as the double-peaked profile seen for the Ca II triplet in the spectra of some WDs, can be modeled using the emissivity with distance from the star. For the species shown above (Ca II, O I, Mg II, and Fe II), the emissivities are not constant. These predictions could improve double-peaked profile modeling. The cause of the discontinuities visible in a number of these models is unknown, and warrants further investigation.

density, the temperature is not isothermal.

5.3.4 Grains

A decision about whether or not to include grains should be made with care. Even if there is no observable evidence of grains, i.e., a thermal infrared excess, for these systems with metallic gas, grains should likely be included due to their effect on the gas temperature. Grains contribute to (a.) the overall heating of the gas through the photoelectric effect and the thermionic effect, and (b.) the cooling of the gas through condensation onto grain-surfaces. If grains might be co-located with the gas, their exclusion will likely mean that the computed gas temperature is incorrect.

If grains are included and destroyed due to sublimation, the material contained within them must be returned to the gas phase to be self-consistent. While the code advises the user when grains could exist and survive based on the gas temperature and composition, Cloudy does not automatically account for the possible destruction of grains.

I do not currently include grains, but instead highlight their importance and my intention to include them in future models.

Figure 5.4: Temperature profiles for models with Black Body Photospheres

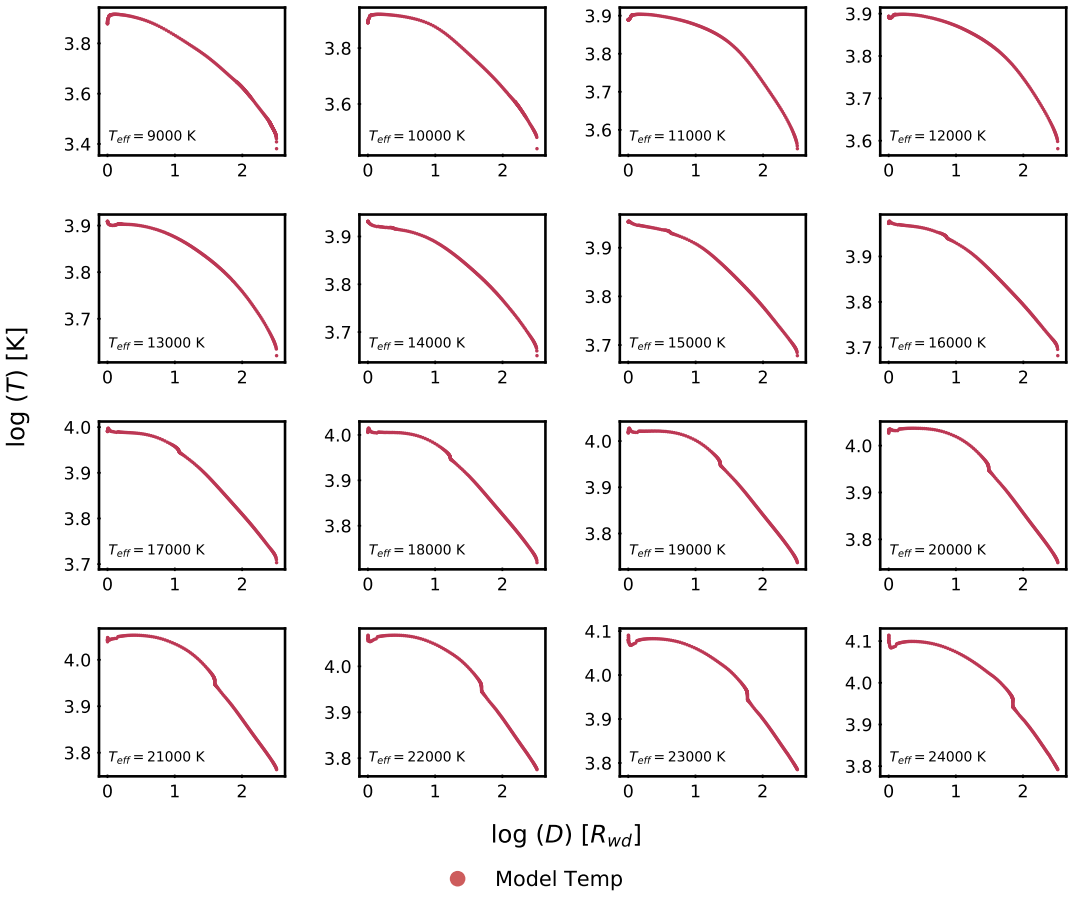

NOTE – Temperature profiles for gas around black body photospheres with $T_{\rm eff} = 9000 - 24000$ K. The profils show a flattening in temperature at smaller radii with increasing model photosphere temperature.

5.3.5 Other Gas Properties

Considering atomic level populations, the ratio of the number of atoms in the upper stage n_u to the number of atoms in the lower stage n_l is

$$\frac{n_u}{n_l} = \frac{2Z_u}{n_e Z_l} \left(\frac{2\pi m_e KT}{h^2} \right)^{3/2} \exp^{-\chi_l / kT}, \tag{5.3}$$

where Z_u and Z_l are partition functions[6] for the upper and lower levels, n_e is the electron (number) density, m_e is the electron mass, T is the gas temperature and χ is the ionization energy required to remove an electron from an atom in the ground state.[7] As the number density of free electrons increases, there are more electrons available for recombination with ions, so the number of atoms in the upper state decreases. For a photoionization code, the electron density is thus an important quantity (older versions of the Cloudy code used the electron number density in place of the hydrogen number density). I show the calculated electron number density profiles in Figure 5.5.

For the Cloudy code, the electron density affects the absorption coefficient per neutral hydrogen atom and it is calculated by using line ratios of certain species. The radius at which the value of the electron density falls below the value of the H density marks the H ionization front.

[6] Recall that the partition function is the weighted sum of the possible arrangements of an atom's electrons with the same energy.

[7] This equation is the Saha Equation, named after Meghnad Saha (1894-1956), who first derived it in 1920.

Figure 5.5: Electron Density of Gas around Black Body Photospheres

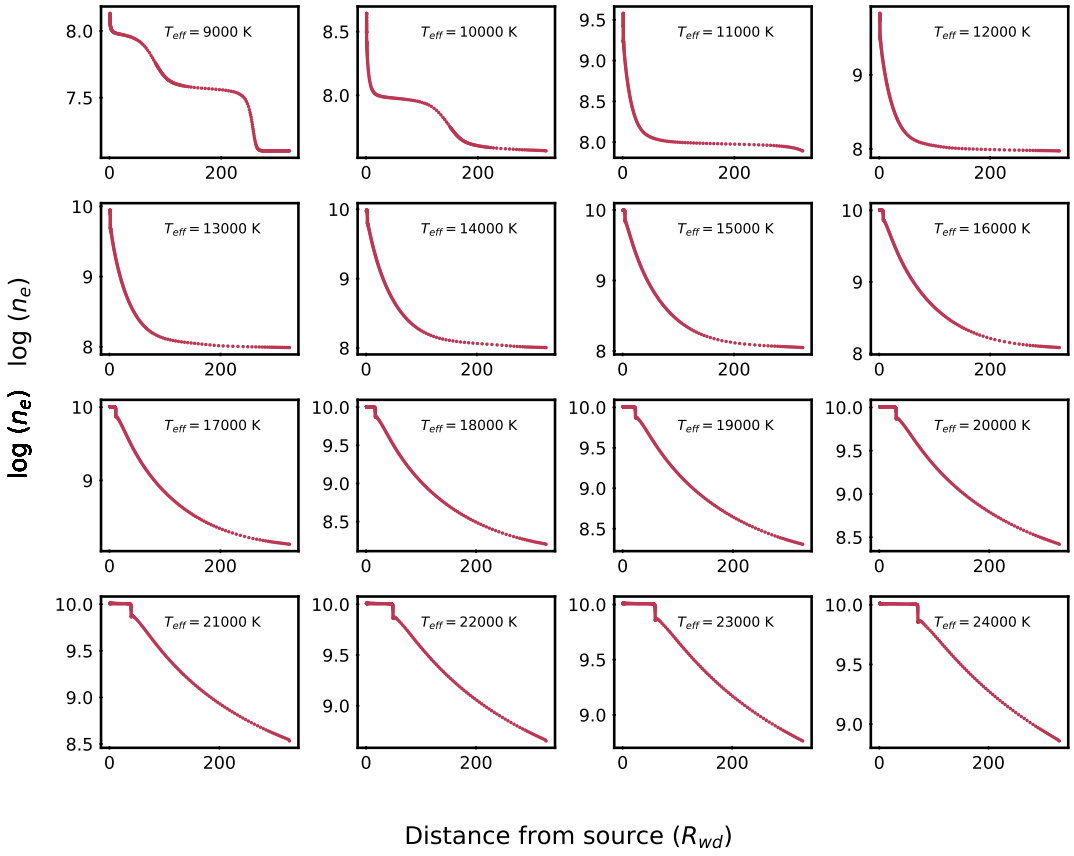

NOTE – The electron density with radial distance.

5.4 Results: Comparison of Models to WDs with C-S Gas

Inspired by observations of WDs with C-S features (see Table 5.1), I used Cloudy to model C-S gas with mean CI chondrite and bulk Earth abundances around DA white dwarfs. Within the output of my model grid, I have the temperature profile, the optical depths of all transitions with $\tau > 0.001$, line emissivities with distance (by volume, for specific lines), the electron density with depth, the line populations for all species (which allows for a calculation of the column density for all species), the flux density for lines of interest, and more.

In this particular work[8], I fix the hydrogen density to $\log[(n_{\rm H}/({\rm cm}^{-3})] = 5.0$, and set the hydrogen abundance to -5.5 dex for models with chondritic abundances and -3.0 dex for models with bulk Earth abundances. Cloudy works with a hydrogen abundance of 0, so a user-defined hydrogen abundance of -5.5 dex has the effect of Cloudy increasing all other abundances by 5.5 dex to make the hydrogen abundance 0. The gas extends from $1R_{\rm wd}$ to $\sim 100R_{\rm wd}$ and has a scale height of $10\%R_{\rm wd}$. I ran models with and without a "metals deplete" command. I report my results on the temperature profile, the strongest spectral line features, and a broad comparison to WDs with C-S gas previously studied in the literature, using equivalent widths to investigate the physical conditions of the gas in these systems.

[8]This work is Part I of a series.

5.4.1 Temperature profiles, Heating, and Cooling

Efforts to model C-S gas around WDs tend to assume the temperature is isothermal, yet Hartmann et al. (2016) modeled the emission from C-S gas around SDSS J1228+1040 (J1228) assuming a Shakura and Sunyaev viscous α-disk using the accretion-disk code AcDc (Nagel et al., 2004). Rather than assume the disk has an isothermal profile, they let the gas temperature vary. However, they chose the temperature for each component in their disk model, rather than solve for it. Their resulting temperature profile decreases from the inner edge, reaches a minimum, and then increases until the outer edge of the disk (full extent 40 $R_{\rm wd}$to 135 $R_{\rm wd}$, see Figure 3 in Hartmann et al. 2016).

I plot the predicted temperature profiles for all four grids in Figures 5.6, 5.7, 5.9, and 5.8. I include a dashed line showing a power-law temperature dependence that describes the general trend of the profile. I include a power-law "fit" to the model temperature profile to highlight the general trend of profile and any departures from a straight line (dashed gray line in Figures 5.6 through 5.9). The profiles were fit using a non-linear least squares Python SciPy routine (curvefit) at radii between $5R_{\rm wd}$ and $\sim 50R_{\rm wd}$ to avoid non-linear regions. The power law is $T \propto R^{-q}$ where R is the distance from the star and q is the spectral index (Andrews et al., 2009).

In the DA mean CI chondrite and bulk Earth models, the gas temperature profile declines roughly as $T \propto r^{-0.2}$ at stellar temperatures of $\sim$ 9000 K, and as $T \propto r^{-0.5}$ at stellar temperatures of $\sim$20,000 K. When there's metal depletion, the

gas temperature profile declines roughly as $T \propto r^{-0.2}$.[9] The profiles are less steep when metals are depleted. When the metals are not depleted, the temperature profile shows an inversion with a discontinuity that appears at increasingly larger radii with increasing model temperature. This could be a shock or pressure front that moves to larger radii with increasing temperature. When metals are depleted, the temperature profile tends to better follow a power-law.

The temperature of the gas is determined by Cloudy self-consistently and depends on heating and cooling mechanisms. In my Cloudy models, heating and cooling are controlled by iron, carbon, calcium, silicon, and magnesium. Iron, sulfur, sodium and oxygen are solely responsible for cooling, while carbon, silicon, and aluminum contribute to heating. I show the species responsible for heating and cooling in the chondrite models in Figure 5.10 and for the bulk Earth models in Figure 5.11.

5.4.2 A Selection of Optical Depth Profiles

The main parameters I use to compare the models to the observed parameters are the optical depth and the emission line equivalent width. These two quantities depend on the temperature of the star, the hydrogen number density of the model, electron density, and the composition of the gas.

The strongest expected lines in the optical typically come from Mg, Ca, and Fe. The strongest transitions for most metals (O, Fe, Si, and Mg), that would help

[9] By comparison, the temperature profile of the mid-plane in a planetary disk can have $q \approx 0.5 - 0.6$ (Andrews et al., 2009).

Figure 5.6: Temperature Profiles - DA, Mean Chondrite, Metals Depleted

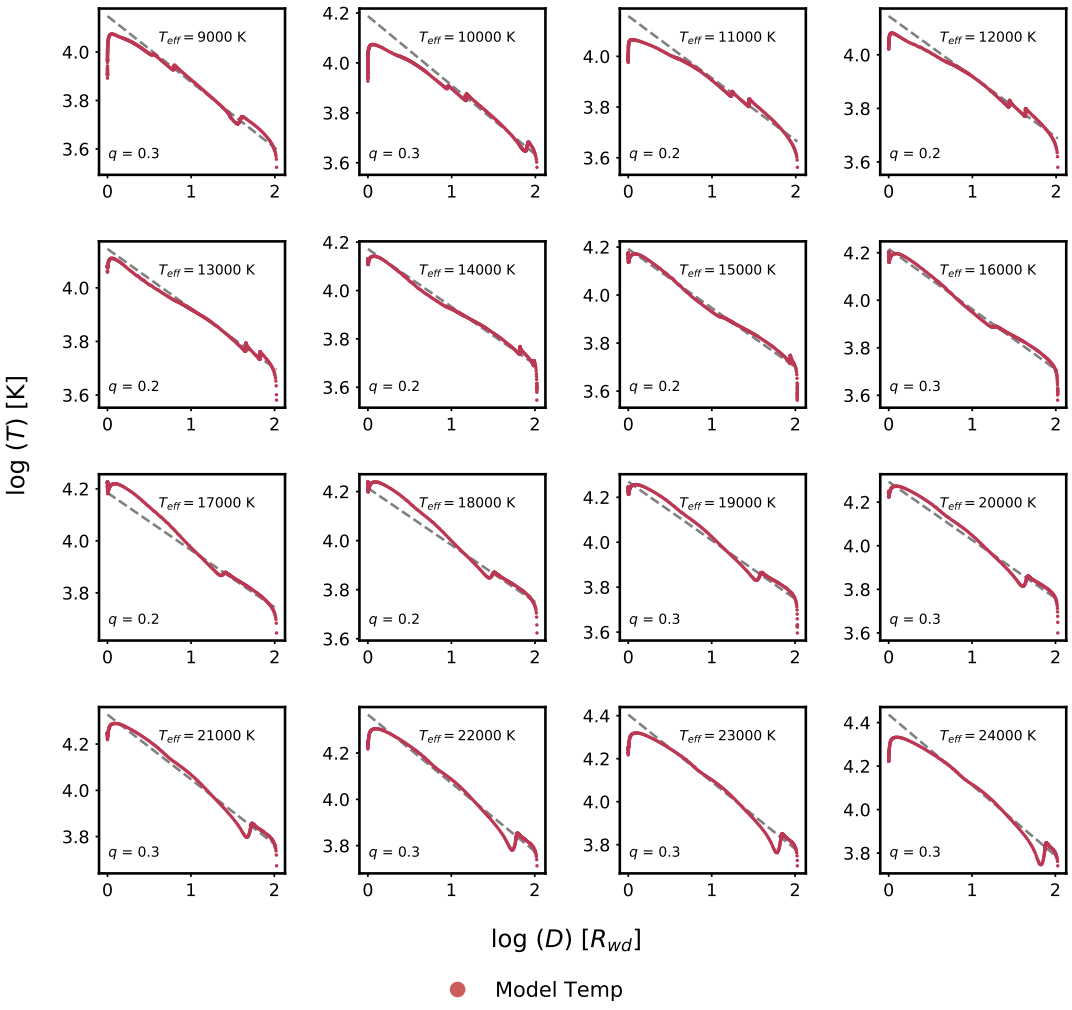

Note — The temperature with distance for each of the models of gas around a DA photosphere. The gas has a mean CI chondrite composition (metals depleted, see Table A.2). The effective stellar temperature is reported in the top right corner. The temperatures are plotted with a red line (actually closely spaced red circles). I include a dashed gray line showing a true power-law relation between temperature and radius. The value of the exponent is q, given for each model in the lower left corner.

Figure 5.7: Temperature Profiles - DA, Mean Chondrite

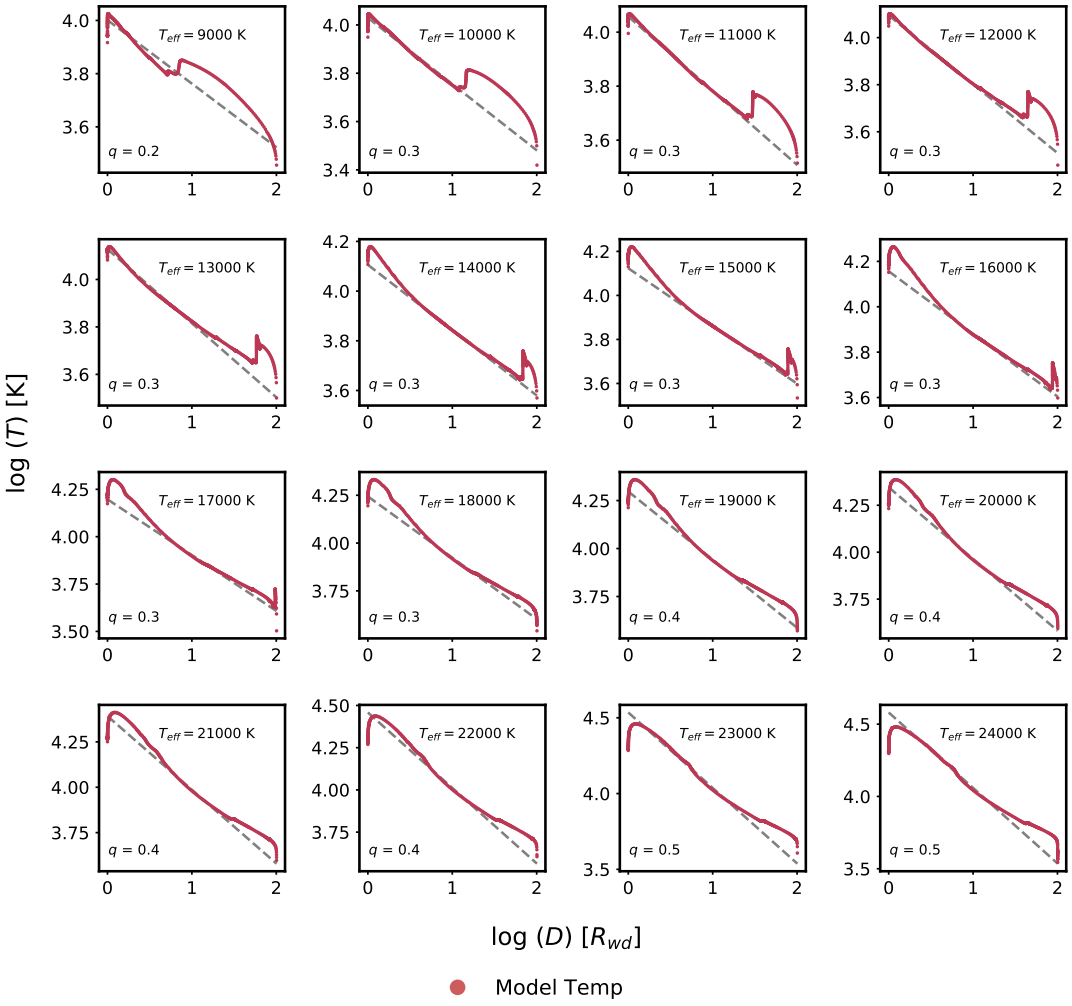

NOTE — The temperature with distance for each of the models of gas around a DA photosphere. The gas has a mean CI chondrite composition. The effective stellar temperature is reported in the top right corner. The temperatures are plotted with a red line (actually closely spaced red circles). I include a dashed gray line showing a true power-law relation between temperature and radius. The value of the exponent is q, given for each model in the lower left corner. A temperature inversion is seen for stars with effective temperature $T_{\rm eff} < 17,000$ K.

Figure 5.8: Temperature Profiles - DA, Bulk Earth

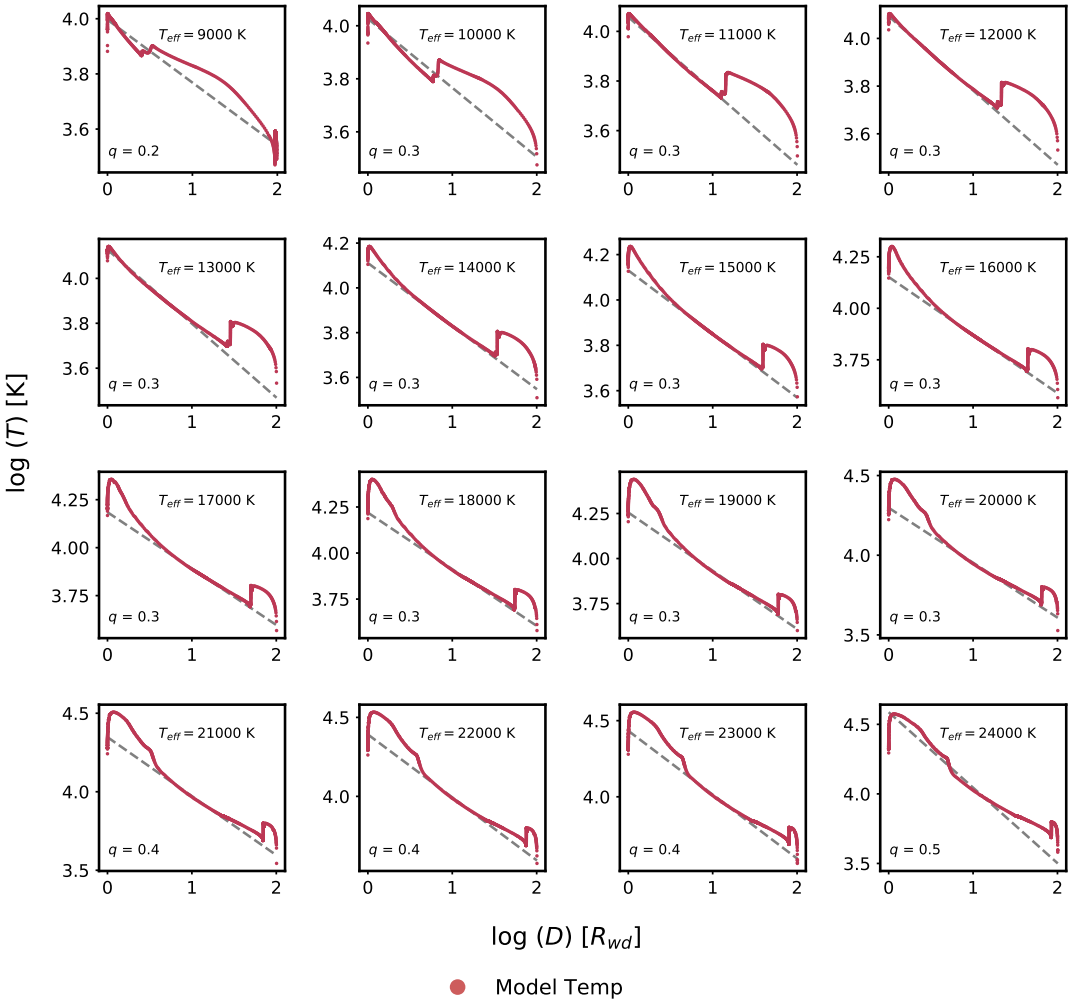

NOTE — The temperature with distance for each of the models of gas around a DA photosphere. The gas has a bulk Earth composition. The effective stellar temperature is reported in the top right corner. The temperatures are plotted with a red line (actually closely spaced red circles). I include a dashed gray line showing a true power-law relation between temperature and radius. The value of the exponent is q, given for each model in the lower left corner. A temperature inversion is seen in all of the models and there are deviations from a single power law at the inner edges of the model disks.

Figure 5.9: Temperature Profiles - DA, Bulk Earth, Metals Depleted

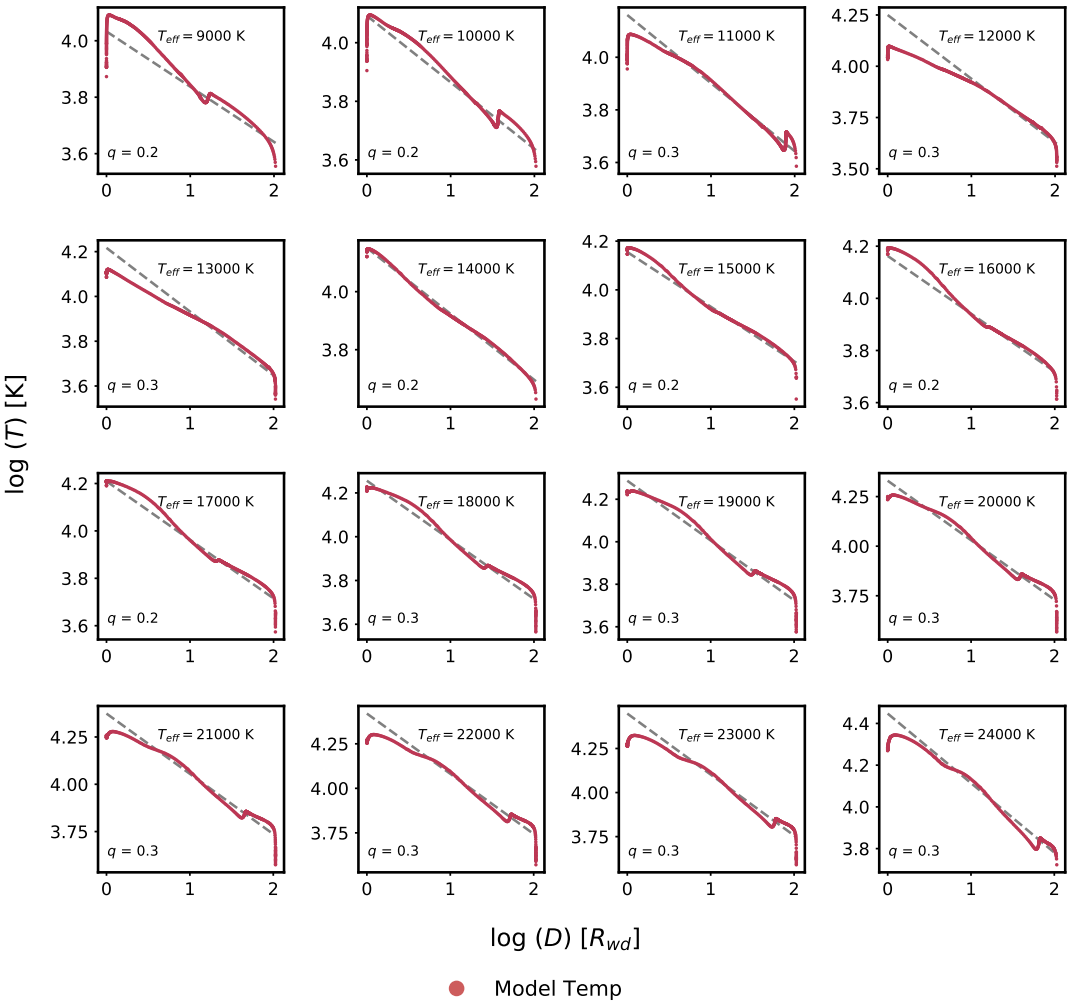

NOTE — The temperature with distance for each of the models of gas around a DA photosphere. The gas has a bulk Earth composition (metals depleted, see Table A.2). The effective stellar temperature is reported in the top right corner. The temperatures are plotted with a red line (actually closely spaced red circles). I include a dashed gray line showing a true power-law relation between temperature and radius. The value of the exponent is q, given for each model in the lower left corner.

Figure 5.10: Heating and Cooling - DA, Mean Chondrite

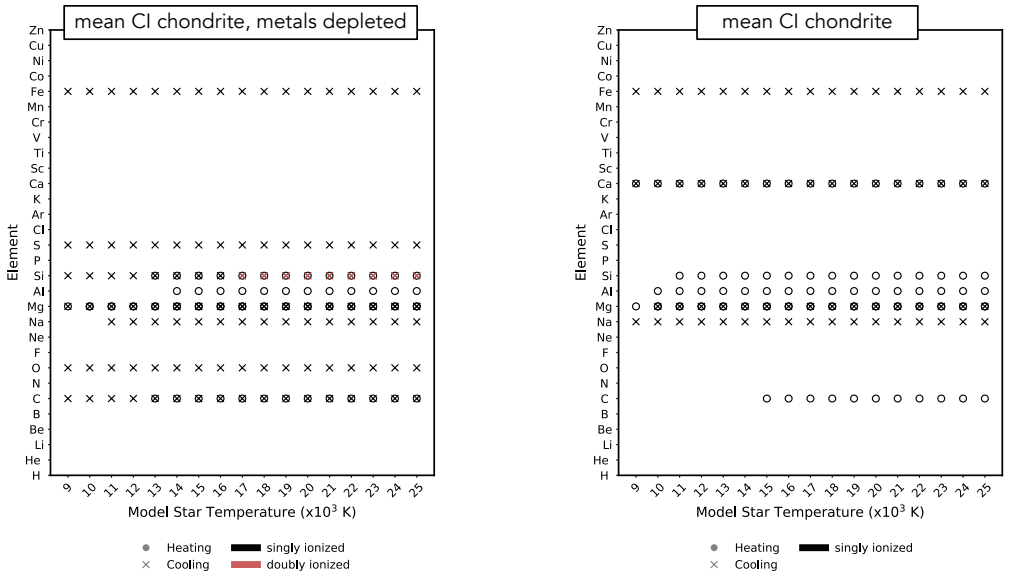

NOTE – The species responsible for heating (open circles) and cooling ("x"). Singly-ionized species are shown in black and doubly-ionized species are shown in red. Fe, S, Na, and O are responsible for cooling in all models. Heating is dominated by C, Mg, Al, and Si.

Figure 5.11: Heating and Cooling - DA, Bulk Earth

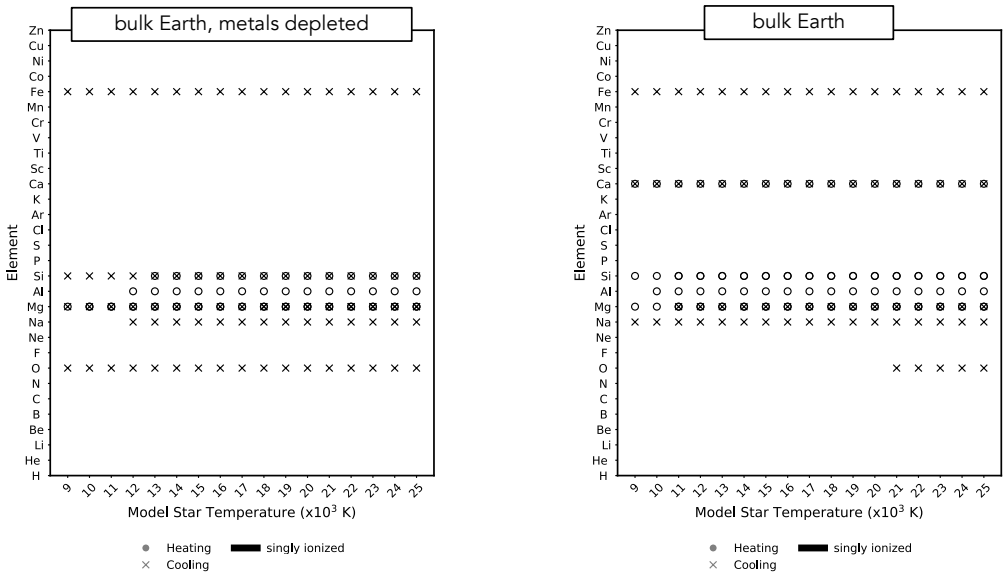

NOTE – The species responsible for heating (open circles) and cooling ("x"). Fe, S, Si, O, and Na are responsible for cooling in all models. Heating is dominated by C, Mg, Al, and Si.

constrain the gas composition, and therefore the sublimation temperature, are in the UV. Obtaining UV detections of Si, C, and O in particular can constrain how water-rich or C-rich these planetesimals are. The models with $n_{\rm H} = 5$ g cm^{-3} predict a plethora of very strong ($\tau \gg 1$) lines. In Figures 5.12 and 5.13, I show the optical depths (log scale) for mean CI chondrite and bulk Earth models that have depleted metals. I predict very strong Mg and Fe absorption lines at UV wavelengths. For systems that have these high optical depths and no absorption features, I suggest that the gas is inclined relative to the line of sight to the WD and not viewed directly in front of the WD.

5.4.3 Comparison of Models to WDs with C-S Gas

The majority of WDs with known C-S gas show emission lines (see Table 5.1), especially emission at the IR calcium triplet (Manser et al., 2016). The strengths of the emission lines are reported in most cases in terms of their equivalent widths. Using the observations to guide the reporting of the results, I plot the equivalent widths of emission lines predicted by the Cloudy models with bulk Earth and mean CI chondrite compositions, focusing on the calcium triplet and other species that have been reported in the literature.

As a reminder, I fixed the hydrogen number density to $n_{\rm H} = 5$ cm^{-3} and the hydrogen abundance to -5.5 dex (chondrite) or -3 dex (bulk Earth). This has the effect of increasing all other abundances so that hydrogen ultimately has an abundance of 0. I ran models with and without a "metals deplete" command.

Figure 5.12: Select optical depth profiles - DA, Mean CI Chondrite, Metals Depleted

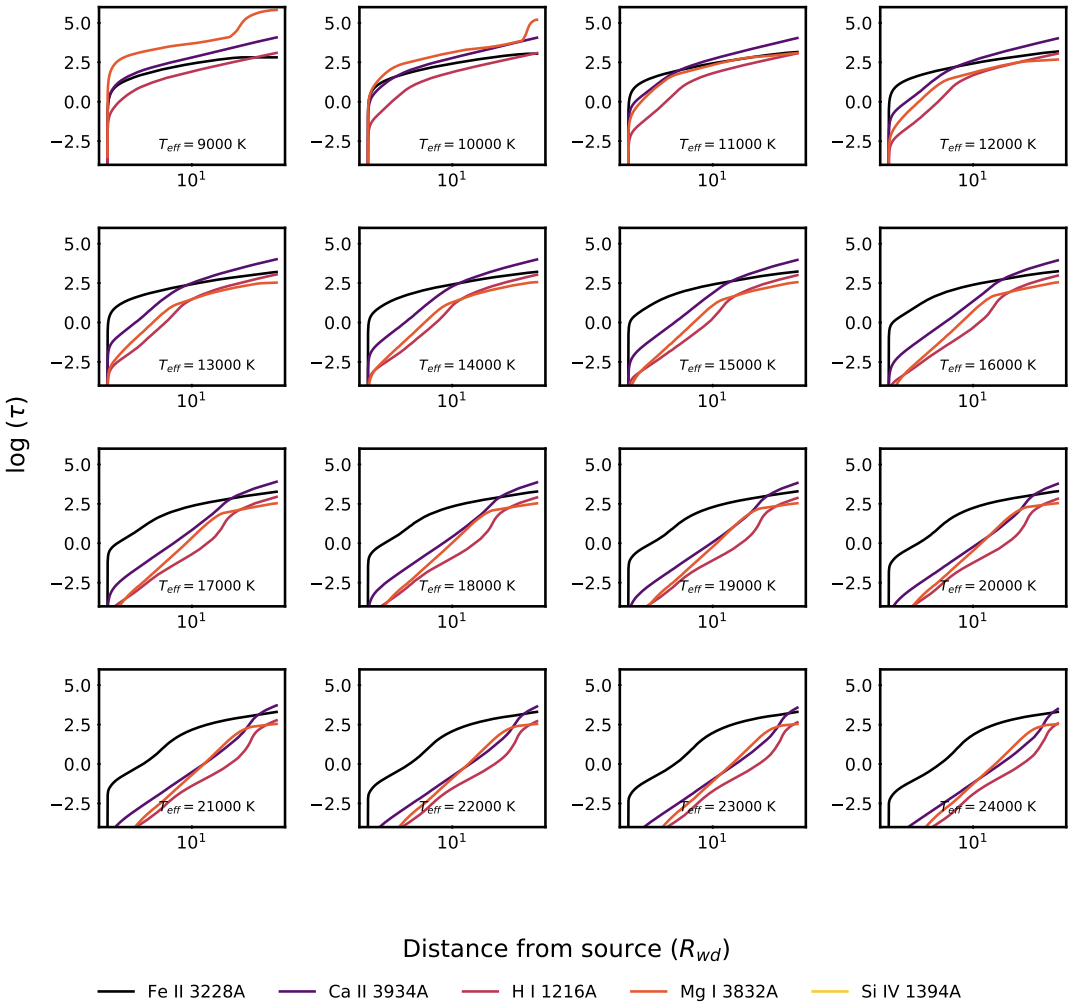

NOTE — Optical depths with distance for a number of species: Fe II, Ca II, H I, Mg I, and Si IV. The gas has a mean CI chondrite composition with metals depleted (see Table A.2). The optical depths are not constant with distance for most species. Si IV absorption would be easily detected.

Figure 5.13: Select optical depth profiles - DA, Bulk Earth, Metals Depleted

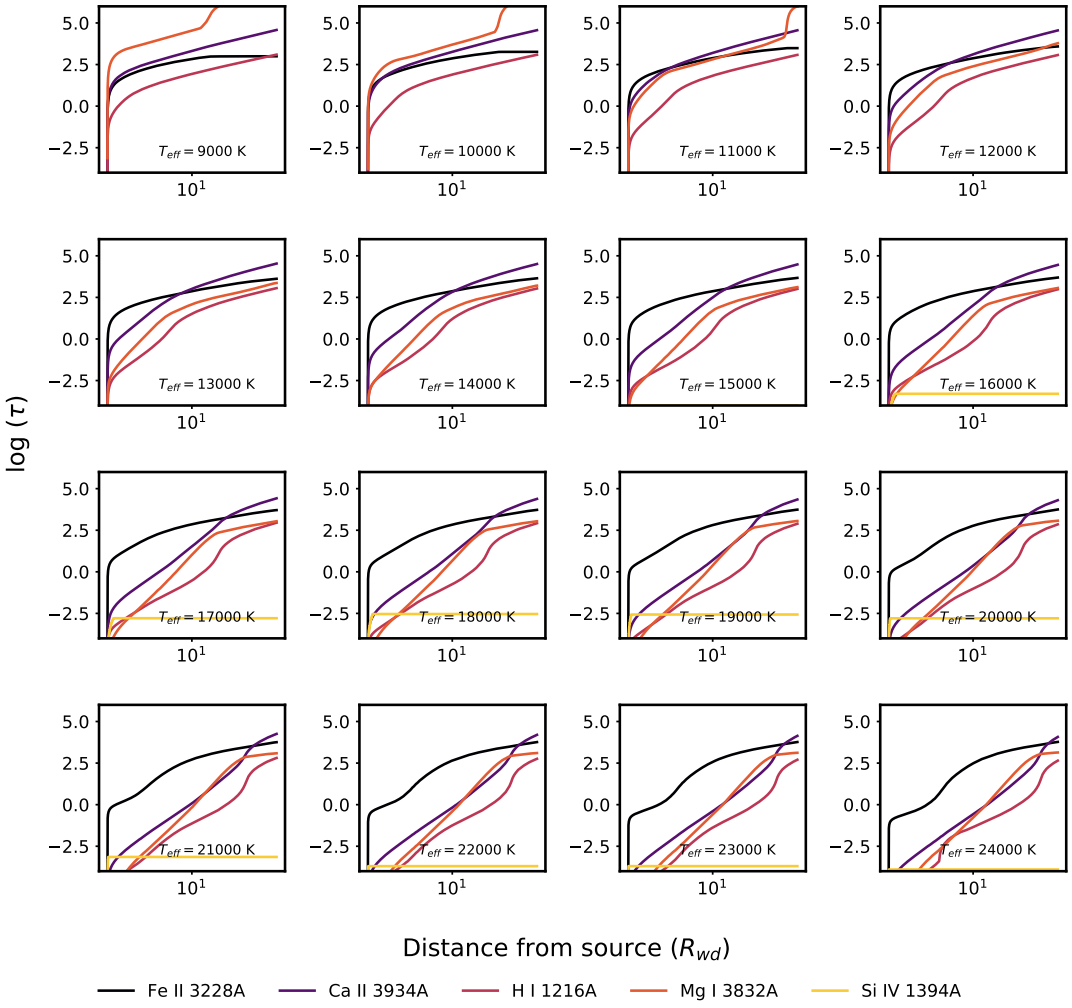

NOTE — Optical depths for a number of species. Optical depths with distance for a number of species: Fe II, Ca II, H I, Mg I, and Si IV. The gas has a bulk Earth with metals depleted (see Table A.2). The optical depths are not constant with distance for most species. Si IV absorption might be detected around stars with $T_{\rm eff} \gtrsim 17000$ K.

Table 5.2: The Equivalent Widths of a Sample of WDs

SDSS J1228+1040			
Species	Wavelength (Å)	EQW (error) (Å)	Ref
Mg II	2803	−7.9 (0.4)	*a*
Ca II	3934	−0.893 (0.007)	*a*
Ca II	3969	−1.485 (0.009)	*a*
Mg II	4482	−0.061 (0.002)	*a*
Fe II	5170	1.3 (0.1)	*b*
O I	7774	−2.20 (0.02)	*a*
O I	8446	−1.50 (0.02)	*a*
Ca II	8500	−16.73 (0.03)	*a*
Ca II	8542	−23.45 (0.03)	*a*
Ca II	8662	−20.76 (0.03)	*a*
Ca II Triplet-only			
	8500Å	8542Å	8662Å
Star	EQW (error) (Å)	EQW (error) (Å)	EQW (error) (Å)
HE 1349-2305[c]	−1.9 (0.2)	−1.7 (0.2)	−1.6 (0.3)
SDSS J1043+0855[b]	−7.0 (0.5)	−7.0 (0.6)	−8.1 (1.2)
WD 1144+0529[d]	−1.3 (0.4)	−1.7 (0.4)	−1.5 (0.5)

NOTE—Equivalent widths are from the following sources: [a]Manser et al. (2016), [b]Melis et al. (2010), [c]Melis et al. (2012), [d]Guo et al. (2015)

The equivalent widths of various emission lines predicted by these models with a mean CI chondrite gas composition are shown for DA WDs in Figures 5.15 and 5.14. Models for a bulk Earth composition are shown in Figures 5.17 and 5.16. I compare four WDs to my models: SDSS J1228 + 1040 (J1228), SDSS J1043 + 0855 (J1043), HE 1349 − 2305, and WD 1144+0529. The latter three WDs only show the Ca II triplet. Using just these three stars, I cannot rule out a chondritic or bulk Earth composition. Next, I discuss trends observed in the plots, focusing on J1228.

5.4.3.1 Mean CI Chondrite Gas Models

For the chondrites, the model equivalent widths show more spread in their values when the "metals deplete" command is used, but there is a slightly better agreement with the expected relative line strengths among the metals. If all other lines are compared to the Ca triplet for J1228, then in the case of the metals depleted model with $\log n_{\rm H} = 5$, O, Fe, and Mg are over-predicted, and the strength of the Ca II H and K lines relative to the Ca triplet is "inverted" for the hotter WDs (the Ca H & K line equivalent widths should be less than those of the Ca triplet). Compared to J1228, the models with an unaltered mean CI chondrite composition, the Ca H and K lines are too strong, as is the Fe II 5170Å line. The relative strength of the Ca II triplet to the O I line is, however, closer to the observed value for J1228.

5.4.3.2 Bulk Earth Gas Models

WD 1145+017 has been reported as having C-S gas with a composition consistent with the the bulk Earth (Fortin-Archambault et al., 2020; Xu et al., 2016). The equivalent widths of various emission lines predicted by the models with a bulk Earth composition around DA WDs are shown in Figures 5.17 and 5.16. For the gas with bulk Earth abundances, the model equivalent widths show similar amounts of spread in their values when the "metals deplete" commands is used, with the exception of Mg.

The relative strength of the Ca H and K lines to the Ca II triplet is too large. The strength of the UV Mg II 2803 line relative to the Mg II 4483 line is more

Figure 5.14: Emission Line Equivalent Width Predictions - DA, Mean Chondrite

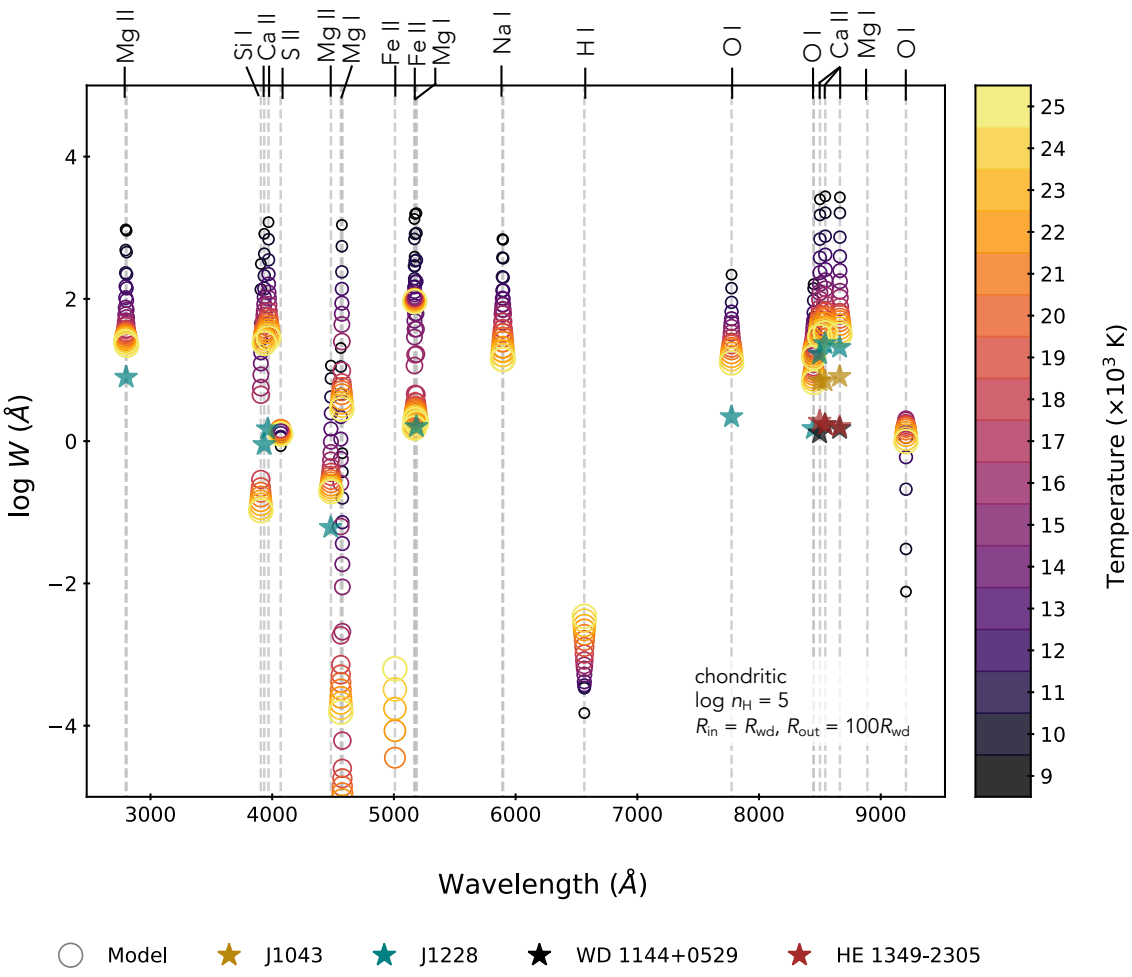

NOTE – Equivalent widths expected from the models. The stellar temperature increases from 9000 K up to 25,000 K with increasing circle size. Though all the lines are too strong, the relative ratios of the Mg II lines are close to what is expected from the observations of J1228, shown with the teal stars. The relative strengths of the Ca II H & K pair to the Ca II triplet are too strong. The H I (Hα) line at 6563 Å is weak and would likely not be detectable. The O I lines at 7777 Å (a triplet) and 8448 Å appear at close to their expected strengths. The Ca II triplet is weak relative to the H & K pair.

Figure 5.15: Emission Line Equivalent Width Predictions - DA, Mean Chondrite, depleted metals

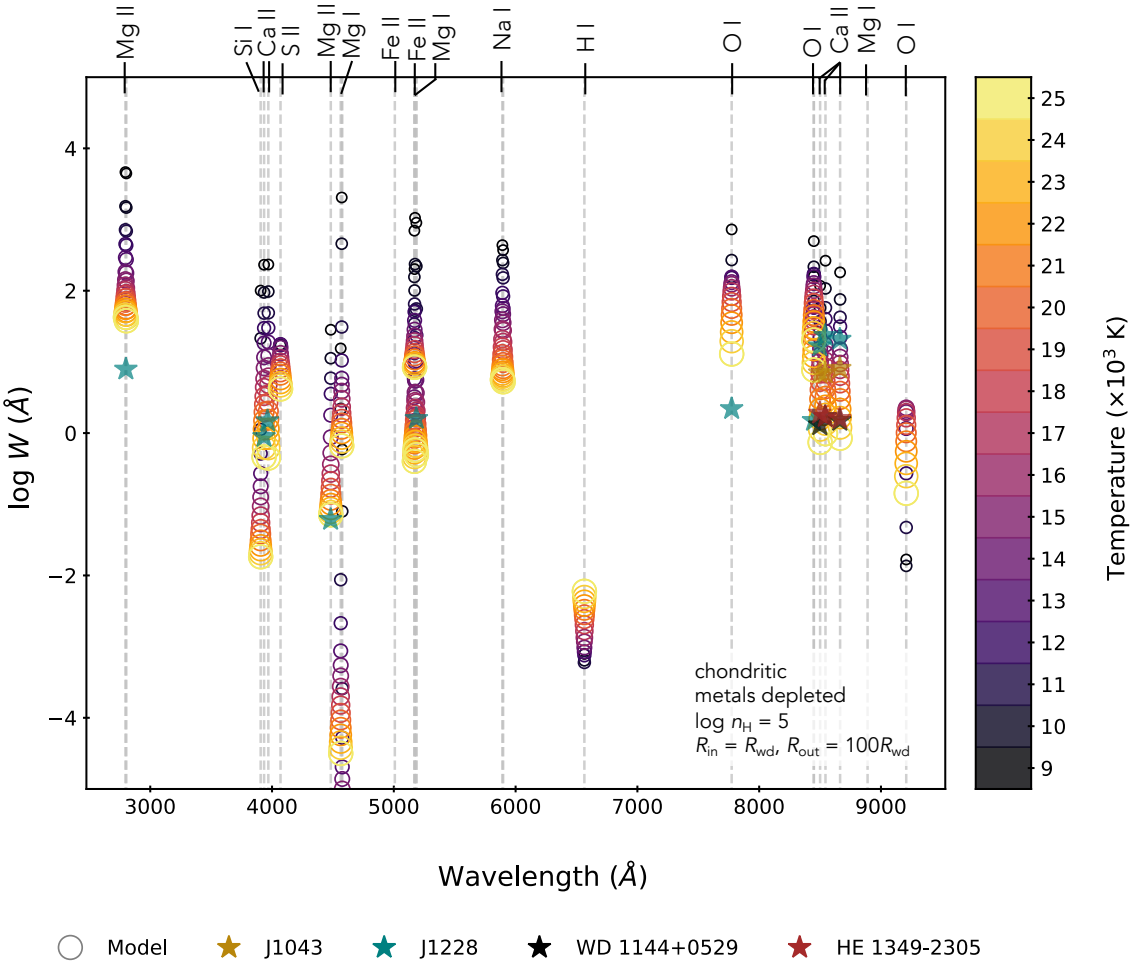

NOTE – Observations from left to right: the relative strength of the Mg II 2803 Å line is too large compared to the Mg II 4482 Å line. The Fe II 5170Å line is too strong. The H I (Hα) line at 6563 is weak and would likely not be detectable. The relative strengths of the O I lines at 7777 Å (a triplet) and 8448 Å do not appear at their expected relative strengths. The O I 8448 Å line is too strong. The Ca II triplet is weak relative to the H & K pair. The stellar temperature increases from 9000 K up to 25,000 K with increasing circle size.

shallow than it should be, but there is good agreement with the equivalent widths of J1228 and the models. When metals are not depleted the relative strengths of the O lines to the Ca lines improves. No Hα emission is expected. I explore relative line ratios in more detail in Section 5.5.2.

5.4.4 Output Continuum

While many species have high optical depths and large equivalent widths, the output or transmitted continuum predicted by Cloudy when metals are depleted shows features that resemble those seen in observed WD spectra. I show the input WD photosphere (orange) compared to the "total" and "net transmitted" continuum models with a mean CI chondrite composition (Figures 5.18 and 5.19), and bulk Earth composition (Figures 5.20 and 5.21). The total spectrum (red) is the sum of the transmitted and reflected continua and lines, including the attenuated incident continuum (the WD photosphere). The net transmitted continuum is the sum of the attenuated incident WD photosphere and any diffuse continua and lines. This curve in blue is what would be observed if the source were viewed through the gas. However, the output continua must be convolved with a velocity profile to account for any bulk motion of gas.

When metals are depleted (Figure 5.18), there are less features that would be observed in absorption compared to the number and depth of lines predicted for the non-depleted composition (Figure 5.19). The predicted absorption is not observed in the spectrum of J1228. This can be explained if the gas is inclined to

Figure 5.16: Emission Line Equivalent Width Predictions - DA, Bulk Earth

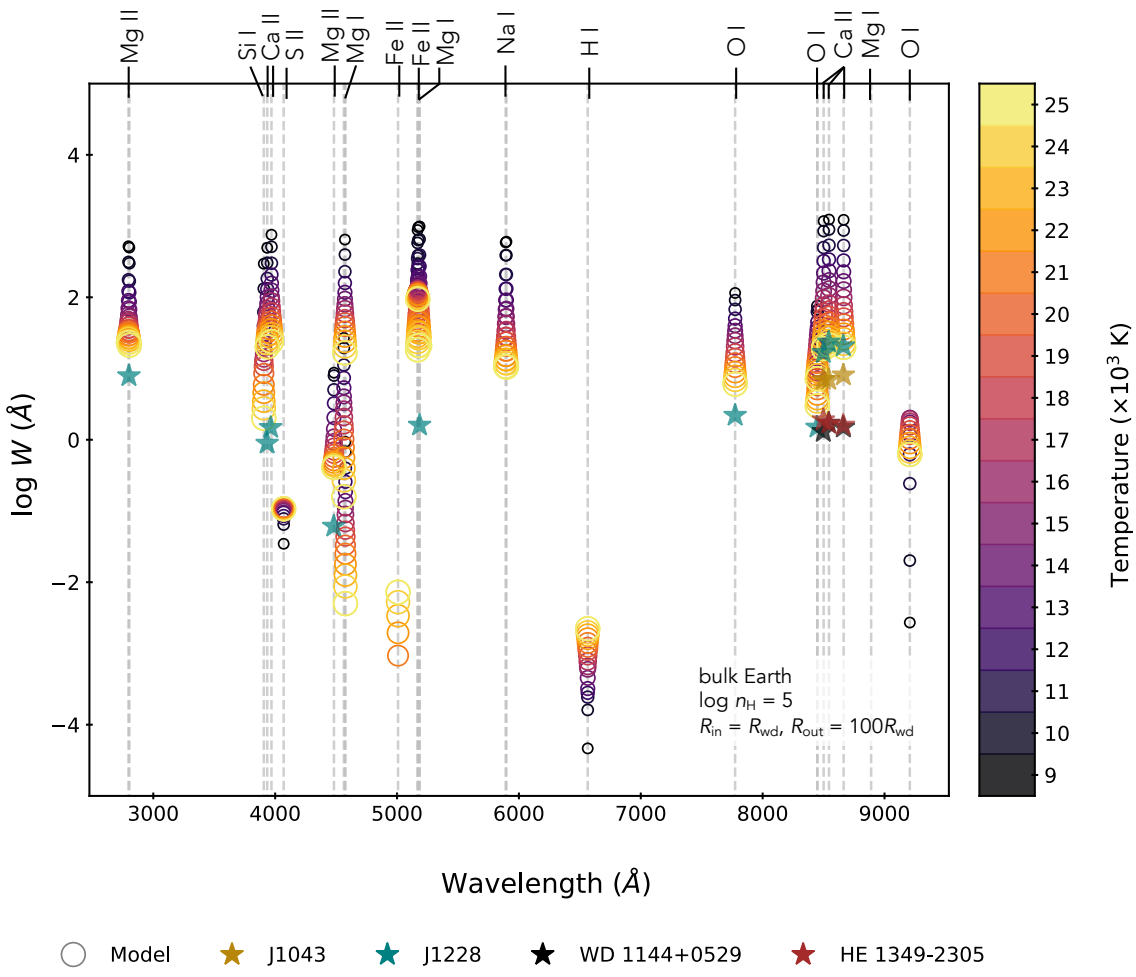

NOTE – Observations from left to right: the Mg II 2803 line is relatively well-matched, though the Ca II H and K lines at 3934 and 3969 A are too strong. The relative strength of the Mg II 4482 line is too large compared to the Mg II 2803 line. The Fe II 5170 A line is too strong. The H I (α) line at 6563 is weak and would likely not be detecatable. The O I lines at 7777 A (a triplet) and 8448 A appear at close to their expected strengths. The Ca II triplet is weak relative to the H & K pair. The stellar temperature increases from 9000K up to 25000K with increasing circle size.

Figure 5.17: Emission Line Equivalent Width Predictions - DA, Bulk Earth, depleted metals

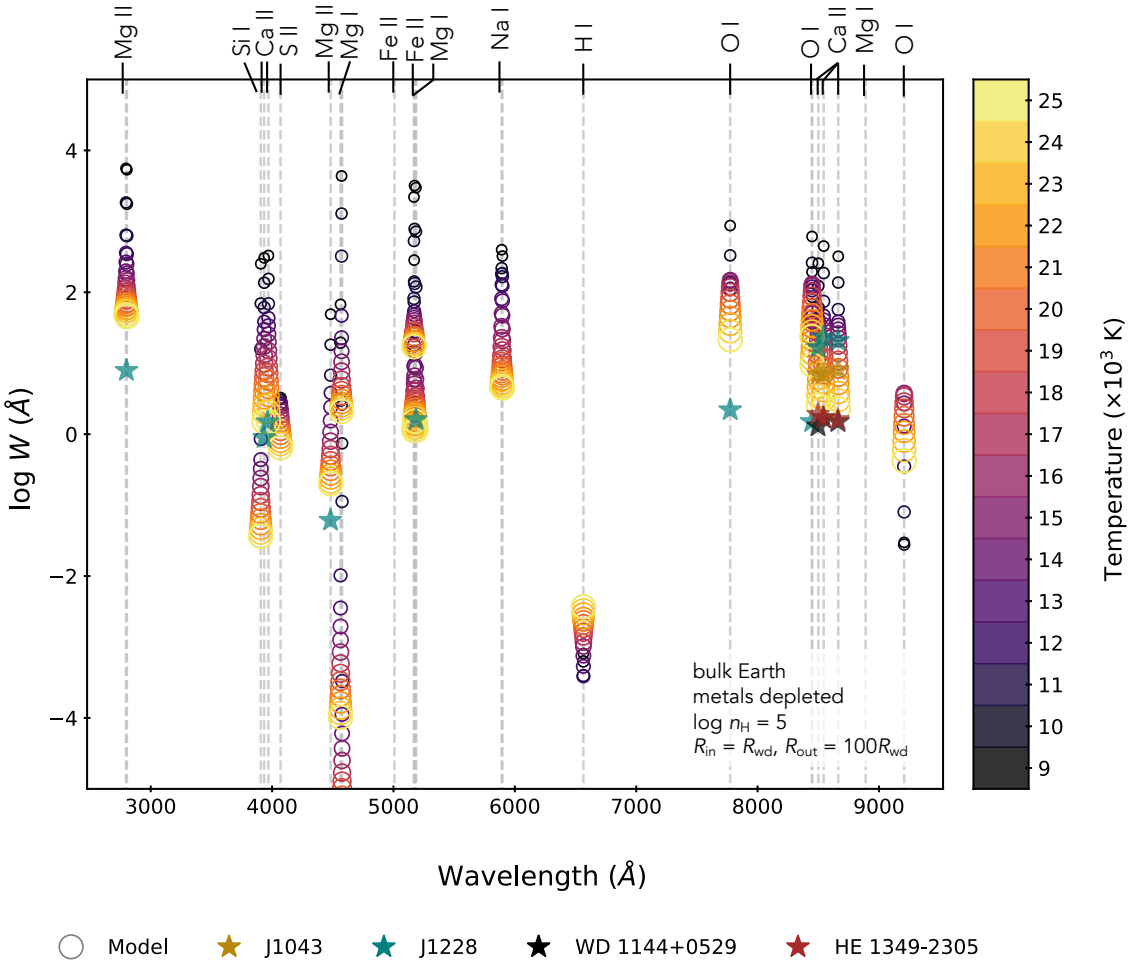

NOTE – Similar to Figure 5.16 except for slightly weaker Ca II H and K, and Fe II lines.

Table 3: Properties of the Model C-S Gas

	Mean CI Chondrite		Bulk Earth	
	regular	metal deplete	regular	metal deplete
H density [$\log n_{\rm H}/(\ {\rm cm}^3)$]	5	5	5	5
H abundance [$\log(El/H)$]	-5.5	-5.5	-3	-3
Mean density (g cm^{-3})	1.95×10^{-12}	9.38×10^{-13}	1.08×10^{-12}	4.52×10^{-11}
Mass (g)	$4.94 - 5.31 \times 10^{18}$	$2.37 - 2.55 \times 10^{18}$	$2.73 - 2.93 \times 10^{19}$	$1.18 - 1.23 \times 10^{20}$

NOTE— The properties of the Cloudy Models. The H density and H abundance are chosen inputs, while the mean density and mass are reported in the main output for each model run.

the line of sight by some angle i and the depth of absorption is decreased by a factor $\propto \exp(\tau/\cos i)$ (Zabot et al., 2009). The gas disk of J1228 is inclined by 70° (Farihi et al., 2012).

5.5 Discussion

5.5.1 Hydrogen Density

Most planetesimals accreted onto WDs are water-poor, so there should be very little hydrogen gas present around these systems, assuming a planetesimal origin (see section 5.3 of Jura & Young 2014, and references therein). The hydrogen number density $n_{\rm H}$ is a major unknown for WDs with C-S gas from water-poor planetsimals, yet Cloudy uses this parameter to set the conditions within a cloud. If a C-S gas spectrum has features due to hydrogen, one could probe the maximum amount of hydrogen present in the system by calculating the column density due to H, $N_{\rm H}$, and making the assumption that every H atom participates in the line transition (by populating an upper or lower state). As a comparison to other C-S disks, the maximum possible value of $N_{\rm H}$ for TW Hydrae is $\log(N_{\rm H\ I}/1\ {\rm cm}^2) \sim 19.75$ (Herczeg et al., 2004), and the H column density for β Pictoris is $\log(N_{\rm H}/1\ {\rm cm}^2) \sim 18.6 \pm 0.1$,

Figure 5.18: Continuum Prediction - DA, Chondrite, depleted metals

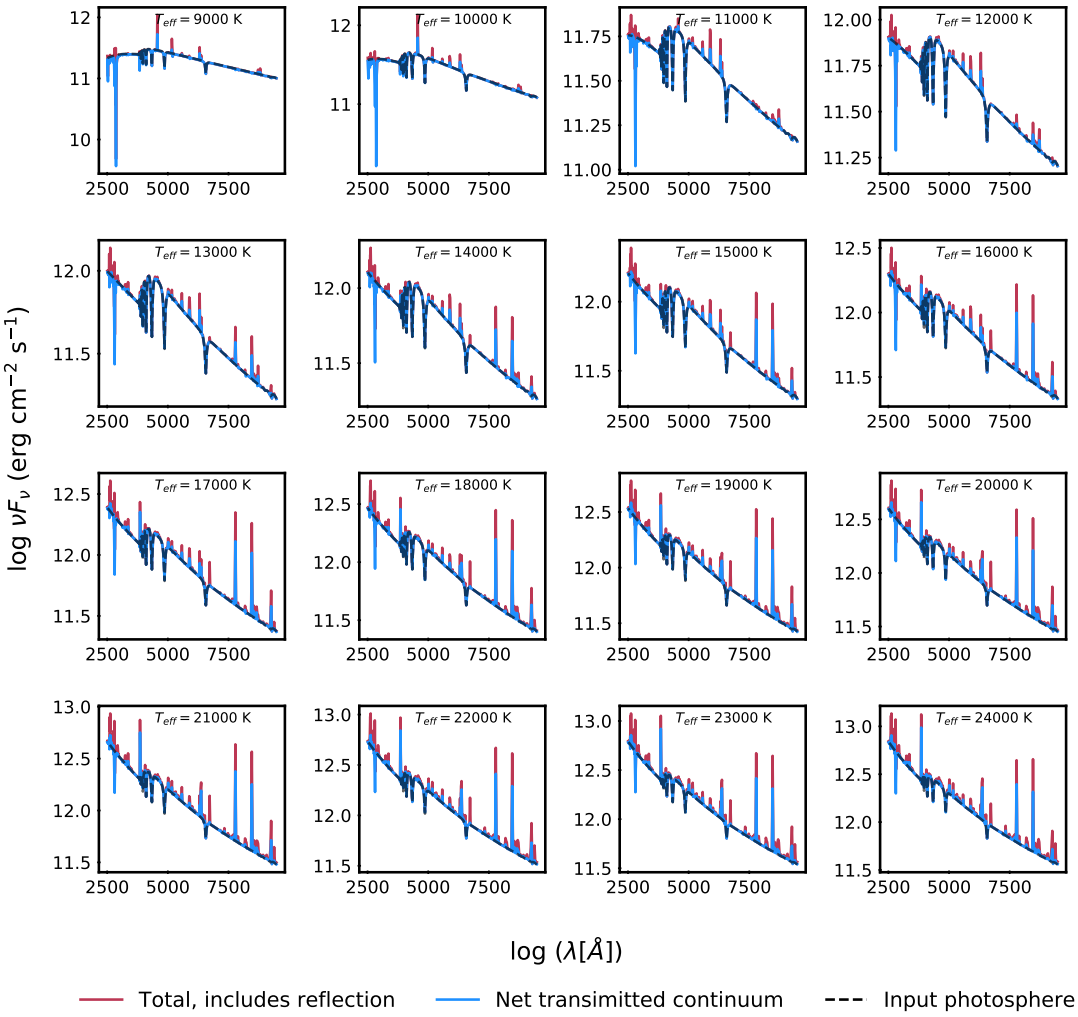

Note — Continuum predictions for a gas with a mean CI chondrite composition with depleted metals. The input model photosphere is shown with a dashed (- -) gray line, the total continuum is shown in red, and the net transmitted continuum is shown in blue. There is predicted absorption at 2803Å from Mg II.

Figure 5.19: Continuum Prediction - DA, Chondrite

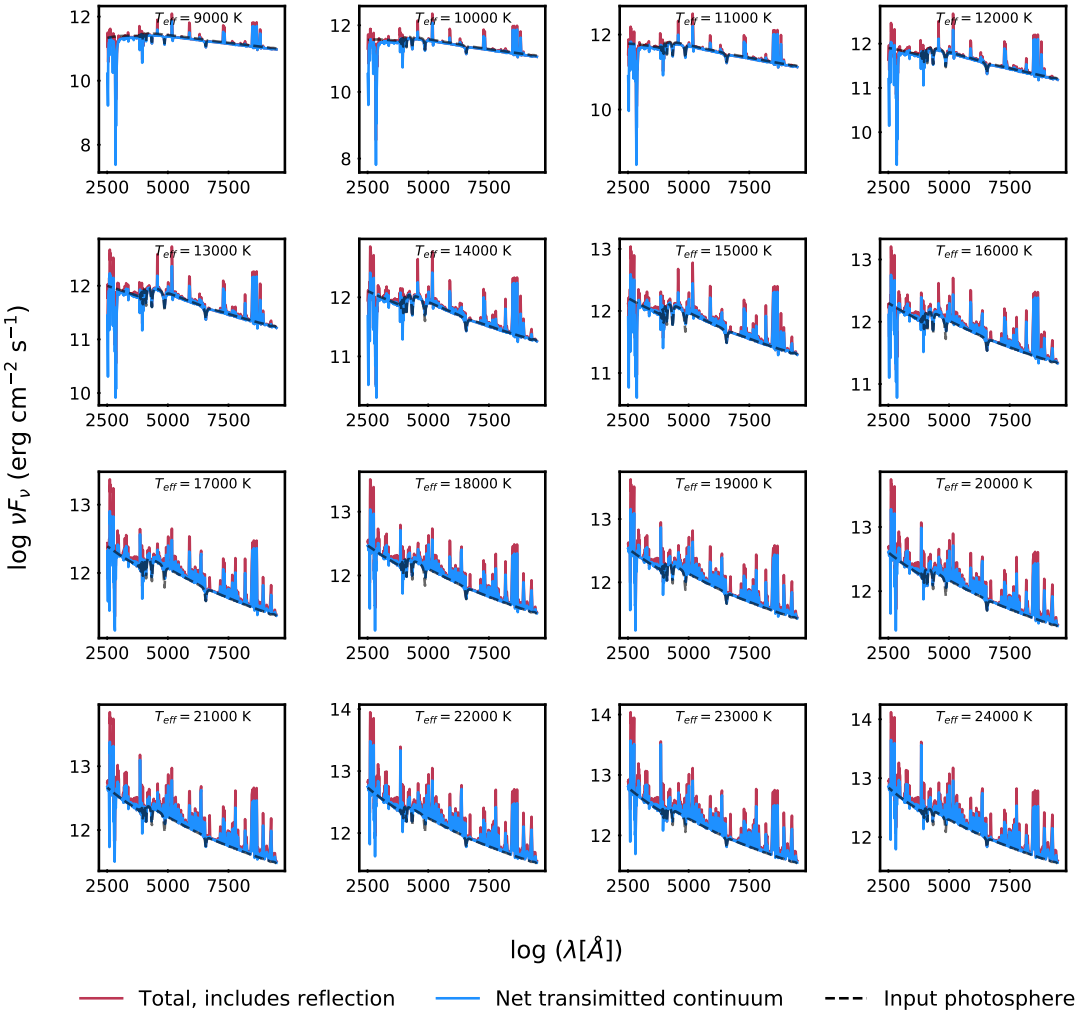

NOTE – Continuum predictions for a gas with a mean CI chondrite composition with depleted metals. The input model photosphere is shown with a dashed (- -) gray line, the total continuum is shown in red, and the net transmitted continuum is shown in blue. There is predicted absorption at 2803Å from Mg II and other metals in the optical and UV.

Figure 5.20: Continuum Prediction - DA, Bulk Earth, depleted metals

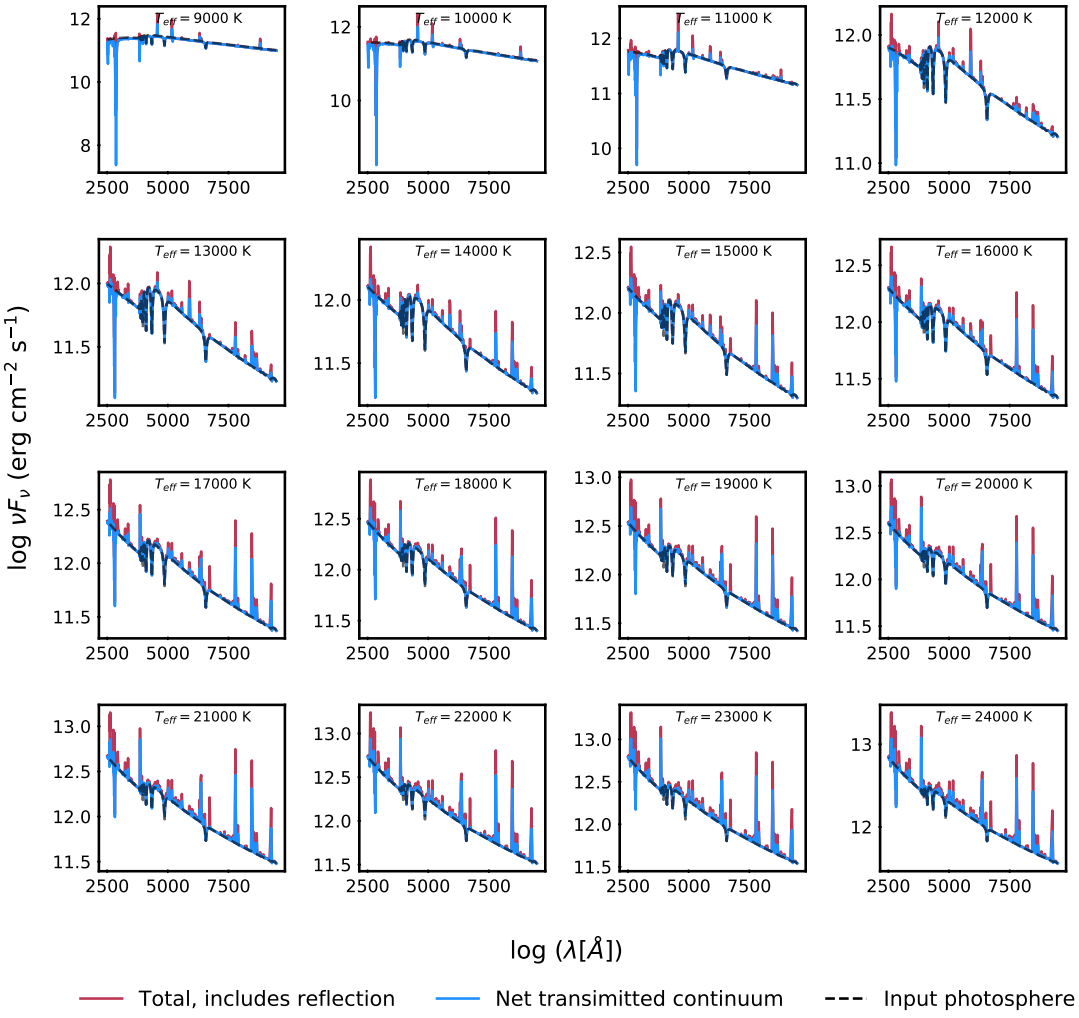

NOTE — Continuum predictions for a gas with a bulk Earth composition with depleted metals. The input model photosphere is shown with a dashed (- -) gray line, the total continuum is shown in red, and the net transmitted continuum is shown in blue. There is predicted absorption at 2803Å from Mg II.

Figure 5.21: Continuum Prediction - DA, Bulk Earth

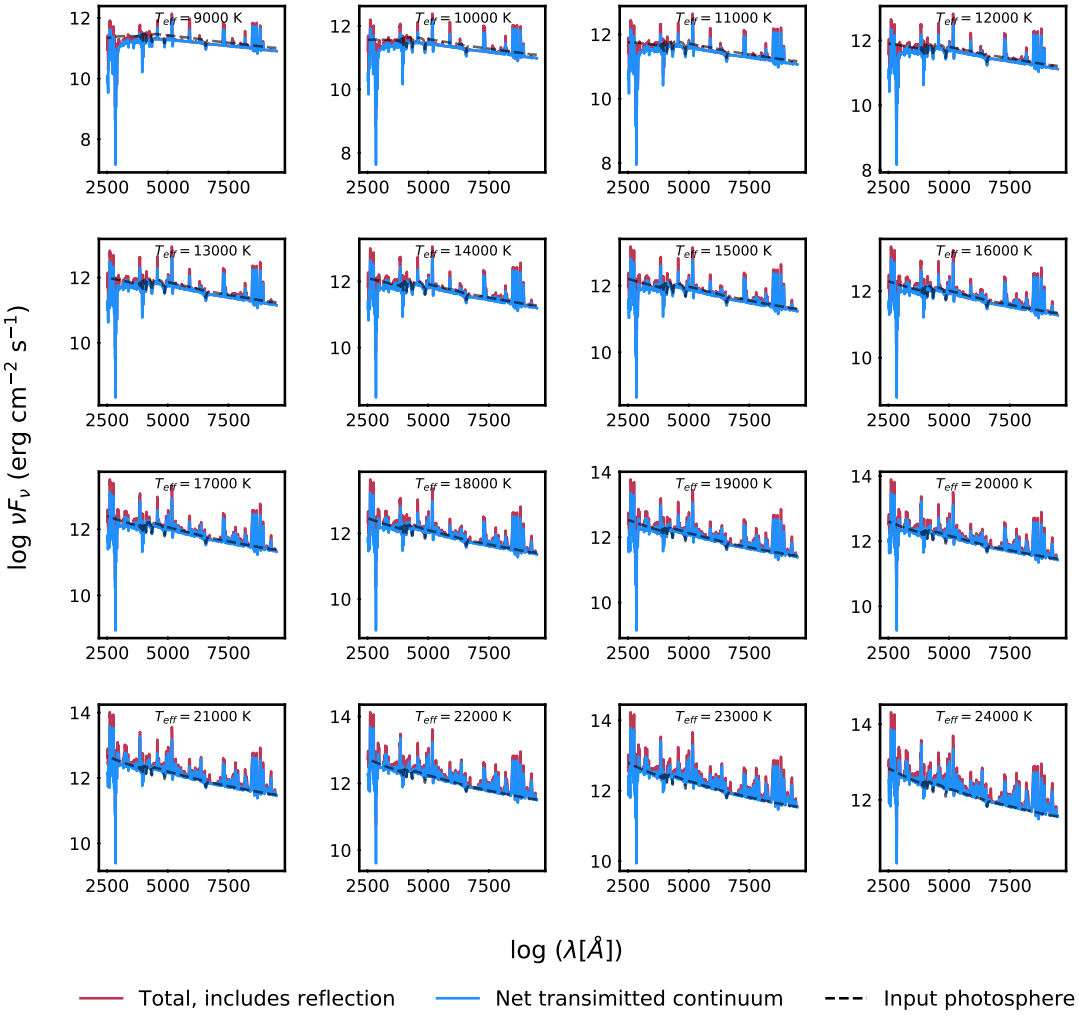

NOTE – Continuum predictions for a gas with a bulk Earth composition with depleted metals. The input model photosphere is shown with a dashed (- -) gray line, the total continuum is shown in red, and the net transmitted continuum is shown in blue. There is predicted absorption at 2803Å from Mg II and other metals in the optical and UV.

(Wilson et al., 2017).

Additionally, I have chosen to keep the hydrogen density constant with distance from the star, yet this is likely an oversimplification. Future steps with this work should include a more broad grid with $n_{\rm H}$ varying with distance.

5.5.2 Emission Line Ratios

The emissivity of a line depends on the population of the upper level n_u[10], the probability of the transition A , the electron density n_e and the temperature of the gas. The intensity of an emission line is determined by integrating the volume emissivity. In Figures 5.22 and 5.23, I show the volume emissivity for the same species for which I explore equivalent widths in Section 5.4.3. Similar trends are seen for the bulk Earth models.

The ratio of emissivities of two emission features provides insight on the temperature and density in a gaseous region and has been shown to be a powerful diagnostic tool (Draine, 2011). For these models, the hydrogen density, paired with the relative abundances of metals to hydrogen, affects the number of potential electrons in the gas, which affects the level populations of individual species. I show that the temperature profile of the C-S is not constant, so a dependence on temperature is linked to a dependence on the inner radius of the gas. The outer edge of the gas increases the amount of emitting material and also the number of potential interactions among atoms as light from the main source propagates through the

[10]The upper level population is usually more important for emission because it is the number of atoms just waiting to take a swan dive onto the couch of their ground state or lower level, releasing energy in the process.

Figure 5.22: Emissivity Profile - DA, Mean Chondrite, depleted metals

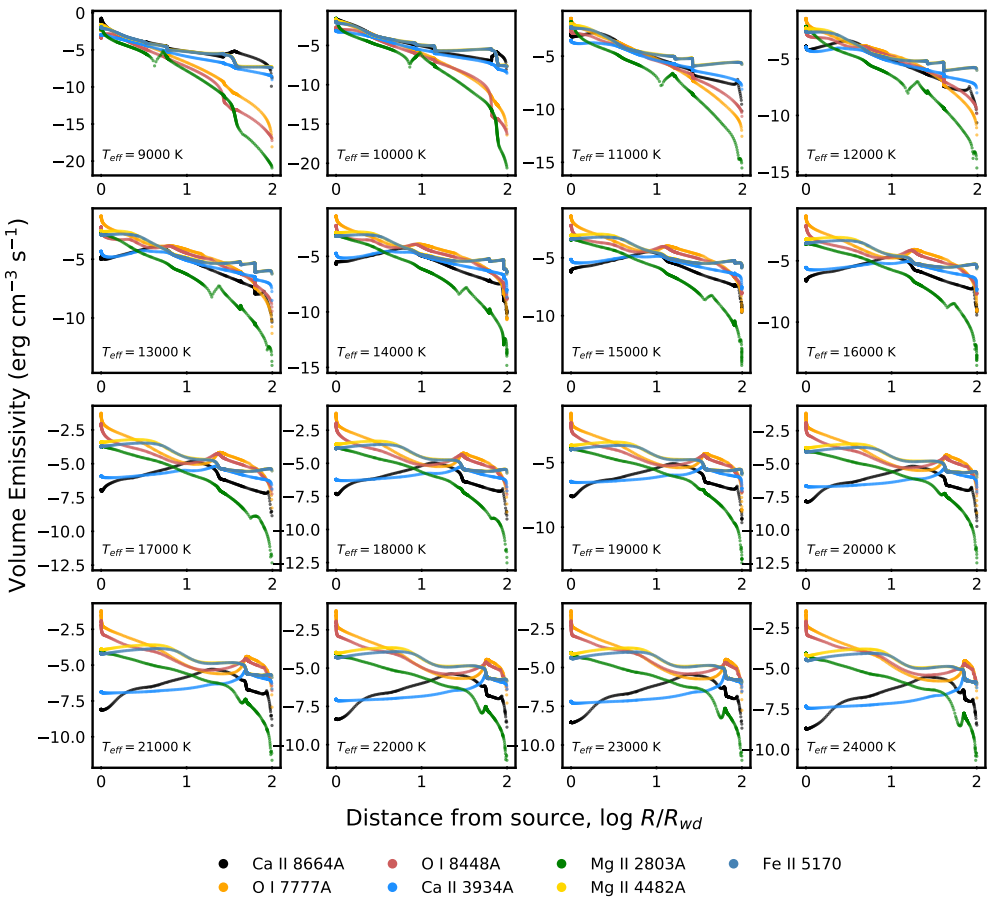

NOTE – The volume emissivity for Ca II, O I, Mg II, and Fe II species from a cloud with depleted metals. The hydrogen number density is $\log n_{\rm H} = 5$.

Figure 5.23: Emissivity Profile - DA, Mean Chondrite

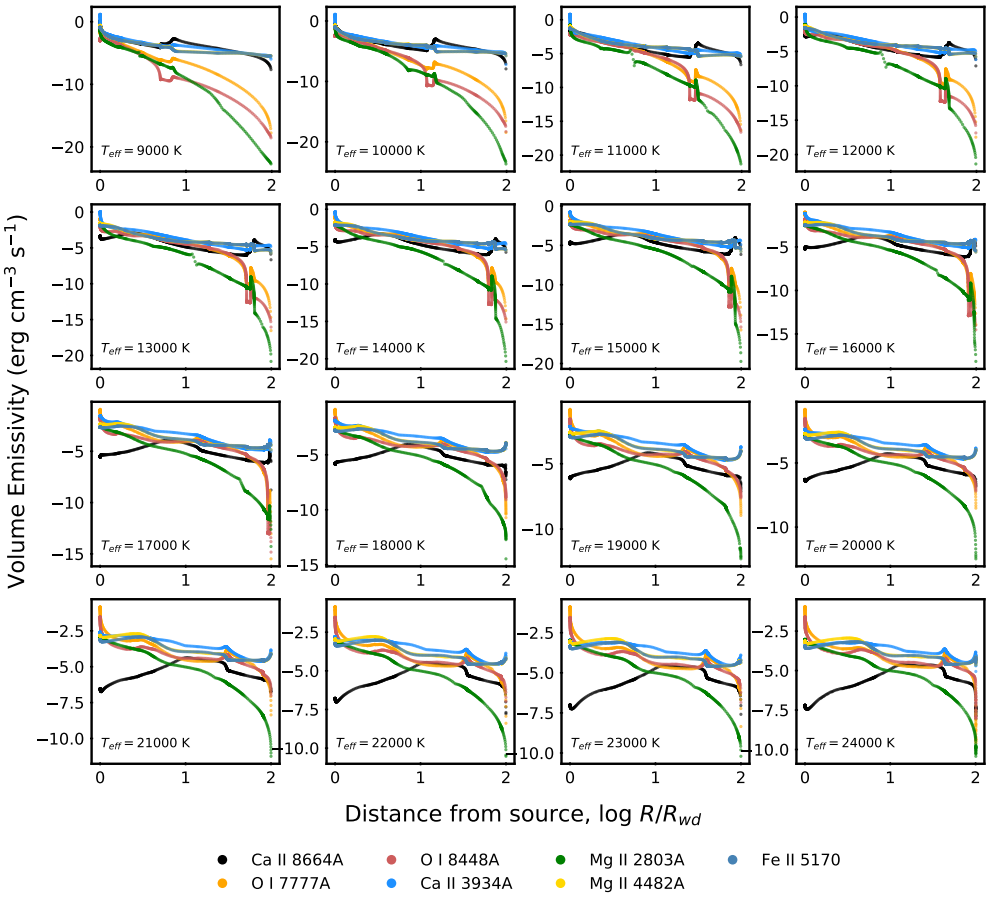

NOTE – The volume emissivity for Ca II, O I, Mg II, and Fe II species. The hydrogen number density is $\log n_{\rm H} = 5$.

cloud. These dependencies highlight how line ratios can provide useful information about the environments of WDs with C-S gas.

To investigate line strengths with the available data, I use ratios of the equivalent widths. Recall that the equivalent width, W can be expressed as

$$W = \lambda \frac{F_{\rm line}}{\lambda F_{\lambda,\rm cont}} \tag{5.4}$$

where λ is the line wavelength, $F_{\rm line}$ is the flux in the line [erg s^{-1} cm^{-2}, and $\lambda F_{\lambda,\rm cont}$ is the incident continuum level at the line [erg s^{-1} cm^{-2}]. Note that $\lambda F_{\lambda,\rm cont} = \nu F_{\nu,\rm cont}$. A ratio of equivalent widths W_1 and W_2 of lines with central wavelengths λ_1 and λ_2 would be

$$\frac{W_1}{W_2} = \frac{\lambda_1}{\lambda_2}\frac{\nu F_{\nu,2}}{\nu F_{\nu,1}}\frac{F_1}{F_2}, \tag{5.5}$$

where $\frac{F_1}{F_2}$ is the typical ratio I would care about. The method of using equivalent widths as a diagnostic tool was explored by Kobulnicky & Phillips (2003) to measure the metallicities of galaxies. They determined that for two flux calibrated lines I_1 and I_2, their equivalent width ratio is $\frac{I_1}{I_2} = \frac{W_1}{W_2}\alpha$, where α is now a factor to account for reddening and the difference in the attenuation of the emitting gas and the continuum light (Kobulnicky & Phillips, 2003).

I compare the ratios of the equivalent widths for Ca II, Mg I, and O I observed in the spectrum of J1228 to the ratios of the volume emissivity for the mean CI chondrite models as a function of distance from the star (see Figures 5.24 and 5.25). For the models, I am plotting the ratio of the volume emissivity [erg s^{-1} cm^{-3}],

which varies with distance. For the data, I am plotting $\frac{W_1}{W_2} \cdot \frac{\lambda_2}{\lambda_1}$, which is constant. I show the expected ratio with a dashed line in the same color for the species. The trends seen in these plots are also displayed in the plots with the equivalent widths, except now I can see if there are particular radii at which the observed line ratios occur. As an example, from the curves in Figures 5.24 and 5.25, it appears that the Mg would be better fit by the models if it were depleted in the gas at about $10 R_{\rm wd}$. A test of this hypothesis would be to run a grid keeping the density and composition constant and limit the gas to regions where species are populated at the observed ratios. I will test this hypothesis in future work. Based on the equivalent ratios, I conclude that J1228 is well fit by either metal depleted model. A more detailed exploration is needed.

The electron density with distance from the star is shown for the mean CI chondrite composition models in Figures 5.28 and 5.29. When the metals are depleted, the electron density is about 0.3 dex lower and the overall profile shape varies between the two models. Similar trends are seen for the bulk Earth models.

5.5.3 Compositions and Mass

I was able to reproduce the emission line strengths for systems that were previously found to be polluted by an object with a bulk Earth composition. What would deviations from these abundances mean? Jura & Young (2014) investigate abundance ratios of metals for seven externally polluted white dwarfs, chondrites, and nearby F and G stars. Rather than focus on individual systems (each modeled by

Figure 5.24: Line Ratios - DA, Mean Chondrite, depleted metals

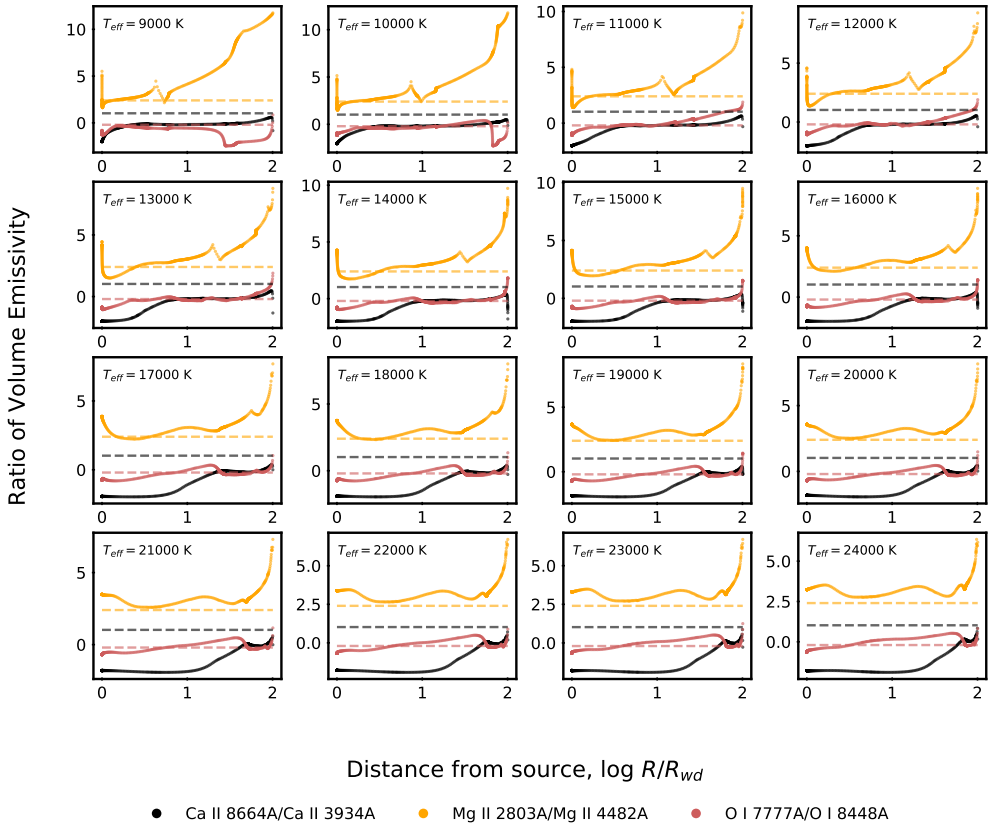

NOTE — Observed Ca II, Mg II, and O I equivalent width line ratios compared to emissivity line ratios for models with a mean CI chondrite composition (depleted metals), as a function of distance from the star. The observed ratios are calculated using the equivalent widths observed for SDSS J1228+1040, and are plotted with dashed lines. The model ratio is shown with the lines and vary over distance. The models over-predict the relative strengths of the Mg II lines toward the outer edge of the disk, and under-predict the strengths of the Ca II lines toward the inner disk, at higher temperatures. The models seem to match the O I ratio.

Figure 5.25: Line Ratios Comparison - DA, Mean Chondrite

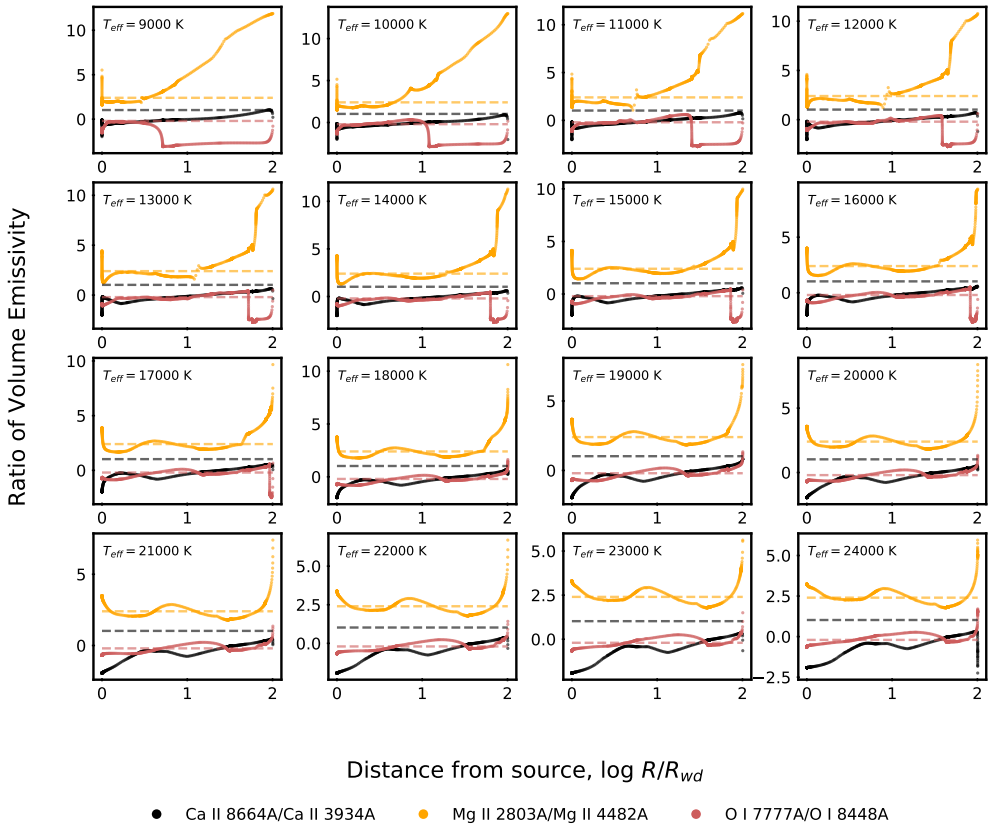

NOTE — Observed Ca II, Mg II, and O I equivalent width line ratios compared to emissivity line ratios for models with a mean CI chondrite composition, as a function of distance from the star. The observed ratios are calculated using the equivalent widths observed for SDSS J1228+1040, and are plotted with dashed lines. The model ratio is shown with the lines and vary over distance. The models over-predict the relative strengths of the Mg II lines toward the outer edge of the disk, and under-predict the strengths of the Ca II lines. The models seem to match the O I ratio.

Figure 5.26: Line Ratios - DA, Bulk Earth, depleted metals

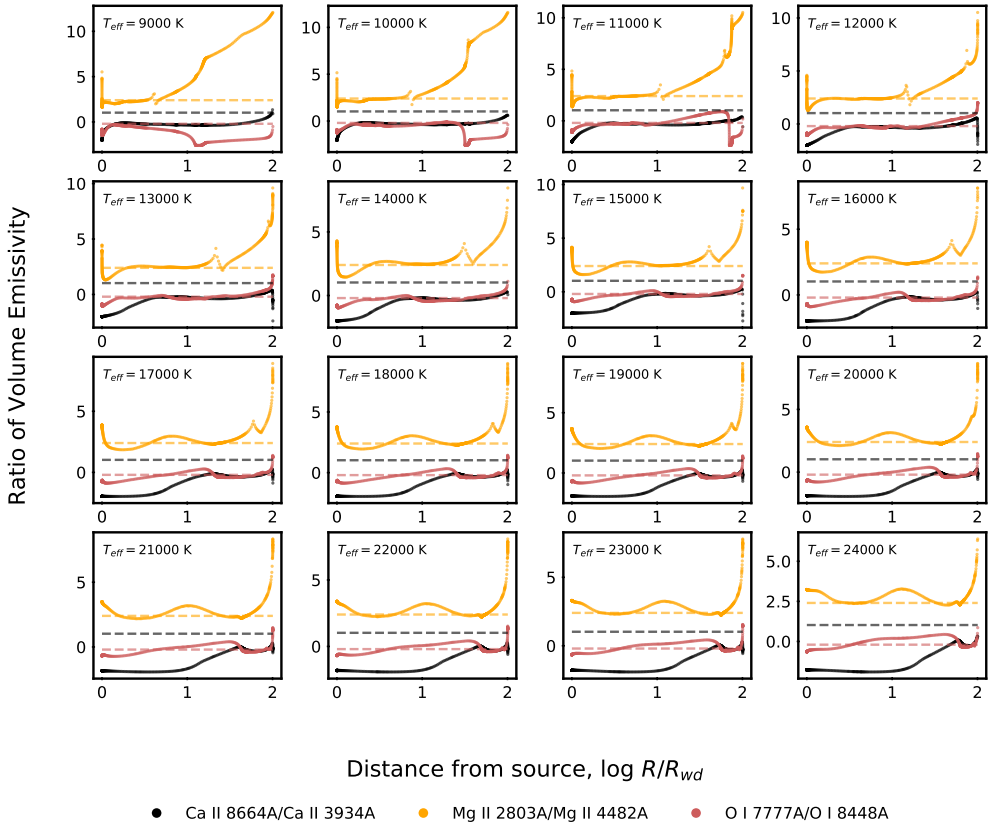

NOTE — Observed Ca II, Mg II, and O I equivalent width line ratios compared to emissivity line ratios for models with a bulk Earth composition (depleted metals), as a function of distance from the star. The observed ratios are calculated using the equivalent widths observed for SDSS J1228+1040, and are plotted with dashed lines. The model ratio is shown with the lines and vary over distance. The models over-predict the relative strengths of the Mg II lines toward the outer edge of the disk, and under-predict the strengths of the Ca II lines toward the inner disk, at higher temperatures. The models seem to match the O I ratio.

Figure 5.27: Line Ratios - DA, Bulk Earth

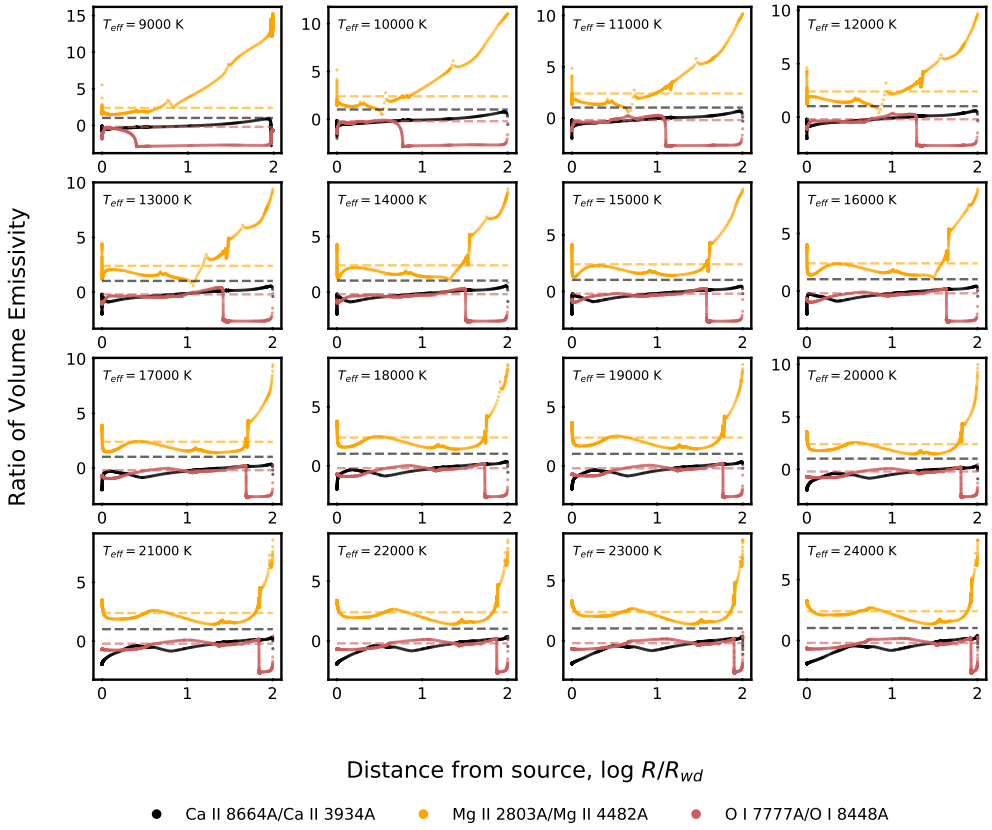

NOTE — Observed Ca II, Mg II, and O I equivalent width line ratios compared to emissivity line ratios for models with a bulk Earth composition, as a function of distance from the star. The observed ratios are calculated using the equivalent widths observed for SDSS J1228+1040, and are plotted with dashed lines. The model ratio is shown with the lines and vary over distance. The models over-predict the relative strengths of the Mg II lines toward the outer edge of the disk, and under-predict the strengths of the Ca II lines. The models seem to match the O I ratio in the inner disk, but there's a sharp drop in the volume emissivity ratio that occurs at increasingly larger radii.

Figure 5.28: Electron Density Profile - DA, Mean Chondrite

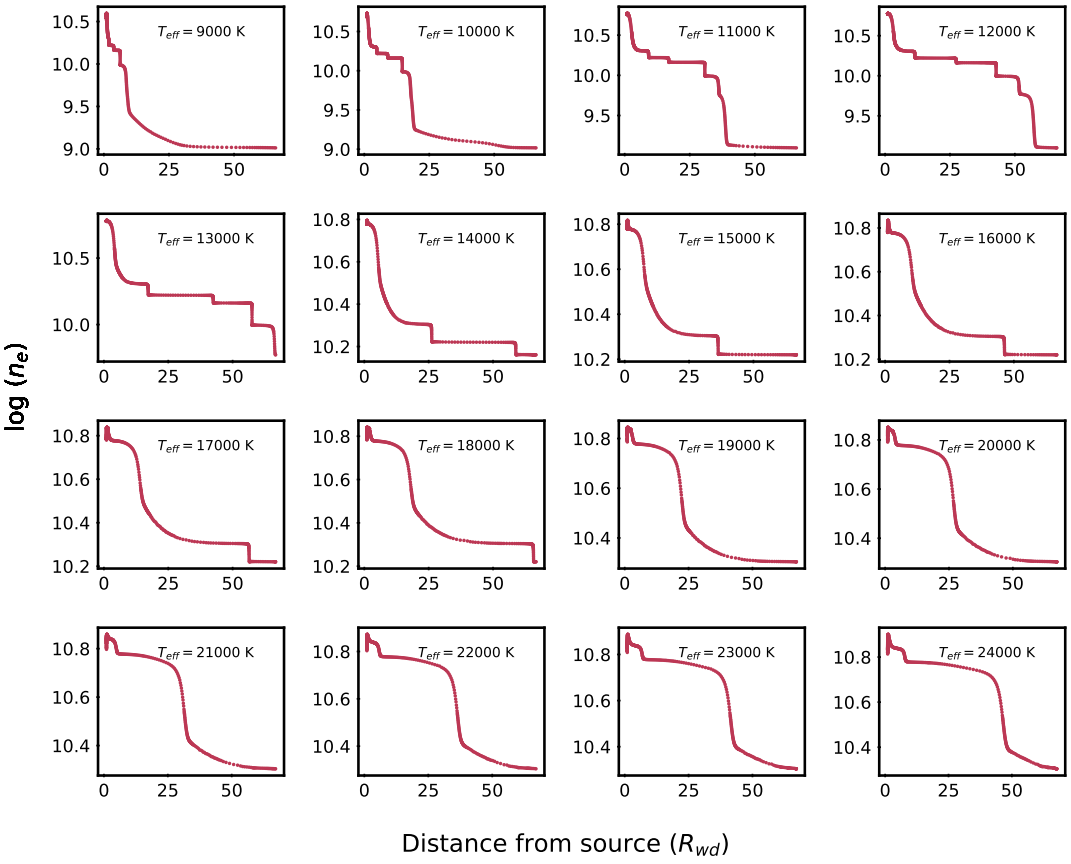

NOTE – The electron density profiles. The hydrogen number density is $\log n_{\mathrm{H}} = 5$.

Figure 5.29: Electron Density Profile - DA, Mean Chondrite, depleted metals

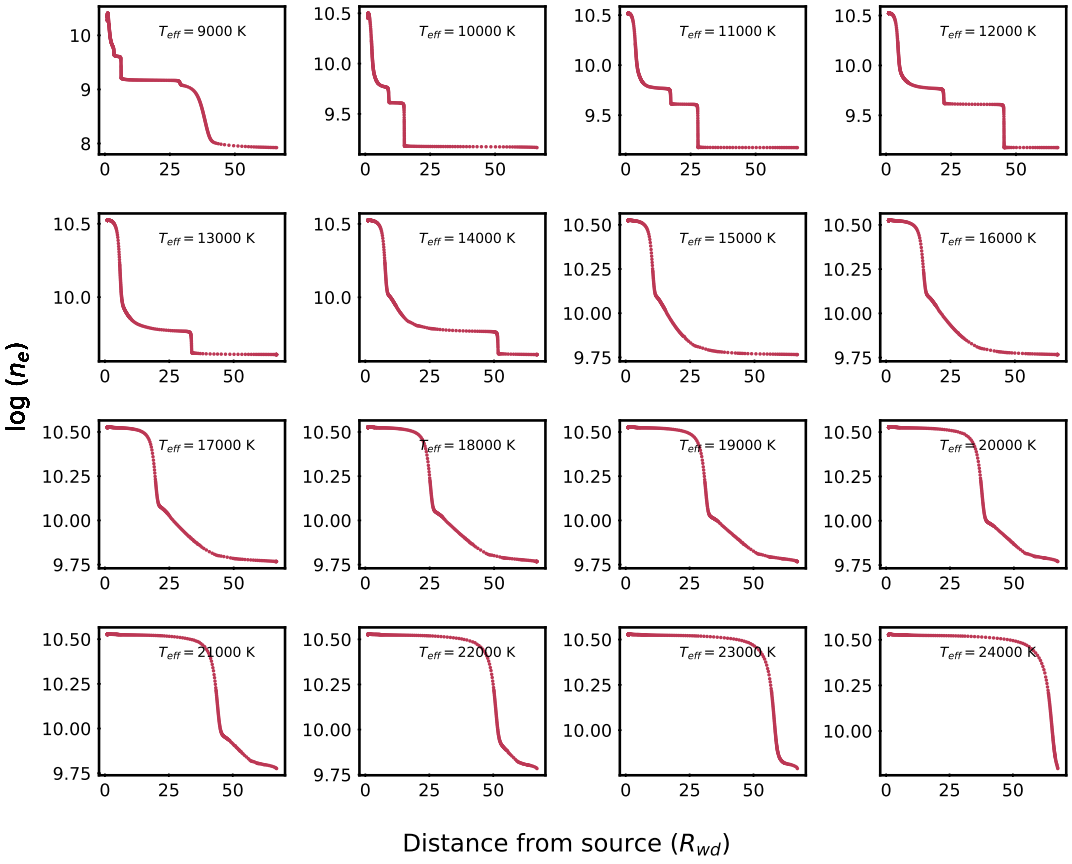

NOTE – The electron density profiles models with depleted metals. The hydrogen number density is $\log n_{\rm H} = 5$.

an individual group), they consider abundance *patterns* of potential parent bodies to investigate core and crust formation. Core formation is probed through the relative abundances of the siderophile elements Cr, Mn, and Ni to Fe. Crust formation is probed through the relative abundances of the refractory lithophile elements Al, Ca, and Ti to Si. The logic put forth in Jura & Young (2014) is that if Fe-rich cores form, then there should exist Fe-poor crusts, possibly rich in Al and Si, as seen in the Solar System. Their comparison lends support to the idea that differentiation has occurred in the planetesimals similarly to what is seen among Solar System objects.

One open question is why the Ca abundance tends to be high for many of the polluted WDs. While I do not present an answer to this question, the models for DA white dwarfs do tend to produce strong Ca features at most temperatures and hydrogen densities. It is possible that the conditions within the C-S gas contribute to this observed trend.

5.5.4 Output Spectrum and Line Profiles

One of the main outputs for a Cloudy model is the net transmitted spectrum, which results when the ionizing radiation passes through the cloud before reaching the observer. This model spectrum is useful for quickly checking the validity of a set of input parameters (investigating whether other absorption or emission features are produced), and to predict a spectrum ranging from the far UV to submillimeter. The profiles are thermally broadened, but the absorption lines do not have sufficient

resolution to convolve with a Gaussian. All of the absorption features that have been investigated are demarcated by just 3 points, making the profile a triangular shape. Additionally, it is currently not possible to provide a velocity field to Cloudy to produce double peaked lines and broad absorption profiles. Creating these profiles must be done after the fact using a code of one's choice.

Without considering bulk motion, the absorption line profile can be constructed by taking the convolution of (1) a Voigt line profile broadened due to Maxwellian distributed velocities and a gas temperature determined by Cloudy and (2) the instrumental resolving power. The line profile is approximated using a series expansion as $\phi(x) \propto \exp(-x^2)+a/(\pi^{1/2}x^2)+2a/(\pi^{3/4}x^4)$, where $x = (\nu-\nu_0)/\Delta\nu_{\rm Dopp}$ and $\Delta\nu_{\rm Dopp}$ is the FWHM of the line. The output intensity, I is of the form $I = I_{\rm in}\exp[-\tau\phi(x)]$, where τ is the optical depth at line center. $\Delta\nu_{\rm Dopp}$ depends heavily on the temperature and velocity structure.

To model bulk motion, the temperature, optical depth (or mass density), chemical composition, and velocity need to be defined for each cell in a 2- or 3-D grid containing the gas. The output intensity, I still has the form $I = I_{\rm in}\exp[-\tau\phi(x)]$, except now the velocity is the Keplerian orbital velocity defined in each cell. The profile is the sum of all filled cells.

For the emission lines, the double peaked line profile produced by an accretion disk is described by Horne & Marsh (1986). The continuum-subtracted line intensity from the emission layer is give by their Equation 22:

$$I_\nu = I_\nu^B \exp(-\tau_c)[\exp(-\tau_\nu) - 1] + S_L \exp(-\tau_c)[1 - \exp(-\tau_\nu)] \qquad (5.6)$$

where I_ν^B is the intensity of the background radiation, τ_c and τ_ν are continuum and line optical depths, and S_L is the line source function in the emission layer. The local emission line profile is given by the term $S_L[1 - \exp(-\tau_\nu)]$. The bulk motion appears in the line optical depth term, $\tau_n u$ (Equation 18, Horne & Marsh 1986),

$$\tau_\nu = \frac{W}{\cos i} \frac{1}{\sqrt{2\pi}\Delta\nu} \exp\left[-\frac{1}{2}\left\{\frac{\nu - \nu_D(0)}{\Delta\nu}\right\}^2\right], \tag{5.7}$$

where W is the equivalent width, i is the inclination of the disk relative to the observer's line-of-sight, $\nu_D(0)$ is the Doppler-shifted frequency corresponding to the orbit velocity of material at the midpoint of the emission layer. For material orbiting an object with mass M at a radius R and an angle θ relative to the line-of-sight, the frequency of the observed frequency relative to the rest frequency ν_0 is given by the local Doppler frequency, ν_D,

$$\nu_D = \nu_0 \left[1 - \left(\frac{GM}{Rc^2}\right)^{1/2} \sin i \sin\theta\right]. \tag{5.8}$$

5.6 Known Issues

Here, I summarize known issues with the grid of models and my methodology. First, for the models that produce emission lines at the observed strengths, there are also deep absorption lines that should be observed, but are not. This could be due to the geometry of the C-S disk, but I need to run additional models to in investigate this trend.

The choice to include the bulk Earth as a potential composition is motivated by observations and modeling of existing WDs. However, does this really make sense given that we saw in Chapter 3 that material within ~ 3 au will be be obliterated due to the evolution of the host star? I also mention the importance of grains but choose to exclude them. These results might change with grains included. I will focus on this in future work.

A number sources are best fit when the metals deplete command is used. This command is essentially changing the gas phase abundance from being either bulk Earth or mean CI chondrite. However, I chose to explore these models because dust is expected to be the source of the gas for H-poor polluting bodies. If certain elements would be more likely to be bound than others, then this command is one way to explore that scenario.

I have found that it is difficult to constrain the hydrogen density when there are no hydrogen features and few spectral features present (see Chapter 4). The main method I use to constrain the density when modeling individual systems is to determine the minimum strength a feature would need to have in order to be statistically significant and ensure that no features are detectable.

The spatial extent of a C-S disk can be constrained by modeling the width of and absorption or emission line profile. From the line ratios, I find that it might be possible to constrain the radial locations of individual species and compare those locations to the expected sublimation radii.

5.7 Conclusions

I use the photoionization code Cloudy to create a grid of models of C-S gas around white dwarfs with a DA spectral type, extending the work of Chapter 4. I have generated sets of models of bulk Earth and mean CI chondrite gas around WDs with temperatures ranging from 9000 K to 24,000 K. These models allow for a number of physical properties of the C-S gas to be probed with distance from the stars including the temperature, optical depths, electron density, and line emissivity.

Previous abundance analyses have had to alter their models in order to account for the presence of strong Si IV lines ($\sim$ 1394 and 1402Å) in the spectra of some WDs (Fortin-Archambault et al., 2020; Gänsicke et al., 2012). Gänsicke et al. (2012) suggest that the Si IV lines arise from gas close to the WDs. I show that Si IV absorption occurs for stars with temperatures greater than $\sim 14,000$ K (depending on the composition). I also provide support for the idea that the gas must be close to the WD surface, given the models presented in this work, which begin at the WD surface.

Additionally, I found for all models that the temperature profiles follow a power law and thus, should not be modeled as isothermal. I compared the equivalent widths of my models and find relative agreement with the strengths of lines for both a bulk Earth and mean CI chondrite composition. The ratios of equivalent widths for species of Mg II and Ca II can be used as a diagnostic tool, and suggests that these transitions have a radial, and therefore, temperature dependence. These grids will be expanded and made available to the public in the near future.

Chapter 6: Conclusions and Future Work

This thesis explored case studies of circumstellar gas and dust on and off the main sequence. For the debris disks around main sequence solar analogues explored in Chapter 1, we find that they are consistent with scaled-up versions of the Solar system's Kuiper belt. The inner radii of the debris belts tend to be a factor of a few larger than predicted from blackbody equilibrium calculations alone, implying that the disks contain small grains produced in a collisional cascade.

Moving off the main sequence in Chapter 3, we characterize the dust around a sample of 20 post-MS stars with infrared excesses. We determine the basic properties of the dust, finding that most of the systems have micron-sized grains at temperatures around 100K. We report the spectral indices of the long wavelength emission and find evidence of grain growth. There is evidence of current planetary engulfment and mass loss for a number of the targets in our sample. The systems that show evidence of planetary engulfment and spectral indices approaching the black body value can potentially be used to constrain the timescale for grain growth/destruction in the environment of a post-MS star. The existence of white dwarf stars with circumstellar disks containing gas with a bulk Earth composition requires that rocky bodies survive stellar evolution.

In Chapter 4, we outline how to use the Cloudy radiative transfer code to model C-S gas viewed in absorption around WD 1124-293 to characterize the circumstellar gas around a polluted WD. We create a grid of models to explore the abundances of elements from He to Zn relative to hydrogen, and obtain line optical depths, species column densities, and the temperature profile through the gas disk. With these models, we place constraints on the potential masses and abundances that could result in a spectrum dominated by calcium species for WD 1124-293, find that the C-S gas is not isothermal, and show that the Cloudy microphysics code, which is typically used to model active galactic nuclei and HII regions, can also be used to model C-S gas absorption features of polluted white dwarfs.

In Chapter 5, we generated sets of models of bulk Earth and mean CI chondrite gas around WDs with temperatures ranging from 9000 K to 24,000 K, expanding the work of Chapter 4. The models allow for a number of physical properties of the C-S gas to be probed with distance from the stars including the temperature, optical depths, electron density, and line emissivity. We show that Si IV absorption occurs for stars with temperatures greater than 14,000 K and that the temperature profiles follow a power law, and should not be modeled as isothermal. These grids will be expanded and made available to the public in the near future.

6.1 Future Work

6.1.1 Need for interferometric mm-wavelength observations

Millimeter-wavelength observations are highly complementary to observations at shorter wavelengths. Infrared observations probe ∼10- to ∼100μm-sized grains and can provide direct compositional information through emission features. Detecting CO emission would provide kinematic information for the material and allow a gas mass to be estimated. Millimeter interferometry traces the thermally emitting, gravitationally interacting mass in a system while also revealing sharp structures if present. PDS 355 has dust at a broad range of spatial scales (spanning 2 dex), and would require an interferometer to map those features. Interferometry is also needed to resolve the dust and any molecular gas around these stars. Resolving the potential disk (or shell) at (sub)millimeter wavelengths breaks the degeneracy between particle size and distance from the star. Small, inefficiently emitting, hot grains at large distances from the star can resemble cooler, efficiently emitting grains closer to the star. A complete model of circumstellar material should match all of the available data, including images, gas masses, and the thermal spectral energy distribution (SED).

6.1.2 Models of IRAS 12327

Several authors have previously modeled the C-S environments of AGB stars. To thoroughly explore the gas, we could use the photoionization code Cloudy to

create a model of IRAS 12327. The model would allow for an exploration of both molecules and dust (with build in PAH grain information) in the C-S environment of this evolved star. Cloudy could also possibly be applied to the other systems to explore their chemical abudances. Comparison with a high-resolution spectrum would be useful. Another code that could be used to explore the dust is the code Dusty.

6.1.3 Isochrone Fitting

For the isochrone exploration, we do not complete a minimization. A next step would be to set up a χ-squared minimization between the observed parameters and the individual tracks. Part of this analysis could include using different filters, and also letting A_V be a free parameter. Alternatively, we could attempt to determine a local A_V by observing a different star along the same line of sight at a distance between Earth and the target.

6.1.4 Improved SED Fitting

We can improve the SED fitting by performing a detailed study of the grains and their expected temperatures. The equilibrium temperature of a grain requires that the power absorbed from the star, $P_{\rm in}$ be equal to the thermal power the grain reradiates, $P_{\rm out}$. We address temperature of the grain population in the following way: for each tabulated set of optical constants for a particular sized grain of some composition, we calculate the temperature the grain would have at some distance

from the star, effectively creating a temperature lookup table for different sized grains around each star. Once the temperature of a grain at some distance from the star is known, the grain temperature, $T_{\rm gr}$ then depends on the distance from the star

$$T_{\rm gr} = T_\star \left(\frac{2D_{\rm gr}}{R_\star} \right)^{-1/2}, \tag{6.1}$$

scaling as $1/D_{\rm gr}^{1/2}$. In our fitting process, for some chosen grain size and distance from the star, we first calculate the temperature by interpolating the table to the chosen grain size, obtaining the temperature of a grain at a fixed distance. We then scale that temperature to some (randomly, i.e. through MCMC) chosen distance, and calculate the temperature there. We use this temperature to determine the flux density from the dust. This calculation assumes that the dust is optically thin, though this is not necessarily the case for each system. To determine the suitability of the model to the available data, we should use an affine-invariant Monte Carlo Markov Chain (MCMC) algorithm to explore the n-dimensional parameter space that exists for a star with n free parameters. We would use version 2.0/3.0 (depending on access) of `emcee` (Foreman-Mackey et al., 2013) to implement this algorithm for IRAS 12327.

6.1.5 Cloudy on and off the Main Sequence

SDSS J0914 is unique in being the only WD in this sample that does not show emission features at the Ca II triplet. Gänsicke et al. (2019) describe the C-S gas as arising from the disruption of a Jupiter-like planet. J0914 also has emission at the

Hα 6536Å line, a rare feature for WDs with C-S gas. The detection of Hα allows for the hydrogen number density to be better constrained. Exploring the hydrogen density in future models will allow for a more robust determination of $n_{\rm H}$.

A natural extension of this work is to look back toward the main sequence. Cloudy has been used to model the molecules around an AGB star, making IRAS 12327-239 that natural first target. It might also be possible to apply this code to gas-rich protoplanetary and transition disks.

We should also include grains to make these models more realistic. In the case of WD 1145+017, the tidal disruption is ongoing and producing grains though a collisional cascade. The light passing through the gas and dust is likely interacting with grains, so they should be included for a model of that system.

Appendix A: Abundances

Table comments: The abundances relative to hydrogen by number for the sun, chondrites (a mean), the (bulk) Earth, and the ISM. References for the values follow. The Solar and ISM values are from [1]the Cloudy Hazy 1 manual–we provide individual values. For the solar abundances, values without a subscript are from Grevesse & Sauval (1998). Others are [a]Allende Prieto et al. (2002)[a], [b]Holweger (2001), [c]Allende Prieto et al. (2001), and [d]Grevesse et al. (2010). The ISM abundances are described in the Hazy 1 manual as an average from Cowie and Songaila (1986) (warm and cold phases of the ISM) together with Savage and Sembach, 1996 (warm and cool phases towards η Oph). Exceptions to these averaged abundances are O, [g]Meyer et al. (1998), and F, [h]Snow et al. (2007).

Table A.1: Abundances Relative to Hydrogen, log ($N_{\rm El}/N_{\rm H}$)

El	Solar[1]	Chondrite[2]	Bulk Earth[3]	ISM[1]
H	0.00	0.00	0.00	0.00
He	-1.00[1]	-6.96	-8.38	-1.01
Li	-8.69	-5.00	-2.05	-10.27
Be	-10.58	-6.87	-3.86	-20.00
B	-9.21	-5.50	-3.19	-10.05
C	-3.61[a]	-0.85	0.58	-3.60
N	-4.07[b]	-2.00	-2.61	-4.10
O	-3.31[c]	0.14	2.74	-3.50[g]
F	-7.52[d]	-3.82	-2.14	-7.70[h]
Ne	-4.00[b]	-9.37	-7.84	-3.91
Na	-5.67	-1.98	0.46	-6.50
Mg	-4.46[c]	-0.72	2.25	-4.90
Al	-5.53	-1.82	1.18	-7.10
Si	-4.46[c]	-0.74	2.22	-5.50
P	-6.50	-2.85	-0.22	-6.80
S	-4.74	-1.09	0.59	-4.49
Cl	-6.72	-3.02	-2.12	-7.00
Ar	-5.60	-8.76	-5.13	-5.55
K	-6.88	-3.19	-0.93	-7.96
Ca	-5.64	-1.96	1.04	-9.39
Sc	-8.83	-5.21	-2.22	-20.00
Ti	-6.98	-3.36	-0.36	-9.24
V	-8.00	-4.28	-1.31	-10.00
Cr	-6.33	-2.62	0.34	-8.00
Mn	-6.54	-2.78	-0.16	-7.64
Fe	-4.55[c]	-0.80	2.14	-6.20
Co	-7.08	-3.39	-0.43	-9.00
Ni	-5.75	-2.06	0.89	-7.74
Cu	-7.79	-4.02	-1.56	-8.82
Zn	-7.40	-3.64	-2.00	-7.70

NOTE — The abundances relative to hydrogen by number for the sun, chondrites (a mean), the (bulk) Earth, and the ISM. References: [1]the Cloudy Hazy 1 manual. For the solar abundances, values without a subscript are from Grevesse & Sauval (1998). Others are [a]Allende Prieto et al. (2002)[a] [b]Holweger (2001), [c]Allende Prieto et al. (2001), and [d]Grevesse et al. (2010). The ISM abundances are described in the Hazy 1 manual as an average from Cowie and Songaila (1986) (warm and cold phases of the ISM) together with Savage and Sembach, 1996 (warm and cool phases towards η Oph). Exceptions to these averaged abundances are O[g]Meyer et al. (1998) and F[h]Snow et al. (2007).

Table A.2: Metal Depletion Factors

El	Factor	Reference
He	1.0	noble gas
Li	0.16	White, 1986
Be	0.6	York et al., 1982
B	0.13	Federman et al., 1993
C	0.4	
N	1.0	
O	0.6	
F	0.3	Snow and York, 1981
Ne	1.0	noble gas
Na	0.2	
Mg	0.2	
Al	0.01	
Si	0.03	
P	0.25	Cardelli et al., 1991
S	1.0	
Cl	0.4	
Ar	1.0	noble gas
K	0.3	Chaffee and White, 1982
Ca	1.0×10^{-4}	
Sc	5.0×10^{-3}	Snow and Dodgen, 1980
Ti	8.0×10^{-3}	Crinklaw et al., 1994
V	6.0×10^{-3}	Cardelli, 1994
Cr	6.0×10^{-3}	Cardelli et al., 1991
Mn	5.0×10^{-2}	Cardelli et al., 1991
Fe	1.0×10^{-2}	
Co	1.0×10^{-2}	
Ni	1.0×10^{-2}	
Cu	1.0×10^{-1}	Cardelli et al., 1991
Zn	2.5×10^{-1}	Cardelli et al., 1991

NOTE — This table is reproduced from the Hazy 1 manual. The list of abundances is known to be incomplete.

Appendix B: Facilities and Software used in this Thesis

1. Cloudy (ASCL:9910.001)

   Calculations in Ch. 5 were performed with version 17.00 of Cloudy, last described by Ferland et al. (2017).[1]

2. White Dwarf Database (MWDD)

   This work made use of the Montreal White Dwarf Database (MWDD), which was supported in part by the NSERC Canada[2] *and by the Fund FRQ-NT (Québec)*[3]*. For more, see "The Montreal White Dwarf Database: a Tool for the Community".*

3. SIMBAD

   This research has made use of the SIMBAD database, operated at CDS, Strasbourg, France. [4]

4. Scipy

   This dissertation made use of the `curvefit` *package of scipy* [5]

5. MAKEE

[1] `https://www.nublado.org/`
[2] `http://www.nserc-crsng.gc.ca/index_eng.asp`
[3] `http://www.frqnt.gouv.qc.ca/en/accueil`
[4] 2000,A&AS,143,9 , "The SIMBAD astronomical database", Wenger et al.
[5] `https://www.scipy.org/citing.html`

MAKEE (MAuna Kea Echelle Extraction): `https://www2.keck.hawaii.edu/inst/common/makeewww/`

6. emcee

   `emcee` is free software made available under the MIT License (Foreman-Mackey et al. (2013))

7. yorp, the UMD campus computer server

   Analysis was performed on the YORP cluster administered by the Center for Theory and Computation, part of the Department of Astronomy at the University of Maryland.[6]

8. SVO

   This research has made use of the Spanish Virtual Observatory[7] *Database, supported from the Spanish MICINN/FEDER through grant AyA2017-84089.*

9. Lowell Perkins Telescope

   This dissertation relied on data taken by the Lowell Observatory 1.8m (72inch) Perkins Telescope at the Lowell Observatory in Flagstaff, Arizona.

[6] `https://www.astro.umd.edu/twiki/bin/view/AstroUMD/YorpCluster`
[7] `http://svo.cab.inta-csic.es`

Bibliography

Alcock, C., Fristrom, C. C., & Siegelman, R. 1986, *ApJ*, 302, 462

Alexander, J. B. 1967, The Observatory, 87, 238

Allègre, C., Manhès, G., & Lewin, É. 2001, Earth and Planetary Science Letters, 185, 49

Allende Prieto, C., Lambert, D. L., & Asplund, M. 2001, *ApJL*, 556, L63

Allende Prieto, C., Lambert, D. L., & Asplund, M. 2002, *ApJL*, 573, L137

Andrae, R., Fouesneau, M., Creevey, O., et al. 2018, *A&A*, 616, A8

Andrews, S. M., Wilner, D. J., Hughes, A. M., Qi, C., & Dullemond, C. P. 2009, *ApJ*, 700, 1502

Apai, D., Schneider, G., Grady, C. A., et al. 2015, *ApJ*, 800, 136

Ardila, D. R., Golimowski, D. A., Krist, J. E., et al. 2004, *ApJL*, 617, L147

Artymowicz, P., & Clampin, M. 1997, *ApJ*, 490, 863

Astropy Collaboration, Robitaille, T. P., Tollerud, E. J., et al. 2013, *A&A*, 558, A33

Astropy Collaboration, Robitaille, T. P., Tollerud, E. J., et al. 2013, *A&A*, 558, A33

Aumann, H. H., Gillett, F. C., Beichman, C. A., et al. 1984, *ApJL*, 278, L23

Backman, D. E., & Paresce, F. 1993, in Protostars and Planets III, ed. E. H. Levy & J. I. Lunine, 1253–1304

Balachandran, S. C., Fekel, F. C., Henry, G. W., et al. 2000, *ApJ*, 542, 978

Ballering, N. P., Su, K. Y. L., Rieke, G. H., & Gáspár, A. 2016, *ApJ*, 823, 108

Barber, S. D., Belardi, C., Kilic, M., et al. 2016, *MNRAS*, 459, 1415

Barucci, M. A., Boehnhardt, H., Cruikshank, D. P., & Morbidelli, A. 2008, The Solar System Beyond Neptune: Overview and Perspectives, ed. M. A. Barucci, H. Boehnhardt, D. P. Cruikshank, A. Morbidelli, & R. Dotson, 3–10

Bear, E., & Soker, N. 2013, *NA*, 19, 56

Beckwith, S. V. W., & Sargent, A. I. 1991, *ApJ*, 381, 250

Beichman, C. A., Lisse, C. M., Tanner, A. M., et al. 2011, *ApJ*, 743, 85

Bergeat, J., Knapik, A., & Rutily, B. 2001, *A&A*, 369, 178

Bernstein, R., Shectman, S. A., Gunnels, S. M., et al. 2003, *Proceedings of the SPIE*, 1694

Bharat Kumar, Y., Reddy, B. E., Muthumariappan, C., et al. 2015, *A&A*, 577, A10

Blommaert, J. A. D. L., van der Veen, W. E. C. J., & Habing, H. J. 1993, *A&A*, 267, 39

Boley, A. C., Payne, M. J., Corder, S., et al. 2012, *ApJL*, 750, L21

Bonsor, A., Kennedy, G. M., Wyatt, M. C., Johnson, J. A., & Sibthorpe, B. 2014, *MNRAS*, 437, 3288

Bonsor, A., Kennedy, G. M., Crepp, J. R., et al. 2013, *MNRAS*, 431, 3025

Bonsor, A. & Wyatt, M. 2010, *MNRAS*, 409, 1631. doi:10.1111/j.1365-2966.2010.17412.x

Bonsor, A., & Wyatt, M. C. 2011, American Institute of Physics Conference Series, 1331, 41

Booth, M., Kennedy, G., Sibthorpe, B., et al. 2013, *MNRAS*, 428, 1263

Booth, M., Jordán, A., Casassus, S., et al. 2016, *MNRAS*, 460, L10. doi:10.1093/mnrasl/slw040

Booth, M., Dent, W. R. F., Jordán, A., et al. 2017, *MNRAS*, 469, 3200

Boss, A. P. 1994, *ICAR*, 107, 422

Bressan, A., Marigo, P., Girardi, L., et al. 2012, *MNRAS*, 427, 127

Bressan, A., Marigo, P., Girardi, L., et al. 2013, European Physical Journal Web of Conferences, 43, 03001

Bressan, A., Marigo, P., Girardi, L., et al. 2012, *MNRAS*, 427, 127

Brown, J. A., Sneden, C., Lambert, D. L., et al. 1989, *ApJS*, 71, 293

Brown, D. J. A., Cameron, A. C., Hall, C., et al. 2011, The Astrophysics of Planetary Systems: Formation, Structure, and Dynamical Evolution, 276, 267

Buenzli, E., Thalmann, C., Vigan, A., et al. 2010, *A&A*, 524, L1

Caffau, E., Ludwig, H.-G., Steffen, M., et al. 2011, *Solar Physics*, 268, 255

Cameron, A. G. W. & Fowler, W. A. 1971, *ApJ*, 164, 111

Carlberg, J. K., Cunha, K., Smith, V. V., et al. 2012, *ApJ*, 757, 109

Carlberg, J. K., Cunha, K., Smith, V. V., & Majewski, S. R. 2013, Astronomische Nachrichten, 334, 120

Carry, B. 2012, *Planetary Space Science*, 73, 98

Carpenter, J. M., Bouwman, J., Silverstone, M. D., et al. 2008, *ApJS*, 179, 423

Carpentier, Y., Féraud, G., Dartois, E., et al. 2012, *A&A*, 548, A40

Cauley, P. W., Farihi, J., Redfield, S., et al. 2018, *ApJL*, 852, L22

Charbonnel, C., & Balachandran, S. C. 2000, *A&A*, 359, 563

Charbonnel, C. & Balachandran, S. C. 2000, *A&A*, 359, 563

Chen, C. H., Sargent, B. A., Bohac, C., et al. 2006, *ApJS*, 166, 351

Chen, C.-H. R., Indebetouw, R., Muller, E., et al. 2014, *ApJ*, 785, 162

Chen, C. H., Sheehan, P., Watson, D. M., et al. 2009, *ApJ*, 701, 1367

Chen, Y., Girardi, L., Bressan, A., et al. 2014, *MNRAS*, 444, 2525

Chen, Y., Bressan, A., Girardi, L., et al. 2015, *MNRAS*, 452, 1068

Chen, Y., Girardi, L., Fu, X., et al. 2019, *A&A*, 632, A105

Chiang, E., Kite, E., Kalas, P., Graham, J. R., & Clampin, M. 2009, *ApJ*, 693, 734

Chiang, E. I., Jordan, A. B., Millis, R. L., et al. 2003, *AJ*, 126, 430

Corder, S., Carpenter, J. M., Sargent, A. I., et al. 2009, *ApJL*, 690, L65

Cowie, L. L., & Songaila, A. 1986, *ARA&A*, 24, 499

Cox, N. L. J., Kerschbaum, F., van Marle, A.-J., et al. 2012, *A&A*, 537, A35

Cox, N. L. J., Kerschbaum, F., van Marle, A.-J., et al. 2012, *A&A*, 537, A35

Croll, B., Dalba, P. A., Vanderburg, A., et al. 2015, arXiv:1510.06434

Croll, B., Dalba, P. A., Vanderburg, A., et al. 2017, *ApJ*, 836, 82

Currie, T., Thalmann, C., Matsumura, S., et al. 2011, *ApJL*, 736, L33

Cutri, R. M., & et al. 2012, VizieR Online Data Catalog, 2311, 0

Rodrigues da Silva, R., Canto Martins, B. L., & De Medeiros, J. R. 2015, *ApJ*, 801, 54

Rodrigues da Silva, R., Canto Martins, B. L., & De Medeiros, J. R. 2015, *ApJ*, 801, 54

Davidsson, B. J. R. 1999, *ICAR*, 142, 525

Debes, J. H., Weinberger, A. J., & Kuchner, M. J. 2009, *ApJ*, 702, 318

Debes, J. H., & Sigurdsson, S. 2002, *ApJ*, 572, 556

Debes, J. H., Kilic, M., Faedi, F., et al. 2012, *ApJ*, 754, 59

Debes, J. H., Kilic, M., Faedi, F., et al. 2012, *ApJ*, 754, 59

de Boer, J., Girard, J. H., Canovas, H., et al. 2017, *MNRAS*, 466, L7

de Boer, J., Girard, J. H., Canovas, H., et al. 2017, *MNRAS*, 466, L7

de la Reza, R., Drake, N. A., da Silva, L., et al. 1997, *ApJL*, 482, L77

de la Reza, R., Drake, N. A., Oliveira, I., & Rengaswamy, S. 2015, *ApJ*, 806, 86

Dent, W. R. F., Greaves, J. S., & Coulson, I. M. 2005, *MNRAS*, 359, 663

Dent, W. R. F., Wyatt, M. C., Roberge, A., et al. 2014, Science, 343, 1490

Dohnanyi, J. S. 1969, *JGR*, 74, 2531

Dong, R., Wang, Y., Lin, D. N. C., & Liu, X.-W. 2010, *ApJ*, 715, 1036

Draine, B. T. 2011, Physics of the Interstellar and Intergalactic Medium by Bruce T. Draine. Princeton University Press

Draine, B. T., & Lee, H. M. 1984, *ApJ*, 285, 89

Draine, B. T. 2006, *ApJ*, 636, 1114

Draine, B. T. 2006a, *ApJ*, 636, 1114

—. 2006b, *ApJ*, 636, 1114

Draine, B. T., & Lee, H. M. 1984, *ApJ*, 285, 89

Drake, N. A., de la Reza, R., da Silva, L., et al. 2002, *AJ*, 123, 2703

Dufour, P., Kilic, M., Fontaine, G., et al. 2012, *ApJ*, 749, 6

Dufour, P., Blouin, S., Coutu, S., et al. 2017, 20th European White Dwarf Workshop, 3

Dupuis, J., Fontaine, G., Pelletier, C., et al. 1993, *ApJS*, 84, 73

Dupuis, J., Fontaine, G., & Wesemael, F. 1993, *ApJS*, 87, 345

Dutrey, A., Semenov, D., Chapillon, E., et al. 2014, Protostars and Planets VI, 317

Ertel, S., Wolf, S., Metchev, S., et al. 2011, *A&A*, 533, A132

Evans, D. W., Riello, M., De Angeli, F., et al. 2018, *A&A*, 616, A4

Faedi, F. 2015, *Nature*, 526, 515

Farihi, J., Gänsicke, B. T., Steele, P. R., et al. 2012, *MNRAS*, 421, 1635

Farihi, J., Gänsicke, B. T., & Koester, D. 2013, Science, 342, 218

Fekel, F. C. & Balachandran, S. 1993, *ApJ*, 403, 708

Fekel, F. C., Webb, R. A., White, R. J., & Zuckerman, B. 1996, *ApJL*, 462, L95

Ferland, G. J., Chatzikos, M., Guzmán, F., et al. 2017, *Revista Mexicana de Astronomia y Astrofisica*, 53, 385

Fisher, R. S., Telesco, C. M., Piña, R. K., et al. 2003, *ApJL*, 586, L91

Foreman-Mackey, D., Hogg, D. W., Lang, D., & Goodman, J. 2013, *PASP*, 125, 306

Fortin-Archambault, M., Dufour, P., & Xu, S. 2020, *ApJ*, 888, 47

Gaia Collaboration 2016, VizieR Online Data Catalog, 1337,

Gaia Collaboration 2018, VizieR Online Data Catalog, 1345,

Gaia Collaboration 2016, VizieR Online Data Catalog, 1337,

Gaia Collaboration, Brown, A. G. A., Vallenari, A., et al. 2018, *A&A*, 616, A1

Gaia Collaboration, Brown, A. G. A., Vallenari, A., et al. 2018, *A&A*, 616, A1

Galicher, R., Marois, C., Macintosh, B., et al. 2016, *A&A*, 594, A63. doi:10.1051/0004-6361/201527828

Gänsicke, B. T., Marsh, T. R., Southworth, J., et al. 2006, Science, 314, 1908

Gänsicke, B. T., Marsh, T. R., & Southworth, J. 2007, *MNRAS*, 380, L35

Gänsicke, B. T., Schreiber, M. R., Toloza, O., et al. 2019, *Nature*, 576, 61

Gänsicke, B. T., Koester, D., Girven, J., et al. 2010, Science, 327, 188

Gänsicke, B. T., Koester, D., Farihi, J., et al. 2012, *MNRAS*, 424, 333

Gänsicke, B. T., Koester, D., Farihi, J., et al. 2012, *MNRAS*, 424, 333

Gáspár, A., Psaltis, D., Rieke, G. H., & Özel, F. 2012, *ApJ*, 754, 74

Gilroy, K. K., & Brown, J. A. 1991, *ApJ*, 371, 578

Goodman, J., & Weare, J. 2010, Communications in Applied Mathematics and Computational Science, 5, 65

Grevesse, N., & Sauval, A. J. 1998, *SSRv*, 85, 161

Grevesse, N., Asplund, M., Sauval, A. J., et al. 2010, *Ap&SS*, 328, 179

Griffin, M. J., Abergel, A., Abreu, A., et al. 2010, *A&A*, 518, L3

Goodman, J., & Weare, J. 2010, Communications in Applied Mathematics and Computational Science, 5, 65

Guo, J., Tziamtzis, A., Wang, Z., et al. 2015, *ApJL*, 810, L17

Hahn, J. M., & Malhotra, R. 2005, *AJ*, 130, 2392

Hankins, M. J., Herter, T. L., Maercker, M., Lau, R. M., & Sloan, G. C. 2018, *ApJ*, 852, 27

Hartmann, S., Nagel, T., Rauch, T., et al. 2016, *A&A*, 593, A67

Heisler, J., Tremaine, S., & Alcock, C. 1987, *ICAR*, 70, 269

Herczeg, G. J., Wood, B. E., Linsky, J. L., et al. 2004, *ApJ*, 607, 369

Hillenbrand, L. A., Carpenter, J. M., Kim, J. S., et al. 2008, *ApJ*, 677, 630

Hines, D. C., Schneider, G., Hollenbach, D., et al. 2007, *ApJL*, 671, L165

Holanda, N., Drake, N. A., & Pereira, C. B. 2020, *AJ*, 159, 9

Holanda, N., Drake, N. A., & Pereira, C. B. 2020, *AJ*, 159, 9

Holland, W. S., Greaves, J. S., Dent, W. R. F., et al. 2003, *ApJ*, 582, 1141

Holweger, H. 2001, Joint SOHO/ACE Workshop "solar and Galactic Composition", 23

Höfner, S., & Olofsson, H. 2018, *Astronomy and Astrophysics Reviews*, 26, 1

Horne, K. & Marsh, T. R. 1986, *MNRAS*, 218, 761

Hughes, A. M., Wilner, D. J., Andrews, S. M., et al. 2011, *ApJ*, 740, 38

Hughes, A. M., Wilner, D. J., Mason, B., et al. 2012, *ApJ*, 750, 82

Hughes, A. M., Lieman-Sifry, J., Flaherty, K. M., et al. 2017, *ApJ*, 839, 86

Hughes, A. M., Duchêne, G., & Matthews, B. C. 2018, *ARA&A*, 56, 541

Iben, I. 1974, *ARA&A*, 12, 215

Iben, I. 1973, *ApJ*, 185, 209

Iben, I. 1967, *ApJ*, 147, 650

Iben, I. 1967, *ApJ*, 147, 624

Iben, I. 1967, *ARA&A*, 5, 571

Janson, M., Carson, J. C., Lafrenière, D., et al. 2012, *ApJ*, 747, 116

Jasniewicz, G., Parthasarathy, M., de Laverny, P., et al. 1999, *A&A*, 342, 831

Jasniewicz, G., Parthasarathy, M., de Laverny, P., et al. 1999, *A&A*, 342, 831

Jorissen, A., Van Winckel, H., Siess, L., et al. 2020, *A&A*, 639, A7

Jura, M. 1999, *ApJ*, 515, 706. doi:10.1086/307064

Jura, M. 2003, *ApJL*, 584, L91

Jura, M. 2003, *ApJ*, 582, 1032

Jura, M., Bohac, C. J., Sargent, B., et al. 2006, *ApJL*, 637, L45

Jura, M., Bohac, C. J., Sargent, B., et al. 2006, *ApJL*, 637, L45

Jura, M., Farihi, J., & Zuckerman, B. 2007, *ApJ*, 663, 1285

Jura, M. 2008, *AJ*, 135, 1785

Jura, M., & Xu, S. 2013, *AJ*, 145, 30

Jura, M., & Young, E. D. 2014, Annual Review of Earth and Planetary Sciences, 42, 45

Jura, M., & Young, E. D. 2014, Annual Review of Earth and Planetary Sciences, 42, 45

Jura, M., Dufour, P., Xu, S., et al. 2015, *ApJ*, 799, 109

Kalas, P., Graham, J. R., Fitzgerald, M. P., & Clampin, M. 2013, *ApJ*, 775, 56

Kalas, P., Liu, M. C., & Matthews, B. C. 2004, Science, 303, 1990

Kastner, J. H., Montez, R., Rodriguez, D., et al. 2010, *ApJL*, 719, L65

Kastner, J. H., Zuckerman, B., & Forveille, T. 2008, *A&A*, 486, 239

Keller, L. D., Sloan, G. C., Forrest, W. J., et al. 2008, *ApJ*, 684, 411

Kennedy, G. M., Wyatt, M. C., Sibthorpe, B., et al. 2012, *MNRAS*, 426, 2115

Kennedy, G. M., & Wyatt, M. C. 2014, *MNRAS*, 444, 3164

Kharchenko, N. V., & Roeser, S. 2009, VizieR Online Data Catalog, 1280, 0

Kobulnicky, H. A. & Phillips, A. C. 2003, *ApJ*, 599, 1031

Kobayashi, H., Kimura, H., Watanabe, S.-. i ., et al. 2011, Earth, Planets, and Space, 63, 1067

Koerner, D. W., Sargent, A. I., & Ostroff, N. A. 2001, *ApJL*, 560, L181

Koester, D., Gänsicke, B. T., & Farihi, J. 2014, *A&A*, 566, A34

Koester, D. 2009, *A&A*, 498, 517

Koester, D., & Wilken, D. 2006, *A&A*, 453, 1051

Koester, D. 2010, *Mem. Societa Astronomica Italiana*, 81, 921

Koester, D., Rollenhagen, K., Napiwotzki, R., et al. 2005, 14th European Workshop on White Dwarfs, 334, 215

Koester, D., Gänsicke, B. T., & Farihi, J. 2014, *A&A*, 566, A34

Kóspál, Á., Moór, A., Juhász, A., et al. 2013, *ApJ*, 776, 77

Krivov, A. V. 2007, Dust in Planetary Systems, 643, 123

Krist, J. E., Ardila, D. R., Golimowski, D. A., et al. 2005, *AJ*, 129, 1008

Kuchner, M. J., & Stark, C. C. 2010, *AJ*, 140, 1007

Kumar, Y. B., Reddy, B. E., & Lambert, D. L. 2011, *ApJL*, 730, L12

Lagrange, A.-M., Bonnefoy, M., Chauvin, G., et al. 2010, Science, 329, 57

Lagrange, A.-M., Boccaletti, A., Milli, J., et al. 2012, *A&A*, 542, A40

Lebreton, J., Augereau, J.-C., Thi, W.-F., et al. 2012, *A&A*, 539, A17

Lebreton, J., Beichman, C., Bryden, G., et al. 2016, *ApJ*, 817, 165

Lejeune, T., Cuisinier, F., & Buser, R. 1997, *A&AS*, 125, 229

Livio, M. & Soker, N. 1984, *MNRAS*, 208, 763

Lloyd Evans, T. 2010, Journal of Astrophysics and Astronomy, 31, 177

Lodders, K. 2003, *ApJ*, 591, 1220

Lyra, W., & Kuchner, M. 2013, *Nature*, 499, 184

Lyra, W., & Kuchner, M. 2013, *Nature*, 499, 184

MacGregor, M. A., Wilner, D. J., Rosenfeld, K. A., et al. 2013, *ApJL*, 762, L21

MacGregor, M. A., Wilner, D. J., Chandler, C., et al. 2016, *ApJ*, 823, 79. doi:10.3847/0004-637X/823/2/79

MacGregor, M. A., Weinberger, A. J., Hughes, A. M., et al. 2018, *ApJ*, 869, 75. doi:10.3847/1538-4357/aaec71

Maercker, M., Ramstedt, S., Leal-Ferreira, M. L., Olofsson, G., & Floren, H. G. 2014, *A&A*, 570, A101

Maercker, M., Vlemmings, W. H. T., Brunner, M., et al. 2016, *A&A*, 586, A5

Maercker, M., Mohamed, S., Vlemmings, W. H. T., et al. 2012, *Nature*, 490, 232

Malmberg, D., & Davies, M. B. 2009, *MNRAS*, 394, L26

Malmberg, D., Davies, M. B., & Heggie, D. C. 2011, *MNRAS*, 411, 859

Malmberg, D., de Angeli, F., Davies, M. B., et al. 2007, *MNRAS*, 378, 1207

Mamajek, E. E., & Bell, C. P. M. 2014, *MNRAS*, 445, 2169

Maness, H., Kalas, P., Fitzgerald, M., et al. 2010, in Bulletin of the American Astronomical Society, Vol. 42, American Astronomical Society Meeting Abstracts 215, 361.04

Maness, H. L., Fitzgerald, M. P., Paladini, R., et al. 2008, *ApJL*, 686, L25

Manser, C. J., Gänsicke, B. T., Marsh, T. R., et al. 2016, *MNRAS*, 455, 4467

Manser, C. J., Gänsicke, B. T., Koester, D., et al. 2016, *MNRAS*, 462, 1461. doi:10.1093/mnras/stw1760

Manser, C. J., Gänsicke, B. T., Eggl, S., et al. 2019, Science, 364, 66

Marigo, P., Girardi, L., Bressan, A., et al. 2017, *ApJ*, 835, 77

Marigo, P., Girardi, L., Bressan, A., et al. 2017, *ApJ*, 835, 77

Marigo, P., Girardi, L., Bressan, A., et al. 2017, *ApJ*, 835, 77

Marino, S., Matrà, L., Stark, C., et al. 2016, *MNRAS*, 460, 2933

Marois, C., Zuckerman, B., Konopacky, Q. M., Macintosh, B., & Barman, T. 2010, *Nature*, 468, 1080

Marois, C., Macintosh, B., Barman, T., et al. 2008, Science, 322, 1348

Marzari, F., & Picogna, G. 2013, *A&A*, 550, A64

Mathis, J. S., Rumpl, W., & Nordsieck, K. H. 1977, *ApJ*, 217, 425

Matthews, B. C., Krivov, A. V., Wyatt, M. C., Bryden, G., & Eiroa, C. 2014, Protostars and Planets VI, 521

McCook, G. P., & Sion, E. M. 1999, *ApJS*, 121, 1

McDonald, I., Zijlstra, A. A., & Watson, R. A. 2017, *MNRAS*, 471, 770.

McSween, Jr., Harry Y. & Huss, Gary R. 2001, Cosmochemistry, Cambridge University Press

Melis, C., Zuckerman, B., Song, I., Rhee, J. H., & Metchev, S. 2009, *ApJ*, 696, 1964

Melis, C., Gielen, C., Chen, C. H., et al. 2010, *ApJ*, 724, 470

Melis, C., Gielen, C., Chen, C. H., et al. 2010, *ApJ*, 724, 470

Melis, C., Dufour, P., Farihi, J., et al. 2012, *ApJL*, 751, L4

Melo, C. H. F., de Laverny, P., Santos, N. C., et al. 2005, *A&A*, 439, 227

Metzger, B. D., Rafikov, R. R., & Bochkarev, K. V. 2012, *MNRAS*, 423, 505

Meyer, D. M., Jura, M., & Cardelli, J. A. 1998, *ApJ*, 493, 222

Miglio, A., Brogaard, K., Stello, D., et al. 2012, *MNRAS*, 419, 2077

Miroshnichenko, A. S., Bergner, Y. K., & Kuratov, K. S. 1996, *A&A*, 312, 521

Miroshnichenko, A. S., Manset, N., Kusakin, A. V., et al. 2007, *ApJ*, 671, 828

Moór, A., Juhász, A., Kóspál, Á., et al. 2013, *ApJL*, 777, L25

Morales, F. Y., Bryden, G., Werner, M. W., & Stapelfeldt, K. R. 2013, *ApJ*, 776, 111

Morales, F. Y., Rieke, G. H., Werner, M. W., et al. 2011, *ApJL*, 730, L29

Moro-Martin, A. 2013, Dusty Planetary Systems, ed. T. D. Oswalt, L. M. French, & P. Kalas, 431

Mouillet, D., Larwood, J. D., Papaloizou, J. C. B., & Lagrange, A. M. 1997, *MNRAS*, 292, 896

Mustill, A. J., Veras, D., & Villaver, E. 2014, *MNRAS*, 437, 1404

Nagel, T., Dreizler, S., Rauch, T., et al. 2004, *A&A*, 428, 109

Najita, J., & Williams, J. P. 2005, *ApJ*, 635, 625

Nordhaus, J. & Spiegel, D. S. 2013, *MNRAS*, 432, 500

Nordhaus, J., Spiegel, D. S., Ibgui, L., et al. 2010, *MNRAS*, 408, 631

Ott, S. 2010, Astronomical Data Analysis Software and Systems XIX, 434, 139

Pan, M., & Schlichting, H. E. 2012, *ApJ*, 747, 113

Parthasarathy, M. 1991, *A&A*, 247, 429

Parthasarathy, M. 1991, *A&A*, 247, 429

Pastorelli, G., Marigo, P., Girardi, L., et al. 2019, *MNRAS*, 485, 5666

Patience, J., Bulger, J., King, R. R., et al. 2011, *A&A*, 531, L17

Pawellek, N., Krivov, A. V., Marshall, J. P., et al. 2014, ArXiv e-prints, arXiv:1407.4579

Peeters, E., Hony, S., Van Kerckhoven, C., et al. 2002, *A&A*, 390, 1089

Planck Collaboration, Abergel, A., Ade, P. A. R., et al. 2014, *A&A*, 571, A11

Piétu, V., di Folco, E., Guilloteau, S., Gueth, F., & Cox, P. 2011, *A&A*, 531, L2

Pino, T., Dartois, E., Cao, A.-T., et al. 2008, *A&A*, 490, 665

Pinte, C., Ménard, F., Duchêne, G., et al. 2006, *A&A*, 459, 797. doi:10.1051/0004-6361:20053275

Pinte, C., Harries, T. J., Min, M., et al. 2009, *A&A*, 498, 967. doi:10.1051/0004-6361/200811555

Poglitsch, A., Waelkens, C., Geis, N., et al. 2010, *A&A*, 518, L2. doi:10.1051/0004-6361/201014535

Press, W. H., Teukolsky, S. A., Vetterling, W. T., & Flannery, B. P. 2002, Numerical recipes in C++ : the art of scientific computing

Punzi, K. M., Kastner, J. H., Melis, C., et al. 2018, *AJ*, 155, 33

Quillen, A. C. 2006, *MNRAS*, 372, L14

Rappaport, S., Gary, B. L., Kaye, T., et al. 2016, *MNRAS*, 458, 3904

Rebull, L. M., Carlberg, J. K., Gibbs, J. C., et al. 2015, *AJ*, 150, 123

Reddy, B. E. & Lambert, D. L. 2005, *AJ*, 129, 2831

Reddy, B. E., & Lambert, D. L. 2005, *AJ*, 129, 2831

Reddy, B. E., Lambert, D. L., Hrivnak, B. J., et al. 2002, *AJ*, 123, 1993

Reimers, D. 1975, Memoires of the Societe Royale des Sciences de Liege, 8, 369

Ricarte, A., Moldvai, N., Hughes, A. M., et al. 2013, *ApJ*, 774, 80

Ricci, L., Carpenter, J. M., Fu, B., et al. 2015, *ApJ*, 798, 124

Roccatagliata, V., Henning, T., Wolf, S., et al. 2009, *A&A*, 497, 409

Rodigas, T. J., Stark, C. C., Weinberger, A., et al. 2015, *ApJ*, 798, 96

Roussel, H. 2013, *PASP*, 125, 1126. doi:10.1086/673310

Sackmann, I.-J. & Boothroyd, A. I. 1999, *ApJ*, 510, 217

Sackmann, I.-J. & Boothroyd, A. I. 1995, *Mem. Societa Astronomica Italiana*, 66, 403

Sackmann, I.-J. & Boothroyd, A. I. 1992, *ApJL*, 392, L71

Schneider, G., Silverstone, M. D., Hines, D. C., et al. 2006, *ApJ*, 650, 414

Schneider, G., Grady, C. A., Hines, D. C., et al. 2014, *AJ*, 148, 59

Scicluna, P., Kemper, F., Trejo, A., et al. 2020, *MNRAS*, 494, 2925

Siess, L. & Livio, M. 1999, *MNRAS*, 308, 1133

Skinner, C. J. 1994, *MNRAS*, 271, 300

Sloan, G. C., Jura, M., Duley, W. W., et al. 2007, *ApJ*, 664, 1144

Sloan, G. C., Jura, M., Duley, W. W., et al. 2007, *ApJ*, 664, 1144

Smith, B. A., & Terrile, R. J. 1984, Science, 226, 1421

Smolders, K., Acke, B., Verhoelst, T., et al. 2010, *A&A*, 514, L1

Snow, T. P., Destree, J. D., & Jensen, A. G. 2007, *ApJ*, 655, 285

Soummer, R., Perrin, M. D., Pueyo, L., et al. 2014, *ApJL*, 786, L23

Stark, C. C. 2011, *AJ*, 142, 123

Stark, C. C., Schneider, G., Weinberger, A. J., et al. 2014, *ApJ*, 789, 58

Steele, A., Hughes, A. M., Carpenter, J., et al. 2016, *ApJ*, 816, 27

Stephenson, C. B. 1986, *ApJ*, 300, 779

Strubbe, L. E., & Chiang, E. I. 2006, *ApJ*, 648, 652

Su, K. Y. L., Rieke, G. H., Stapelfeldt, K. R., et al. 2009, *ApJ*, 705, 314

Su, K. Y. L., Rieke, G. H., Malhotra, R., et al. 2013, *ApJ*, 763, 118

Subasavage, J. P., Jao, W.-C., Henry, T. J., et al. 2017, *AJ*, 154, 32

Swift, J. J., Johnson, J. A., Morton, T. D., et al. 2013, *ApJ*, 764, 105

Sylvester, R. J. & Mannings, V. 2000, *MNRAS*, 313, 73

Tang, J., Bressan, A., Rosenfield, P., et al. 2014, *MNRAS*, 445, 4287

Tielens, A. G. G. M. 2008, *ARA&A*, 46, 289

Torres, C. A. O., Quast, G. R., de La Reza, R., & da Silva, L. 2000, The Light Elements and their Evolution, 198, 320

Tremblay, P.-E., & Bergeron, P. 2009, *ApJ*, 696, 1755

Vanderburg, A., Johnson, J. A., Rappaport, S., et al. 2015, *Nature*, 526, 546

Vanderburg, A., Johnson, J. A., Rappaport, S., et al. 2015, *Nature*, 526, 546

Vanderburg, A., Rappaport, S. A., Xu, S., et al. 2020, *Nature*, 585, 363. doi:10.1038/s41586-020-2713-y

Vennes, S. & Kawka, A. 2013, *ApJ*, 779, 70

Veras, D., Leinhardt, Z. M., Bonsor, A., et al. 2014, *MNRAS*, 445, 2244

Veras, D., Leinhardt, Z. M., Bonsor, A., & Gänsicke, B. T. 2014, *MNRAS*, 445, 2244

Veras, D., Eggl, S., & Gänsicke, B. T. 2015, *MNRAS*, 452, 1945

Veras, D., Mustill, A. J., Gänsicke, B. T., et al. 2016, *MNRAS*, 458, 3942

Villaver, E. & Livio, M. 2009, *ApJL*, 705, L81

Villaver, E. & Livio, M. 2007, *ApJ*, 661, 1192

Vogt, S. S., Allen, S. L., Bigelow, B. C., et al. 1994, *Proceedings of the SPIE*, 362

Voss, B., Koester, D., Napiwotzki, R., et al. 2007, *A&A*, 470, 1079

Wallerstein, G., Iben, I., Parker, P., et al. 1997, Reviews of Modern Physics, 69, 995

Wallerstein, G. & Sneden, C. 1982, *ApJ*, 255, 577

Watanabe, S., Hirabayashi, M., Hirata, N., et al. 2019, Lunar and Planetary Science Conference, 1265

Weiler, M. 2018, *A&A*, 617, A138. doi:10.1051/0004-6361/201833462

Whitelock, P. A., Menzies, J. W., Catchpole, R. M., et al. 1991, *MNRAS*, 250, 638

Williams, J. P., Najita, J., Liu, M. C., et al. 2004, *ApJ*, 604, 414

Williams, J. P. & Cieza, L. A. 2011, *ARA&A*, 49, 67

Wilner, D. J., Andrews, S. M., & Hughes, A. M. 2011, *ApJL*, 727, L42

Wilner, D. J., Andrews, S. M., MacGregor, M. A., & Hughes, A. M. 2012, *ApJL*, 749, L27

Wilner, D. J., Holman, M. J., Kuchner, M. J., & Ho, P. T. P. 2002, *ApJL*, 569, L115

Wilson, D. J., Gänsicke, B. T., Koester, D., et al. 2014, *MNRAS*, 445, 1878

Wilson, D. J., Gaensicke, B. T., Koester, D., et al. 2015, 19th European Workshop on White Dwarfs, 493, 279

Wilson, P. A., Lecavelier des Etangs, A., Vidal-Madjar, A., et al. 2017, *A&A*, 599, A75

Wyatt, M. C. 2003, *ApJ*, 598, 1321

—. 2006, *ApJ*, 639, 1153

—. 2008a, ArXiv e-prints, arXiv:0807.1272

—. 2008b, *ARA&A*, 46, 339

Wyatt, M. C., & Dent, W. R. F. 2002, *MNRAS*, 334, 589

Xu, S., & Jura, M. 2012, *ApJ*, 745, 88

Xu, S., Jura, M., Koester, D., Klein, B., & Zuckerman, B. 2014, *ApJ*, 783, 79

Xu, S., & Jura, M. 2014, *ApJL*, 792, L39

Xu, S., Jura, M., Klein, B., et al. 2013, *ApJ*, 766, 132

Xu, S., Jura, M., Dufour, P., et al. 2016, *ApJL*, 816, L22

Xu, S., Jura, M., Dufour, P., & Zuckerman, B. 2016, *ApJL*, 816, L22

Xu, S., Hallakoun, N., Gary, B., et al. 2019, *AJ*, 157, 255

Xu, S., Dufour, P., Klein, B., et al. 2019, *AJ*, 158, 242

Zakamska, N. L., & Tremaine, S. 2004, *AJ*, 128, 869

Zabot, A., Kanaan, A., & Cid Fernandes, R. 2009, *ApJL*, 704, L93

Zuckerman, B., Melis, C., Song, I., et al. 2008, *ApJ*, 683, 1085

Zhang, X. & Jeffery, C. S. 2013, *MNRAS*, 430, 2113

Zuckerman, B., Melis, C., Song, I., et al. 2008, *ApJ*, 683, 1085-1103

Zuckerman, B., Koester, D., Reid, I. N., & Hünsch, M. 2003, *ApJ*, 596, 477

Zuckerman, B., Koester, D., Melis, C., Hansen, B. M., & Jura, M. 2007, *ApJ*, 671, 872